A-priori analysis of LES subgrid scale models applied to wall turbulence with pressure gradients

Cuicui Li

N^o d'ordre: 231

ECOLE CENTRALE DE LILLE

THESE

présentée en vue
d'obtenir le grade de

DOCTEUR

en

Mécanique

par

Cuicui LI

DOCTORAT DELIVRÉ PAR L'ÉCOLE CENTRALE DE LILLE

Titre de la Thèse:

Analyse a-priori de modèles LES sous-mailles appliqués à la turbulence de paroi avec gradients de pression

A-priori analysis of LES subgrid scale models applied to wall turbulence with pressure gradients

Soutenue le 18 Novembre 2013 devant le jury composé de:

Président du jury	Pr. E. Leriche, LML, Université des Sciences et Technologies de Lille
Rapporteur	Pr. E. Lamballais, PPRIME, Université de Poitiers
Rapporteur	Dr. L. Shao, LMFA, Ecole Centrale de Lyon
Examinateur	Pr. P. Sagaut, IJLRA, Université Pierre et Marie Curie - Paris 6
Examinateur	Dr. E. Lévêque, Laboratoire de Physique, Ecole Normale Supérieure de Lyon
Directeur de thèse	Pr. M. Stanislas, LML, Ecole Centrale de Lille
Encadrant	Dr. J.-P. Laval, LML, CNRS, Lille

Thèse préparée au Laboratoire de Mécanique de Lille
Ecole Doctorale SPI 072 (Lille I, Lille III, Artois, ULCO, UVHC, EC Lille)
PRES Université Lille Nord-de-France

Remerciements

Je tiens tout d'abord à remercier chaleureusement Monsieur E. Lamballais, L. Shao, P. Sagaut, E. Lévêque, E. Leriche pour avoir accepté d'être membres du jury. Je tiens à remercier plus particuliérement Monsieur E. Lamballais, L. Shao pour le temps qu'ils ont consacré à rapporter ce travail.

Ma reconnaissance va aussi à Monsieur M. Stanislas, mon directeur de thèse, pour m'avoir guidé tout au long de ce travail et pour m'avoir fait profiter de ses connaissances en turbulence. Ses remarques, toujours pertinentes, ont grandement contribué à l'avancement de ce travail.

Ma gratitude va aussi à Monsieur J.-P. Laval, mon co-encadrant, pour le temps qu'il m'a consacré et pour la résolution des divers problémes rencontrés. Je le remercie aussi pour ses explications claires et toujours données dans la bonne humeur.

Ma reconnaissance va aussi à tous mes collégues et tous les membres de l'équipe ER2 du labo, qui m'ont accueilli à bras ouverts et qui ont largement contribué à me donner de bonnes conditions de travail.

Je tiens à remercier tous mes amis pour leurs aides pendant les trois ans.

Finalement, ma reconnaissance va aussi à mes parents pour m'avoir permis de poursuivre mes études dans des trés bonnes conditions.

Résumé

Après plus de 50 ans de recherche, l'intéret de la simulation des grandes échelles pour la simulation des écoulements instationnaire a été largement démontrée et cette méthode est aujourd'hui utilisée pour une grande variété d'applications industriels. Plusieurs classes de modèles sous-maille ont été proposées dont celle très connue des modèles de viscosité sous-maille souvent préférrées pour leur simplicité et leur robustesse. La formulation de ces modèles comporte un coefficient qui doit être ajusté ppour chaque type d'écoulement et qui a été analysé pour des géométries simples. L'objectif de ce travail est de réaliser des analyses a-priori de modèles sous-mailles dans un canal plan et un canal convergent-divergent à relativement grand nombre de Reynolds. Les influences du type de filter et de la largeur du filtre sont systématiquement abordées pour chacune des statistiques. Le transfert d'énergie sous-maille et la dissipation sous-maille sont tout d'abord étudiés. Ensuite, les coefficients des modèles Smagorinsky, Smgorinsky dynamique, WALE et du modèle Sigma nouvellement proposé sont estimés a-priori. Il est démontré que les coefficients des quatres modèles sont non-homogème dans le domaine de simulation est sont largement affectés par le gradient de pression adverse, principalement dans la zone de recirculation. enfin, les corrélations entre les quantités exactes et leur équivalents modélisés sont examinés. Les résultats montrent un faible niveau de prédiction des modèles sous-maille et une grande variabilité des quantités modélisées dans les regions de fort gradient de pression adverse. Ceci peut expliquer les difficultés pour obtenir de bons résultats LES dans une telle configuration.

Abstract

After more than 50 years of investigation, Large Eddy Simulation has demonstrated its benefit for unsteady flow simulation and is currently applied in a wide variety of engineering applications. Several classes of subgrid scale models were proposed, including the well known eddy viscosity models, usually preferred because of their simplicities and robustness. The formulation of these models includes a coefficient which needs to be analyzed for each flow configuration and which has been investigated in simple geometries. The aim of present work is to perform a-priori analysis of subgrid scale models in plane channel flow and in a converging-diverging channel flow at fairly large Reynolds number. The influences of the filter type and filter width are systematically addressed in analyses of all statistics. The SGS energy transfer and SGS energy dissipation are firstly analyzed. Then, the a priori estimate of the coefficients of subgrid scale models, including the standard Smagorinsky, Dynamic Smagorinsky, the WALE and the new updated σ models, are investigated in detail. It is shown that, the coefficients of the four models are non-homogeneous in the simulation domain and are largely affected by the adverse pressure gradient, especially in the recirculation region. Finally, the correlations between the exact quantities and their counterparts modeled by the subgrid scale models with respect to three criteria are explored. The results show a low predictability of subgrid scale models and a strong variability of the modeled quantities in the region of strong adverse pressure gradient. This may explain the difficulty to obtain accurate LES results in such flow configuration.

Contents

List of Figures

List of Tables

Chapter 1

Introduction

1.1. The nature of turbulence

In fluid dynamics, turbulence is a flow regime characterized by chaotic and stochastic property changes. This includes low momentum diffusion, high momentum convection, and rapid variation of pressure and velocity in space and time (Fig. 1.1). Turbulence was recognized as a distinct fluid behavior by Leonardo da Vinci more than 500 years ago (Fig. 1.2). It is Leonardo who termed such motions "turbolenze", and hence the origin of our modern word for this type of fluid flow. There are many opportunities to observe turbulent flows in our everyday surroundings, whether it be smoke from a chimney, water from a river or waterfall, or the buffeting of a strong wind. In observing a waterfall, we immediately see that the flow is unsteady, irregular, seemingly random and chaotic, and surely the motion of every eddy or droplet is unpredictable (Pope 2000 [116]). But it wasn't until the beginning of the last century that researchers were able to develop a rigorous mathematical treatment of turbulence. The first major step was taken by Taylor during the 1930s, who introduced formal statistical methods involving correlations, Fourier transform and power spectra into the turbulence literature. In a paper published in 1935 in the Proceedings of the Royal Society of London, Taylor very explicitly presented the assumption that turbulence is a random phenomenon and then proceeded to introduce statistical tools for the analysis of homogeneous, isotropic turbulence. In 1941 the Russian statistician Kolmogorov published three papers (in Russian) that provided some of the most important and most often quoted results of turbulence theory. These results represented a major success of the statistical theory of turbulence. This theory provided a prediction for the energy spectrum of a 3D isotropic homogeneous turbulent flow. Kolmogorov proved that even though the velocity of an isotropic homogeneous turbulent flow fluctuates in an unpredictable fashion, the energy spectrum (how much kinetic energy is present on average at a particular scale) is predictable. The spectral theory of Kolmogorov had a profound impact on the field of turbulence and it also represented the foundation of many theories of turbulence.

Nobel Laureate R. Feynman described turbulence as "the most important unsolved problem of classical physics" [142], but Pordal (2006) [117] explained that, due to the advent of faster computers especially the access of supercomputers, the role of computational methods in engineering design and analysis has greatly increased during the last

Figure 1.1: Turbulence on many different scales in a high Reynolds number

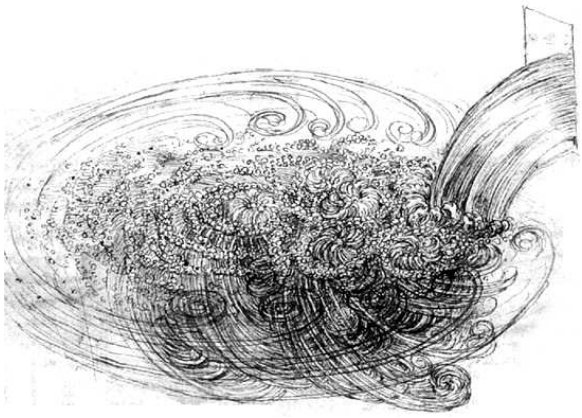

Figure 1.2: Leonardo da Vinci's observation of turbulent flow

decade. The application of Computational Fluid Dynamics (CFD) for solving problems of turbulence has increased dramatically in the last 50 years with the objective to compute the more precise solutions of the Navier-Stokes equations.

1.2. Wall turbulence

Over the past years, wall turbulence has attracted a lot of attentions from scientists, due to its complexity and challenges in understanding its mechanisms. Among the different regions of the boundary layer, the wall region is particularly challenging because the dimensions are getting so small that they are difficult to investigate (Stanislas *et al.* 2009 [134]).

1.2.1. Flow near the wall

When a viscous fluid flows along a fixed impermeable wall, or past the rigid surface of an immersed body, an essential condition is that the velocity at any point on the wall or other fixed surface is zero. This condition modifies the general character of the flow depending upon the value of the viscosity. If the body is of streamlined shape and if the viscosity is small without being negligible, the modifying effect appears to be confined within narrow regions adjacent to the solid surfaces, these are called "boundary layers". Within such layers the fluid velocity changes rapidly from zero to its main stream value, and this may imply a steep gradient of shearing stress. As a consequence, not all the viscous terms in the equation of motion will be negligible, even though the viscosity, which they contain as a factor, is itself very small. Thus the boundary layers at high Reynolds number are extremely thin.

The boundary layers may be either laminar (layered), or turbulent (disordered) depending on the value of the Reynolds number. At low Reynolds number, the boundary layer is laminar and the streamwise velocity changes uniformly as one moves away from the wall, as shown on the left side of the Fig. (1.3). At high Reynolds number, the boundary layer is turbulent and the streamwise velocity is characterized by unsteady (changing

with time) swirling flows inside it. The external flow reacts to the edge of the boundary layer just as it would to the physical surface of an object. So the boundary layer gives any object an "effective" shape which is usually slightly different from the physical shape. To make things more confusing, the boundary layer may lift off or "separate" from the body and create an effective shape much different from the physical shape. This happens because the flow in the boundary has very low energy (relative to the free stream) and is more easily driven by changes in pressure. Flow separation is the reason for wing stall at high angle of attack.

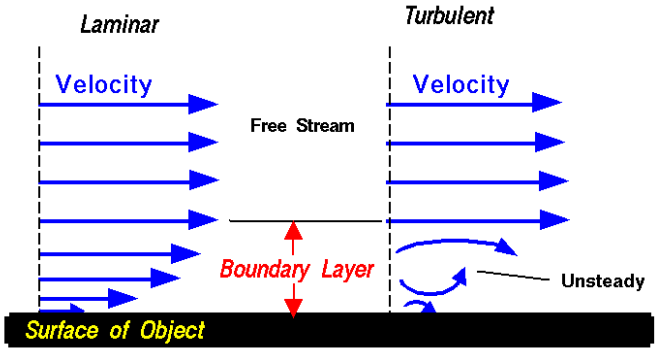

Figure 1.3: Boundary layer of plane channel flow (velocity is zero at the surface), figure from Glenn Research Center, NASA

Knowing this, it's easy to find various boundary layers in practice. Such as the flow around aircraft and ships' hulls, the atmospheric boundary layer, and the flow of rivers. In each of these flows the mean velocity vector is nearly parallel to the wall, and the near-wall behaviors in each of these cases are very similar (Pope 2000 [116]). Various wall-bounded flows occur frequently in engineering applications. The simplest is the plane channel flow, since homogeneity can be assumed in the streamwise and spanwise directions. For this reason, a lot of studies have focused on plane channel flow as an important reference case for the testing and development of subgrid scale (SGS) turbulence models (Mayers *et al.* 2007 [98]).

1.2.2. The law of the wall

The general fluid equations have been known for many years, but solutions to these equations have not properly described the observed flow effects (like boundary layers). The theory describing the boundary layer effects was first presented by Prandtl in the early 1900's. Prandtl was the first to realize that the relative magnitude of the inertial and viscous forces changed from a layer very near the surface to a region far from the surface. He first proposed the interactively coupled, two layers solution which properly models many flow problems.

The description of a stationary 2D flat plate boundary layer is given in Fig. (1.4). Quantities made non-dimensional using friction velocity u_τ and kinematic viscosity ν are said to be expressed in wall units and denoted by a superscript + ($u^+ = u/u_\tau, y^+ = yu_\tau/\nu$). The boundary layer is usually divided into two parts, the wall-layer (or inner layer), which extends though the bottom $10 - 20\%$ of the layer and is usually defined as $y/\delta < 0.1$ (y is the distance from the wall, δ is half-height of the channel), and the outer

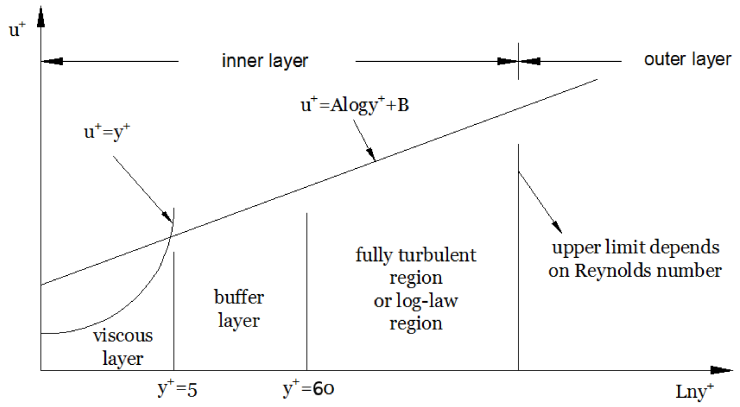

Figure 1.4: Mean velocity profile of a smooth-flat-plate turbulent boundary layer plotted in log-linear coordinates with law-of-the-wall normalizations

layer which covers the remainder [109]. The wall layer is characterized by large velocity gradients, significant production and dissipation of turbulence.

Prandtl (1925) postulated that, at high Reynolds number, close to the wall ($y/\delta << 1$), there is an inner layer, in which the turbulent stress is negligible and the mean velocity profile is determined by the viscous scale. This viscous sublayer extends until approximately $y^+ = 5$. The velocity profile can be written as:

$$u^+ = y^+ \tag{1.1}$$

Above the viscous sublayer is the buffer layer extending to $y^+ \approx 60$, in which the viscous effects progressively become less important. This region contains the peak of turbulent kinetic energy and turbulence production, which often occurs at $y^+ = 12$. It's also the transitional region between the viscosity dominated and the turbulence dominated parts of the flow [109].

Above this, it's the overlap region between the wall layer and the outer layer, which is called the logarithmic layer. In this region, the turbulent stress plays a dominant role. The velocity profile complies with the logarithmic law:

$$u^+ = Alog(y^+) + B \tag{1.2}$$

Where A and B are constant. This law is consistent in both inner and outer layer. In the outer layer, the fluid velocity increases with distance from the wall to freestream velocity. This is known as fully developed flow.

1.3. Turbulence modelling

Turbulence modeling is a key issue in most CFD simulations. Virtually all engineering applications are turbulent and hence require a turbulence model. Various methods have been proposed in the process of turbulence research.

A Direct Numerical Simulation (DNS, Orszag and Steven 1970) is a simulation in computational fluid dynamics in which the Navier-Stokes equations are numerically solved

without any turbulence model. This means that the whole range of spatial and temporal scales of turbulence must be resolved. In particular, the grid mesh must resolve the spatial scales, from the smallest dissipative scale (Kolmogorov scale) to the integral scale, which is associated with the motions containing most of the kinetic energy. The computational cost of DNS is very high, even at low Reynolds numbers. For the Reynolds numbers encountered in most industrial applications, the computational resources required by a DNS will largely exceed the capacity of the most powerful computers currently available.

The Reynolds-Averaged Navier-Stokes equations (RANS), which is an idea firstly proposed by Osborne Reynolds (1895), constitute the time averaged equations of fluid motions. The idea behind these equations is the Reynolds decomposition, whereby an instantaneous quantity is decomposed into its time-averaged and fluctuating quantities. Thus, RANS can be used to give approximate solutions to the time averaged Navier-Stokes equations, using approximations based on the knowledge of turbulence properties. To do so, RANS needs to compute the Reynolds stresses. Thus, it usually can be done by three main categories of RANS-based turbulence models: the linear eddy viscosity models, nonlinear eddy viscosity models and Reynolds stress models (RSM).

Large Eddy Simulation (LES) was initially proposed by Smagorinsky (1963), to simulate atmospheric air currents. But many of the issues unique to LES were firstly explored by Deardorff (1970). According to the "local isotropy" hypothesis of Kolmogorov, at sufficiently high Reynolds number, the small scales are statistically isotropic. Based on this hypothesis, LES operates on the Navier-Stokes equations by a low-pass filter to filter out the small scales of flow. This allows to reduce the length scales range of solution. So the computational cost can be reduced at the same time. LES models the effect of the small (unresolved) scales on the large (resolved) scales, which allows better fidelity than RANS methods. Since in RANS, all the unsteadiness is averaged and considered as part of the turbulence, only the evolution of the mean quantities is described. In addition, the subgrid model of LES is more economical than directly resolving all the small scales like DNS. It makes the computational cost for practical engineering systems with complex geometry or flow configurations attainable using supercomputers. It can also be applied to high Reynolds 3D complex flows, where DNS is actually not achievable [1].

The difficulties associated with the use of the standard LES models, particularly in near wall regions, has lead to the development of hybrid models that attempt to combine the best aspects of RANS and LES methodologies in a single solution strategy. An example of a hybrid technique is the Detached Eddy Simulation (DES) (Spalart *et al.* 1997) approach. This model attempts to treat near wall regions in a RANS like manner, and treat the rest of the flow in an LES like manner. Regions near solid boundaries and where the turbulent length scale is less than the maximum grid dimension are assigned the RANS mode of solution. As the turbulent length scale exceeds the grid dimension, the regions are solved using the LES mode. Therefore the grid resolution is not as demanding as pure LES, thereby considerably cutting down the cost of the computation. The principal weakness of DES is its response to ambiguous grids, in which the wall-parallel grid spacing is of the order of the boundary-layer thickness (Spalart 2009 [131]). In some situations, DES on a given grid is then less accurate than RANS on the same grid or DES on a coarser grid. Partial remedies have been found, yet dealing with thickening boundary layers is a central challenge.

Among these available methods of turbulence modelling, LES is still a very prevalent

way due to its specific advantages.

1.4. Objectives of research

This thesis aims at conducting a priori analysis of the energy transfer mechanisms and a priori evaluation of subgrid scale model coefficients respectively in plane channel flow and converging-diverging channel flow at high Reynolds number. Standard subgrid scale models (Smagorinsky, Dynamic Smagorinsky and WALE models) as well as model developed recently (the σ model) are investigated in wall flows with and without pressure gradient. The correlation and predictive capabilities of the models are also assessed. The influence of the filter type and filter width on several a priori evaluation of the models is examined in detail, using both the classical Gaussian and the new-developed least square spline filters. The present research can provide some useful information for the implementation of LES and the development of subgrid scale models for wall turbulence with pressure gradient and separation as encountered in many practical applications.

1.5. Organization of the thesis

This thesis is divided into six chapters. After a general introduction in chapter one and a brief literature review of large eddy simulation in the second chapter, the third chapter introduces the a priori approach and the methodology used in our research. It outlines a new filter adapted to our a priori analysis and databases, the formulations of the energy transfer mechanisms and the subgrid models analyzed a priori in the present research. The a priori analysis of the subgrid scale models are first validated for isotropic turbulence. Then, the databases of both plane and converging-diverging channel flows are described. The fourth chapter presents the results for the plane channel flow at high Reynolds number. The energy transfer mechanisms, the evaluation of subgrid scale models, as well as the a priori performances of the subgrid scale models are investigated. chapter five provides the results of a priori analysis for converging-diverging channel flow at high Reynolds number. The SGS energy transfer, SGS energy dissipation and evaluation of coefficients of subgrid scale models are firstly investigated. Then, the correlations between the exact and modeled counterparts and the predictive capabilities of subgrid scale models are explored. The results for plane and converging-diverging channel flows are compared. The final chapter summarizes the main results and conclusions drawn from this study and makes some recommendations for future work.

Chapter 2

Large Eddy Simulation

2.1. Introduction

According to Richardson (1922), a turbulent flow is composed by different scale eddies, in which the large eddies are unstable and eventually break up into smaller eddies and so on. So the energy is passed down from the large scales of the motion to smaller scales until reaching a sufficiently small length scale such that the viscosity of the fluid can effectively dissipate the kinetic energy (Fig. 2.1).

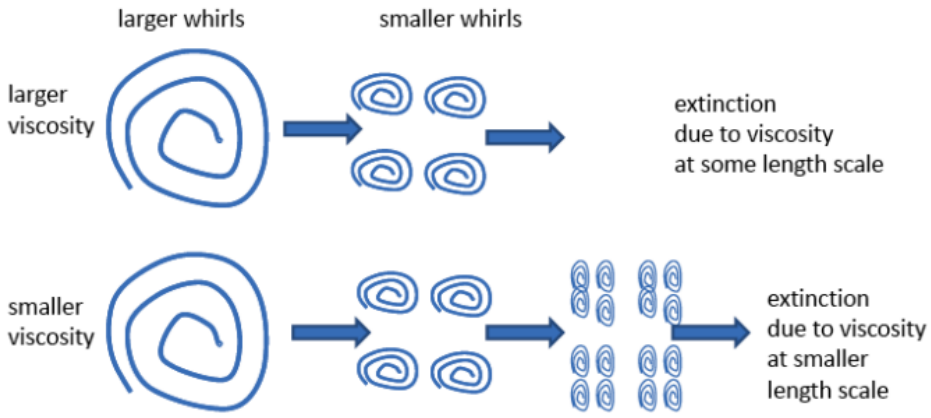

Figure 2.1: Richardson's energy cascade (from K. Khusnutdinova, 2009)

The development of the energy transfer theory in turbulent flows at high Reynolds number began with Kolmogorov (1941) who laid the basis of the ideal subgrid scale models. Hypothesis of Kolmogorov supposes that, at very high Reynolds number, the turbulent motions with length scales much smaller than the integral length scale of turbulence are statistically independent of the components of the motion at energy-containing scales. The energy-containing scales of the motion may be inhomogeneous and anisotropic at large scales, but this information is gradually lost by the energy cascade so that at much smaller scales the motion is locally homogeneous and isotropic. Thus, Kolmogorov hypothesis supposes that, the statistics of components in the equilibrium range is universally and uniquely determined by the viscosity ν and the rate of energy dissipation ϵ. At very high Reynolds number, the statistics of scales in the range between the integral and Kolmogorov

length scales ('inertial subrange') are universally and uniquely determined by its scale k and the rate of energy dissipation ϵ. Then, in the inertial subrange, the turbulence energy spectrum $E(k)$ should be of the form:

$$E(k) = C_k \epsilon^{2/3} k^{-5/3} \tag{2.1}$$

C_k is the Kolmogorov constant, experimentally found to be approximately 1.5. This is the famous 'Kolmogorov's 5/3 law. Many studies have been made of the spectrum of turbulence at large Reynolds number (see Fig. 2.2).

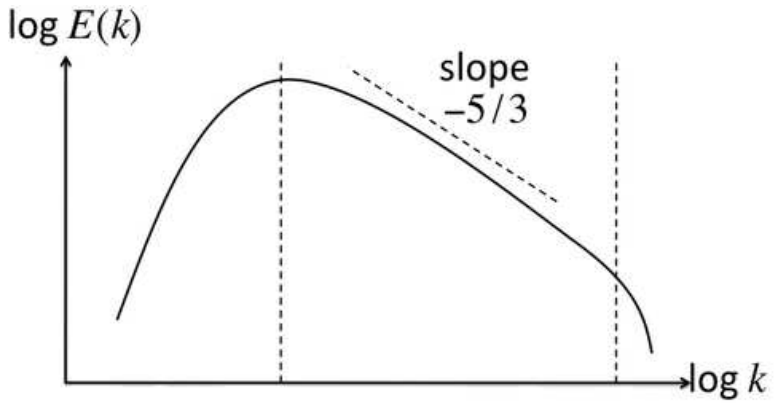

Figure 2.2: Kolmogorov's energy spectrum.

In consideration of turbulent motions of various scales, the notions of the energy cascade and Kolmogorov hypothesis provide an invaluable conceptual framework. However, both conceptually and empirically, there are some shortcomings (Pope 2000 [116]). It's certainly an oversimplification to suppose that the energy cascade of the one way transfer of energy from large size eddies to the smaller ones and that this energy transfer depends solely on motions of large eddies. Domaradzki and Rogallo (1990) proposed that there is energy transfer both to smaller and to larger scales, with the net transfer being toward smaller scales. Although many research work has focused on the shortcomings of the original Kolmogorov hypothesis, it should be emphasized that in the context of the mean velocity field and Reynolds stresses in turbulent flows, these issues are of minor significance. This does not affect its importance as a foundation of turbulence research.

2.2. LES modelling

In large eddy simulation, large scales are obtained by applying a low-pass filter on Navier-Stokes equations, while the small scales are modeled by subgrid scale models. In this section, several important elements of the large eddy simulation (the filter, the subgrid scale models, the methods of implementation of LES) as well as several different flow configurations using LES will be discussed.

2.2.1. The governing equations

The basic governing equations for an incompressible Newtonian fluid are Navier-Stokes equations expressed as:

$$\begin{aligned} \frac{\partial u_i}{\partial x_i} &= 0 \\ \frac{\partial u_i}{\partial t} + \frac{\partial}{\partial x_j}(u_i u_j) &= -\frac{1}{\rho}\cdot\frac{\partial p}{\partial x_i} + \nu\frac{\partial}{\partial x_j}(\frac{\partial u_i}{\partial x_j} + \frac{\partial u_j}{\partial x_i}), \quad i = 1,2,3 \end{aligned} \tag{2.2}$$

In which, t is the time, x_i is the i^{th} component of the position vector, u_i is the velocity components in direction i, ρ is the fluid density, p and ν are respectively the static pressure and kinematic viscosity. In LES the Navier-Stokes equations are filtered using a low-pass filter. A filtered (resolved, or large scale) variable, denoted by an over bar, is defined as:

$$\overline{f}(x) = \int_{\mathcal{D}} f(x')G(x,x')dx' \tag{2.3}$$

where $\mathcal{D}$ is the entire domain and G is the filter kernel. $\overline{\Delta}$ is the filter width which is externally specified. In order to manipulate the Navier-Stokes equations after applying a filter, it's required that the filter should verify the three following properties (Sagaut 1998 [123]):

- Conservation of constants

$$\overline{a} = a \Longleftrightarrow \int_{-\infty}^{\infty}\int_{-\infty}^{\infty} G(x,x',t')dx'dt' = 1 \tag{2.4}$$

- Linearity

$$\overline{f_1(x) + f_2(x)} = \overline{f_1}(x) + \overline{f_2}(x) \tag{2.5}$$

  This property is automatically satisfied, since the convolution product verifies it independently of the characteristics of the kernel G.

- Commutation with derivation

$$\frac{\overline{\partial f}(x)}{\partial s} = \frac{\partial \overline{f}(x)}{\partial s}, \quad s = x,t \tag{2.6}$$

The filtered Navier-Stokes equations are then obtained as:

$$\begin{aligned} \frac{\partial \overline{u}_i}{\partial x_i} &= 0 \\ \frac{\partial \overline{u}_i}{\partial t} + \frac{\partial}{\partial x_j}(\overline{u_i}\overline{u_j}) &= -\frac{1}{\rho}\frac{\partial \overline{p}}{\partial x_i} + \nu\frac{\partial}{\partial x_j}(\frac{\partial \overline{u}_i}{\partial x_j} + \frac{\partial \overline{u}_j}{\partial x_i}) \end{aligned} \tag{2.7}$$

thus, the large scales can be selected according to turbulence theory and available computational resources. Leonard (1974) expressed the non-linear term in the form of sum-

mation:

$$\begin{aligned} \overline{u_i u_j} &= \overline{(\overline{u_i} + u_i')(\overline{u_j} + u_j')} \\ &= \overline{\overline{u}_i \overline{u}_j} + \overline{\overline{u}_i u_j'} + \overline{\overline{u}_j u_i'} + \overline{u_i' u_j'} \end{aligned} \tag{2.8}$$

The non-linear term is now written entirely as a function of the filtered quantity $\overline{u}_i$ and the fluctuation u_i'. The Leonard tensor L_{ij} represents the interactions among the large scales that result from subgrid scale contributions,

$$L_{ij} = \overline{\overline{u}_i \overline{u}_j} - \overline{u}_i \overline{u}_j \tag{2.9}$$

The cross-stress tensor C_{ij} represents the interactions between the resolved and subfilter scales and is defined as:

$$C_{ij} = \overline{\overline{u}_i u_j'} - \overline{\overline{u}_j u_i'} \tag{2.10}$$

the Reynolds subgrid tensor:

$$R_{ij} = \overline{u_i' u_j'} \tag{2.11}$$

represents the interactions between subgrid scales. Grouping together all the terms, the subgrid tensor becomes:

$$\tau_{ij} = L_{ij} + C_{ij} + R_{ij} = \overline{u_i u}_j - \overline{u}_i \overline{u}_j \tag{2.12}$$

The filtered Navier-Stokes equations can be written as:

$$\begin{aligned} \frac{\partial \overline{u}_i}{\partial x_i} &= 0 \\ \frac{\partial \overline{u}_i}{\partial t} + \frac{\partial}{\partial x_j}(\overline{u}_i \overline{u}_j) &= -\frac{1}{\rho}\frac{\partial \overline{p}}{\partial x_i} + \nu \frac{\partial}{\partial x_j}\left(\frac{\partial \overline{u}_i}{\partial x_j} + \frac{\partial \overline{u}_j}{\partial x_i}\right) - \frac{\partial \tau_{ij}}{\partial x_j} \end{aligned} \tag{2.13}$$

These equations are in the standard form, containing the residual-stress tensor τ_{ij} (or subgrid scale stress tensor) that accounts for subgrid scale motion and needs to be modeled.

2.2.2. The filters

In DNS, the velocity field has to be resolved on lengthscales down to the Kolmogorov scale. In LES, a low-pass filtering operation is performed so that the resulting filtered velocity field can be adequately resolved on a relatively coarse grid. In the ideal case, the filter width is somewhat smaller than the size of the smallest energy-containing motions so that the energy-containing motions are fully resolved (Pope 2000 [116]).

2.2.2.1. Implicit and explicit filtering

The filtering operation in large eddy simulation can be implicit or explicit. It is often assumed that the discretization operations performed on a particular grid act as an implicit filter. In such a scheme, the filter width is set by the computational grid size and the filter

kernel is set by the numerical method used to determine the derivatives. Alternatively, an explicit filter scheme can be used, which filters the field at a scale larger than the computational grid. Explicit filtering allows the filter kernel to be tailored to have desired characteristics, but requires greater computational resolution for an equivalent filter size. Hence, implicit filtering is commonly used for a long time. And it has allowed to evidence some drawbacks of this filter.

Foremost among these is the issue of consistency. While it is true that the discrete derivative operators have a low-pass filtering effect, the associated filter acts only in a single spatial direction in which the derivative is taken. This fact implies that each term in the Navier-Stokes equations is acted on by a distinct one-dimensional filter, and thus there is no way to derive the discrete equations through the application of a single three-dimensional filter (Vasilyev *et al.* 1998 [141]). Considering this ambiguity in the definition of the implicit filter, it is not possible to calculate the Leonard term (equation 2.9) that appears as a computable portion in the decomposition of the subgrid-scale stress. And it is also nearly impossible to make detailed comparisons of LES results with the filtered data. These are due to the fact that the implicit filtering can not provide an accurate representation of the filtered field. Next, when increasing the number of degrees of freedom, additional length scales are added each time the mesh is refined. And owing to the inherent dependence of the filtering operation on the discretized operators, the solutions of implicitly filtered LES are extremely sensitive to the mesh resolution (Bose *et al.* 2010 [16]). However, the continual refinement of the mesh size makes it difficult to distinguish between the effects of reduced numerical error and the increase in the range of resolved length scales. Another significant limitation of the implicit filtering approach is the inability to control numerical error (Vasilyev *et al.* 1998 [141]). Without an explicit filter, there is no direct control on the energy in the high frequency portion of the spectrum. Significant energy in this portion of the spectrum coupled with the nonlinearities in the Navier-Stokes equations can produce significant aliasing error. Furthermore, all discrete derivative operators become rather inaccurate for high frequency solution components, and this error interferes with the dynamics of the small scale eddies. This error can be particularly harmful (Lund *et al.* 1995) when the dynamic model is used, since it relies entirely on information contained in the smallest resolved scales. So it's difficult to assess the fidelity of the closure model owing to the observed sensitivity of the subgrid model to numerical errors. In addition, it is difficult to define the test to primary filter ratio which is needed as an input to the dynamic procedure. Therefore, all of these defects call for the emergence of a more robust filtering method.

Explicit filtering reemerged a decade ago as a method to rigorously derive the constitutive equations for the large scale field and to separate the filtering and discretization operations (Bose *et al.* 2010 [16], Lund 2003 [86]). According to the previous researches (Kennedy 1994 [68], Vasilyev *et al.* 1998 [141]), the difficulties associated with the implicit filtering approach as mentioned above, can be alleviated by performing an explicit filtering operation as part of the solution process. Explicit filtering was found to provide several advantages. Firstly, explicit filtering can provide an accurate representation of the filtered field, the shape of the filter is known exactly, which facilitates comparison with experimental data and is able to compute the Leonard term. Secondly, explicit filtering reduces the effective resolution of the simulation, but allows the filter size to be chosen independently of the mesh spacing, this alleviates the sensitivity to the grid mesh. In par-

ticular, if the filter width is held fixed as the mesh is refined, the velocity field will converge to the true solution of the LES equations. The use of an explicit filter provides a means for both assessing and minimizing the effects of numerical error in practical simulations. As demonstrated by Lund 1997 [84], explicit filtering eliminates aliasing errors from the nonlinear advection term. Finally, explicit filtering has the potential to reduce numerical errors that are associated with the finite difference schemes used as implicit filters, even if the magnitude of the truncation error is larger than the contribution of the smallest, dynamically relevant, physical scale (Bose *et al.* (2010) [16]). By damping the energy in the high-frequency portion of the spectrum, it is possible to reduce or eliminate the various sources of numerical error that dominate this frequency range, which become most severe for length scales on the order of the mesh size (Vasilyev *et al.* 1998 [141]). Furthermore the various sources of numerical error that would otherwise enter the stresses sampled in the dynamic model can be controlled, which can ultimately result in a more accurate estimate for the subgrid scale model coefficient. In addition, explicit filtering eliminates aliasing errors from the nonlinear advection term, as demonstrated by Lund(1997). But the exact computational cost of the explicitly filtered LES is largely dependent on the characteristics of the filter employed, in addition to the choice of the subgrid model and the corresponding numerical implementation (Bose *et al.* 2010 [16]).

2.2.2.2. Three classical filters

Spatial filtering (Leonard 1974) is the most common approach to decompose the velocity field into large and small scales. Pope (2000) [116] presents an exhaustive discussion of various filters and their properties. But three common explicit filters are often used in large eddy simulation in order to benefit the advantages of an explicit filter (Sagaut 1998 [123]). They are the Box or tophat filter, the Gaussian filter, and the spectral or sharp cutoff filter. Their kernel functions in physical and spectral space are given in Table 2.1. The spectral cutoff filter clearly separates between scales. The box filter has good

	In physical space	In Fourier space
Tophat	$G(x-\xi) = \begin{cases} \frac{1}{\overline{\Delta}} & if\ \lvert x-\xi\rvert \leq \frac{\overline{\Delta}}{2} \\ 0 & otherwise \end{cases}$	$\widehat{G}(k) = \frac{sin(k\overline{\Delta}/2)}{k\overline{\Delta}/2}$
Gaussian	$G(x-\xi) = \left(\frac{\gamma}{\pi\overline{\Delta}^2}\right) exp\left(\frac{-\gamma\lvert x-\xi\rvert^2}{\overline{\Delta}^2}\right)$	$\widehat{G}(k) = exp\left(\frac{-\overline{\Delta}^2 k^2}{4\gamma}\right)$
Cutoff	$G(x-\xi) = \left(\frac{sin(k_c(x-\xi))}{k_c(x-\xi)}\right),\ k_c = \frac{\pi}{\overline{\Delta}}$	$\widehat{G}(k) = \begin{cases} 1 & if\ \lvert k\rvert \leq \lvert k_c\rvert \\ 0 & otherwise \end{cases}$

Table 2.1: Formulations of three classical filters in physical and Fourier spaces

spatial localization but does not allow unambiguous separation between scales because of spectral overlap. The Gaussian filter has intermediate localization properties in both physical and spectral space. Many research (Piomelli *et al.* 1991 [112], Najjar *et al.* 1996 [100]) have found that explicit filtering implies the sensitivity of the LES solution to the particular filter employed, because the filter function determines the size and structure of the small scales.

2.2.2.3. Commutation error

In large eddy simulation of turbulent flows, the differential equations describing the space-time evolution of the large-scale structures are obtained from the Navier-Stokes equations (equation 2.2) by applying a low-pass filter (equation 2.3). In order for the resulting LES equations to have the same structure as the Navier-Stokes equations, the differentiation and filtering operations must commute. Introducing the commutator $[f, g]$ of two operators f and g applied to the dummy variable ϕ

$$[f, g]\phi = f \circ g(\phi) - g \circ f(\phi) = f(g(\phi)) - g(f(\phi)) \tag{2.14}$$

The relation (2.6) can be re-written symbolically:

$$[G\star, \frac{\partial}{\partial s}] = \frac{\overline{\partial \phi}}{\partial s} - \frac{\partial \overline{\phi}}{\partial s} = 0 \tag{2.15}$$

In the above relation, it is assumed that the filter is homogeneous. But in inhomogeneous turbulent flows, the minimum size of eddies that need to be resolved varies in different regions of the flow. For example, turbulent boundary layers, multi-phase flows and strongly localized combustion phenomena. Thus the filtering operation should be performed with a variable filter width. In general, filtering and differentiation do not commute when the filter width is nonuniform in space (Vasilyev *et al.* 1998 [141], Geurts *et al.* 2006 [55]). Using the commutator equation (2.14), the most general form of the filtered Navier-Stokes equations by applying non-homogeneous convolution filters are obtained:

$$\frac{\partial \overline{u_i}}{\partial x_i} = -\left[G\star, \frac{\partial}{\partial x_i}\right](u_i) \tag{2.16}$$

$$\begin{aligned} \frac{\partial \overline{u_i}}{\partial t} + \frac{\partial}{\partial x_j}(\overline{u_i u_j}) \quad &+ \quad \frac{\partial \overline{p}}{\partial x_i} - \nu \frac{\partial}{\partial x_j}\left(\frac{\partial \overline{u_i}}{\partial x_j} + \frac{\partial \overline{u_j}}{\partial x_i}\right) = \frac{\partial \tau_{ij}}{\partial x_j} - \left[G\star, \frac{\partial}{\partial t}\right](u_i) \\ &- \quad \left[G\star, \frac{\partial}{\partial x_j}\right](u_i u_j) - \left[G\star, \frac{\partial}{\partial x_i}\right](p) + \nu \left[G\star, \frac{\partial^2}{\partial x_k \partial x_k}\right](u_i) \end{aligned} \tag{2.17}$$

According to Geurts and Holm (2006) [55], who investigated the theory of general nonuniform filters, the independent control over the commutator errors can be obtained by appropriately restricting the spatial variations of the filter-width and filter-skewness (earlier studies can be extended by allowing the filter to be skewed [15]). Ghosal and Moin (1995) [58] introduced an alternate definition of the filtering operation (a second-order commuting filter, SOCF) based on the mapping function of the nonuniform grid. It is shown that with this modified definition the filtering and differentiation operations commute up to an error which is second order of the filter width. They established an equation to show what the commutation error is at most of order $(k\overline{\Delta})^{2m}$ ($\overline{\Delta}$ is a constant filter width, m is any positive integer, k is the wave number in Fourier space). By developing an asymptotic expansion for the commutation error, it can be approximated to any degree of accuracy in terms of the filtered fields. Thus it ensures that the commutation error does not exceed the discretization error in a numerical simulation. In brief, the studies above agreed that an increase in the order of the spatial filter allows a control over the

magnitude of the commutator error (Ghosal and Moin (1996) [56]) which can be reduced in size by explicitly restricting the variations in filter-width and the normalized skewness of the filter (Geurts and Holm 2006 [55]).

In addition, Ghosal and Moin (1995) suggested that the leading correction term can be retained if high-order numerical schemes are used to discretize the LES equations. This involves additional numerical complexities which can be avoided using filters with specific properties. Vasilyev *et al.* (1998) formulated the general requirements for a filter using nonuniform filter width to ensure that the differentiation and filtering operations commute to any desired order. Minimization of the commutation error is achieved by requiring that the filter has a number of vanishing moments. Marsden *et al.* (2002), Haselbacher and Vasilyev (2003) extended their applicability to unstructured meshes.

Vreman and Geurts (2002) [145] proposed a new treatment for the commutation-problem in which the spatial filtering of the convective term is directly combined with the derivative-operator rather than interchanged with this operator. The latter would lead to additional commutation-errors. This re-formulation gives rise to an adaptation of the remaining subgrid modeling problem which is considered in a new dynamic context. Unlike the traditional dynamic procedure, the new procedure does not require the assumption that the model coefficient is slowly varying on the test-filter scale. The new approach was tested on a moderately stretched grid and provided satisfactory results when the new dynamic models were employed.

2.2.3. Subgrid scale models

In 1877, Boussinesq postulated that the momentum transfer caused by turbulent eddies can be modeled with an eddy viscosity. By analogy, Smagorinsky supposed that the subgrid scale action can be modeled by a term having a mathematical structure similar to that of molecular diffusion, in which the molecular viscosity is replaced by the subgrid viscosity ν_{sgs}. The mathematical form of the subgrid model is written [123]:

$$\tau_{ij} - \frac{1}{3}\tau_{kk}\delta_{ij} = -2\nu_{sgs}\overline{S}_{ij} \tag{2.18}$$

Where δ_{ij} is the Kronecker symbol. $\overline{S}_{ij}$ is the strain-rate tensor:

$$\overline{S}_{ij} = \frac{1}{2}(\frac{\partial \overline{u}_i}{\partial x_j} + \frac{\partial \overline{u}_j}{\partial x_i}) \tag{2.19}$$

2.2.3.1. The Smagorinsky Model (SM)

For the classical Smagorinsky (1963) model, the SGS eddy viscosity is derived under the assumption that the small-scale turbulence is locally in equilibrium regarding production and dissipation of kinetic energy. This leads to

$$\nu_{sgs} = (C_s\overline{\Delta})^2|\overline{S}| \tag{2.20}$$

$\overline{\Delta}$ is the filter scale, C_s a coefficient which, in principle, may depend on space and scale. $|\overline{S}| = \sqrt{2\overline{S}_{ij}\overline{S}_{ij}}$. The Smagorinsky model was previously analyzed by Moin and Kim

(1982) [99], Rogallo and Moin (1984) [122], Lesieur and Metais (1996) [74], and later in depth by Pope (2000) [116]. For isotropic turbulence with an inertial range in the spectrum, when the filter width lies in this inertial range, $C_s = 0.18$ (Lilly 1967 [77]), which, however, was found to be too large in practice. Various values of C_s have been recommended depending on the type of flow and mesh resolution (Lilly 1967 [77], Deardorff *et al.* 1970 [36], Pope (2000) [116], Meyers *et al.* 2006 [97]). However, the subgrid scales of motion in the near wall region are far from equilibrium and contain an important fraction of the total kinetic energy. The assumption that C_s is a universal constant is invalid in such case. Furthermore, the operator $|\overline{S}|$ is not vanishing in near wall region. This major drawback has motivated the use of Van Driest Damping functions (see Van Driest 1956) $C_s = C_s(y^+)(1 - e^{-y^+/A^+})$, A is the van Driest constant [13]. $A^+ = 25$ is often used in many studies. This idea is to reduce the Smagorinsky constant C_s to 0 as the boundary is approached such that averages of the flow variables satisfy the boundary layer theory. Although its deficiency, the Smagorinsky model is able to correctly predict the global kinetic energy dissipation of the energy cascade in turbulent flows (Pantano 1999 [128]). Thus, it's always a very prevalent model for larger eddy simulations.

Subsequently, many attempts to use Smagorinsky model in more complex cases have been done. For example, Scotti *et al.* (1993) [126] implemented the Smagorinsky model on anisotropic grids. Instead of Deardorffs estimate involving an equivalent grid scale $\overline{\Delta} = (\Delta_1\Delta_2\Delta_3)^{1/3}$ for moderate resolution anisotropies, the eddy viscosity is recasted as $\nu_{sgs} = [C_s\overline{\Delta}f(a_1, a_2)]^2|\overline{S}|$. where $f(a_1, a_2)$ is a function of the grid aspect ratios a_1 and a_2 ($a_1 = \Delta_1/\Delta_3$ and $a_2 = \Delta_2/\Delta_3$). For very large filter anisotropies, $f(a_1, a_2) \approx cosh\{(4/27)[(ln(a_1))^2 - ln(a_1)ln(a_2) + (ln(a_2))^2]\}^{1/2}$. It is argued that these results should be used in conjunction with the dynamic model of Germano *et al.* whenever the anisotropy of the test-filter differs significantly from that of the basic grid.

Another attempt to alleviate the drawbacks of the Smagorinsky model for different turbulent fields near solid walls or in transitional regimes is based on the dynamic procedure which will be presented in the following.

2.2.3.2. The Dynamic Smagorinsky Model (DSM)

The Dynamic Smagorinsky model was suggested by Germano *et al.* (1991) [52] and improved by Lilly (1992) [77]. This model is modified by employing the mixed model of Bardina *et al.* 1983 [7] as base model. The coefficient C_d of Dynamic Smagorinsky model is no longer assumed to be constant, but is considered a function of space and time. In the dynamic model, this is achieved by introducing a second filter $\widehat{\Delta}$ (the so-called 'test filter') in addition to the original filter $\overline{\Delta}$. By assuming that the SGS stresses due to both the original filter and the test filter are similar and can be modeled in a similar way, the coefficient C_d can be derived with the test-scale defined similarly to those for the original filter. The subtest-scale stress T_{ij} is approximated as:

$$T_{ij} - \frac{1}{3}\delta_{ij}T_{kk} = -2(C_d\widehat{\Delta})^2|\widehat{\overline{S}}|\widehat{\overline{S}}_{ij} \tag{2.21}$$

The resolved turbulent stresses are:

$$L_{ij} = T_{ij} - \widehat{\tau}_{ij} = \widehat{\overline{u}_i\overline{u}_j} - \widehat{\overline{u}}_i\widehat{\overline{u}}_j \tag{2.22}$$

Besides, there is:

$$L_{ij} - \frac{1}{3}\delta_{ij}L_{kk} = -2C_d^2 M_{ij} \tag{2.23}$$

and

$$M_{ij} = \overline{\Delta}^2\widehat{|\overline{S}|\overline{S}_{ij}} - \widehat{\Delta}^2|\widehat{\overline{S}}|\widehat{\overline{S}}_{ij} \tag{2.24}$$

Consequently, the coefficient C_d of the Dynamic Smagorinsky model is given by:

$$C_d^2 = \frac{1}{2}(L_{ij}M_{ij}/M_{ij}^2) \tag{2.25}$$

which is expressed only by the resolved scales and is calculated locally in space and time. The hypothesis of the Smagorinsky model, that the smaller dissipative scales have an isotropic character and can be modeled with an isotropic eddy viscosity, is maintained also in the dynamic model. As a result, the SGS stresses are forced to be aligned with the strain rate tensor, which is actually not true. Indeed, even in isotropic homogeneous turbulence there are structures present at all scales in the inertial range that produce local departure from isotropy (Abbà *et al.* 2003 [1]).

Analysis of DNS data and experimental data revealed that the value of C_d predicted by formula (2.25) varies strongly in space and contains a significant fraction of negative values which become a source of kinetic energy for the resolved scales. And these values represent the occurrence of back scatter in physical space. However the negative values of C_d constitute a numerical destabilizing process. The remedy often adopted to avoid excessively large negative values of C_d includes averaging the numerators and denominators of (2.25) in space and/or time in price of losing some of the conceptual advantages of the dynamic local formulation (Lesieur *et al.* 1996 [74]). In order to avoid the numerical instability, some authors suggest that a clipping on negative values can be applied (Abbà 2003 [1], Piomelli and Chasnov (1996) [114]). However, in practical computations, C_d is normally set artificially to zero whenever its values are negative.

Many researchers often consider that the Dynamic Smagorinsky model is insensitive to the test filtering parameter (Tsubokura 2006 [139]). Generally the test filter scale $\widehat{\Delta}$ is smaller than $\overline{\Delta}$. And $\widehat{\Delta} = 2.0\overline{\Delta}$ is most often used and is thought to yield the best results in many studies (Germano *et al.* 1991 [53], Najjar *et al.* 1996 [100], Collis *et al.* 1999 [119]). In addition, Meneveau *et al.* (1997) [94] investigated the dynamic Smagorinsky model and scale-dependent coefficients in the viscous range of turbulence. They pointed that, since the standard dynamic procedure is based on the scale-invariance assumption, the model coefficient is the same at the grid and test-filter levels. In many applications this condition is not met. By considering the case when the filter-length ($\overline{\Delta}$) approaches the Kolmogorov scale, the model coefficient (C_d) approaches zero, they showed that the standard dynamic Smagorinsky model yields the coefficient value corresponding to a test-filter scale ($a\overline{\Delta}$, a is constant) instead of the grid scale ($\overline{\Delta}$). Najjar *et al.* (1995) performed a study of discrete test filters and finite difference approximations for the dynamic subgrid scale model in simulations of the turbulent channel flow. For the same test filtering operation, the results are found to be sensitive to the ratio of the characteristic lengths of the test and grid filters.

The dynamic model has been reported to predict the distributions of eddy viscosity better than the traditional Smagorinsky model (Rodi *et al.* 1997). It also has been demonstrated that the dynamic Smagorinsky model is capable of self-adjustment to the effects of

anisotropy (Vorobev *et al.* 2007 [143]). But these improvement does not necessarily lead to better flow predictions mainly owing to numerical issues. It also should be noted that although the improvement of the dynamic procedure, the Dynamic Smagorinsky model does not necessarily perform better than the Smagorinsky model. For example, the behavior of subgrid-scale models near the turbulent/non-turbulent interface in jets which were conducted by Silva (2009) [33] showed that near the jet edge the Smagorinsky model is superior to the dynamic Smagorinsky.

2.2.3.3. The wall-adapting local eddy-viscosity model (WALE)

As it's known, the Smagorinsky model vanishes for pure rotation but not for pure shear. Although the Van Driest exponential damping function compensates the defects of the Smagorinsky model in the near wall region (as an *ad hoc* modification based on the distance to the wall), this way is hard to implement in the general case for complex geometries, especially without direction of flow homogeneity and/or with unstructured numerical methods. Also it may not produce the proper near-wall scaling for the eddy-viscosity due to the dependence on the used damping function. In addition to the development of the dynamic procedure, another possible remedy for this is the Wall-Adapted Local Eddy-viscosity model (WALE model of Nicoud and Ducros (2000) [102]) which is formulated locally and define the eddy-viscosity by:

$$\nu_{sgs} = (C_w\overline{\Delta})^2 \frac{(S_{ij}^d S_{ij}^d)^{3/2}}{(\overline{S}_{ij}\overline{S}_{ij})^{5/2} + (S_{ij}^d S_{ij}^d)^{5/4}} \tag{2.26}$$

where C_w is the coefficient of the WALE model, which has to be fixed a priori. S_{ij}^d denotes the traceless symmetric part of the square of the velocity gradient tensor $S_{ij}^d = (\overline{g}_{ij}^2 + \overline{g}_{ji}^2)/2 - \delta_{ij}\overline{g}_{kk}^2/3$, where $\overline{g}_{ij}^2 = \overline{g}_{ik}\overline{g}_{kj}$, with $\overline{g}_{ij} = \partial\overline{u}_i/\partial x_j$. The WALE model is based on the square of the velocity gradient tensor and accounts for the effects of both the strain and the rotation rate to obtain the local eddy-viscosity. The main advantages of the WALE model are the capability to reproduce the laminar to turbulent transition and to give the correct near wall behavior of the SGS viscosity which goes naturally to zero at the wall with neither damping function nor dynamic procedure needed. It offers the same advantages as the Dynamic Smagorinsky-Lilly model with a lower complexity, and therefore can be easily assessed on any kind of computational grid.

Since its emergence, the WALE model has been gradually applied to a variety of flows. Ducros *et al.* (1998) [42] applied it to the transition to turbulence of the flow in a pipe on an unstructured grid. The results showed that the WALE model improves the prediction of the wall stress rate and the turbulent intensities, compared with the Smagorinsky model. Liu *et al.* (2012) [79] did large eddy simulations using the WALE model of the fully developed turbulent flows near a flat wall. The results showed that the WALE model predicts excellent damped eddy viscosity near the wall.

2.2.3.4. The σ model (σ)

Nicoud *et al.* 2011 [103] proposed the σ model which has, by construction, the property to automatically vanish as soon as the resolved field is either two-dimensional or two-component, including the pure shear and solid rotation cases. In addition, the model

generates no subgrid-scale viscosity when the resolved scales are in pure axisymmetric or isotropic contraction/expansion. They also showed that the σ model has an appropriate cubic behavior in the vicinity of solid boundaries without requiring any ad-hoc treatment. The model is defined as:

$$\nu_{sgs} = (C_\sigma \overline{\Delta})^2 D_\sigma \tag{2.27}$$

$$D_\sigma = \frac{\sigma_3(\sigma_1 - \sigma_2)(\sigma_2 - \sigma_3)}{\sigma_1^2} \tag{2.28}$$

Where σ_1,σ_2,σ_3 are three singular values of the resolved velocity gradient tensor. They are in order such that $\sigma_1 \geq \sigma_2 \geq \sigma_3$. C_σ is the coefficient of the σ model.

Results for two classical test cases (decaying isotropic turbulence and periodic turbulent channel flow) have been obtained by Nicoud (2011) [103]. The results obtained with the proposed model are systematically equivalent or slightly better than the results from the Dynamic Smagorinsky model. Still, the σ model has a low computational cost, is easy to implement, and does not require any homogeneous direction in space or time. It is thus anticipated that it has a high potential for the computation of non-homogeneous, wall-bounded flows. The performance of the σ model for wall-bounded flows was investigated by computing LES of turbulent channel flows at friction Reynolds number $Re_\tau = 395$ and 590 by Baya Toda *et al.* (2010) [9]. Their results were in fact slightly better than with the dynamic Smagorinsky model. They also illustrated that, for some cases, the proper asymptotic behavior was obtained by the dynamic Smagorinsky model only when the dynamic procedure is applied planewise, by accounting for the homogeneous directions in the channel flow configuration. But this procedure can be used only for simple cases with homogeneous directions. The asymptotic behavior is built in the σ model's differential operator itself and no specific dynamic procedure/homogeneous directions is required.

As it's a new subgrid model, no substantial literature have been conducted on the σ model, but its superiority calls for implementations on various simulations, especially on flows with complex geometries and high Reynolds number.

2.2.3.5. Other models

Subgrid scale models commonly used in LES of turbulent flows mainly fall into several general categories: eddy viscosity models, scale similar and mixed models and the developing trend using the dynamic procedure (Gernamo *et al.* 1991, Lilly 1992, and Ghosal *et al.* 1995) which allows computation of model coefficients from a resolved field rather than prescribing them as constants. All of these subgrid scale models will be discussed in the following.

Within the large choice of subgrid scale models, eddy viscosity models are more popular since they are robust and able to reproduce the main dissipative effect of small scale turbulence. In the previous sections we have described several eddy viscosity models, including the traditional Smagorinsky model, the dynamic Smagorinsky model, the wall-adapting local eddy-viscosity model and the σ model. A growing body of literature has been reviewed to exhibit their strengths and weaknesses (Piomelli *et al.* 1991 [112, 115], Liu *et al.* 1994 [80], Lesieur *et al.* 1996 [74], Meneveau and Lund 1997 [94], Canuto and Cheng 1997 [22], Liu *et al.* 1999 [78], Pope 2000 [116]). The deficiencies of the eddy viscosity models are apparent in the underestimation of the standard deviation of the subgrid scale stresses and the inability to predict transfers of kinetic energy from the

subfilter scales to the resolved scales (Carper *et al.* 2008 [25]).

In recent years, many variants of the Smagorinsky model have appeared. For example, a different way of defining the eddy viscosity (Schumann 1975 [125]), the structure function model (Metais and Lesieur 1992 [96]). Other eddy viscosity models are also proposed successively according to different practical needs. For example, a two-part SGS eddy-viscosity model (Sullivan *et al.* 1994 [136]) in order to achieve better agreement between LES and similarity forms in the surface layer. Some other eddy viscosity models applied to different flows. For example, an eddy-viscosity model proposed by Vreman (2004) [144] and applied in large-eddy simulation of turbulent shear flows with quite satisfactory results. This model is able to adequately handle not only turbulent but also transitional flow. Another different approach to subgrid scale modeling (Stolz 2005 [135]) is designed for laminar, transitional, and turbulent flows without ad-hoc adaptation by employing high-pass filtered eddy-viscosity models. Subsequently, a dynamic subgrid-scale eddy viscosity model for 3D turbulent jet in a cross flow (Taeibi-Rahni *et al.* 2010 [137]) and the dynamic subgrid-scale eddy viscosity model for LES of turbulent flows in complex geometry (Park *et al.* (2006) [106]) are developed.

The scale similar model was first introduced by Bardina *et al.* (1980) [6] with the assumption of scale invariance in a strong and almost literal sense. The full structure of the velocity field at scales below the filter scale is postulated to be similar to that at scales above the filter scale. This postulate has been given an empirical basis from band-pass-filtered PIV measurements (Liu *et al.* 1994 [80]). In that paper, vector maps from successive bands of scales show that certain structures occur simultaneously at different scales at nearly the same locations (Meneveau *et al.* 2000 [93]). Consequently, it is suggested that the subgrid scale tensor must also be similar to a stress tensor constructed from the resolved velocity field,

$$\tau_{ij} = \overline{\overline{u}_i \overline{u}_j} - \overline{\overline{u}}_i \overline{\overline{u}}_j \tag{2.29}$$

If a cutoff filter is used, then $\overline{\overline{u}}_i = \overline{u}_i$ and $\tau_{ij} = 0$, so the similarity model produces nothing. The scale similar models can provide back scatter in a numerically stable and physically realistic manner, and predict SGS stresses in regions that are well correlated with the locations where large Reynolds stress occurs (Sarghini *et al.* 1999 [124]). Martín *et al.* 2000 [89] analyzed the scale similar model using the flow field obtained from the direct simulation of compressible homogeneous isotropic turbulence. It was found to give more accurate prediction of the subgrid scale stresses and heat fluxes than eddy-viscosity, as well as improved predictions of the subgrid scale turbulent diffusion, the subgrid scale viscous dissipation, and subgrid scale viscous diffusion. However, in the later applications of large eddy simulation, it was found that the scale similar model hardly dissipates any energy and thus can not serve as a 'stand alone' subgrid scale model.

To correct for the lack of dissipation, it's necessary to combine the eddy viscosity and scale similar models to produce the 'mixed' model, which can improve the quality of the simulations. If the subgrid scale stresses are decomposed in terms of $\overline{u}_i$ and u_i', the "large subgrid scales" can be obtained by filtering the subgrid scale velocity $u_i' = u_i - \overline{u}_i$ to yield $\overline{u_i'} = \overline{u}_i - \overline{\overline{u}}_i$. The mixed model can be written as:

$$\tau_{ij} = -2\nu_{sgs}\overline{S}_{ij} + \overline{\overline{u}_i \overline{u}_j} - \overline{\overline{u}}_i \overline{\overline{u}}_j \tag{2.30}$$

The last two terms in equation (2.30) represent the scale similar model, the eddy-viscosity

contribution provides the dissipation that is underestimated by the scale similar part alone (Piomelli 2010 [109]). The mixed model has been used in a number of simulations with considerable success (Zang *et al.* (1993) [150], Vreman *et al.* (1994) [146], Winckelmans *et al.*(1998) [147], Sarghini *et al.* 1999 [124], Lodato *et al.* (2009) [81]). For example, the research of Sarghini *et al.* 1999 [124] showed that the mixed models with the Lagrangian ensemble averaging, compared to eddy viscosity models, give results in the best agreement with the direct simulation and experimental data of a high Reynolds number plane channel flow, and a three-dimensional, nonequilibrium flow. According to Winckelmans *et al.*(1998) [147] who conducted research on the mixed model in LES of decaying homogeneous turbulence, the mixed model performs significantly better than the dynamic Smagorinsky model with same Gaussian filtering.

As described above, the concept of a dynamic model was originally proposed by Germano *et al.* 1991 [53]. This approach is better called a procedure than a model as it takes one of the subgrid models as a basis. Except the procedure of Germano *et al.*, many other dynamic procedures have been developed recently and applied in large eddy simulation (Ghosal *et al.* 1995 [57], Andrés *et al.* 2004 [2], Tsubokura 2006 [139]). Although the concept of a dynamic model is very appealing, significant problems have been encountered when the procedure is put into practice. The difficulty is that the coefficient of dynamic procedure varies very rapidly as a function of the spatial coordinates and time and takes on large values of both signs, leading to large eddy viscosity with both signs. To overcome this problem, several cures have been suggested, such as averaging over homogeneous directions and limiting the magnitude of negative viscosity, using a combination of local spatial and temporal averaging.

In addition, many other subgrid scale models have been used, such as the spectral models (Chollet *et al.* 1981 [27], Métais *et al.* 1996 [95]), the nonlinear or gradient models (Lu and Porté-Agel 2010 [82], Berselli *et al.* 2003 [12]), models based on RANS models and so on.

2.2.3.6. Discussion

In LES, a model has to satisfy various requirements. Firstly, the gradient of the subgrid scale shear stress has a direct influence on the mean flow. Secondly, the net energy transfer between the resolved scales and the unresolved ones has to be correctly represented. This transfer includes the dominant dissipative effect associated with the forward scatter, and the backward transfer from the unresolved scales to the resolved ones (Abba *et al.* (2003) [1]). Furthermore, the subgrid scale model, the numerical technique, and the filter have to be consistent in order to get a reasonable result of LES. In practice, the use of LES models in non-spectral methods can be difficult because of the presence of large discretization errors at coarse resolutions. When the mesh is coarse, the differentiation and interpolation errors may be very significant and could become of equal importance as the model contribution. In that case, the physical relevance of the numerical results becomes questionable. Several studies highlighted the influence of discretization errors on the subgrid modeling. Some works emphasized the use of high-order methods or explicit filtering to damp scales close to the grid size (Ghosal 1996 [56]; Carati *et al.* 2001 [23]; Chow and Moin 2003 [28]). Others have focused on the minimization of the total error (Lund and Kaltenbach (1995) [85]; Balaras *et al.*(1996) [5]; Najjar and Tafti (1996) [100]). Nevertheless, our understanding of the interplay between numerical and modeling issues

is presently quite limited.

In aspect of combination between the subgrid scale models and the filter, many research have demonstrated that the performances of the subgrid model greatly depend on the type of filter used (Piomelli 1988 [113]; Liu *et al.* 1994 [80]), the subgrid model cannot be specified independently of the filter (Pruett *et al.* 2000 [120]). Piomelli *et al.* (1988) [113] looked at the combinations between filters and subgrid scale stress models for LES. They found that the consistent combinations of filters and models is essential to ensure accurate LES results. This is due to the fact that a good consistency gives more accurate turbulence statistics than that if the subgrid model is chosen independently of the filter. The cutoff filter is a distinctive one among the classical filters of large eddy simulation, since it clearly separates the resolved scales and subfilter scales. Most successful tests typically use spectral methods and cutoff filter in homogeneous directions. But this is limited to flows with simple geometries. More flexible filters which can be used for flows with complex geometries is still a great lack in large eddy simulations.

2.2.4. Evaluation of subgrid scale models

Various criteria to evaluate the model performance have been discussed in previous research, including a posteriori and a priori analysis based on direct numerical simulation and experimental data.

2.2.4.1. A posteriori and a priori studies

In order to evaluate the performance of a subgrid scale model, the statistics of LES with a particular model can be compared with the same statistics of available reference data. The data can be from DNS or from experiments, typically in the form of mean velocity and Reynolds stress distributions, spectra, etc. Piomelli *et al.* (1988) proposed the name a posteriori tests for such comparisons to emphasize that the model is evaluated only after it has been implemented in a simulation. A posteriori tests are considered to be the ultimate tests of model performance. However, owing to the integrated nature of the results (combining effects of numerical discretization, time integration, and averaging), a posteriori tests typically do not provide much insight into the detailed physics of models and the reasons why they success or fail to provide good results.

A complementary and perhaps more fundamental approach is based on direct comparison between $\tau_{ij}(x,t)$ and its modeled counterpart $\tau_{ij}^{mod}(x,t)$. Such a comparison requires data at high spatial resolution to resolve the subgrid-scale range. $\tau_{ij}(x,t)$ is evaluated based on its definition (Eq. 2.18), and $\tau_{ij}^{mod}(x,t)$ is evaluated by processing the filtered data. For such analysis, one uses the name 'a-priori' to emphasize that no actual LES computation is involved. The data for such studies can be generated using DNS, which allows processing the full three-dimensional velocity field, but is generally limited to low Reynolds numbers and simple geometries. Clark *et al.* (1979), McMillan & Ferziger (1979), and Bardina *et al.* (1980) are early examples of such studies, and Hauët *et al.* (2007) [64], Bou-Zeid *et al.* (2008) [18],van Stratum (2012) [140] are more recent examples of a priori analysis of subgrid scale models.

It should be emphasized that the two approaches, a priori and a posteriori studies, yield different results because the flows in the two simulations evolve differently. A posteriori

test includes the contribution of the LES model, while a priori test is an analysis based on databases of a DNS or experiment. This difference has been observed in previous research. Bardina *et al.* (1980) [6] proposed the improved subgrid models for LES, which generate good results in a priori studies, but performed poorly in a posteriori tests. So, it's essential to perform not only a priori but also a posteriori tests to evaluated the LES performances of a subgrid model.

2.2.4.2. Tests of model performance

A priori study has been used to test the performances of subgrid scale models in many research (Meneveau 1994; Liu *et al.* 1994; Meneveau and Katz 2000, Abba *et al.*(2003) [1], De Stefano *et al.* 2005 [35]). An integrated figure of merit of the local agreement between real and modeled stresses within realizations of the flow has often been given in terms of their correlation coefficient (Clark *et al.* 1979 [31]) or by the average angle between two tensors (Abbà 2003 [1]). The average angle between the modeled and the exact subgrid scale stress tensor, the angle between the subgrid scale stresses and the strain rate tensor have been computed on isotropic turbulence by Abbà (2003) [1]. Generally, the eddy viscosity models show very low correlations with true subgrid scale stresses in a priori test for various flows (Pruett *et al.* 2000 [120], O'Sullivan *et al.* 2001 [105], Park 2005 [107]), while they work adequately in actual simulations. In addition, it has been reported that high correlations coefficients observed in a priori tests mostly come from deterministic correlations between the resolved subfilter scale stresses and their approximations when formally invertible filters are adopted. If such correlations are removed by adopting spectral cutoff filter to mimic the discretization, all the existing SGS models perform poorly in a priori tests, no matter how they perform in a posteriori tests. However, this poor performance in a priori tests does not indicate a failure of such models but the fundamental limitation of a priori test itself (Park 2005 [107]). So, the filter type can influence the correlation coefficient and this has been observed by Abbà 2003 [1] who found that when a filter with an overlapping between resolved and unresolved scale in physical space is used, the modeled subgrid scale quantities are much more correlated to the exact ones than when a sharp cutoff filter is employed. In addition, this correlation is also influenced by the grid resolution. According to Abbà [1], all the models show worse correlations when resolution is decreased. Especially the original dynamic model, most probably because the stress tensor is forced to be aligned to the strain rate tensor.

2.2.4.3. Discussion

The eddy-viscosity model has low spatial correlation with the measured stress, but it predicts mean stresses with the same accuracy as the other models (Carper *et al.* 2008 [25]). This deficiency of eddy viscosity models was originally observed from DNS data by Clark *et al.* (1979) [31], McMillan and Ferziger (1980), and Bardina *et al.* (1980) [6]. Quantitatively, the correlation coefficient typically ranges from 0 to 0.25 (Clark *et al.* 1979 [31], Liu *et al.* 1994 [80]). The correlations are slightly larger (about 0.4) when the subgrid scale force $\bigtriangledown \cdot \tau_{ij}$ is compared with $\bigtriangledown \cdot \tau_{ij}^{mod}$. Typically the correlation is still higher (in the range $[0.5 - 0.7]$) when comparing the local SGS dissipation rate $\tau_{ij}\overline{S}_{ij}$ with $\tau_{ij}^{mod}\overline{S}_{ij}$ (Clark *et al.* 1979 [31]) for homogeneous isotropic turbulence.

However, the other models often have larger correlations than eddy viscosity models.

According to the results of Pruett *et al.* 2000 [120] on the decay of isotropic turbulence in a compressible flow, eddy-diffusivity model correlates poorly against exact stresses (less than 0.2), the gradient model correlates moderately well ($C \approx 0.6$), and a stress-similarity model correlates remarkably well (in the range $[0.8 - 1.0]$). The mixed model examined by Winckelmans *et al.*(1998) [147] in a priori test using DNS shows that the correlation is greater than 0.9.

In addition, it has been found that the correlation of subgrid scale models depend on the filter type and filter size. According to Borue and Orszag 1998 [14], the correlation coefficient between the actual subgrid scale stress tensor and the scalar eddy viscosity representation decreases as the scale decreases. This is nearly independent of Reynolds number. However, the correlation decreases by nearly a factor of two when a cut-off filter is used. This observation is consistent with the results of Liu *et al.* (1994) [80]. Bardina *et al.* 1980 [6] also noticed that the subgrid scale stresses at larger filter scales show higher correlations. A priori test has been also used on scale dependence analysis of many statistics (Lucor *et al.* 2007 [83]). For example, Bou-Zeid *et al.* (2008) [18] conducted research on scale dependence of subgrid-scale model coefficients by an a priori study. Carper *et al.* (2008) [25] studied subfilter-scale fluxes over a surface roughness transition. The model coefficients are found to be scale dependent when the filter scales fall into the production subrange of the turbulence where the flow scales are anisotropic. A priori analysis has been also conducted on other situations, such as the effect of subgrid-scale models on the vortices (Silva *et al.* (2004) [34]).

Generally, the results of the a priori test conducted on homogeneous flow are not much related to those of the LES of channel flows. On one hand, the types of flow are different since in the channel flow we have the presence of boundaries which are absent in homogeneous isotropic turbulence. on the other hand, the filtering procedures are quite different and this produces very different behavior in the models (Abba *et al.* (2003) [1]).

2.3. LES of wall-bounded flows

The research on turbulent boundary layers is carried out for more than a century. The basic characteristics of turbulent boundary layer were widely believed to be well understood, but it bothered only a few that real shear stress measurements differed consistently from (theoretical) results (George 2006 [51]). Thus, during the last decade this problem started to be re-examined.

In unbounded flows, the large eddies, carrying most of the turbulent kinetic energy, set the length and time scales that describe the rest of the small-scale turbulence. This picture is reversed near the wall, where the most energetically productive eddies are necessarily part of the small-scale motion. Further, both configurations are present in wall-bounded flows, and both contribute significantly to the overall turbulent flow field (Hutchins and Marusic 2007 [66]).

Townsend (1976) [138] originally proposed the existence of very large anisotropic scales in the overlap layer under the 'attached eddy' hypothesis, he described them as 'inactive', not containing Reynolds stresses. Perry, Henbest and Chong (1986) [108] repeated that assertion. Jiménez (1998) showed however that this characterization is only partly correct, and that the very large anisotropic scales carry a substantial fraction of the Reynolds

stresses. Alamo (2001) [37] reported further evidence that they carry a substantial part of the turbulent energy in the flow and they are 'active' in Townsend's sense. Other people described that the near-wall turbulence is well organized with coherent structures (Kline *et al.* 1971, Kim *et al.* 1971, Stanislas *et al.* 2008).

If we want to solve the near-wall region, a very fine mesh is necessary. The number of points needed increases at least like $Re^{1.8}$ (Piomelli *et al.* 2002 [111]). A lot of effort has been done in order to reduce the computational cost [46]. An estimation of LES cost was provided by Chapman [26]. He showed that the cost of a wall-resolved LES is proportional to $Re^{2.4}$. This requirement makes LES application to high Reynolds number (order of $10^6 - 10^8$) practically impossible. The near wall resolution is thus a strong limit for the LES methods at high Reynolds number. To bypass this problem, various methods have been proposed. The first one is to circumvent the very costly resolution of the near-wall turbulence structures by bridging the wall region with the aid of empirical boundary conditions for the outer layer (Deardorff 1970 [36], Piomelli, Ferziger & Moin 1988 [113]). These empirical boundary conditions correspond to the wall functions often applied in statistical turbulence simulations. The second approach consists in keeping a fine grid at the wall but solving a simplified set of equations weekly coupled with to the outer flow. In general, no further empirical information about the near-wall flow is required in this approach. This approach was first employed by Balaras *et al.* [5], who used a simplified set of equations, based on thin-boundary-layer assumption, in the inner layer. The third one consists in using a relatively coarse grid at the wall and to mimic the dynamical effects of the energy-containing eddies in the wall-layer through a wall model, such models were first employed by Schumann in a channel flow simulation. Modification of Shumann's model has been proposed later by Grötzbach [59] and Spalding [133]. In addition, a review of wall models used in LES can be found in various references (Cabot *et al.* 2000 [21], Piomelli *et al.* 2002 [111, 110]). The fourth one is the so-called hybrid methods, using RANS equations in the inner layer, while LES equations are solved away from the wall (Fröhlich and von Terzi [49]). The last one is the detached eddy simulation (DES) method introduced by Spalart *et al.* [132], which attempts to treat the near-wall regions in a RANS-like manner, and treat the rest of the flow in an LES-like manner.

2.3.1. Wall turbulence without pressure gradient

Wall turbulence has attracted much attention in LES research with various flow configurations (Grötzbach 1987 [59], Gullbrand 2001 [60], Del Álamo 2003 [38], Fröhlich *et al.* 2005 [48], Brandt 2006 [20], Elsner *et al.* 2009 [45], Chung *et al.* 2009 [29], Kuban *et al.* 2012 [70]). But much understanding of wall turbulence have been gained on simple configurations, such as plane channel flow.

The only economical way to perform LES of high Reynolds-number attached flows, is by computing the outer layer only. The grid size can, under these conditions, be determined by the outer-flow eddies, and the cost of the calculation becomes only weakly dependent on the Reynolds number. Because the grid is too coarse to resolve the inner-layer structures, the effect of the wall layer must be modeled. This requirement spurred the development of models for the wall layer (Piomelli 2002 [111]). Many models have been developed and applied to resolve the wall turbulence depending on different practical needs (Bagwell *et al.* 1993; Hartel *et al.* (1998) [61]; Nicoud *et al.* 2001; Efros (2006) [44]).

All of the models applied to flows on flat walls with mild pressure gradients are almost certainly inadequate for flows which separate and reattach or flows over complex-shaped walls. Furthermore, the development of trustworthy methods for simulating complex flows, especially the development of models for separated flows is more problematical, due to that the experimental data are scarce and lack detail (Ferziger 1995 [47]).

2.3.2. Wall turbulence with pressure gradient

L. Prandtl suggested in 1904 that an Adverse Pressure Gradient (APG), with the pressure increasing in the flow direction, could possibly retard the flow to stagnation (zero velocity) allowing the fluid particles to separate by recirculation. Adverse pressure gradient boundary layers occur in many practical applications, for example in diffusers, at the trailing edge of airfoils and the aft section of ship hulls, and they often play a critical role in determining the performance of engineering devices. In many cases, accurate knowledge of the adverse pressure gradient boundary layer development is the most critical factor in predicting the overall device performance. For example, the design objective in diffusers and aircraft high lift systems often is to obtain the maximum pressure recovery, while avoiding separation.

Mathematically, the adverse pressure gradient can be expressed as $dP/dx > 0$. This is important for boundary layers, since increasing the fluid pressure is akin to increasing the potential energy of the fluid, leading to a reduced kinetic energy and a deceleration. Since the fluid in the inner part of the boundary layer is relatively slow, it is more affected by the increasing pressure gradient. Nagano *et al.* (1993) suggested that this near-wall reduction in turbulent kinetic energy is due to a decrease in the production. In general, as the magnitude of an APG increases, the mean velocity profile develops a large wake region and the turbulent kinetic energy decreases in the near wall region. If a turbulent boundary layer flow encounters a large APG, the flow becomes unstable. If the APG is sufficiently large, this fluid may slow to zero velocity or even become reversed. When flow reversal occurs, the flow is said to be separated from the surface. Such separation almost always has negative consequences such as drag increase and loss of heat transfer. This has very significant consequences in aerodynamics since flow separation significantly modifies the pressure distribution along the surface and hence the lift and drag characteristics. Thus it's of practical importance to investigate the effects of APG on turbulent boundary layers. Turbulent boundary layers tend to be able to sustain an adverse pressure gradient better than an equivalent laminar boundary layer. The more efficient mixing which occurs in a turbulent boundary layer transports kinetic energy from the edge of the boundary layer to the low momentum flow at the solid surface, often preventing the separation which would occur for a laminar boundary layer under the same conditions. This physical fact has led to a variety of schemes to actually produce turbulent boundary layers when boundary layer separation is dominant at high Reynolds numbers.

Many important features of APG turbulent boundary layer are quite well understood (Clauser 1954 [32], Bech *et al.* 1998 [10], Aubertine *et al.* 2005 [4, 3], Drobniak *et al.* 2009 [41], Elsner *et al.* 2009 [46], Harun *et al.* 2010 [63], Laval *et al.* 2010 [72]). The law of the wall has been proven to be valid for higher Reynolds number APG flows (Skare *et al.* 1994 [129] and Bernard *et al.* 2003 [11]). In the outer layer, the statistics were found to be significantly affected by a strong APG (Skåte & Krogstad 1994 [129]) and the

turbulent intensity profiles in the outer region of APG flows collapse onto a single curve when normalized by the inlet free-stream velocity (Nagano *et al.* 1993). In addition, Clauser (1954) [32] suggested a new class of equilibrium boundary layer with an APG, in which the ratio of the pressure gradient force to the wall shear force remains constant. The mean velocity profiles in an equilibrium boundary layer at different streamwise locations show similarity when properly scaled. In addition, many researches also focused on the vortices (Robinson 1991 [121], Bech *et al.* 1998 [10], Skote *et al.* 2002 [130], Laval *et al.* 2012 [73]).

Turbulent flows with an APG have been regarded as being among the most difficult flows to predict using turbulence models (Wilcox, 1993). The major difficulty in simulating a spatially evolving turbulent boundary layer within an APG is imposing the conditions of free stream flows and realistic turbulent inflows. Since there is no systematic way to choose boundary conditions that result in a specific pressure distribution, an interactive procedure is required (Na and Moin, 1998). In spite of difficulties, many researches have been attempted with subgrid scale models, such as the model of a turbulent boundary layer with a non zero pressure gradient by Barenblatt *et al.* (2002) [8]. Elsner *et al.* (2009) did a research on the subgrid scale modeling of turbulent channel flow with one curved wall, in which way the pressure gradient was imposed. The influence of grid density as well as subgrid scale models on the solution has been analyzed. By comparing to the DNS of Marquillie *et al.* 2011 [87], the results of computations performed on the finer grid demonstrate that both Smagorinsky and WALE model give almost the same skin friction coefficient along both walls apart from the separation region on the bump. For both models the separation point is located at the same position and agrees well with the DNS. However, the reattachment point is different and the Smagorinsky model overestimates the length of the recirculation zone while WALE model predicts it in accordance with DNS. Duprat *et al.* (2011) proposed a new wall layer model with the goal to perform high Reynolds number large eddy simulations of wall bounded flows in the presence of a streamwise pressure gradient. The model is validated by a priori comparisons with direct numerical simulation data of various flows with and without streamwise pressure gradient and with eventual flow separation. Large eddy simulations are then performed using the wall model as wall boundary condition. It is shown that the new wall model allows for a good prediction of the mean velocity profile both with and without streamwise pressure gradient [43]. Kuban *et al.* (2012) [70] conducted research on channel flow with a curved wall and reported that the influence of the grid size related to the filter scale is more important for optimization of subgrid models.

Most of the prior researches have been performed on different types of adverse pressure gradient flows with different geometrical configurations. Most of the findings are exclusive and do not have versatility for different given geometrical configuration. In addition, many of these applications are at Reynolds numbers significantly higher than can be examined even in large scale laboratory experiments. Therefore a detailed LES analysis on channel flow with pressure gradient, which is expected a promising research, is an opportunity to make progress in understanding the performances of different models.

This issue becomes more complex when one considers the turbulent boundary layer at large Reynolds numbers with the presence of pressure gradient, where the lack of reliable data is particularly evident. As it has been pointed out by Shah *et al.* 2009 [127] and George *et al.* 2010 [50], the Adverse Pressure Gradient (APG) turbulent boundary layer

is particularly problematic, because of the lack of proper experimental data for sufficiently large Reynolds numbers and for experimental conditions corresponding to real engineering applications.

Chapter 3

A priori approach and methodology

This Chapter presents the definition of new developed least square spline filter. The energy transfer mechanisms and the subgrid scale models examined in our research are also introduced. The a priori analysis of subgrid scale model are first tested using both the least square spline and Gaussian filters in isotropic turbulence. The general description of DNS databases of plane and converging-diverging channel flow are also given finally.

3.1. Least square spline filter

In large eddy simulation, the velocity field can be decomposed into resolved and subfilter scale components by the classical filters described in Chapter 2. Among them, the cutoff filter has the most compact support in wave space and avoids the attenuation of energy in resolved scales. This property explains the significant performances obtained in various research for LES using spectral methods (Piomelli *et al.* 1991 [112], Abbà *et al.* 2003 [1], Brandt 2006 [19]). However, the cutoff filter is more favorable for flow with regular geometries and homogeneous directions due to its limitation to spectral methods. This rises challenges for flows with complex geometries in practical engineering applications which must be computed in the physical space. Thus, a least square spline filter was designed with the expectation of overcoming this limitation, as it can be applied in the physical space while keeping excellent filtering properties. For high spline order, the shape of the transfer function of the least square spline filter is quite similar to the cut off filter and much sharper than other classical filters defined in physical space. The most important property of a least square spline filter is that it has a better flexibility to easily filter on both homogeneous and non-homogeneous grids. Least square spline filter will be used hence to filter both the plane and converging-diverging channel flow.

3.1.1. The original filter

The least square spline filter uses B-spline method to fit a smoothing spline function of order n, with a given node sequence in the weighted mean-square sense, meaning that the sum: $\sum_i W_i|f(x) - \overline{f}(x)|^2$ (W_i is weight coefficient, $f(x)$ is original signal, $\overline{f}(x)$ is the filtered function) is minimized. The filter width will be directly related to the node distance and can therefore easily vary in space. The filter is easy to be used on functions

distributed on non-homogeneous grid as the filter width is defined independently of the grid. A Fortran library of least square spline is provided by Dierckx 1975 [39]. The filtering operation in physical space can be defined as a convolution product:

$$\overline{f}(x) = \int_{-\infty}^{\infty} f(\xi)H(x-\xi)d^3\xi = H \star f(\xi) \tag{3.1}$$

which corresponds to the product in Fourier space:

$$\widehat{\overline{F}}(k) = \widehat{F}(k)\widehat{H}(k) \tag{3.2}$$

where k is wave number, $\widehat{\overline{F}}(k)$, $\widehat{F}(k)$, $\widehat{H}(k)$ are the Fourier transforms of $\overline{f}(x)$, $f(x)$ and $H(x)$. So, in Fourier space, there is:

$$\widehat{H}(k) = \frac{\widehat{\overline{F}}(k)}{\widehat{F}(k)} \tag{3.3}$$

It is difficult to derive a mathematical expression of its transfer function. However, its graphical representation in Fourier space can be deduced by applying the filter to a given function and analyzing its filtered counterpart as shown in Fig. 3.1. Where,

$$\widehat{G}(k) = \frac{|\widehat{\overline{F}}(k)|}{|\widehat{F}(k)|} \tag{3.4}$$

In order to avoid the disturbances of fluctuations, we compute $\widehat{G}(k)$ based on the average of 100 functions $f_l(x)$ defined as:

$$f_l(x) \;=\; \frac{1}{n}\sum_{j=1}^{n} cos(w_j x + \varphi_i), \quad x \in [-1,1], \quad l \in [1,100] \tag{3.5}$$

Where w_j and φ_i are the frequency and the phase shift. The cutoff wave number k_c can be defined corresponding to the intersection of the transfer function $\widehat{G}(k)$ and the curve $\frac{\sqrt{2}}{2}\widehat{F}(k)$. The cutoff wave number of $\widehat{G}(k)$ corresponding to each spline order does not collapse each other, and moves toward the intersection (corresponding to $L/(2\overline{\Delta})$, L is the domain size) of curves $\overline{F}(k)_{r=1}$, $\overline{F}(k)_{r=3}$ and $\overline{F}(k)_{r=5}$ as increasing the spline order. Therefore, the relationship between the cutoff wavenumber k_c and the filter width $\overline{\Delta}$ can be approximated as $k_c \approx L/(2\overline{\Delta})$, independently of the spline order.

The normalized function $\widehat{G}(k\overline{\Delta})$ in Fig. 3.2 shows that $\widehat{G}(k\overline{\Delta})$ decreases as a function of the spline order $k^{-2(r+1)}$. Thus, the 5^{th}-order least square spline (Lss-5^{th}) is the sharpest one. The transfer functions of the Lss-5^{th}, cutoff and Gaussian filters are compared in Fig. 3.3. The Lss-5^{th} filter is very compact and nearly comparable to the cutoff filter, and is much sharper than the classical Gaussian filter.

The commutation error is an important factor to assess the properties of a filter. Fig. 3.4 shows the commutation error of the least square spline filter for three different spline orders. It's evaluated on a one-dimensional signal as expressed in Equation (3.5). The

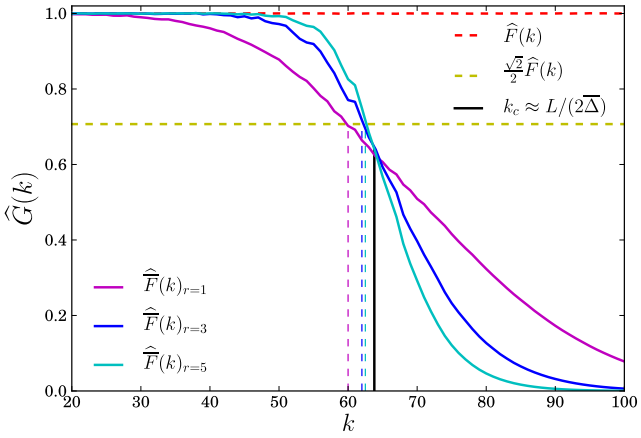

Figure 3.1: Periodic least square spline filter for 3 spline orders ($r = 1, 3, 5$, $\overline{\Delta}$ is filter width, the dashed line is the cutoff wave number).

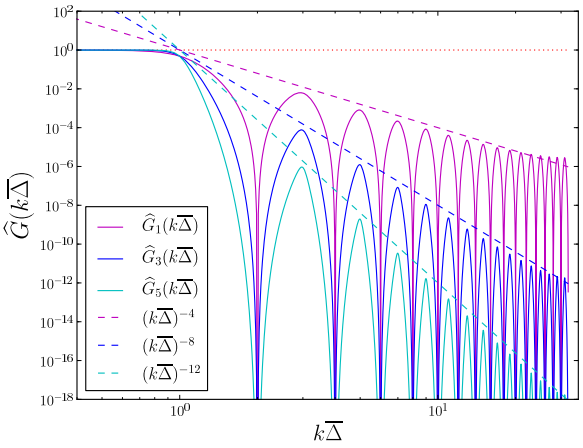

Figure 3.2: Periodic least square spline filter for 3 spline orders ($\widehat{G}(k\overline{\Delta})$ is a function of $r = 1, 3, 5$, the dashed line is $(k\overline{\Delta})^{-2(r+1)}$).

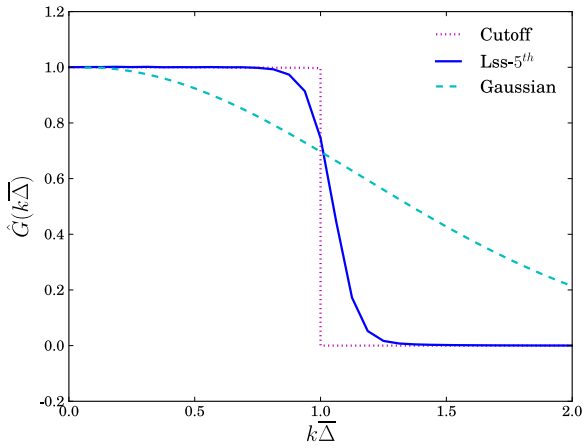

Figure 3.3: Comparison of the transfer functions of the Lss-5^{th}, Gaussian and cut-off filters

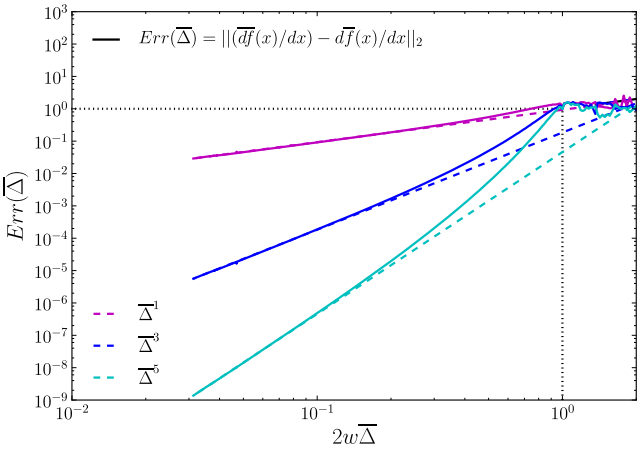

Figure 3.4: Commutation errors with 3 spline orders ($r = 1, 3, 5$, w is the signal frequency).

commutation error is defined as a function of the filter width $\overline{\Delta}$:

$$Err(\overline{\Delta}) = \sqrt{\sum_{i=1}^{m}\left(\frac{\partial\overline{f}(x_i)}{\partial x} - \frac{\partial\overline{f}(x_i)}{\partial x}\right)^2} \Bigg/ \sqrt{\sum_{i=1}^{m}\left(\frac{\partial\overline{f}(x_i)}{\partial x}\right)^2} \tag{3.6}$$

The errors for the three different spline orders reach to the maximum 1.0 at $2w\overline{\Delta} = 1$. Fig. 3.4 exhibits that, the commutation error decreases approximately as a function of the spline order r. The smallest commutation error $Err(\overline{\Delta}) \approx \overline{\Delta}^5$ occurs at the highest spline order $r = 5$. It is smaller than that of classical filters whose commutation error is found to be a second order function of the filter width (Ghosal and Moin 1995 [58]).

3.1.2. The promoted filter

The original least square spline filter discussed above has its own deficiency. Because the distribution of the inner nodes is not homogeneous, the fluctuations accumulated in $(\overline{f^2}(x) - \overline{f}^2(x))$ exhibits a systematic deviation at the fixed positions of the spline junctions. This will contaminate the other statistics associated with it. Therefore, an optimized version of least square spline filter (denoted as Lss-ave) is proposed.

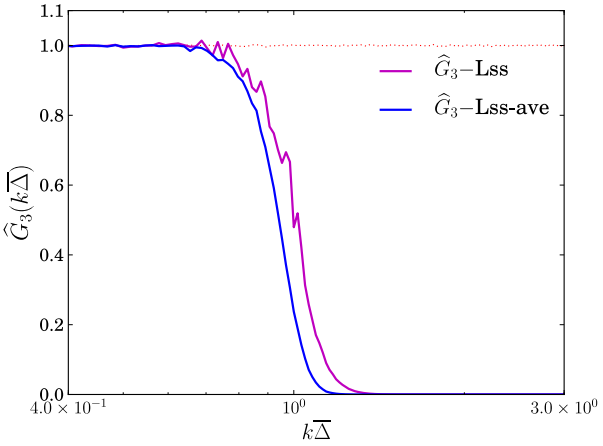

Figure 3.5: Comparison of original Lss and the promoted Lss-ave for a spline order $r = 3$, the cutoff wavenumber is $k\overline{\Delta} = 1$.

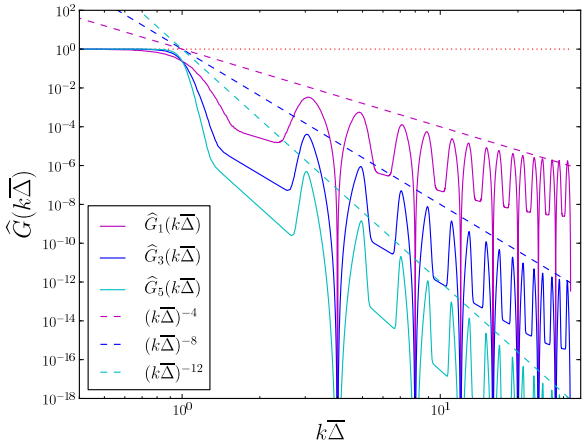

Figure 3.6: The promoted Lss-ave with 3 spline orders ($r = 1, 3, 5$), using the same legend as in Fig. 3.2.

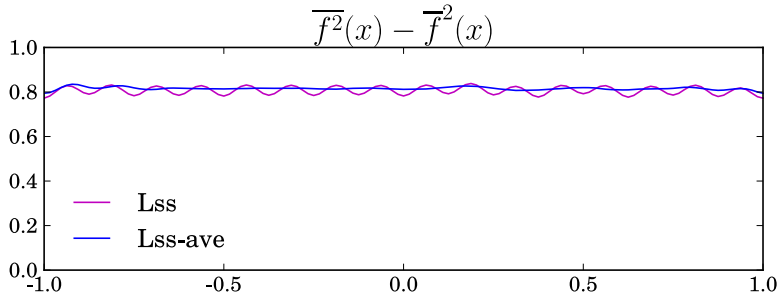

Figure 3.7: Comparison of statistics obtained with the original least square spline filter (Lss) and the promoted one (Lss-ave) for a function $f(x)$ defined in Equation (3.5).

Lss-ave filters a field twice using both the original and the shifted positions of the inner nodes. In the optimized definition, each inner node moves forward half of the distance of the two adjacent original inner nodes:

$$x(i+1) = x(i) + 0.5 \times (x(i+1) - x(i)),\ i = 1, 2...(n-1) \tag{3.7}$$

where n is the number of inner nodes. Then the oscillations observed for $(\overline{f^2}(x) - \overline{f}^2(x))$ can be counteracted by the averaging operation on the summation of the two filtered quantities as shown in Fig. 3.7. Here, we set $\overline{f_1}(x)$ as the filtered field with the original definition of the inner nodes, $\overline{f_2}(x)$ as the filtered field using the shifted nodes. Thus, for

the original least square spline filter (Lss), we have:

$$\overline{f}(x)_{Lss} = \overline{f_1}(x) \tag{3.8}$$

for the promoted one (Lss-ave), it's defined as:

$$\overline{f}(x)_{Lss-ave} = 0.5 \times (\overline{f_1}(x) + \overline{f_2}(x)) \tag{3.9}$$

Fig. 3.5 demonstrates the differences between Lss and Lss-ave for spline order $r = 3$. The optimized filter Lss-ave is smoother than the original one Lss, especially at the cutoff wave number ($k\overline{\Delta} = 1$). Lss-ave can successfully avoid the oscillations in the filtering process as presented in Fig. 3.7, and leads to smoother statistics. More converged results can be obtained in this way. However, as shown in Fig. 3.6, the shape of the transfer function of Lss-ave is slightly modified as compared to the original Lss filter. The modified least square spline filter requires twice computational time and more memory as compared to the original one.

Thus, the advantages of least square spline filter are mainly in that, its transfer function $\widehat{G}$ is much sharper, so the application of low pass filter leaves more energy in the large scale than smoother filters like the Gaussian one. The commutation error of least square spline filter can be kept small as it is a function of the spline order. The main advantage is that the Lss filter can be used to filter both homogeneous and inhomogeneous flows. In the following analysis, the 5^{th}-order least square spline filter is used and denoted as Lss-5^{th} hereafter.

3.2. Energy transfer mechanism

In large eddy simulations, the dissipative scales of motion are resolved poorly, or not at all. As it's known, the main role of the subgrid-scale model is to extract energy from the large scales. In order to better understand the interaction between resolved and unresolved scales, the energy transport equation can be written as the following with the total resolved energy $\overline{q}^2$ ($\overline{q}^2 = \overline{u}_i\overline{u}_i/2.0$) and subgrid scale kinetic energy q^2_{sgs} ($q^2_{sgs} = \tau_{kk}/2.0$),

$$\begin{aligned}\frac{\partial \overline{q}^2}{\partial t} + \underbrace{\frac{\partial}{\partial x_j}(\overline{q}^2\overline{u}_j)}_{Advection\ of\ \overline{q}^2} &= - \underbrace{\frac{\partial}{\partial x_j}(\overline{p}\overline{u}_j)}_{Press.\ Diff.\ of\ \overline{q}^2} + \underbrace{\frac{\partial}{\partial x_j}\left(\nu\frac{\partial \overline{q}^2}{\partial x_j}\right)}_{Visc.\ Diff.\ of\ \overline{q}^2} \\ &- \underbrace{\frac{\partial}{\partial x_j}(\tau_{ij}\overline{u}_i)}_{SGS\ Diff.} - \underbrace{\nu\frac{\partial \overline{u}_i}{\partial x_j}\frac{\partial \overline{u}_i}{\partial x_j}}_{Visc.\ Diss.\ of\ \overline{q}^2} + \underbrace{\tau_{ij}\overline{S}_{ij}}_{SGS\ Diss.}\end{aligned} \tag{3.10}$$

$$\frac{\partial q_{sgs}^2}{\partial t} + \underbrace{\frac{\partial}{\partial x_j}(q_{sgs}^2 \overline{u}_j)}_{Advection\ of\ q_{sgs}^2} = - \underbrace{\frac{\partial}{\partial x_j}(\overline{u_i u_i u_j} - \bar{u}_i \bar{u}_i \bar{u}_j)}_{Turb.\ Transport} - \underbrace{\frac{\partial}{\partial x_j}(\overline{p u_j} - \bar{p}\bar{u}_j)}_{Press.\ Diff.\ of\ q_{sgs}^2} + \underbrace{\frac{\partial}{\partial x_j}\left(\nu \frac{\partial q_{sgs}^2}{\partial x_j}\right)}_{Visc.\ Diff.\ of\ q_{sgs}^2} + \underbrace{\frac{\partial}{\partial x_j}(\tau_{ij}\overline{u}_i)}_{SGS\ Diff.} - \underbrace{\nu\left(\overline{\frac{\partial u_i}{\partial x_j}\frac{\partial u_i}{\partial x_j}} - \frac{\partial \overline{u}_i}{\partial x_j}\frac{\partial \overline{u}_i}{\partial x_j}\right)}_{Visc.\ Diss.\ of\ q_{sgs}^2} - \underbrace{\tau_{ij}\overline{S}_{ij}}_{SGS\ Diss.} \tag{3.11}$$

Both equations (3.10) and (3.11) show that the resolved scales exchange energy with unresolved (or resolved) scales and the surroundings through several mechanisms. The advection and diffusion terms only redistribute energy. Both resolved and subgrid scale energy are destroyed by molecular dissipation, which is represented by the terms $-\nu\frac{\partial \overline{u_i}}{\partial x_j}\frac{\partial \overline{u_i}}{\partial x_j}$ for resolved scales and $-\nu\left(\overline{\frac{\partial u_i}{\partial x_j}\frac{\partial u_i}{\partial x_j}} - \frac{\partial \overline{u}_i}{\partial x_j}\frac{\partial \overline{u}_i}{\partial x_j}\right)$ for subgrid scales. These terms are always negative, thus of a purely dissipative nature.

The SGS energy dissipation,

$$\epsilon_{sgs} = \tau_{ij}\overline{S}_{ij} \tag{3.12}$$

appears with opposite signs in equations (3.10) and (3.11). Typically ϵ_{sgs} acts as a sink of resolved kinetic energy and as a source term for SGS kinetic energy q_{sgs}^2.

The total transfer of energy between large and subgrid scales is the SGS energy transfer, sum of SGS diffusion and dissipation, defined as:

$$T_{sgs} = \frac{\partial}{\partial x_j}(\overline{u}_i \tau_{ij}) - \epsilon_{sgs} \tag{3.13}$$

The term $\partial(\overline{u}_i\tau_{ij})/\partial x_j$ accounts for a spatial redistribution of large scale kinetic energy due to SGS motions.

Both ϵ_{sgs} and T_{sgs} can be positive or negative depending of the local physics of turbulence. On the average, energy flows from the large to the small scales, and $\epsilon_{sgs} < 0$ or $T_{sgs} > 0$ (forward scatter), reversed energy flow $\epsilon_{sgs} > 0$ or $T_{sgs} < 0$ (back scatter) from the small scales to the large ones may also occur intermittently.

The positive (ϵ_{sgs}^+) and negative (ϵ_{sgs}^-) contributions of ϵ_{sgs} can be defined as:

$$\epsilon_{sgs}^+ = \frac{1}{2}(\epsilon_{sgs} + |\epsilon_{sgs}|),\ \epsilon_{sgs}^- = \frac{1}{2}(\epsilon_{sgs} - |\epsilon_{sgs}|) \tag{3.14}$$

Similar to equation (3.14), the positive and negative contributions of T_{sgs} can be computed as well by:

$$T_{sgs}^+ = \frac{1}{2}(T_{sgs} + |T_{sgs}|),\ T_{sgs}^- = \frac{1}{2}(T_{sgs} - |T_{sgs}|) \tag{3.15}$$

As it plays an important role in LES, SGS energy transfer mechanism has been the focus of a number of studies in channel flow (Piomelli *et al.* 1991 [112]; Horiuti 1997 [65]; Härtel *et al.* 1998 [61]; Abbà *et al.* 2003 [1]; Hauët *et al.* 2007 [64]; Cimarelli and De Angelis 2012 [30]). Many research based on DNS of turbulent channel flow have shown that the SGS dissipation tends to zero in the laminar sublayer and an inverse cascade of turbulent kinetic energy occurs in the buffer layer (Härtel *et al.* 1994 [62]). The inverse transfer cannot generally be described by the simple eddy viscosity type of subgrid models. Härtel *et al.* 1994 supposed that the inverse cascade of turbulent kinetic energy is primarily caused by subgrid scale stresses aligned with the mean rates of strain. Härtel and Kleiser (1998) [61] showed that the correlation of the wall normal subgrid stress and the wall-normal derivative of the streamwise resolved velocity plays the key role in the occurrence of the inverse cascade and is strongly enhanced by coherent motions, such as the well known bursting events (Härtel *et al.* 1994 [62]). The magnitude of this inverse transfer is very sensitive to the cutoff wavenumber, but it was found to depend little on the shape of the filter applied (Härtel and Kleiser 1998 [61]). Generally it's considered that the correct reproduction of inverse energy transfer plays a key role in the estimation of near-wall statistics, especially when the viscous sublayer is not properly resolved (Lodato *et al.* 2009 [81]).

3.3. A priori analysis of subgrid scale models

Many a priori tests for subgrid scale models have been performed using classical filters on homogeneous turbulence (McMillan and Ferziger 1979 [91]; Liu *et al.* 1994 [80]; Borue and Orszag *et al.* 1998 [14]; Pope 2000 [116]; Meneveau and Katz 2000 [93]; Pruett and Adams 2000 [120]; Wollblad and Davidson 2008 [148]), or on plane channel flow at low Reynolds number (Piomelli *et al.* 1991 [112]; Härtel *et al.* 1994 [62]; Horiuti 1997 [65]; Abbà *et al.* 2003 [1]; Cimarelli and De Angelis 2012 [30]), or other flow configurations, such as in a wind tunnel by Carper and Porté-Agel 2008 [25].

In the present research, the a priori analysis of subgrid scale models will be performed using both the classical filter (Gaussian filter) and the new developed filter (Lss-5^{th} filter). The a priori tests of our research will be conducted on classical subgrid scale models, such as the Smagorinsky model (SM), the dynamic Smagorinsky model (DSM), the wall-adapting local eddy-viscosity model (WALE), as well as a recent model, the σ model. These models will be analyzed on a DNS of plane channel flow at high Reynolds number ($Re_\tau = 950$) and a DNS of converging-diverging channel flow at $Re_\tau = 617$.

3.3.1. A priori evaluation of model coefficients

The model coefficients can be evaluated using a mathematical form of the eddy viscosity subgrid scale models,

$$\tau_{ij} - \frac{1}{3}\tau_{kk}\delta_{ij} = -2\nu_{sgs}\overline{S}_{ij} \tag{3.16}$$

The coefficient of subgrid scale models can not be directly computed from Equation 3.16, as it is a tensorial relation composed of 6 independent scalar equations that must be

satisfied. In order to reduce the number of equations to one, we use the following form defined as:

$$\left\langle \tau_{ij}^{mod} \overline{S}_{ij} \right\rangle = \left\langle \tau_{ij} \overline{S}_{ij} \right\rangle \tag{3.17}$$

where the superscript "mod" indicates the modeled quantity. Following this, a priori estimations of the model coefficients $\langle C_s \rangle$ of Smagorinsky model, $\langle C_w \rangle$ of the WALE model and $\langle C_\sigma \rangle$ of the σ model can be evaluated by matching the measured and modeled subgrid scale dissipation for each model that needs to be analyzed a priori as:

$$\langle C_s^2 \rangle = \frac{\langle \tau_{ij} \overline{S}_{ij} \rangle}{-2(\overline{\Delta})^2 \langle |\overline{S}| \overline{S}_{ij} \overline{S}_{ij} \rangle} \tag{3.18}$$

$$\langle C_w^2 \rangle = \frac{\langle \tau_{ij} \overline{S}_{ij} \rangle}{-2(\overline{\Delta})^2 \left\langle \frac{(S_{ij}^d S_{ij}^d)^{3/2} \overline{S}_{ij} \overline{S}_{ij}}{(\overline{S}_{ij} \overline{S}_{ij})^{5/2} + (S_{ij}^d S_{ij}^d)^{5/4}} \right\rangle} \tag{3.19}$$

$$\langle C_\sigma^2 \rangle = \frac{\langle \tau_{ij} \overline{S}_{ij} \rangle}{-2(\overline{\Delta})^2 \left\langle \frac{\sigma_3(\sigma_1 - \sigma_2)(\sigma_2 - \sigma_3)}{\sigma_1^2} \overline{S}_{ij} \overline{S}_{ij} \right\rangle} \tag{3.20}$$

The coefficient $\langle C_d \rangle$ of Dynamic Smagorinsky model is computed from equation (2.25) with the effective test filter scale $\widehat{\Delta} = 2.0\overline{\Delta}$ in most instances of our research except special indication. Unlike the standard Smagorinsky model, the coefficient $\langle C_d \rangle$ of Dynamic Smagorinsky model is calculated only from resolved scales, and it is expected to be comparable with coefficient $\langle C_s \rangle$ of Smagorinsky model for the same flow.

For the 3D filter of our isotropic turbulence database, the grid scale $\overline{\Delta}$ is defined as:

$$\overline{\Delta} = \sqrt{(\overline{\Delta}_x^2 + \overline{\Delta}_y^2 + \overline{\Delta}_z^2)/3.0} \tag{3.21}$$

Where $\overline{\Delta}_x, \overline{\Delta}_y, \overline{\Delta}_z$ are filter widths respectively in x, y, z directions. In plane channel flow with or without pressure gradient, a 2D filter will be used (with no filtering in the normal direction) that will be defined as:

$$\overline{\Delta} = \sqrt{(\overline{\Delta}_x^2 + (\Delta_{gridy})^2 + \overline{\Delta}_z^2)/3.0} \tag{3.22}$$

In order to simplify the research, no explicit filter is conducted in wall normal direction. The mesh grid along y behaves as an implicit filter, so the contribution of grid spacing Δ_{gridy} in wall normal direction is considered to calculate $\overline{\Delta}$. As Δ_{gridy} is small with respect to $\overline{\Delta_x}$ and $\overline{\Delta_z}$, this definition only slightly differ from the equivalent definition using only $\overline{\Delta_x}$ and $\overline{\Delta_z}$.

3.3.2. Tests of models behavior

In order to evaluate performances of each SGS model, there are various methods of comparing the modeled and real SGS stresses based on correlation coefficients. We consider here three different necessary conditions that the modeled SGS stress should ideally satisfy to produce accurate flow statistics (Liu *et al.* 1994 [80]; Meneveau and Katz 2000 [93]). They are defined as:

$$\langle \tau_{ij} \rangle = \langle \tau_{ij}^{mod} \rangle \tag{3.23}$$

$$\left\langle \frac{\partial \tau_{ij}}{\partial x_j} \right\rangle = \left\langle \frac{\partial \tau_{ij}^{mod}}{\partial x_j} \right\rangle \tag{3.24}$$

$$\langle \tau_{ij} \overline{S}_{ij} \rangle = \langle \tau_{ij}^{mod} \overline{S}_{ij} \rangle \tag{3.25}$$

The first condition (3.23) is to match the mean SGS stress. The second condition involves the term that actually appears in the filtered Navier-Stokes equations and is referred to as the SGS force (Meneveau and Katz 2000 [93]; Pope 2000 [116]; Geurts 2004 [54]). This condition, which can guarantee that LES with subgrid models produces the correct mean filtered velocity and second order resolved moments, is necessary and important for mean momentum transport when the filter width approaches integral scale. However, it is not a sufficient condition to guarantee correct predictions for the second-order moments $\langle u_i' u_j' \rangle$ (Meneveau 1994 [92]). The third condition reflects the ability of the model to predict the SGS transfer rate of resolved kinetic energy.

The correlations of the form C(E, M) between exact (E) and modeled (M) quantities using subgrid scale models can be defined as:

$$C(E, M) = \frac{\langle EM \rangle - \langle E \rangle \langle M \rangle}{[(\langle E^2 \rangle - \langle E \rangle^2)(\langle M^2 \rangle - \langle M \rangle^2)]^{1/2}} \tag{3.26}$$

This formula has been used by several authors for similar a priori analysis (Clark et al 1979 [31], Borue and Orszag 1998 [14]; Pruett and Adams 2000 [120]). We expect that if the variable M is nearly statistically or instantaneously equivalent to the variable E, then the correlation coefficient C(E, M) should be close to unity.

correlations	E	M
$C_{\tau_{ij}}$	τ_{ij}	$\tau_{ij}^{mod} = -2\nu_{sgs}\overline{S}_{ij} + \frac{1}{3}\delta_{ij}\tau_{kk}$
C_{f_i}	$\frac{\partial \tau_{ij}}{\partial x_j}$	$\frac{\partial \tau_{ij}^{mod}}{\partial x_j} = \frac{\partial}{\partial x_j}(-2\nu_{sgs}\overline{S}_{ij} + \frac{1}{3}\delta_{ij}\tau_{kk})$
$C_{\epsilon_{sgs}}$	$\tau_{ij}\overline{S}_{ij}$	$\tau_{ij}^{mod}\overline{S}_{ij} = (-2\nu_{sgs}\overline{S}_{ij} + \frac{1}{3}\delta_{ij}\tau_{kk})\overline{S}_{ij}$

Table 3.1: Correlations between the exact and modeled quantities.

Accordingly, the three criteria described by equations (3.23-3.25) can be investigated corresponding to the description in Table (3.1). Their correlations are respectively marked

as $C_{\tau_{ij}}$, C_{f_j} and $C_{\epsilon_{sgs}}$ in the following.

3.4. Validation for isotropic turbulence

Homogeneous turbulence is rarely encountered in flows of practical relevance. Nevertheless, the analysis of homogeneous turbulent flows has played a major role in the development, calibration and validation of subgrid scale models. In addition to bringing in more transparency in turbulence dynamics, homogeneous approximation simplifies to a great degree the mathematical description and the solution of the equations. Furthermore, homogeneity in space enables the use of periodic boundary conditions, which, in turn, allow to study the turbulence dynamics in a fraction of actual flow space, making these flows very attractive for direct numerical simulations. Furthermore, flow homogeneity reduces the demands on experimental set up and enables the turbulence phenomena to be studied in well control conditions.

3.4.1. Introduction

In the present study, the a priori analysis is performed on homogeneous isotropic turbulence at $Re_\lambda = 144$ (λ is the Taylor scale). The mesh resolution is 512^3 in a simulation domain of size $(2\pi \times 2\pi \times 2\pi)$. Three cutoff wave numbers $k_c = 8, 16, 24$ are adopted here. Their corresponding filter width are displayed in Table 3.2. The DNS fields are filtered using the three-dimensional periodic Lss-5^{th} filter and Gaussian filters.

k_c	8	16	24
$\overline{\Delta}/\eta$	51.15	25.58	17.05
$L/\overline{\Delta}$	2.0	4.0	6.0

Table 3.2: Three cutoff wavenumbers and their corresponding filter width with regard to the Kolmogorov scale (η) and integral scale (L) for homogeneous isotropic turbulence.

As described by many research (such as Lilly 1992 [76]), the coefficients of subgrid models can be obtained when the cutoff wavenumber lies within a $k^{-5/3}$ Kolmogorov cascade and the ensemble-averaged subgrid dissipation is identical to the energy dissipation rate. The one-dimensional streamwise energy spectrum E_{11} is given in Fig. 3.8. It shows that the three cutoff wave numbers fall fairly well into the short inertial range of the present homogeneous flow.

3.4.2. A priori evaluation of model coefficients

In this section, the coefficients of the Smagorinsky model $\langle C_s \rangle$, Dynamic Smagorinsky model $\langle C_d \rangle$, the WALE model $\langle C_w \rangle$ as well as the σ model $\langle C_\sigma \rangle$ are evaluated a priori on homogeneous isotropic turbulence. According to previous research, the constants of these subgrid models for homogeneous isotropic turbulence are respectively as $\langle C_s \rangle = \langle C_d \rangle \approx$

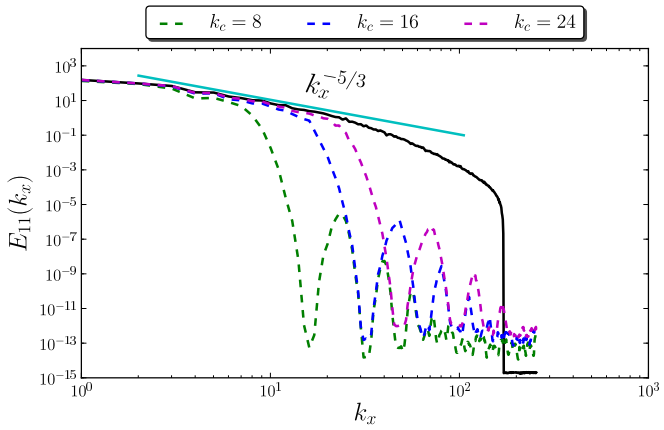

Figure 3.8: One dimensional energy spectra of $E_{11}(x)$ in streamwise direction of homogeneous isotropic turbulence.

0.16 (Lilly 1967 [77]; Meneveau 1997 [94]), $\langle C_w \rangle \approx 0.5$ (Nicoud and Ducros 1999 [102]) and $\langle C_\sigma \rangle \approx 1.5$ (Nicoud *et al.* 2011 [103]).

The results of our present analysis using Lss-5^{th} filter and Gaussian filter are given in Table 3.3. The bracket means the averaging operation on all homogeneous directions of space and time. Results of this analysis demonstrates that the theoretical behaviors of $\langle C_s \rangle$, $\langle C_d \rangle$, $\langle C_w \rangle$ and $\langle C_\sigma \rangle$ in many practical simulations are actually far from constant with respect to the filter width. This is consistent with observations of Meyers and Sagaut 2006 [97]. Hence, we choose the term subgrid model "coefficient" instead of the more commonly used "constant".

k_c		8	16	24
$\langle C_s \rangle$	Lss-5^{th}	0.143	0.122	0.107
	Gaussian	0.142	0.124	0.115
$\langle C_d \rangle$	Lss-5^{th}	0.145	0.141	0.133
	Gaussian	0.151	0.155	0.145
$\langle C_w \rangle$	Lss-5^{th}	0.435	0.367	0.326
	Gaussian	0.440	0.387	0.359
$\langle C_\sigma \rangle$	Lss-5^{th}	1.133	0.983	0.870
	Gaussian	1.132	0.999	0.936

Table 3.3: Coefficients $\langle C_s \rangle$, $\langle C_d \rangle$, $\langle C_w \rangle$, $\langle C_\sigma \rangle$ with three cutoff wave numbers using both Lss-5^{th} and Gaussian filters for homogeneous isotropic turbulence.

Table 3.3 exhibits that all the coefficients of subgrid models are sensitive to the filter width (or cutoff wave number) and filter type. They become slightly smaller in general as the filter width decreases in inertial range. Moreover, for the same filter width, the coefficients are larger with Gaussian filter than with Lss-5^{th} filter.

In addition, the coefficients of Smagorinsky model $0.107 \leq \langle C_s \rangle \leq 0.143$ and Dynamic Smagorinsky model $0.133 \leq \langle C_d \rangle \leq 0.155$ are about 30% smaller than their standard value 0.16. The coefficients of WALE model $0.33 \leq \langle C_w \rangle \leq 0.44$ and σ model $0.87 \leq \langle C_\sigma \rangle \leq 1.2$

are also about 30% smaller than their standard values which are 0.5 and 1.5 respectively at very large Reynolds number and when the filter lies inside the inertial range. This may be owing to the fact that the coefficients of subgrid scale models are very sensitive to the filter type or the mesh size when using implicit filtering LES (Scotti *et al.* 1993 [126]; Nicoud *et al.* 2011 [103]).

3.5. Description of databases

In order to investigate the properties of subgrid scale models on wall turbulence, our analysis is carried out on a direct numerical simulation of the turbulent incompressible flow in plane channel at Reynolds number $Re_\tau = 950$, and on a direct numerical simulation of the converging-diverging channel flow at $Re_\tau = 617$. The description of the two databases will be presented in the following.

3.5.1. Plane channel flow

Most research of plane channel flow are focused on turbulence at low Reynolds number (Piomelli *et al.* 1991 [112]; Härtel *et al.* 1994 [62]; Abbà *et al.* 2003 [1]; Cimarelli and De Angelis 2012 [30]). In order to investigate the energy transfer mechanism and the a priori performances of subgrid scale models on plane channel flow at high Reynolds number, the DNS database at the largest Reynolds number available for us is the one provided by J.Jimenez *et al.* at $Re_\tau = 950$. This Reynolds number is significantly higher than the previous research conducting a priori analysis.

The DNS simulation was performed using periodic boundary conditions in the streamwise (x) and spanwise (z) directions, while no slip conditions were imposed on the two parallel walls. The grid resolution is $N_x \times N_y \times N_z = 2048 \times 385 \times 1535$, in a domain $8\pi \times 2 \times 3\pi$. A Chebychev polynomial is used in wall-normal direction (y). In the present work, only the lower half of the domain will be used for a priori analysis.

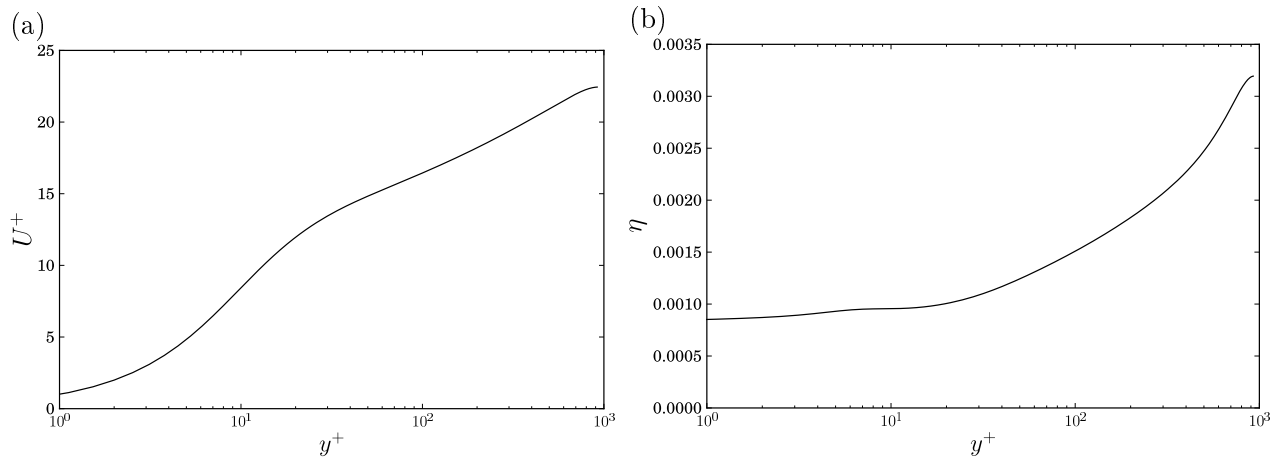

Figure 3.9: Mean streamwise velocity U^+ (a) and the Kolmogorov scale η (b) along wall normal position at the lower half of plane channel flow at $Re_\tau = 950$.

The 2D filtering operations using both Lss-5^{th} filter and Gaussian filter are performed in streamwise and spanwise directions. No filtering is performed in wall normal direction,

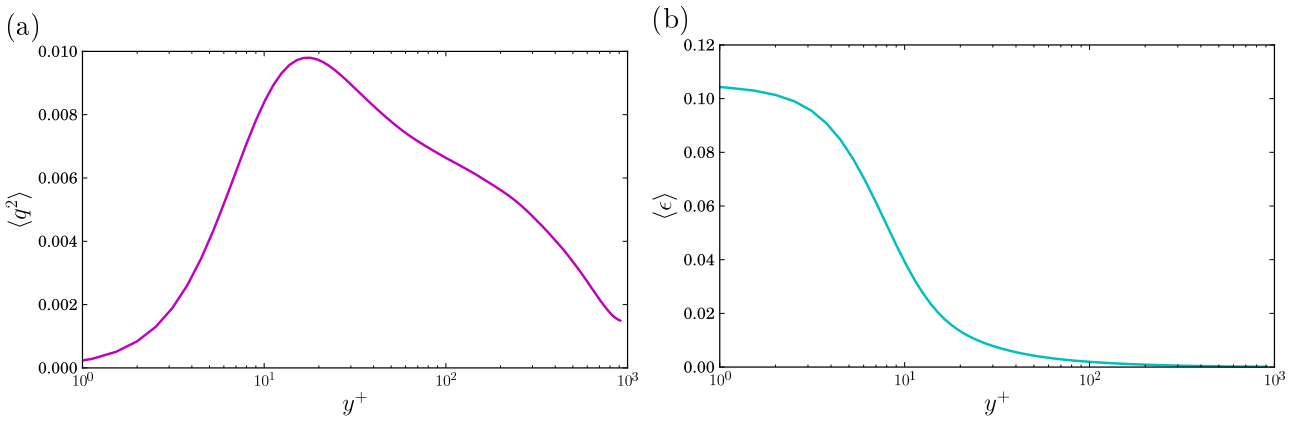

Figure 3.10: Turbulent kinetic energy $\langle q^2 \rangle$ (a) and the plane-averaged rate of dissipation of turbulence kinetic energy $\langle \epsilon \rangle = \langle |2\nu \overline{S}_{ij} \overline{S}_{ij}| \rangle$ (b) along wall normal position of plane channel flow at $Re_\tau = 950$.

since in this direction a rather fine resolution is required to resolve the steep mean-flow gradients. Otherwise, when the actual filter scales are employed, the SGS turbulence will still contain dynamically significant turbulence structures in the near-wall region below the actual filter width.

The mean streamwise velocity in wall unit U^+ along wall normal direction is shown in Fig. (3.9), it keeps increasing toward the center of the channel, the Kolmogorov scale (η) is also plotted. Fig. (3.10) exhibits the total turbulent kinetic energy $\langle q^2 \rangle$, and the energy dissipation rate $\langle \epsilon \rangle$ along wall normal position. These two terms are often used to normalize the other statistics in numerical analysis. The detailed a priori analysis of the four subgrid scale models will be performed in Chapter 4.

3.5.2. Channel flow with adverse pressure gradient

In the present study, we make use of a direct numerical simulation database of converging diverging channel flow documented in Marquillie *et al.* 2011 [87] and Laval *et al.* (2012) [73]. The Reynolds number based on the inlet velocity and half channel width is $Re_\tau = 617$. The simulation domain is $4\pi \times 2 \times \pi$ with a spatial resolution $2304 \times 385 \times 576$. In streamwise direction, the 4^{th}-order explicit finite scheme is adopted. Chebyshev Collocation is used in the normal direction. The Fourier discretization is performed in spanwise direction, while spanwise periodicity is imposed on 2π and a symmetry is imposed on π in this direction. The wall curvature was obtained by a mathematical mapping of the partial differential operators from physical coordinates to Cartesian ones. More details about the mapping of coordinates can be found in Marquillie *et al.* 2008 [88]. In order to increase the convergence of statistics, the results are averaged in the statistically homogeneous spanwise direction and in time. They are denoted with a bracket $\langle \cdot \rangle$. Wall units based on the friction velocity at the summit of the bump ($u_\tau^s = 0.0695$) are denoted with the superscript $+$, the reference wall units based on $u_\tau^o = 0.0494$ at the inlet have the superscript $\star$.

The ratio of the maximum mesh size with respect to the Kolmogorov scale η is shown in Fig. (3.11). In most of the channel, this ratio is less than 2. It is approximately 3 in the diverging part and goes up to 5 very close to the wall. The mesh size in wall units using the

inlet friction velocity is $\Delta_x^\star = 5.1, 0.02 < \Delta_y^\star < 5.1, \Delta_z^\star = 3.4$. The global maximum values are reached in the converging part of the channel with $\Delta_x^\star = 10.7, \Delta_y^\star = 7.9, \Delta_z^\star = 7.4$.

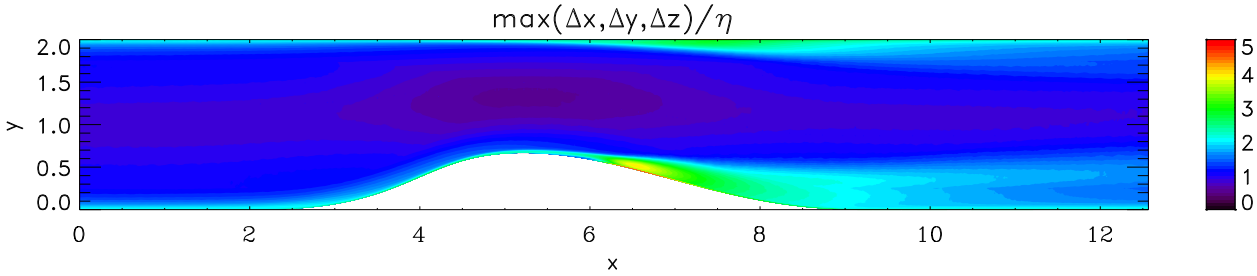

Figure 3.11: Spatial resolution of the DNS with respect to the Kolmogorov scale. $\Delta x, \Delta y, \Delta z$ are the mesh sizes in streamwise, wall-normal and spanwise direction.

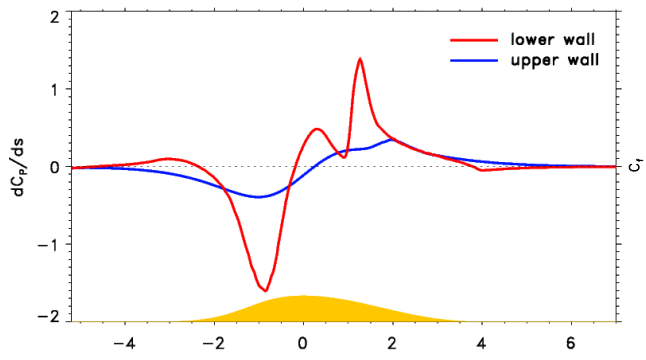

Figure 3.12: Pressure gradient dC_p/ds at the two walls.

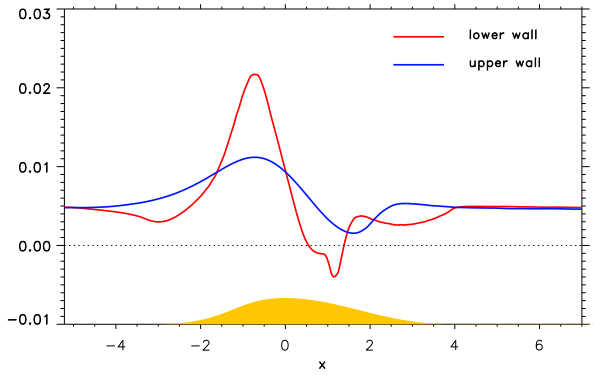

Figure 3.13: Skin friction coefficient $C_f = \tau_w/(\frac{1}{2}\rho U_o^2)$ at the two walls.

The non-dimensional pressure gradient dC_p/ds (s is the tangential direction of the bump) at the two walls is given in Fig. 3.12, where u_τ is the local friction velocity. The pressure gradient at the flat upper wall is smoother and weaker compared to the lower wall. dC_p/ds becomes positive at position $x = 0.2$ and rises up to $dC_p/ds = 0.8$ at about $x = 1.6$. At the lower wall, the positive pressure gradient begins at $x = -0.2$ and increases very sharply near $x = 0.2$. The flow encounters a strong pressure gradient ($dC_p/ds > 0.09$) at both walls. The streamwise location where dC_p/ds becomes larger than 0.09 at the two walls are $x = 0.24$ and $x = 0.75$ respectively.

The friction coefficients $C_f = \tau_w/(\frac{1}{2}\rho U_o^2)$ for the two walls are depicted in Fig. 3.13, where U_o is the maximum velocity at the inlet. Both peaks of C_f at the two walls occur at the same position $x \simeq -0.6$. The figure indicates that the flow slightly separates at the lower wall but not at the upper wall. A thin recirculation region occurs in the range $0.5 < x < 1.5$, which is also visible on the pressure gradient at the lower wall in Fig. 3.12.

The distribution of turbulent kinetic energy $\langle q^2 \rangle$ in the x-y plane is given in Fig. 3.14. Two strong regions of turbulent kinetic energy which are more intense at the lower wall than at the upper wall appear in the APG diverging regions. So as to conduct a detail inspection of this region, one-dimensional normal profiles of turbulent kinetic energy along the two walls are depicted in Fig. 3.15. One can observe a peak initially located close to the wall near $y^\star \sim 11$ at $x = 0.0$ and moving away from the wall when progressing

downstream. These peaks reach a maximum near $y^\star \sim 33$ at $x = 1.2$. This is due to a very sharp increase of the energy production (Laval *et al* 2012 [73]). The location of the peak corresponds to the position around $y^\star \simeq 30$ of the high density peak of vortices near $x \simeq 1.0$ examined by Laval 2012 [71]. Then a new near wall peak is regenerated when the original ones decrease and continue to move apart. This agrees well with observations of the normal profiles of the averaged streamwise fluctuating velocity at the lower wall by Laval *et al.* 2012 [73] who found that the production of energy due to adverse pressure gradient is responsible for the second peak. The energy peak has a similar behavior at the upper wall but slightly shifted downstream due to the slight streamwise shift of the first adverse pressure gradient position (see Fig. 3.12).

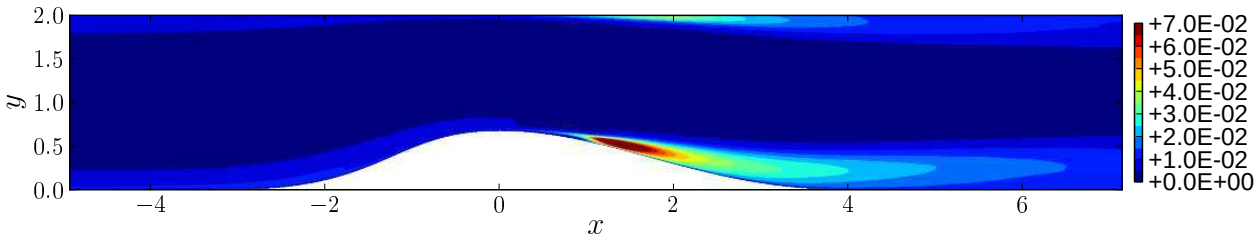

Figure 3.14: Averaged turbulent kinetic energy $\langle q^2 \rangle = \langle \frac{1}{2} u_i' u_i' \rangle$ on channel flow with adverse pressure gradient at $Re_\tau = 617$.

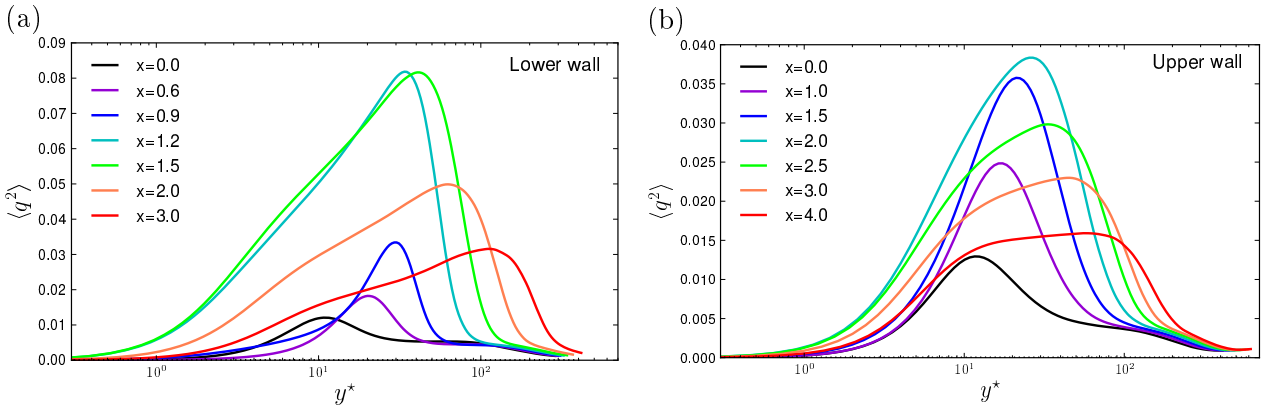

Figure 3.15: Normal profiles of the averaged turbulent kinetic energy $\langle q^2 \rangle$ at the two walls in the adverse pressure gradient regions.

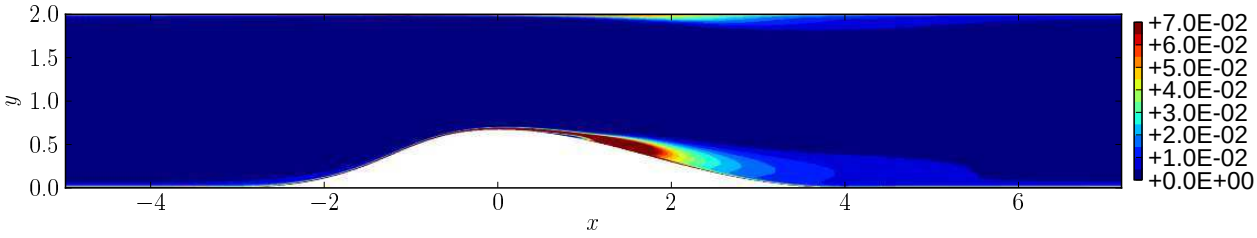

Figure 3.16: Rate of kinetic energy dissipation $\langle \epsilon \rangle = \langle 2\nu S_{ij} S_{ij} \rangle$ in the channel flow with adverse pressure gradient at $Re_\tau = 617$.

So as to normalize the other statistics in Chapter 5, the rate of kinetic energy dissipation $\langle \epsilon \rangle = \langle 2\nu S_{ij} S_{ij} \rangle$ in the x-y plane is given in Fig. 3.16. Two intense regions of

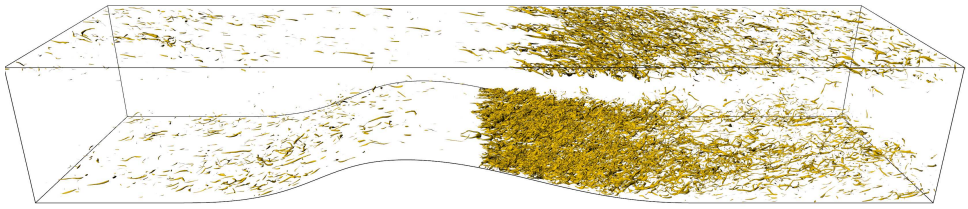

Figure 3.17: Iso-value of the Q-criterion ($Q = \frac{1}{2}[|\Omega|^2 - |S|^2]$ with $S = \frac{1}{2}[\nabla u + (\nabla u)^T]$ and $\Omega = \frac{1}{2}[\nabla u - (\nabla u)^T]$) for the whole simulation domain.

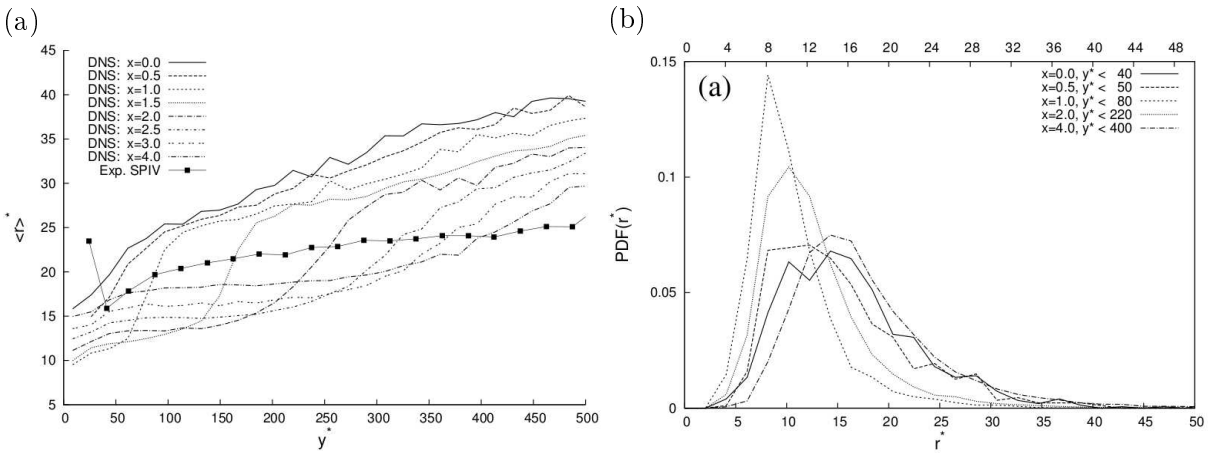

Figure 3.18: The average radius of streamwise vortices (a) and density of probability of the radius of streamwise vortices inside the high turbulent kinetic energy region (b) on channel flow with adverse pressure gradient at $Re_\tau = 617$ (from Laval 2012 [71]).

$\langle\epsilon\rangle$ are also observed in the diverging APG near wall regions. The sharp growth of both turbulent kinetic energy (Fig. 3.15) and dissipation (Fig. 3.16) correspond to regions of high concentration of vortices occurring slightly downstream of the summit of the bump at the lower wall, and more downstream at the upper wall as shown in Fig. 3.17. In the same geometry, the probability density of the streamwise vortices radius in the x-y plane in the region near the peak of turbulent kinetic energy was estimated by Laval 2012 [71], who observed that the density of streamwise vortices near the turbulent energy peak region is almost 30 times that in the other regions. At $x \simeq 1.0$, $y^+ < 50$ occurs the maximum density of streamwise vortices whose average radius is $r^\star \simeq 15$ (less than 10 times of Kolmogorov scale η) in the largest probability (see Fig. 3.18), while the highest probability of the vortices radius is $r^\star \simeq 30$ outside the energy peak region. So the intense energy and dissipation in the diverging near wall regions is mainly caused by the high concentration of small scale vortices.

3.6. Numerical methods and computational issues

As a spectral method is not applicable for the non-homogeneous flow database, an 8^{th}-order (implicit 5-5 stencil) compact finite-difference scheme is used for the spatial derivation for a priori analysis. However, when used with homogeneous grid, high order finite difference derivatives are affected by 'Runge' effect which is spurious oscillations that may

appear at the borders of the domain. As the analysis has to be conducted on the original DNS grid, the only solution to compute the derivative is to restrict the domain for the computation of the statistics by removing the regions affected by the 'Runge' phenomenon. Using high order finite difference scheme, the 'Runge' phenomena is usually restricted to the first $4-5$ points from the boundary. In our case, 48 points respectively at the beginning and at the end of spanwise and streamwise directions in the plane channel flow, and 24 points in the channel flow with adverse pressure gradient are ignored. These are enough to prevent the numerical error associated to the 'Runge' effect to affect the statistics.

The statistics of present research are computed by averaging over 10 fields of plane channel flow, and 465 fields with Lss-5^{th} filter or 186 fields with Gaussian filter for the APG channel flow. The a priori analysis is conducted with a post-processing code written in Fortran 90 parallelized using Message Passing Interface (MPI). The parallel computations were performed with 32 (for plane channel flow) or 35 (for APG channel flow) CPUs on the LML computing server (6 nodes, 4 12-cores AMD CPU, 2.0 Ghz). The execution efficiency and computational time largely depend on the number of processors and the size of the database. The CPU time depends on the subgrid scale models and is affected by the filter type. A typical a priori estimation of the Smagorinsky coefficient computed by 465 fields of the converging-diverging channel flow requires about 100 to 200 hours depending of the filter type. As the full computational domain (half a billion points of grid mesh) is treated at the same time, some computations requires up to 200 Gb of memory.

Chapter 4

Results for the plane channel flow

4.1. Introduction

This chapter presents the results of the a priori tests on the energy transfer mechanisms and a priori evaluations of different subgrid scale models coefficients in plane channel flow at $Re_\tau = 950$. The performances of these subgrid scale models and their predicting capacities are assessed finally. The behavior of subgrid scale models are tested with different 2D filter widths using both Lss-5^{th} and Gaussian filters.

4.2. Choice of filter width

In order to correctly simulate the dynamics of the inner layer of wall turbulence, the energy containing scale should be resolved. Robinson (1991) showed that, the turbulent dynamic in the inner layer is dominated by vortices whose dimensions are constant in wall units, and which should be correctly resolved. In order to satisfy this requirement, later research often suggest the filtering width to be $\overline{\Delta_x^+} \leq 100$ in streamwise and $\overline{\Delta_z^+} \leq 20$ in spanwise direction, and as the outer flow is approached, larger spacing can be used (Zang 1991 [149]; Piomelli 2010 [109]; Cimarelli *et al.* 2012 [30]).

In order to study the influence of the filter width related with the filter type, a large range of filter width summarized in Table (4.1) are investigated in the present research. The different positions of these filters with respect to the one-dimensional energy spectra are given in Fig. (4.1). Three physical locations, respectively at $y^+ = 15$ (buffer layer), $y^+ = 80$ (logarithmic layer) and $y^+ = 600$ (outer region) are illustrated, and different filter sizes are indicated on the figures. In large eddy simulation, the small scales which need to be modeled are separated from the large scales by the filter. This separation depends on the filter width in each direction.

Fig. (4.1) shows that, in the near wall position $y^+ = 15$, the energy spectra of large scales have large difference among E_{11}, E_{22} and E_{33}. As moving toward the channel center, this difference becomes smaller at the other two positions $y^+ = 80$ and $y^+ = 600$. The filter widths chosen in each direction are close to the Kolmogorov spectra range. Most of the cutoff wavenumbers falls inside of the inertial range or at the beginning of the dissipative range. Some cutoff wavenumbers are placed slightly before the inertial range.

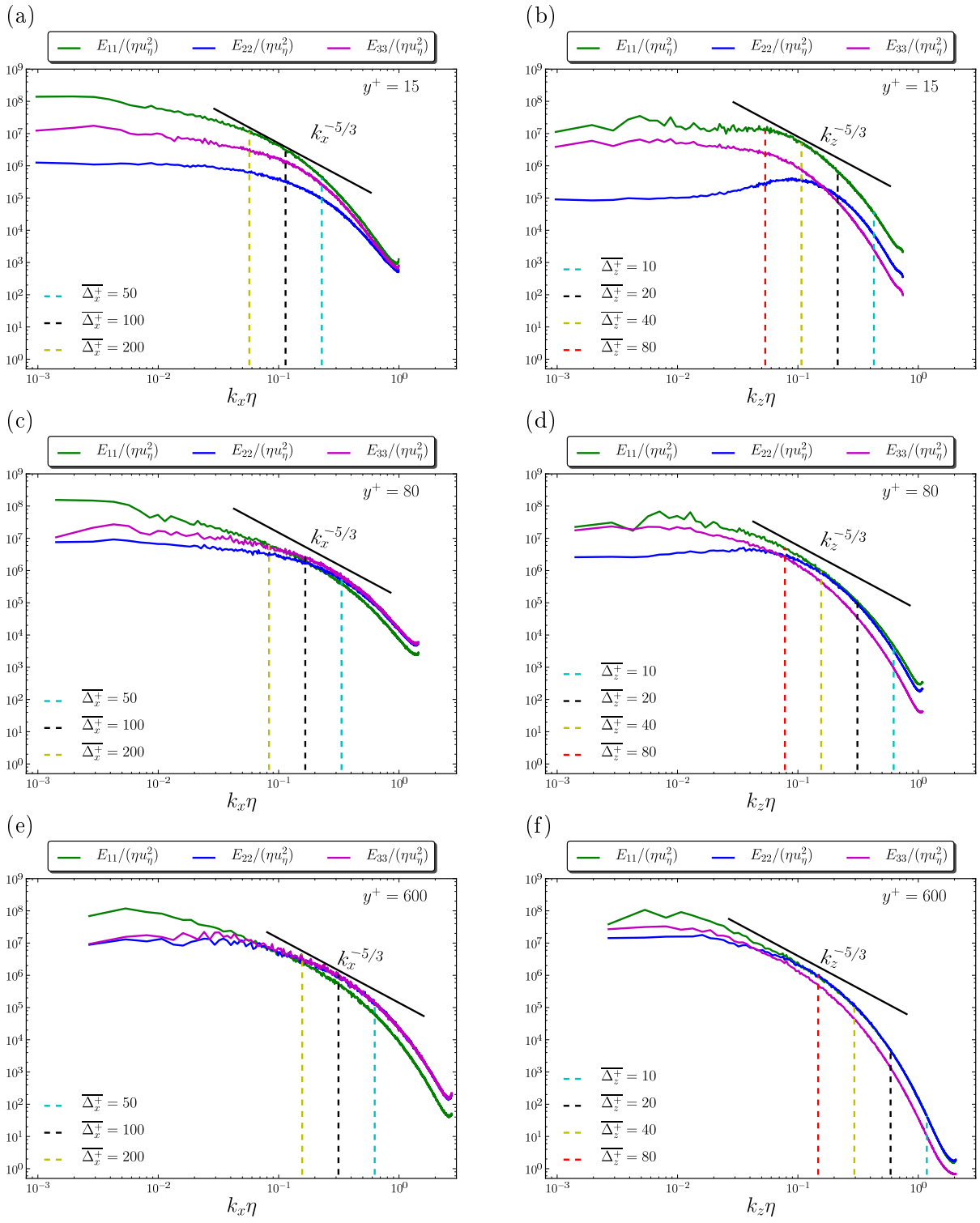

Figure 4.1: The normalized energy spectra along streamwise (a, c, e) and spanwise (b, d, f) directions at three physical locations: buffer layer ($y^+ = 15$), logarithmic layer ($y^+ = 80$) and outer region ($y^+ = 600$). $u_\eta = (\epsilon\nu)^{1/4}$.

But they are supposed not to take significant turbulent kinetic energy, as the inertial range becomes wider for turbulence at high Reynolds number. Fig. (4.1) also displays that, the spanwise filter width $\overline{\Delta_z^+}$ plays a less significant role for the subgrid scale kinetic

energy as moving away from the wall. It filters out less subgrid scale kinetic energy near the channel center ($y^+ = 600$) than in near wall region. Consequently, increasing the spanwise filter width from $\overline{\Delta_z^+} = 10$ to 20 leads to a smaller increase in subgrid scale kinetic energy in the outer region than in near wall region.

In order to evaluate the quantity of subgrid scale kinetic energy corresponding to each filter width, the percentage of the volume-averaged subgrid scale kinetic energy $\langle q_{sgs}^2 \rangle_v$ to the total volume-averaged turbulent kinetic energy $\langle q^2 \rangle_v$ using both Lss-5^{th} and Gaussian filters are presented in Table (4.1). As also shown in Fig. (4.1), the larger the filter width (both in streamwise and spanwise directions), the higher the fraction of turbulent kinetic energy at subgrid scales. However, this fraction is higher with Gaussian filter than with Lss-5^{th} filter when using the same filter width. This is because the Gaussian filter is not as sharp as the Lss-5^{th} filter. It filters out less energy at the small subfilter scales, but it also filters out energy from some large scales. Because of the shape of the kinetic energy spectra, the quantity of subfilter energy is significantly larger with the Gaussian filter than with the Lss-5^{th} filter. In order to investigate the influence of the filter function, the Gaussian filter will be systematically used as a reference for Lss-5^{th} filter in the present research.

		$\overline{\Delta_x^+} = 50$	$\overline{\Delta_x^+} = 100$	$\overline{\Delta_x^+} = 200$
$\overline{\Delta_z^+} = 10$	Lss-5^{th}	2.77%	10.42%	
	Gaussian	6.70%	15.26%	
$\overline{\Delta_z^+} = 20$	Lss-5^{th}	3.14%	10.66%	24.54%
	Gaussian	8.34%	16.53%	29.59%
$\overline{\Delta_z^+} = 40$	Lss-5^{th}		12.62%	25.71%
	Gaussian		20.03%	32.03%
$\overline{\Delta_z^+} = 80$	Lss-5^{th}			30.27%
	Gaussian			37.79%

Table 4.1: Fraction of subgrid scale kinetic energy to the turbulent kinetic energy $\langle q_{sgs}^2 \rangle_v / \langle q^2 \rangle_v$, $\langle q \rangle_v = 0.004$

In order to give a better description of the filter effect, Fig. 4.2 presents the fraction of subgrid scale kinetic energy averaged in a plane parallel to the wall (x,z) to the total plane-averaged turbulent kinetic energy as a function of wall normal position. Results are given respectively in near wall and outer regions. In the outer region, this percentage depends mainly on the streamwise filter width $\overline{\Delta_x^+}$, as it corresponds to horizontal wave numbers where the slope of the energy spectra is flatter than spanwise (see Fig. 4.1). All the curves with the same streamwise filter width collapse in the outer region for $\overline{\Delta_z^+} = 10$ and 20, as the kinetic energy between the wave numbers corresponding to $\overline{\Delta_z^+} = 10$ and 20 is small (see Fig. 4.1). The results of Table. (4.1) also indicates that, all the filter sets with the same streamwise filter width have the smallest increase of the volume-averaged subgrid scale kinetic energy, when increasing the spanwise filter width from $\overline{\Delta_z^+} = 10$ to 20. But the increase of subgrid scale kinetic energy caused by changing the spanwise filter width from $\overline{\Delta_z^+} = 20$ to 40 is slightly larger. This is also consistent with the behavior of energy spectra in Fig. (4.1) and the behavior of the volume-averaged fractions of subgrid scale kinetic energy in Table. (4.1).

Increasing the spanwise filter width from $\overline{\Delta_z^+} = 20$ to 40 and from 40 to 80 leads to a significant rise of fractions of subgrid scale kinetic energy in the near wall region, especially

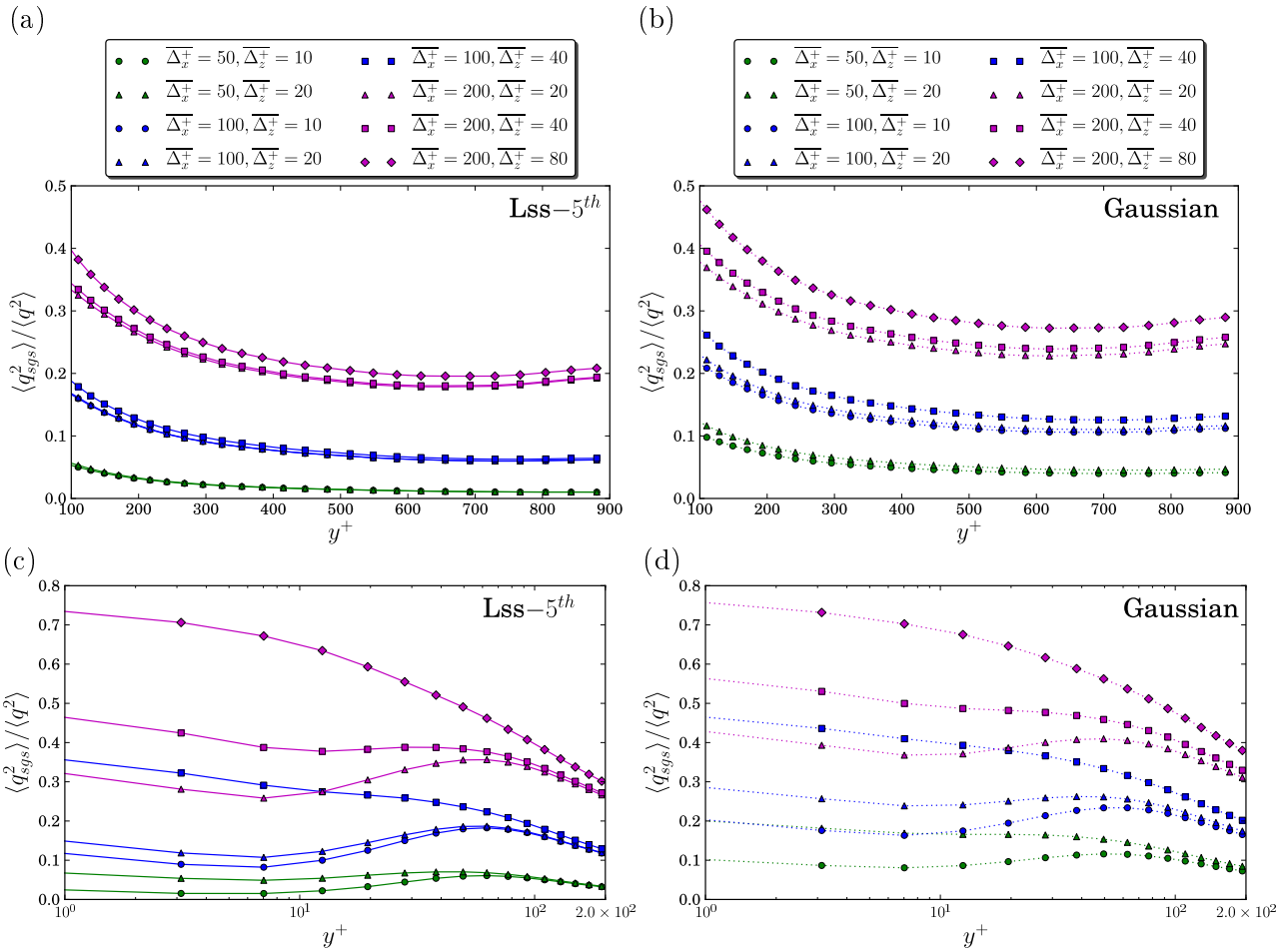

Figure 4.2: Fraction of subgrid scale kinetic energy $\langle q_{sgs}^2 \rangle$ to the total turbulent kinetic energy $\langle q^2 \rangle$ with Lss-5^{th} (a, c) and Gaussian (b, d) filters, in near wall region (a, b) and in outer region (c, d) (The same legend will be used for the filter width in the following figures of the current chapter except special notifications).

in the viscous and buffer layers. This is consistent with the behavior of the energy spectra at $y^+ = 15$ in Fig. (4.1). Furthermore, in the range $y^+ \leq 10$, the filter set at $\overline{\Delta_x^+} = 100$ and $\overline{\Delta_z^+} = 40$ has larger fraction of subgrid scale kinetic energy than the filter set at $\overline{\Delta_x^+} = 200$ and $\overline{\Delta_z^+} = 10$. The filter set with $\overline{\Delta_x^+} = 50$ and $\overline{\Delta_z^+} = 20$ is overlapping with the filter set with $\overline{\Delta_x^+} = 100$ and $\overline{\Delta_z^+} = 10$ using a Gaussian filter. Thus, the subgrid scale kinetic energy has a significant asymmetry between streamwise and spanwise directions. More energy is concentrated in the small spanwise scales. This agrees well with Cimarelli and De Angelis 2012 [30], who found that the turbulent generation mechanisms are stronger in the spanwise direction and are not located at large scales.

4.3. Energy transfer mechanism

In LES, it's important to correctly evaluate the energy exchange between the resolved and unresolved scales. Most of previous research of plane channel flow are focused on the analysis of SGS energy dissipation at low Reynolds number with classical filters (Piomelli

et al. 1991 [112]; Härtel *et al.* 1994 [62]; Horiuti 1997 [65]; Abbà *et al.* 2003 [1]; Cimarelli and De Angelis 2012 [30]). The subgrid scale models are mainly designed to correctly predict the energy dissipation. Seldom studies directly refer to the analysis of the SGS energy transfer or SGS diffusion in physical space. The present research will study the complete effect of the unresolved scales on the resolved ones, including the SGS diffusion and SGS energy dissipation. Special emphasis will be paid to the back scatter of SGS energy.

4.3.1. SGS energy transfer

In the present study, the SGS energy transfer will first be analyzed in physical space, with filter width $\overline{\Delta_x^+} = 100$ and $\overline{\Delta_z^+} = 20$, using a Gaussian filter. We define the direction of energy transfer, such that, the energy is forwardly transfered from large to small scales (forward scatter) when the SGS energy transfer T_{sgs} is positive, and the energy is in turn transfered backward from small to large scales (back scatter) when T_{sgs} is negative. The SGS energy transfer T_{sgs} can be splitted into two contributions as defined in Chapter 3. The positive contribution T_{sgs}^+ indicating the energy transfer from large to small scales, and the negative one T_{sgs}^- indicating an inverse energy transfer. These two contributions are useful to explain the SGS energy transfer in more detail.

The behavior of the total SGS energy transfer, as well as the forward scatter and backward scatter contributions along wall normal position, are given in Fig. (4.3). The statistics are normalized by the plane-averaged rate of kinetic energy dissipation $\langle\epsilon\rangle$ in Fig. 4.3(a) in order to compare the analysis. The fraction of points experiencing back scatter of SGS energy transfer is given in Fig. (4.4).

In the outer region, the positive contribution of SGS energy transfer $\langle T_{sgs}^+\rangle/\langle\epsilon\rangle$ is on average relatively larger than $\langle T_{sgs}^-\rangle/\langle\epsilon\rangle$, indicating a net forward energy cascade from large to small scales. This is driven by a slightly larger fraction of points (less than 4%) of forward scatter compared to back scatter. A similar behavior is observed with Lss-5^{th} filter, except that $\langle T_{sgs}^+\rangle/\langle\epsilon\rangle$ and $\langle T_{sgs}^-\rangle/\langle\epsilon\rangle$ are almost twice of their magnitudes with Gaussian filter (see Fig. A.1 in Appendix A). This may be due to the sharpness of Lss-5^{th} filter. In order to easily present the near wall region at the same time, the statistics are normalized by the volume-averaged rate of kinetic energy dissipation $\langle\epsilon\rangle_v$ as presented in Fig. 4.3(b). The backward and forward dominant regions of SGS energy transfer $\langle T_{sgs}\rangle/\langle\epsilon\rangle_v$ are clearly divided by a demarcation in the whole region. Above $y^+ \approx 15$, the net transfer of energy is from large to small scales. A forward scatter peak of SGS energy transfer $\langle T_{sgs}\rangle/\langle\epsilon\rangle_v$ occurs in the buffer layer, at about $y^+ \approx 21$. This may be due to the influence of the turbulent kinetic energy peak at position $y^+ \approx 18$, as evidenced in Fig. (3.10) of Chapter 3. But slightly more points (about 10%) experience forward scatter than back scatter at this peak location.

A net backward energy cascade of $\langle T_{sgs}\rangle/\langle\epsilon\rangle_v$ from small to large scales occurs in range $y^+ < 15$, as the negative term $\langle T_{sgs}^-\rangle/\langle\epsilon\rangle_v$ is significantly larger than the positive one $\langle T_{sgs}^+\rangle/\langle\epsilon\rangle_v$ in this region. Furthermore, for $y^+ \leq 5$, the positive contribution is almost zero. Most of the points in this region (72%-85%) transfer energy to larger scales. The peak of net back scatter occurs at about $y^+ \approx 6$, where about 85% of the points experience back scatter of SGS energy. This is at the upper limit of the viscous layer. Härtel *et al.* 1994 [62] and Piomelli *et al.* 1996 [114] have also found a reverse energy

(a) Statistics normalized by $\langle\epsilon\rangle$ (b) Statistics normalized by $\langle\epsilon\rangle_v$

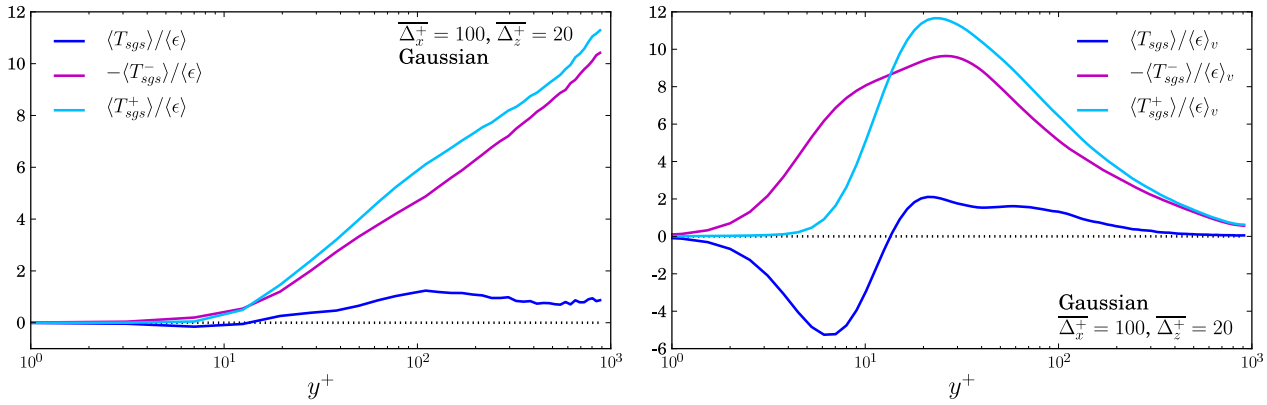

Figure 4.3: SGS energy transfer including the back scatter and forward scatter contributions, normalized by plane-averaged (a) and volume-averaged (b) rate of kinetic energy dissipation. Statistics are given for the same filter width $\overline{\Delta^+_x} = 100$ and $\overline{\Delta^+_z} = 20$ and a Gaussian filter.

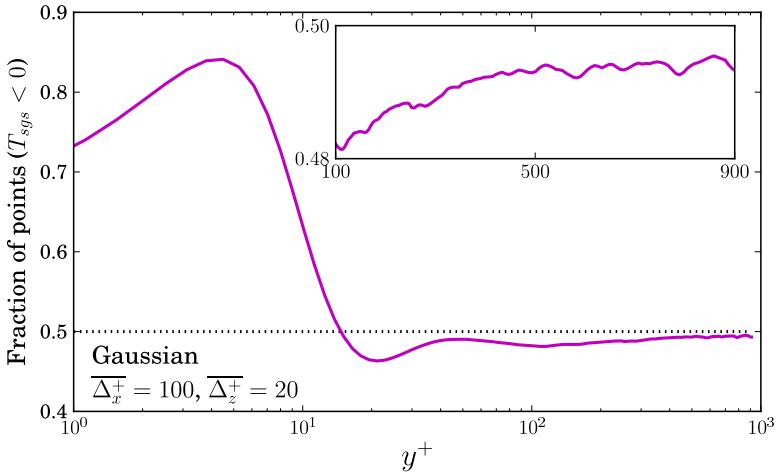

Figure 4.4: Fraction of points experiencing back scatter of SGS energy transfer with the Gaussian filter set at $\overline{\Delta^+_x} = 100$, $\overline{\Delta^+_z} = 20$. The outer region is given in inset.

transfer in the buffer layer. But the forward and backward scatter peaks, especially the back scatter predominant range of SGS energy transfer in near wall region were not observed in previous a priori analysis (Piomelli *et al.* 1991 [112]; Horiuti (1997) [65]; Abbà *et al.* (2003) [1]).

For the filter sets with the same filter width $\overline{\Delta^+_x} = 100$ and $\overline{\Delta^+_z} = 20$ using Lss-5^{th} filter, SGS energy transfer as well as its two contributions show a behavior similar to the above analysis with the Gaussian filter. However, some significant differences with different filter width exist. Fig. 4.5 and 4.6 present the behavior of the plane-averaged SGS energy transfer with different filter width of Lss-5^{th} and Gaussian filters. In the outer region, the transfer is larger in magnitude for larger filter width in both directions, and more dependent on the streamwise filter width than the spanwise one. The tail of SGS energy transfer $\langle T_{sgs}\rangle/\langle\epsilon\rangle$ for Gaussian filters is higher than with Lss-5^{th} filter in the range $y^+ > 500$ as presented in Fig. 4.5(b). This behavior of SGS energy transfer toward the

channel center correspond well with the fraction of points experiencing backward scatter as shown in Fig. 4.7. An evident rise on the fraction of points experiencing forward scatter occurs near the channel center for the Gaussian filter with $\overline{\Delta_x^+} = 200$ and $\overline{\Delta_z^+} = 80$. Thus, in the outer region, the increasing amount of subgrid scale kinetic energy caused by increasing the filter width is consumed to strengthen the magnitude of SGS energy transfer, while the increasing amount caused by filter type will change the developing trend of the plane-averaged SGS energy transfer.

(a) Statistics with Lss-5^{th} filter (b) Statistics with Lss-5^{th} and Gaussian filters

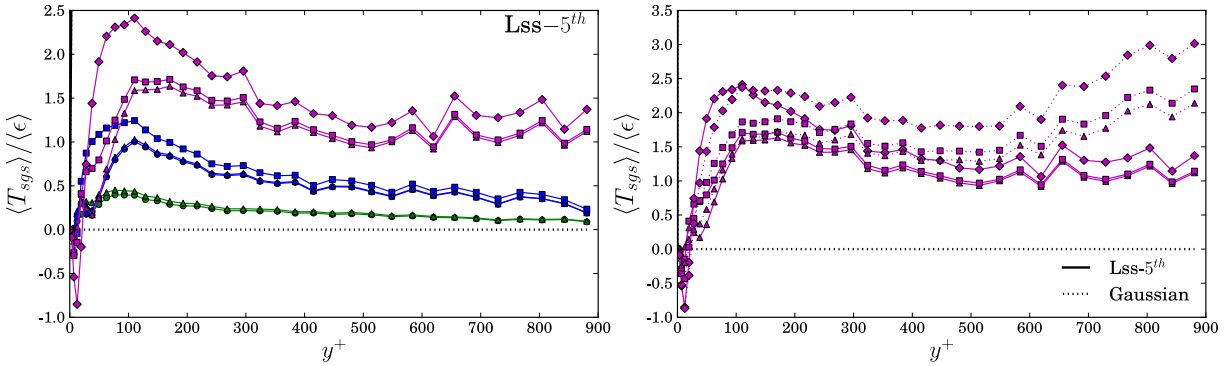

Figure 4.5: Outer region behavior of plane-averaged SGS energy transfer using Lss-5^{th} and Gaussian filters. The same symbols as in Fig. 4.2.

(a) (b)

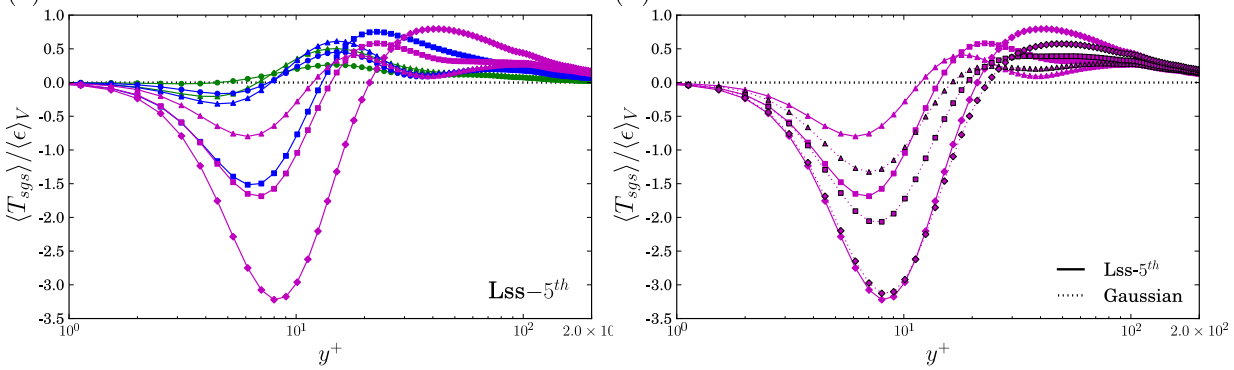

Figure 4.6: Near wall region behavior of plane-averaged SGS energy transfer using Lss-5^{th} and Gaussian filters. The same symbols as in Fig. 4.2.

In near wall region, Fig. 4.5 shows that, the frontier between the backward and forward dominated regions, as well as the backward and forward peaks of SGS energy transfer $\langle T_{sgs}\rangle/\langle\epsilon\rangle_v$ move away from the wall when increasing the filter width both in streamwise and spanwise directions. The Gaussian filter also forces the forward and backward peaks to move toward the channel center as compared to the same filter sets with Lss-5^{th} filter. This corresponds well with the fraction of points experiencing back scatter of SGS energy for each filter set in Fig. 4.7.

In addition, Fig. 4.6 also exhibits significantly larger magnitude of SGS energy transfer $\langle T_{sgs}\rangle/\langle\epsilon\rangle_v$ caused by the larger spanwise filter width in the near wall region than in the outer region as given in Fig. 4.5. The energy bias even occurs on the filter sets with

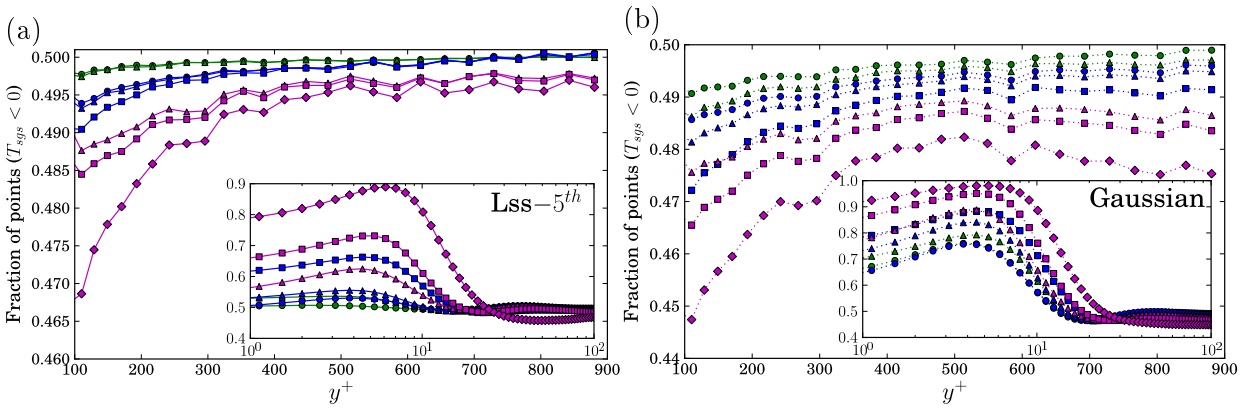

Figure 4.7: Fraction of grid points of $T_{sgs} < 0$ using the Lss-5^{th} (a) and Gaussian (b) filters, the near wall region is plotted in the insert. The same symbols as in Fig. 4.2.

smaller spanwise scales, compared to the prediction of subgrid scale kinetic energy in Fig. 4.2. The plentiful subgrid scale kinetic energy in near wall region, caused by the larger filter width or the filter type, are completely used to strengthen the magnitudes of SGS energy transfer in near wall region.

4.3.2. SGS energy dissipation

The a priori analysis of SGS energy dissipation is conducted on the same filter set as in the previous analysis of SGS energy transfer. The results for a filter width $\overline{\Delta_x^+} = 100$ in streamwise direction and $\overline{\Delta_z^+} = 20$ in spanwise direction, using Gaussian filter are given in Fig. 4.8 and 4.9. The SGS energy dissipation is also normalized by the plane-averaged and the volume-averaged rate of kinetic energy dissipation in Fig. 4.8(a) and 4.8(b) respectively. In order to be consistent with the analysis of previous research (Piomelli *et al.* 1991 [112]; Abbà *et al.* 2003 [1]), we define that $\epsilon_{sgs} > 0$ indicates the energy flow from small to large scales (back scatter), and $\epsilon_{sgs} < 0$ indicates the energy transfer from large to small scales (forward scatter). The equations of the two contributions ϵ_{sgs}^+ and ϵ_{sgs}^- have been defined in Chapter 3.

Unlike the bidirectional energy cascade of SGS energy transfer, the SGS energy dissipation exhibits a single direction of energy cascade from large to small scales at all wall normal positions. But there exists a significant back scatter contribution to the SGS dissipation which must be accounted for in the formulation of robust LES models, as shown in previous research (Natrajan and Christensen 2006 [101]). The negative contribution $\langle\epsilon_{sgs}^-\rangle/\langle\epsilon\rangle$ of SGS energy dissipation keeps larger than the positive one $\langle\epsilon_{sgs}^+\rangle/\langle\epsilon\rangle$ at all wall distances. This is powered by a large fraction of points (more than 60%) of forward scatter in the outer region, as displayed in Fig. 4.9.

In the near wall region, a significant forward scatter peak of SGS energy dissipation occurs at about $y^+ = 11$, as illustrated in Fig. 4.8. A very small SGS energy dissipation peak has been found by Piomelli *et al.* 1991 [112], when the same small or large filter width in streamwise and spanwise direction is used at low Reynolds number $Re_\tau = 180$. The magnitude of this peak becomes more evident at a moderate filter width, using the 2D cutoff filter. Abbà *et al.* 2003 [1] have found a clear forward peak of SGS energy dissipation at Reynolds number $Re_\tau = 660$ for the plane channel flow, using the 3D

(a) Statistics normalized by $\langle\epsilon\rangle$ (b) Statistics normalized by $\langle\epsilon\rangle_v$

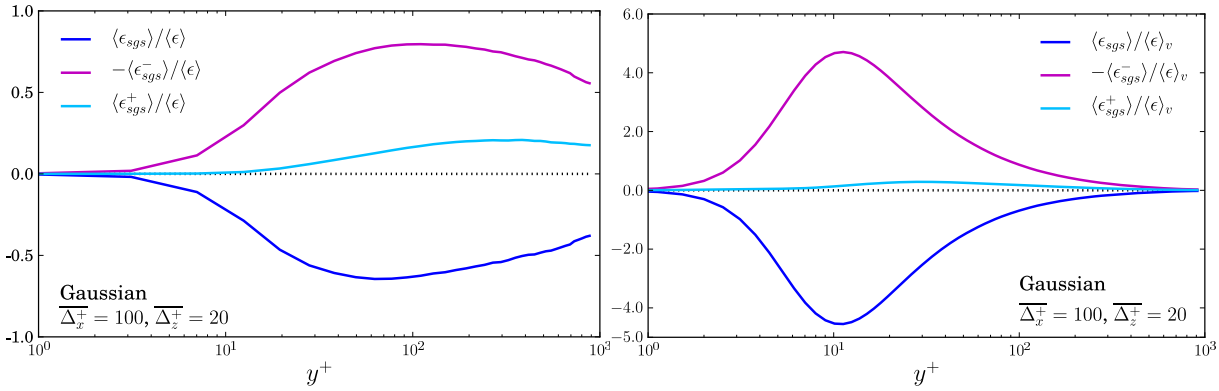

Figure 4.8: SGS energy dissipation and its two contributions normalized by plane-averaged (a) and volume-averaged (b) rate of kinetic energy dissipation respectively, for a Gaussian filter set at $\overline{\Delta_x^+} = 100$, $\overline{\Delta_z^+} = 20$.

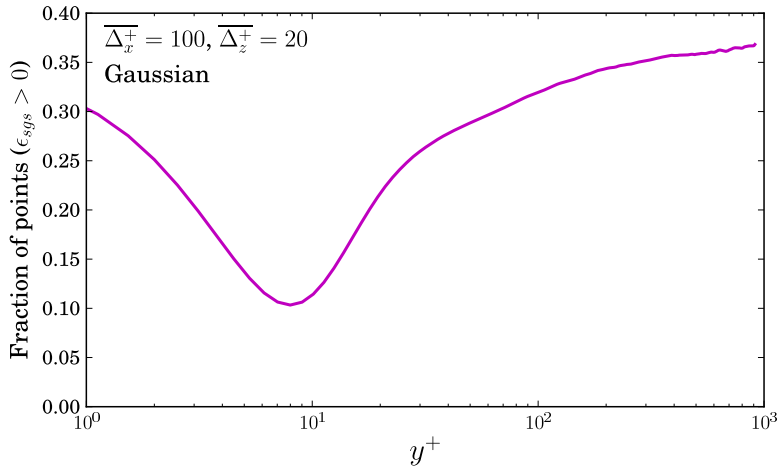

Figure 4.9: Fraction of points experiencing back scatter of SGS energy dissipation, for a Gaussian filter set at $\overline{\Delta_x^+} = 100$, $\overline{\Delta_z^+} = 20$.

tophat filter. Härtel and Kleiser (1998) [61] reported that, the magnitude of SGS energy dissipation increases with Reynolds number. In order to investigate the sensitivity of this forward peak of SGS energy dissipation to the filter width and type, the results for the additional filter sets with different filter width using Lss-5^{th} and Gaussian filters are given in Fig. 4.10. For all filter sets investigated, SGS energy dissipation is larger in magnitude in the near wall region, compared to the outer region. Globally, higher forward peaks are observed for filter sets with larger fractions of subgrid scale kinetic energy as displayed in Fig. 4.2. In the range $y^+ < 10$, for the filter set with $\overline{\Delta_x^+} = 100$ and $\overline{\Delta_z^+} = 40$, this peak is larger in magnitude than for both Lss-5^{th} and Gaussian filters with $\overline{\Delta_x^+} = 200$ and $\overline{\Delta_z^+} = 10$. And the filter set $\overline{\Delta_x^+} = 50$, $\overline{\Delta_z^+} = 20$ and $\overline{\Delta_x^+} = 100$, $\overline{\Delta_z^+} = 10$ have very silimar magnitude in this range using Gaussian filter. Globally, the behavior of SGS dissipation in the near wall region is driven by the amount of subgrid scale kinetic energy, whatever the filter width in each direction or the filter type. In addition, increasing the near wall subgrid scale kinetic energy will drive the forward peak of SGS energy dissipation to move toward the wall. This behavior is reverse as compared to the energy cascade peaks of SGS

energy transfer.

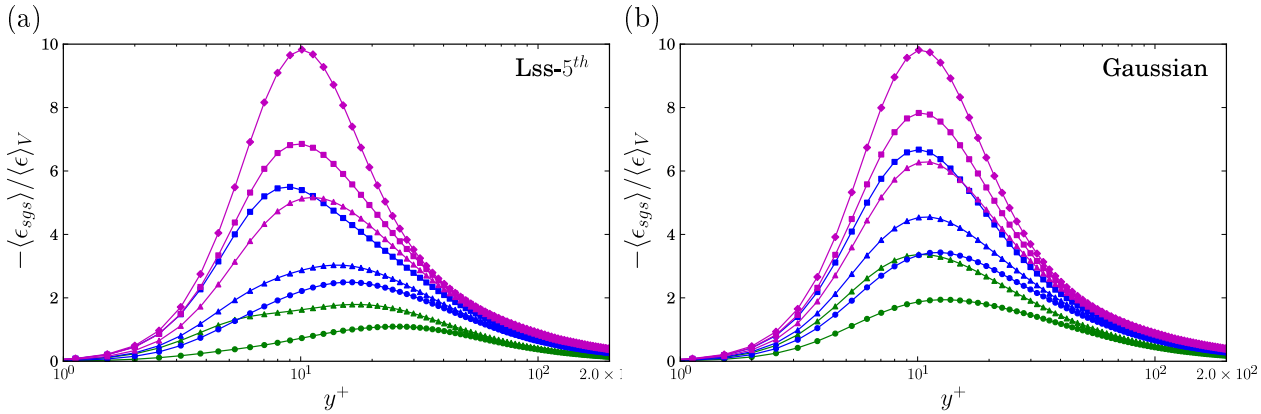

Figure 4.10: Near wall region behavior of SGS energy dissipation with Lss-5^{th} filter (a) and Gaussian filter (b). The same symbols as in Fig. 4.2.

The maximum fraction of points experiencing forward scatter appears at about $y^+ = 8$ as presented in Fig. 4.9. This peak is discernible in the results of Piomelli *et al.* 1991 [112], who found that the energy back scatter is close to 50% throughout the channel at low Reynolds number ($Re_\tau = 180$, using cutoff filter). They claim that this fraction is independent of the filter width and of the distance from the wall. Later, Horiuti (1997) [65] found this forward scatter peak at Reynolds number $Re_\tau = 180$ in a plane channel flow using Gaussian filter. Abbà *et al.* (2003) [1] found this peak of SGS energy dissipation, at Reynolds number $Re_\tau = 660$ in a plane channel flow using a tophat filter. Fig. 4.11 shows that this peak exists in the near wall region independently of the filter width and type. It is more visible with Gaussian filter than with Lss-5^{th} filter.

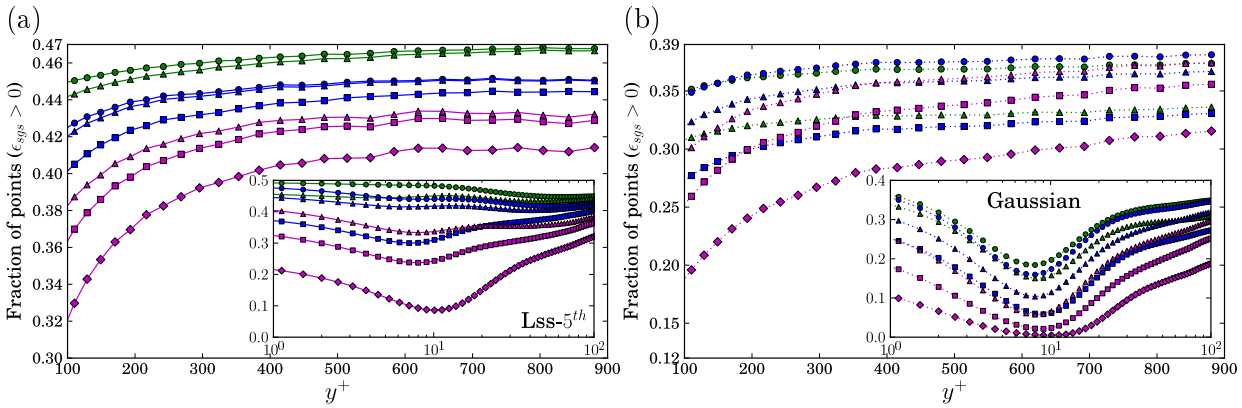

Figure 4.11: Fraction of points experiencing back scatter of SGS dissipation with Lss-5^{th} filter (a) and Gaussian filter (b). A zoom in near wall region is presented in the inset. The same symbols as in Fig. 4.2.

Fig. 4.8 and 4.9 reveal that, there is an offset between the peak in the fraction of points experincing forward scatter of SGS energy dissipation ($y^+ = 8$) and the peak of the positive contribution $\langle\epsilon^+_{sgs}\rangle/\langle\epsilon\rangle_v$ of SGS energy dissipation ($y^+ = 11$). This indicates that, there is a dissymmetry in the statistics of backward and forward scatter of SGS energy dissipation. This is expected in this region, as the turbulence is dominated by

streaks which are well organized structures that can contribute differently to the positive $\langle \epsilon^+_{sgs} \rangle$ and negative $\langle \epsilon^-_{sgs} \rangle$ contributions of SGS energy dissipation. Fig. 4.12 shows that, with the same filter widths $\overline{\Delta^+_x} = 100$ and $\overline{\Delta^+_z} = 20$ as shown in Fig. 4.8 and 4.9 using Lss-5^{th} filter, the peak of the positive contribution $\langle \epsilon^+_{sgs} \rangle / \langle \epsilon \rangle_v$ of SGS energy dissipation occurs at $y^+ = 11$. The fraction of points experiencing backscatter is almost constant along the wall normal distance, with a slight local minimum near $y^+ = 8$ and a second minimum near $y^+ = 40$. So Lss-5^{th} filter leads to a smaller disproportion of points experiencing backward and forward scatter than with a smooth Gaussian filter. In addition, the positive contribution $\langle \epsilon^+_{sgs} \rangle / \langle \epsilon \rangle_v$ of SGS energy dissipation is more pronounced using Lss-5^{th} filter than Gaussian filter. This implies that Lss-5^{th} filter acts similarly to a cutoff filter which more markedly raises the significance of backscatter compared to the Gaussian filter as discovered by Leslie and Quarini 1979 [75] and Piomelli *et al.* 1996 [114].

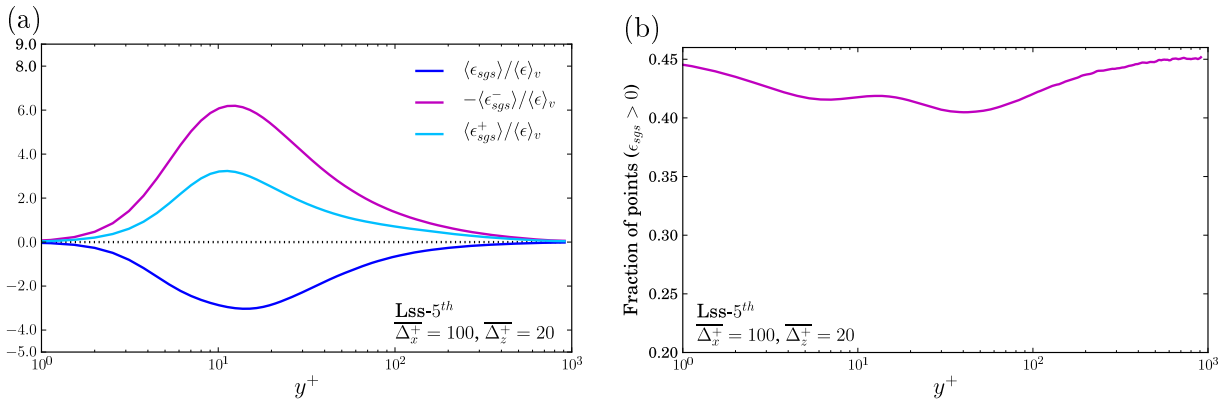

Figure 4.12: SGS energy dissipation (a) and the fraction of points experiencing back scatter with Lss-5^{th} filter (b).

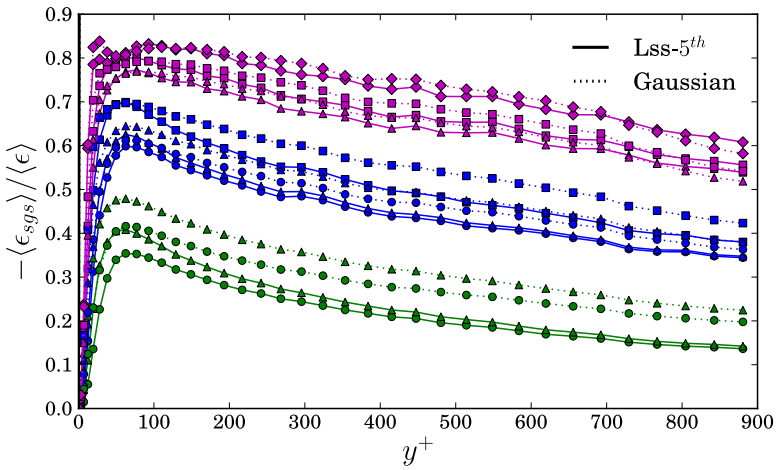

Figure 4.13: Plane-averaged SGS energy dissipation in outer region as function of filter width and filter type. The same symbols as in Fig. 4.2.

Fig. 4.8 also shows that, the plane-averaged SGS energy dissipation reaches its maximum near $y^+ = 100$. Then it decreases gradually toward the channel center. This is independent of the filter type and filter width. But the SGS energy dissipation $\langle \epsilon_{sgs} \rangle / \langle \epsilon \rangle$ remains constant after the maximum according to the observation of Piomelli *et al.*

(1991) [112] and Abbà *et al.* (2003) [1]. The decrease of SGS energy dissipation toward the channel center also occur with other filter sets using Lss-5^{th} and Gaussian filters, as revealed in Fig. 4.13. This is reminiscent of the developing trend of the plane-averaged SGS energy transfer along wall normal distance, which is caused by Gaussian filter as shown in Fig. 4.5(b). Obviously, the plane-averaged SGS energy dissipation is not as sensitive as the plane-averaged SGS energy transfer to the filter type, but increasing the filter width still strengthen the magnitude of the plane-averaged SGS energy dissipation. The SGS energy dissipation was found to be independent of the filter width in an ideal inertial range by Porté-Aget *et al.* 2001 [118]. However, the plane-averaged SGS energy dissipation of the present research has larger magnitude for larger filter width both in streamwise and spanwise directions (Fig. 4.13). Besides, the plane-averaged SGS energy dissipation have larger magnitudes with Gaussian filter than with Lss-5^{th} for all the filter sets, confirming results of O'Sullivan *et al.* 2001 [105], who observed that magnitude of SGS dissipation is strongly influenced by filter type in square duct flow at $Re_\tau = 600$.

Therefore, the energy transfer mechanisms of the present wall-bounded flow do not collapse to the previous research of wall-bounded turbulence at low Reynolds number (Piomelli *et al.* (1991) [112]; Härtel *et al.* 1994 [62]; Horiuti (1997) [65]). Significant backscatter cascades have been found both in SGS energy transfer and SGS energy dissipation in the whole region along wall normal positions. This is in accordence with the observations of Piomelli *et al.* 1996 [114], who found that backward and forward scatter usually occur in close proximity of each other, the back scatter event being generally surrounded by a region of significant forward scatter.

According to Domaradzki *et al.* 1994 [40] and Piomelli *et al.* 1996 [114], in the near-wall region of a plane channel, the occurrence of large energy transfer between the resolved and unresolved scales is strongly correlated with the turbulent structures that characterize the wall bounded flows. A single, quasi-streamwise, vortex (or a pair with a strong leg and a weak one) is more likely to occur in wall-bounded flow at low Reynolds number. According to Piomelli *et al.* 1996 [114], the forward scatter and back scatter apparently arise from different parts of a coherent eddy, and the net transfer is the difference of the two sides. For our research, the significant energy distribution in small spanwise turbulent scales in viscous and buffer layer (Fig. 4.2) is indiscernible in previous research of nearwall turbulence structures. Thus, near wall turbulence structure associated with the energy transfer between resolved and unresolved scales of plane channel flow at a comparable high Reynolds number is expected. The present results show that, the turbulent kinetic energy bias in small spanwise turbulent scales is characterized by a dominant back scatter cascade region (Fig. 4.3(b) and 4.6) of net SGS energy transfer in near wall region. But it's not reflected by the SGS energy dissipation. Thus, the subgrid scale models mainly for dissipating the net energy from resolved scales are not robust. This agrees well with Meneveau and Katz 2000 [93] who thought that for a subgrid scale models, providing the correct mean dissipation is in general only a necessary but not a sufficient condition to reproduce the correct flow statistics.

4.4. A priori evaluation of model coefficients

The a priori studies of classical eddy viscosity models have been performed in different configurations in previous work (for isotropic turbulence by Pruett and Adams 2000 [120];

for turbulence in square duct flow by O'Sullivan *et al.* 2001 [105]; for the atmospheric surface layer by Porté-Aget *et al.* 2001 [118]; for wind tunnel by Carper and Porté-Agel 2008 [24]; for a lake by Bou-Zeid *et al.* 2008 [18] etc...). However, the a priori analysis of subgrid scale models on plane channel flow at high Reynolds number, especially of up-to-date subgrid models, are greatly expected to provide significant information for research and development of these models and of large eddy simulation.

In the present a priori analysis, the coefficients of the Smagorinsky, WALE and σ models are evaluated by matching the measured and modeled SGS transfer rate of resolved kinetic energy, as defined by equation 3.18, 3.19 and 3.20 in Chapter 3. The coefficient of the Dynamic Smagorinsky model is calculated by equation 2.25 in Chapter 2.

4.4.1. Smagorinsky model and Dynamic Smagorinsky model

The standard value of the coefficient of the Smagorinsky model $\langle C_s \rangle \approx 0.16$ is often used for isotropic turbulence (Lilly 1967 [77]; Meneveau 1997 [94]). This value of $\langle C_s \rangle$ has been found too large for plane channel flow by many research (Deardorff 1970 [36]; Moin and Kim 1982 [99]; Piomelli, Moin and Ferziger 1988 [113]). So $\langle C_s \rangle \approx 0.10$ and $\langle C_s \rangle \approx 0.065$ were used respectively by Deardorff 1970 [36] and Moin and Kim 1982 [99] for plane channel flow. Later, Liu *et al.* 1999 [78] reported a range of $0.06 \leq \langle C_s \rangle \leq 0.14$ which can be used in plane channel flow.

The coefficient $\langle C_s \rangle$ of the Smagorinsky model with different filter width using Lss-5^{th} filter are given in Fig. 4.14. In the outer region, the values of $\langle C_s \rangle$ fall in range $0.05 \leq \langle C_s \rangle \leq 0.07$. The lower values obtained in the present analysis, compared to previous research, are probably due to the effect of two-dimensional, instead of three-dimensional filtering, or to sensitivity of subgrid model coefficients to the mesh size (Scotti *et al.* 1993 [126]; Nicoud *et al.* 2011 [103]). The coefficient $\langle C_s \rangle$ is nearly contant for $\overline{\Delta_x^+} = 50$, $\overline{\Delta_z^+} = 20$ and rises somewhat toward the channel center for the other filter widths considered. This is incompatible with the results of Porté-Aget *et al.* 2001 [118], who found that the streamwise filter width has little effect on the main trends of subgrid scale model coefficients. $\langle C_s \rangle$ is smaller in magnitude for larger streamwise $\overline{\Delta_x^+}$, except for the set $\overline{\Delta_x^+} = 50$, $\overline{\Delta_z^+} = 20$ which corresponds to a very small fraction of subgrid scale kinetic energy (less than 10%) as presented in Fig. 4.2. In fact, $\langle C_s \rangle$ has the same streamwise filter width dependence as the plane-averaged SGS energy dissipation $\langle \epsilon_{sgs} \rangle / \langle \epsilon \rangle$ (Fig. 4.13) and as the subgrid scale kinetic energy in the outer region.

Furthermore, the coefficient $\langle C_s \rangle$ is significantly larger in magnitude for larger $\overline{\Delta_z^+}$. This agrees well with the results of Porté-Aget *et al.* 2001 [118]. The fraction of subgrid scale kinetic energy depends slightly on the spanwise filter width in the outer region as shown in Fig. 4.2. Nevertheless, $\langle C_s \rangle$ has a $\overline{\Delta_z^+}$ dependence consistent with the plane-averaged SGS energy dissipation $\langle \epsilon_{sgs} \rangle / \langle \epsilon \rangle$ in outer region. So $\langle C_s \rangle$ is mainly related to SGS energy dissipation rather than the subgrid scale kinetic energy. However, toward the channel center, the evolution of $\langle C_s \rangle$ disconnects from the SGS energy dissipation which gradually decreases. The same filter width dependence of $\langle C_s \rangle$ is observed in the outer region using Gaussian filter.

The classical Smagorinsky operator $|\overline{S}|$ defined in Chapter 3 is known to be non-vanishing near solid boundaries. This major drawback has motivated the use of Van Driest damping functions so as to compensate it by model coefficients. Fig. 4.15 shows

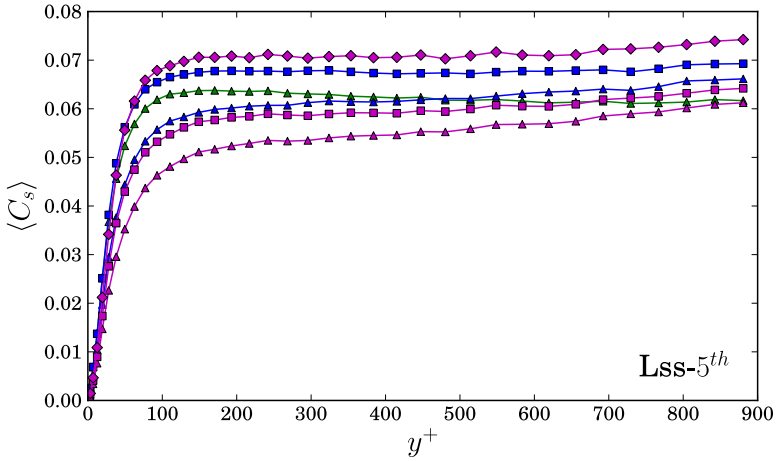

Figure 4.14: A priori estimate of coefficient $\langle C_s \rangle$ of Smagorinsky model with different filter width using Lss-5^{th} filter.

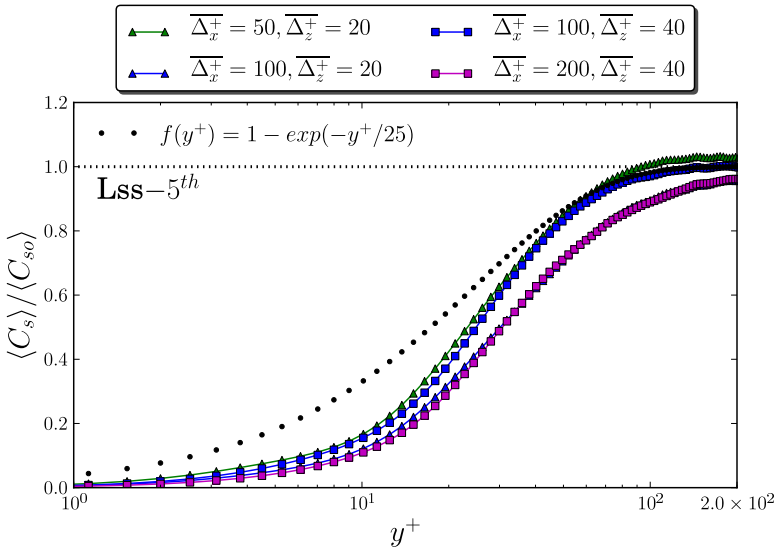

Figure 4.15: A priori estimate of coefficient $\langle C_s \rangle$ of Smagorinsky model in near region using Lss-5^{th} filter. $f(y^+) = 1 - exp(-y^+/25)$ is the Van Driest Damping function.

the comparision of $\langle C_s \rangle$ with Van Driest damping function in the inner region. The statistics are normalized by $\langle C_{so} \rangle$ which is the mean value for each filter set in the range $300 \leq y^+ \leq 850$. The normalized coefficient $\langle C_s \rangle / \langle C_{so} \rangle$ is far from the Van Driest damping function, especially in the range $y^+ < 20$. The shapes of the curves $\langle C_s \rangle / \langle C_{so} \rangle$ mostly rely on the ratio α ($\alpha = \overline{\Delta_x^+} / \overline{\Delta_z^+}$) instead of the filter width, which plays an important role in outer region for the coefficient $\langle C_s \rangle$, as analyzed above . $\langle C_s \rangle / \langle C_{so} \rangle$ is closer to Van Driest damping function for smaller α. It has been checked that the property of $\langle C_s \rangle / \langle C_{so} \rangle$ is almost independent from the filter type.

Fig. 4.16 exhibits the influence of the filter type and filter width on coefficient $\langle C_s \rangle$ with the same ratio $\alpha = 2.5$. Generally, $\langle C_s \rangle$ has larger values with Gaussian filter than with Lss-5^{th} filter in the outer region. The smaller the filter width, the larger the difference in $\langle C_s \rangle$ between Lss-5^{th} and Gaussian filter. So $\langle C_s \rangle$ with small filter width using Gaussian filter is close to the value observed in previous research, since for the same ratio $\alpha = 2.5$

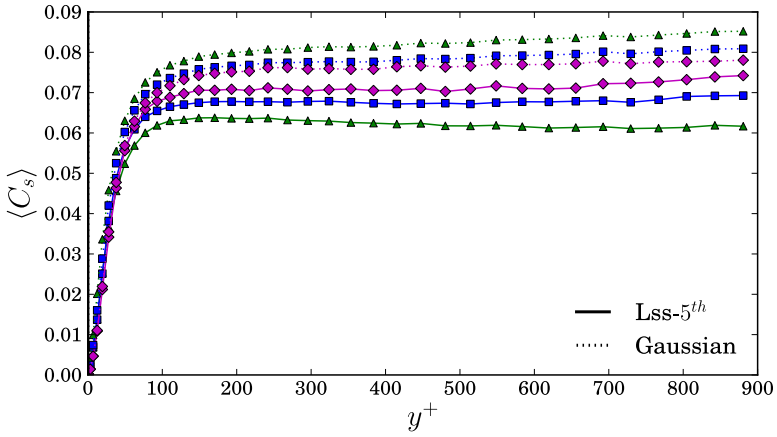

Figure 4.16: Influence of filter type and filter width on $\langle C_s \rangle$ using different filter width for the same ratio $\alpha = 2.5$.

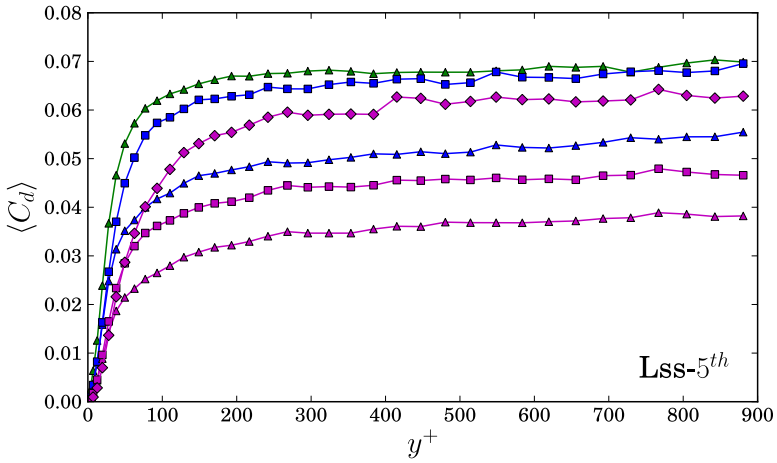

Figure 4.17: A priori estimate of coefficient $\langle C_d \rangle$ of Dynamic Smagorinsky model using Lss-5^{th} filter.

in the outer region, the coefficient $\langle C_s \rangle$ is larger for larger filter set using Lss-5^{th}, but is smaller on large filter set using Gaussian filter.

The coefficient $\langle C_d \rangle$ of the Dynamic Smagorinsky model predicted by the resolved scales is now compared to the a priori estimate of the coefficient $\langle C_s \rangle$ of the Smagorinsky model for each filter set. The wall normal evolution of $\langle C_d \rangle$ is displayed in Fig. 4.17. It is almost constant for each filter set in outer region. However, the range of $\langle C_d \rangle$ which is $[0.03 - 0.07]$ is always smaller than that of $\langle C_s \rangle$ ($[0.05 - 0.07]$) except for ($\overline{\Delta_x^+} = 50$, $\overline{\Delta_x^+} = 20$). Furthermore, $\langle C_d \rangle$ has more scatter than $\langle C_s \rangle$ for the different filter sets. According to Carper and Porté-Agel 2008 [25], this scatter may be due to the fact that a larger test filter width is too large in the dynamic procedure and limits the number of points over which the average is calculated. However, the larger magnitude of $\langle C_d \rangle$ in the outer region drastically relies on smaller ratio α ($\alpha = \overline{\Delta_x^+}/\overline{\Delta_z^+}$), and it is consistently smaller for the larger filter width for each α. Thus, it's believed that the coefficient $\langle C_d \rangle$ is closer to coefficient $\langle C_s \rangle$ for small filter width of the small ratio α for most cases, except the filter set $\overline{\Delta_x^+} = 50$, $\overline{\Delta_z^+} = 20$ for which $\langle C_d \rangle$ is overestimated compared to $\langle C_s \rangle$. However, the filter set ($\overline{\Delta_x^+} = 100$, $\overline{\Delta_z^+} = 40$) for $\alpha = 2.5$ using Lss-5^{th} filter seems to be

the most suitable match for $\langle C_d \rangle$, which is predicted almost the same as $\langle C_s \rangle$ in outer region.

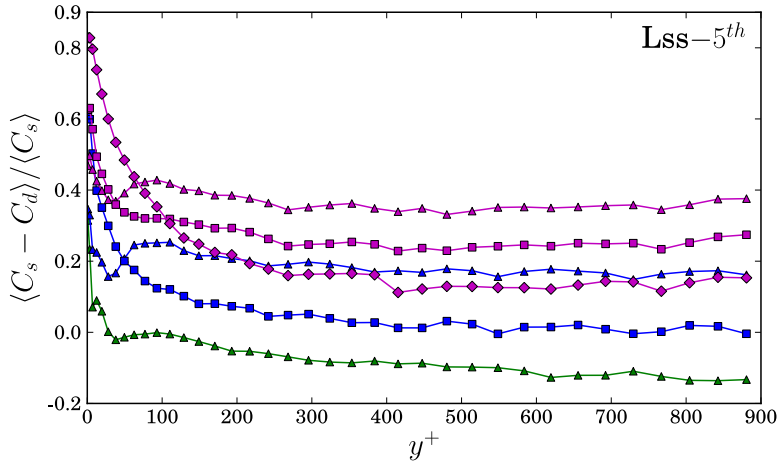

Figure 4.18: Relative error between coefficient $\langle C_s \rangle$ and $\langle C_d \rangle$ using Lss-5^{th} filter.

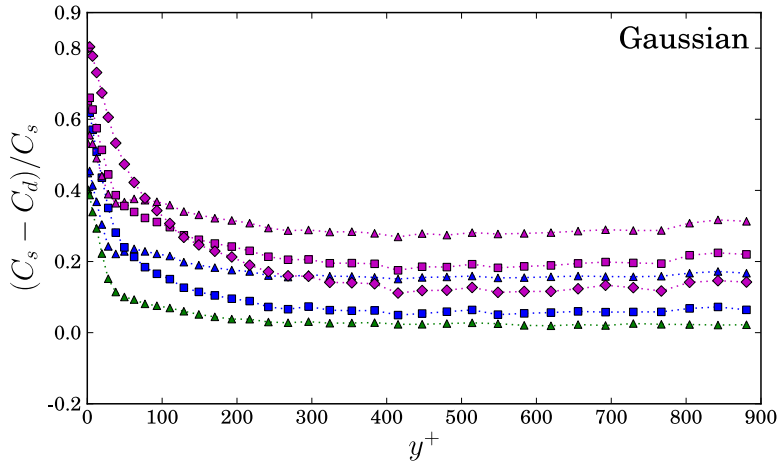

Figure 4.19: Relative error between coefficient $\langle C_s \rangle$ and $\langle C_d \rangle$ using Gaussian filter.

Similarly to present analysis, Bou-Zeid *et al.* 2008[18] observed an underestimate of $\langle C_d \rangle$. In order to clarify the comparison between $\langle C_s \rangle$ and $\langle C_d \rangle$, their differences using both Lss-5^{th} and Gaussian filters are illustrated in Fig. 4.18 and 4.19 respectively. The deviation of $\langle C_d \rangle$ from $\langle C_s \rangle$ in the near wall region (from 0 to 85%) is larger than in outer region (less than 40%). The Dynamic model coefficient is systematically underestimated except for the smaller Lss-5^{th} filter ($\overline{\Delta_x^+} = 50$, $\overline{\Delta_z^+} = 20$). Very similar behaviors are observed for the Gaussian and Lss-5^{th} filters in the whole channel region. However, with a better agreement in the outer region, the small Gaussian filter ($\overline{\Delta_x^+} = 50$, $\overline{\Delta_z^+} = 20$) seems to be the most suitable to match the dynamic Smagorinsky model coefficient $\langle C_d \rangle$ with the a priori estimate $\langle C_s \rangle$. O'Sullivan *et al.* 2001 [105] found that small scale variations of coefficient of Dynamic Smagorinsky model are more evident for cutoff filter compared to Gaussian filter. Thus, the different suitable filter width for Dynamic Smagorinsky model between Lss-5^{th} and Gaussian filters verifies that Lss-5^{th} has properties similar to cutoff filter. Meanwhile the Dynamic Smagorinsky model is shown here to be often under-dissipative compared to the Smagorinsky model, confirming the results of Bou-Zeid

et al. (2008) [18].

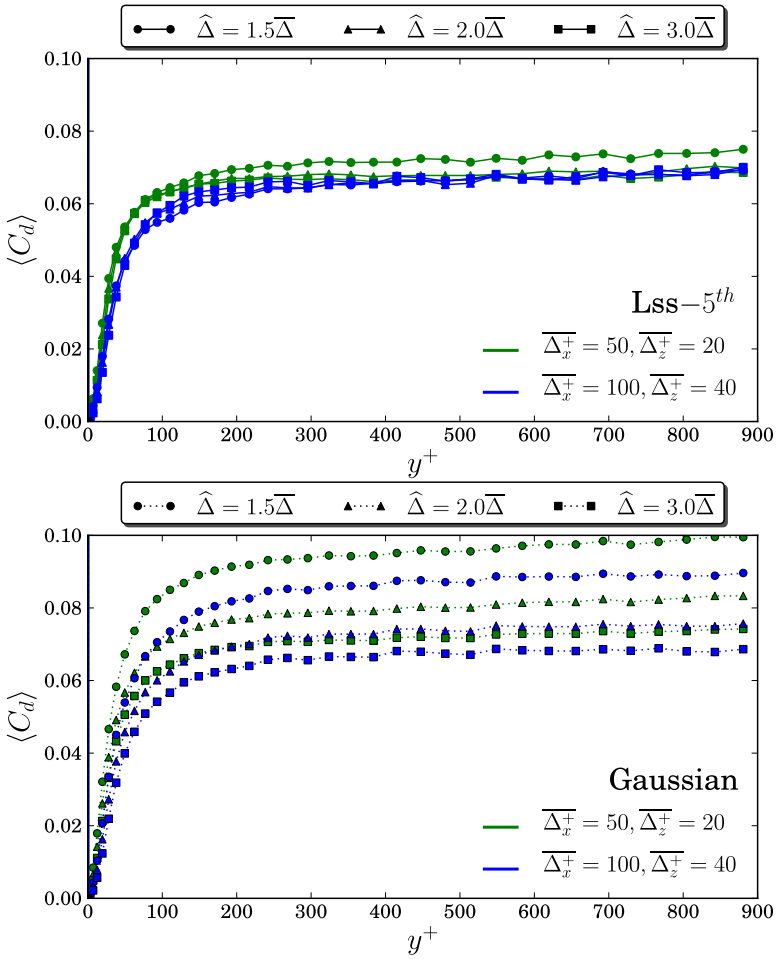

Figure 4.20: Influence of the test filter width of Dynamic Smagorinsky model with Lss-5^{th} and Gaussian filters.

For the Dynamic Smagorinsky model, the test filter width $\widehat{\Delta}$ is often chosen such that $\widehat{\Delta} = 2.0\overline{\Delta}$. Within the inertial range, the Dynamic Smagorinsky coefficient $\langle C_d \rangle$ is supposed to be insensitive to the test filter width $\widehat{\Delta}$ as shown in an open channel flow by Tsubokura 2006 [139]. The influence of the test filter width $\widehat{\Delta}$ on $\langle C_d \rangle$ has been investigated and the main results are given in Fig. 4.20. The test filter width $\widehat{\Delta}$ has a larger influence on the magnitude of $\langle C_d \rangle$ with the Gaussian filter than with Lss-5^{th} in the outer region, especially for the smallest test filter width $\widehat{\Delta} = 1.5\overline{\Delta}$. Such a small test filter width is not advocated for Lss-5^{th} filter, because it has overestimated the coefficient $\langle C_d \rangle$ for the filter set ($\overline{\Delta_x^+} = 50$, $\overline{\Delta_z^+} = 20$). This test filter width has little influence in the inner region. Thus, the smaller the filter and/or test filter width, the closer the coefficient $\langle C_d \rangle$ to $\langle C_s \rangle$ in the outer region with a Gaussian filter, not Lss-5^{th} filter.

4.4.2. Wall-Adapting Local Eddy-Viscosity model

An important feature of the WALE model is that it can recover the proper y^{+3} near-wall scaling for the eddy-viscosity theoretically by accounting for the effects of both the

strain and the rotation rate of the smallest resolved turbulent fluctuations. Thus all the turbulence structures relevant for the kinetic energy dissipation are detected by this model. The WALE model has been observed to perform better than the Smagorinsky model on LES of isotropic turbulence and turbulent pipe flow by Nicoud and Ducros 1999 [102]. All the expected features have been observed: the eddy-viscosity goes naturally to zero in the vicinity of a wall and the model gives zero eddy viscosity for pure shear. The coefficient $\langle C_w \rangle$ of the WALE subgrid scale model is usually used as a constant in LES simulations, notably for the converging-diverging turbulent channel flow by Kuban *et al.* 2012 [70]. However, to our knowledge, no a priori analysis of this WALE model has been conducted on wall turbulence at high Reynolds number in previous research.

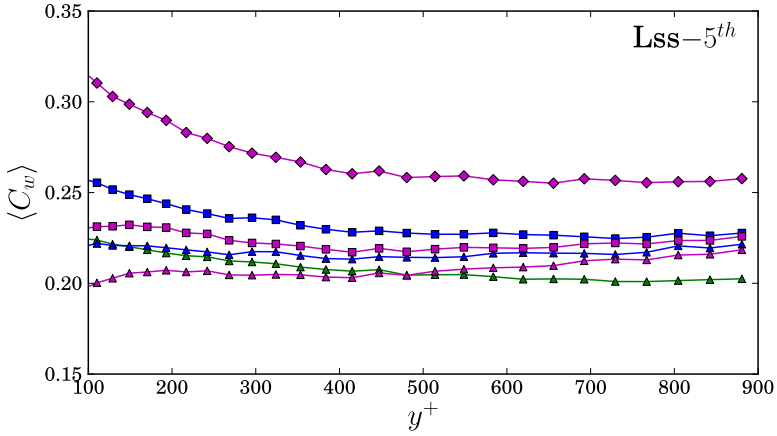

Figure 4.21: A priori estimate of the coefficient $\langle C_w \rangle$ of the WALE model for different Lss-5^{th} filter in the outer region.

The coefficient $\langle C_w \rangle \approx 0.5$ has been recommended for isotropic homogeneous flow by Nicoud and Ducros 1999 [102]. The results are obtained by Kuban *et al.* 2012 [70] with $0.2 \leq \langle C_w \rangle \leq 0.4$ for a converging-diverging channel flow. In the present analysis, the a priori estimate of $\langle C_w \rangle$ is almost constant in the outer region for all Lss-5^{th} filters as presented in Fig. 4.21. The low values of $\langle C_w \rangle$ in the outer region ($0.2 \leq \langle C_w \rangle \leq 0.27$) compared to previous research also reveals its sensitivity to the mesh size or to the 2D filtering like for the Smagorinsky model. The coefficient $\langle C_w \rangle$ is not sensitive to $\overline{\Delta_x^+}$, but is always larger in magnitude for larger $\overline{\Delta_z^+}$ in the outer region, this is the same with the Gaussian filter. This is due to the spanwise filter width dependence of both the SGS energy dissipation (Fig. 4.13) and the approximate equivalent of SGS energy dissipation by the WALE model ($-2.0\langle(\nu_{sgs}/C_w^2)\overline{S}_{ij}\overline{S}_{ij}$).

Nicoud and Ducros 1999 [102] have shown that, for isotropic flow, the relationship between $\langle C_w \rangle$ of the WALE model and $\langle C_s \rangle$ of the Smagorinsky model should be in the range $3.24 \leq \langle C_w \rangle / \langle C_s \rangle \leq 3.36$. The ratio between $\langle C_w \rangle$ and $\langle C_s \rangle$ of the present analysis in the outer region of the channel flow falls in the range $3.31 \leq \langle C_w \rangle / \langle C_s \rangle \leq 3.69$ as given in Table 4.2 for the different filter widths investigated here. They are larger than in isotropic flow, especially for large filter width.

As approaching to the wall, the coefficient $\langle C_w \rangle$ becomes surprisingly larger (about $0.1 \leq \langle C_w \rangle \leq 1.4$) than in the outer region as shown in Fig. 4.22. This is in agreement with the behavior of SGS energy dissipation (Fig. 4.10). It's important to note that, the peak of $\langle C_w \rangle$ for each filter set occurs in the range $y^+ < 10$. This peak is more sensitive to

$\overline{\Delta_z^+}$ than to $\overline{\Delta_x^+}$. It is significantly larger in magnitude for larger spanwise filter width $\overline{\Delta_z^+}$, especially for $\overline{\Delta_z^+} = 80$ using Lss-5^{th} filter where it becomes very large in inner region. This is partly due to the spanwise filter width dependence of SGS energy dissipation (Fig. 4.10). However, it's largely caused by the underlying differential operator $\langle S_{ij}^d S_{ij}^d \rangle$ of the WALE model as displayed in Fig. 4.23. This operator rapidly goes to zero near solid boundaries in a way which is greatly influenced by the filter width. It becomes very small for large spanwise filter width $\overline{\Delta_z^+}$. This leads to an active sensitivity of the approximate modeled SGS energy dissipation by the WALE model to the spanwise filter width as presented in Fig. 4.24. Thus, the exclusive dependence of coefficient $\langle C_w \rangle$ to spanwise filter width $\overline{\Delta_z^+}$ prevails in inner region.

		$\overline{\Delta_x^+} = 50$	$\overline{\Delta_x^+} = 100$	$\overline{\Delta_x^+} = 200$
$\overline{\Delta_z^+} = 10$	Lss-5^{th}	3.35	3.48	
	Gaussian	3.37	3.46	
$\overline{\Delta_z^+} = 20$	Lss-5^{th}	3.31	3.43	3.65
	Gaussian	3.34	3.45	3.69
$\overline{\Delta_z^+} = 40$	Lss-5^{th}		3.35	3.61
	Gaussian		3.39	3.66
$\overline{\Delta_z^+} = 80$	Lss-5^{th}			3.66
	Gaussian			3.64

Table 4.2: Ratio of mean values of $\langle C_w \rangle / \langle C_s \rangle$ in the range $300 \leq y^+ \leq 850$ using Lss-5^{th} and Gaussian filters.

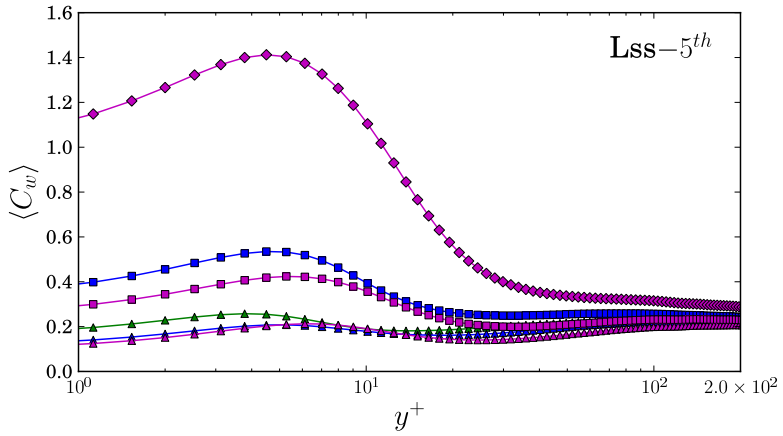

Figure 4.22: A priori estimate of coefficient $\langle C_w \rangle$ of the WALE model in the near wall region using Lss-5^{th} filter.

Meanwhile, because the resolved scales with large spanwise filter width $\overline{\Delta_z^+} = 80$ are not able to reproduce the real streaks in the near wall region, it is difficult to correctly predict the small scale motions which contain most of the turbulent kinetic energy in inner region (Fig. 4.2). Thus, small spanwise filter width $\overline{\Delta_z^+} < 40$ is recommended for the WALE model using Lss-5^{th} filter.

The influence of filter type and filter width on $\langle C_w \rangle$ is studied using the Lss-5^{th} and Gaussian filters as displayed in Fig. 4.25 and 4.26. Along the wall normal position, $\langle C_w \rangle$

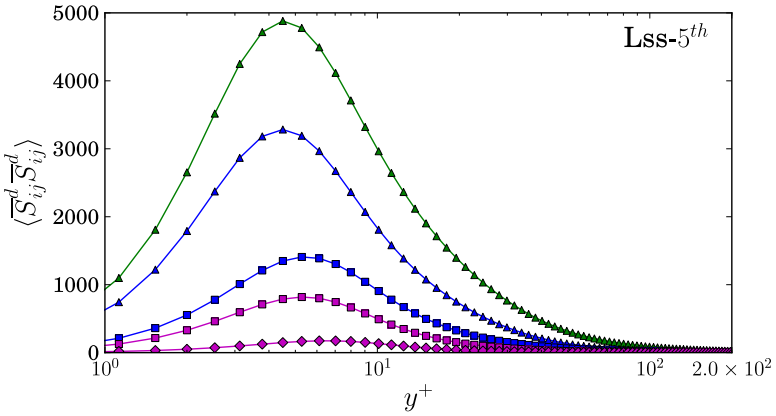

Figure 4.23: Near wall region behavior of the WALE model operator $\langle S_{ij}^d S_{ij}^d \rangle$ using Lss-5^{th} filter.

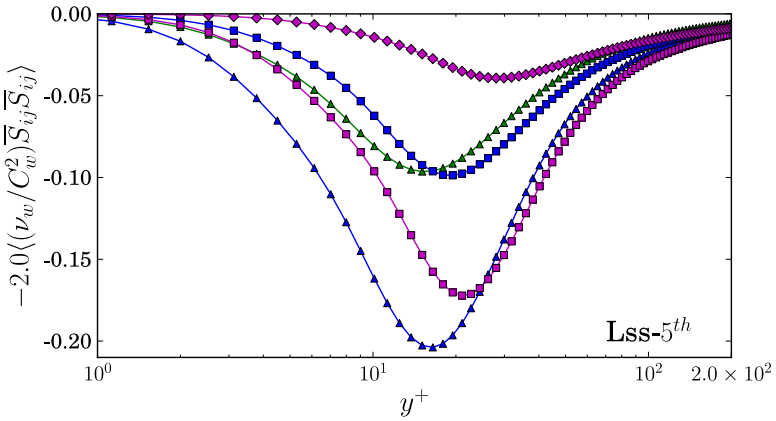

Figure 4.24: Near wall region behaviors of the approximate equivalent of SGS energy dissipation by the WALE model using Lss-5^{th} filter.

is larger with Gaussian than with Lss-5^{th} filter. Except for the filter set ($\overline{\Delta_x^+} = 200$, $\overline{\Delta_z^+} = 80$) in the inner region. The remarkable peak of $\langle C_w \rangle$ with large filter width $\overline{\Delta_z^+} = 80$ is alleviated somewhat in the near wall region by the Gaussian filter. When large spanwise Lss-5^{th} filter width is used, however, the WALE model is less dissipative in the viscous layer ($y^+ < 10$) where pure shear or rotation occurs infrequently. Anyhow, small spanwise filter width $\overline{\Delta_z^+} < 40$ can be recommended in the near wall region for the WALE model using either Lss-5^{th} or Gaussian filter. However, an a posteriori analysis would be necessary to analyze the behavior of $\langle C_w \rangle$ in the near wall region.

4.4.3. σ Model

The σ model detailed in Section 2.2.3.4 of Chapter 2 takes a forward step compared to the WALE model for generating the appropriate cubic behavior in the vicinity of solid boundaries without requiring any ad-hoc treatment. The σ model is designed to automatically vanish as soon as the resolved field is either two-dimensional or two-component, including the pure shear and solid body rotation cases. Still, the σ model has a low computational cost, is easy to implement, and does not require any homogeneous direction in space or time (Nicoud *et al.* 2011 [103]).

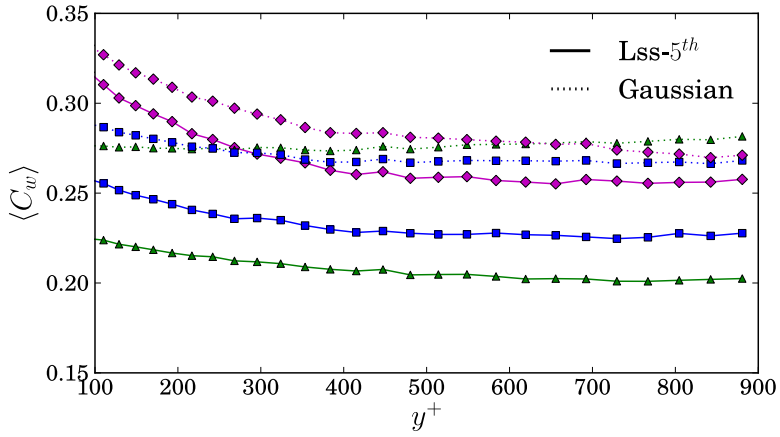

Figure 4.25: Influence of the filter type and filter width on coefficient $\langle C_w \rangle$ in the outer region using Lss-5^{th} and Gaussian filters.

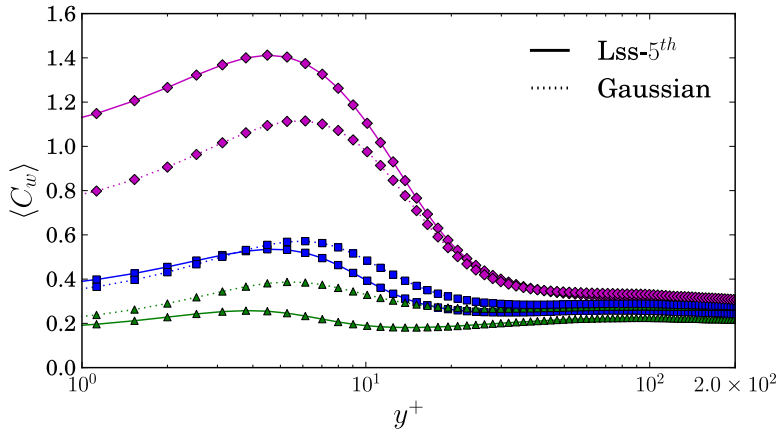

Figure 4.26: Influence of the filter type and filter width on coefficient $\langle C_w \rangle$ in near wall region using Lss-5^{th} and Gaussian filters.

Results of the σ model for decaying isotropic turbulence and periodic channel flow have been obtained by Nicoud *et al.* 2011 [103]. The results are systematically equivalent or slightly better than with the Dynamic Smagorinsky model. The σ model has shown the proper cubic behavior in near-wall regions of plane channel flow at $Re_\tau = 395$ and 590 by Nicoud *et al.* 2011 [103]. But it still needs to be tested on different configurations of non-homogeneous, wall-bounded flows.

According to Nicoud *et al.* 2011 [103], a constant $\langle C_\sigma \rangle \approx 1.5$ is often used for isotropic turbulence. The a priori estimate of coefficient $\langle C_\sigma \rangle$ in our analysis of plane channel flow using the Lss-5^{th} filter is given in Fig. 4.27 and 4.28. As can be seen, $\langle C_\sigma \rangle$ has a behavior very similar to that of $\langle C_w \rangle$ of the WALE model. The magnitude of $\langle C_\sigma \rangle$ in the outer region ($0.55 \leq \langle C_\sigma \rangle \leq 0.75$) is significantly lower than in previous research, owing to the same reason as for $\langle C_s \rangle$ of Smagorinsky model and $\langle C_w \rangle$ of the WALE model.

The coefficient $\langle C_\sigma \rangle$ is also larger in magnitude (about $0.3 \leq \langle C_\sigma \rangle \leq 1.8$) in the near wall region than in the outer region. A maximum of $\langle C_\sigma \rangle$ is located at the same wall distance ($y^+ < 10$) as for $\langle C_w \rangle$ of the WALE model. For the σ model, the peak of $\langle C_\sigma \rangle$ is largely due to the spanwise filter width dependence of the modeled SGS energy dissipation by the σ model. This is mainly caused by the differential operator $\langle D_\sigma \rangle$ (defined by

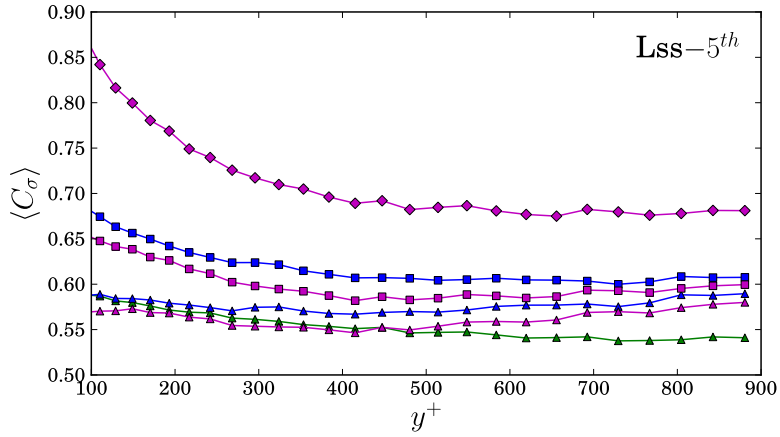

Figure 4.27: A priori estimate of coefficient $\langle C_\sigma \rangle$ of the σ model using Lss-5^{th} filter.

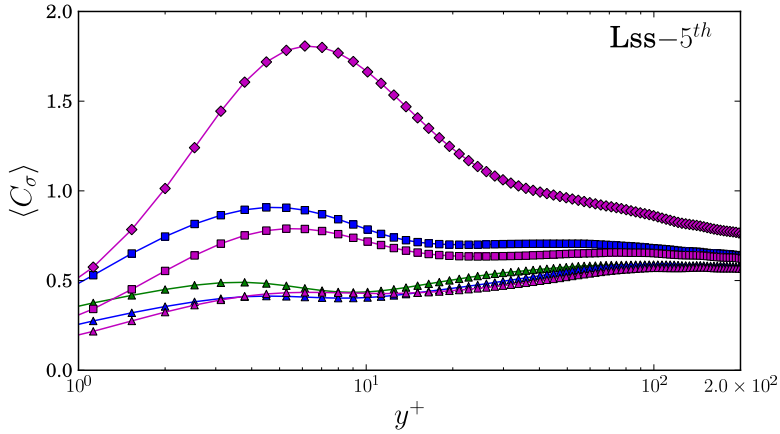

Figure 4.28: A priori estimate of coefficient $\langle C_\sigma \rangle$ of the σ model in near wall region using Lss-5^{th} filter.

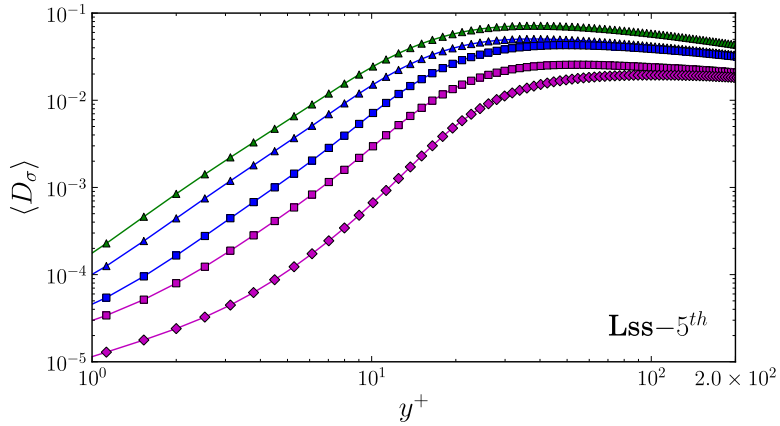

Figure 4.29: Near wall region behavior of the σ model operator $\langle D_\sigma \rangle$ using Lss-5^{th} filter.

equation 2.28 in Chapter 2) of the σ model (Fig. 4.29), as the differential operator $\langle \overline{S}_{ij}\overline{S}_{ij} \rangle$ is not as sensitive as $\langle D_\sigma \rangle$ to the filter width in near wall region (Fig. 4.30).

The influences of the filter type and filter width on $\langle C_\sigma \rangle$ are shown in Fig. 4.31 and 4.32. Changing the filter type or filter width has almost the same effects on $\langle C_\sigma \rangle$ and $\langle C_w \rangle$

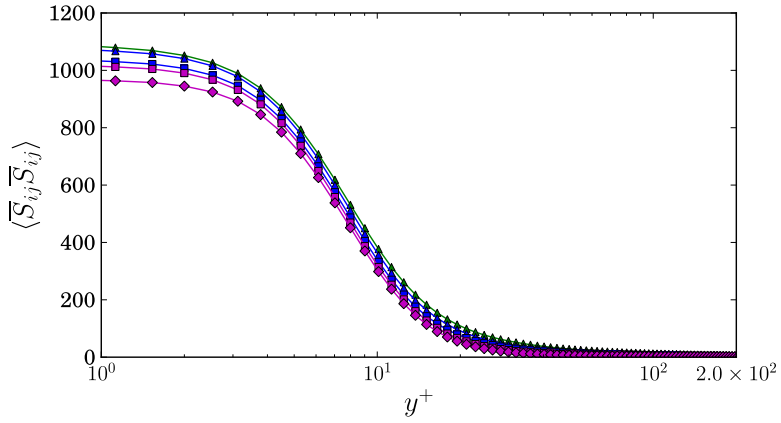

Figure 4.30: Near wall region behavior of the differential operator $\langle \overline{S}_{ij}\overline{S}_{ij} \rangle$ using Lss-5^{th} filter.

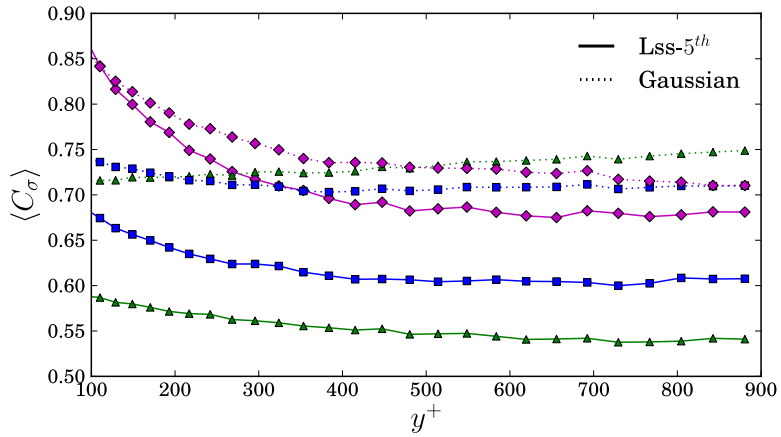

Figure 4.31: Influence of filter type on coefficient $\langle C_\sigma \rangle$ using Lss-5^{th} and Gaussian filters.

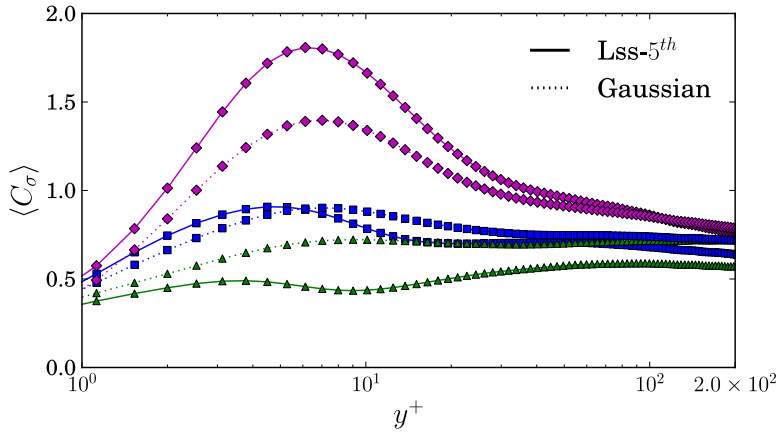

Figure 4.32: Influence of filter type on coefficient $\langle C_\sigma \rangle$ in near wall region using Lss-5^{th} and Gaussian filters.

along the wall normal (see Fig. 4.25 and 4.26). This a priori analysis seems to indicate that the behavior of both σ and WALE models is very similar in terms of modeled SGS energy dissipation. The superiority of the σ model compared to WALE model is not

reflected in the present analysis of the plane channel flow. The coefficient $\langle C_w \rangle$ and $\langle C_\sigma \rangle$ are more sensitive to the spanwise filter width $\overline{\Delta_z^+}$ than the classical Smagorinsky model or Dynamic Smagorinsky model. This is not favorable for practical use of a model constant. Thus, small spanwise filter width $\overline{\Delta_z^+} < 40$ in near wall region is also recommanded for the σ model using both Lss-5^{th} and Gaussian filters.

The failure of invariance of model coefficient has been reported in many studies (O'Neil and Meneveau 1997 [104]; Carper and Porté-Agel 2008 [25], Bou-Zeid *et al.* (2008) [17]) when the filter and/or test filter width fall outside the inertial subrange and inside the so-called production subrange. All the a priori analysis of the coefficients of subgrid scale models in the present research indicate that the uniformity of model coefficient breaks down when approaching the wall. Furthermore, the coefficients of subgrid scale models considered here show great sensitivity to filter width and type. This confirms the results of Porté-Aget *et al.* 2001 [118], who found that filter width has a considerable effect on the various model coefficients, and the large eddy simulations can yield more realistic results by allowing the model coefficient in the eddy-viscosity model to change with filter width. The distinguishing point of the present research lies in that a strong sensitivity to the spanwise filter width of the coefficients of the WALE and σ models has been found, which was not reported by classical subgrid models in previous research. All the results confirm that for LES the subgrid scale models can not be specified independently of the filter, which has been reported by many research (Piomelli 1988 [113]; Liu *et al.* 1994 [80]; Pruett *et al.* 2000 [120]).

4.5. Tests of models behavior

Large eddy simulation for predicting turbulent flux under non-equilibrium flow requires a closer look at how well the subgrid scale models reproduce the statistical behavior of subgrid scale quantities. However, a priori tests evaluating the behavior of subgrid scale models on channel flow are not so numerous in previous research. In this Section, we explore how the subgrid scale models analyzed in Section 4.4 perform to predict the three statistical quantities defined in equation 3.23, 3.24 and 3.25 of Chapter 3. Important information on correlations between exact quantities and their counterparts computed with the subgrid models, as well as the predictive capabilities of eddy viscosity models along wall normal position will be provided. Definition of correlation between exact (E) and modeled (M) quantities is given in equation 3.26 of Chapter 3. The a priori analysis will be conducted primarily on Smagorinsky and WALE models (as the σ model behaves quite similarly to the WALE model as analyzed above). A priori tests are performed using the average model coefficients as function of wall distance calculated in Section 4.4.

4.5.1. Correlation of SGS tensor

Distributions of the exact SGS stresses $\langle \tau_{ij} \rangle$ normalized by the square of the friction velocity u_τ^2 along the wall normal are given in Fig. 4.33 with a filter width $\overline{\Delta_x^+} = 100$, $\overline{\Delta_z^+} = 40$. All components of the SGS stress tensor $\langle \tau_{ij} \rangle$ are slightly larger with Gaussian filter than with Lss-5^{th} filter. Evaluation of model performances are mainly dependent on components $\langle \tau_{11} \rangle$, $\langle \tau_{12} \rangle$, $\langle \tau_{22} \rangle$ and $\langle \tau_{33} \rangle$, as $\langle \tau_{13} \rangle$ and $\langle \tau_{23} \rangle$ are zero due to the spanwise homegeneity. Similar shapes of SGS tress tensor $\langle \tau_{ij} \rangle$ are observed for other filter width.

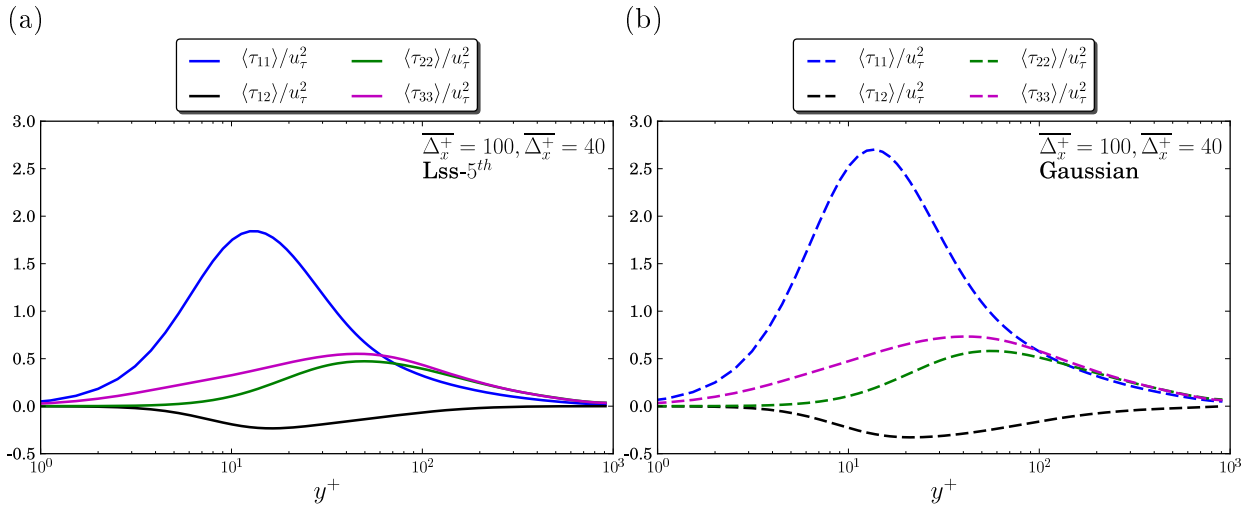

Figure 4.33: Distributions of normalized SGS stress tensor (u_τ being the friction velocity) using Lss-5^{th} (a) and Gaussian (b) filters.

(a) Correlations between $\langle\tau_{ij}\rangle$ and $\langle\tau_{ij}^{SM}+1/3\tau_{kk}\delta_{ij}\rangle$(b) Correlations between $\langle\tau_{ij}\rangle$ and $\langle\tau_{ij}^{SM}\rangle$

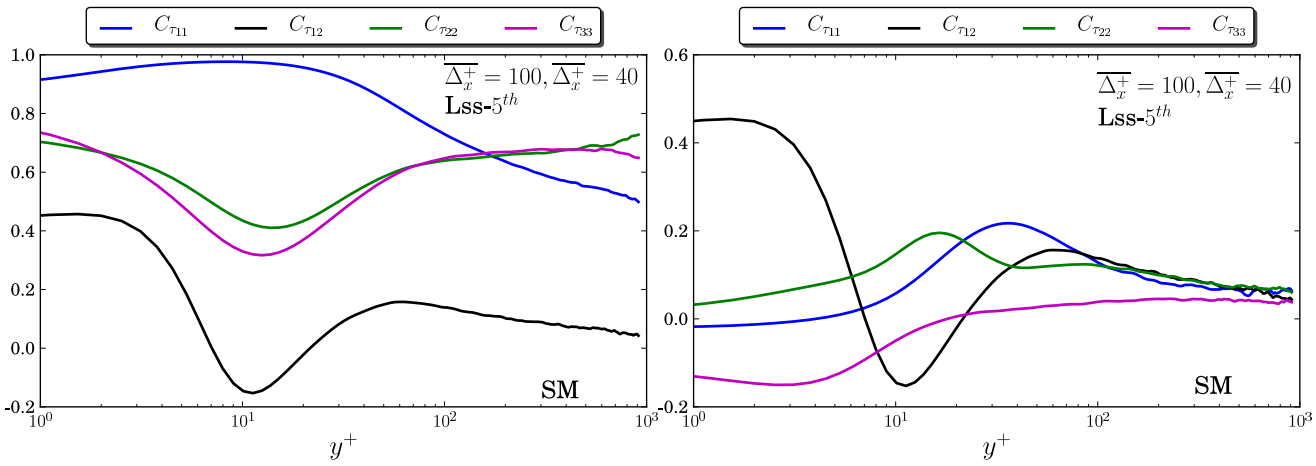

Figure 4.34: Correlations $C_{\tau_{ij}}$ between exact SGS stress tensor and the modeled counterparts by Smagorinsky model using Lss-5^{th} filter.

The eddy-viscosity model accounts for only the deviatoric part of the SGS stress tensor $\tau_{ij} - 1/3\tau_{kk}\delta_{ij}$. For the diagonal components ($i = j$), it's difficult to compare the real SGS stress tensor and the modeled one, as $1/3\tau_{kk}\delta_{ij}$ is non-zero. Correlations between $\tau_{ii} - 1/3\tau_{kk}$ and $-2\nu_{sgs}\overline{S}_{ii} + 1/3\tau_{kk}$ do not indicate an accurate predicting capability of subgrid scale models for the component τ_{ii} of the real SGS stress tensor. Consequently, $1/3\tau_{kk}\delta_{ij}$ is often ignored, or only components $i \neq j$ of SGS stress tensor are tested in previous a priori analysis (Meneveau and Katz 2000 [93]; Wollblad and Davidson 2008 [148]). Recently an alternative way has been followed by Carper and Porté-Agel 2008 [25] who added the real value of $1/3\tau_{kk}\delta_{ij}$ to the modeled subgrid scale tensor in order to provide an appropriate comparison with other non-eddy viscosity models. Our analysis is conducted by both considering and ignoring $1/3\tau_{kk}\delta_{ij}$.

For a priori tests of Smagorinsky model in homogeneous turbulence, McMillan and Ferziger 1979 [91] reported that correlation between the exact SGS stress tensor and

the modeled one by Smagorinsky model is 0.33. Liu *et al.* 1994 [80] found that the correlation in isotropic turbulence is no more than 0.25. The a priori reference of eddy-viscosity models for plane channel flow is very scarce. Correlations $C_{\tau_{ij}}$ between the exact SGS stress tensor and its modeled component by Smagorinsky model are given in Fig. 4.34. They are first analyzed with a filter width $\overline{\Delta_x^+} = 100$, $\overline{\Delta_z^+} = 40$ using the Lss-5^{th} filter. The correlations $C_{\tau_{ij}}$ have large dependence on the distance from the wall. The correlation $C_{\tau_{12}}$ is about 0-0.1 in the outer region, it is smaller than in previous homogeneous turbulence (McMillan and Ferziger 1979 [91], Liu *et al.* 1994 [80]).

High correlations from 0.3 to 1.0 occur on $C_{\tau_{11}}$, $C_{\tau_{22}}$ and $C_{\tau_{33}}$. This is due to $1/3\tau_{kk}$ which contains one third of each τ_{ii}. When $1/3\tau_{kk}\delta_{ij}$ is ignored, correlations $C_{\tau_{11}}$, $C_{\tau_{22}}$ and $C_{\tau_{33}}$ collapse to the order of $C_{\tau_{12}}$, $C_{\tau_{13}}$ and $C_{\tau_{23}}$ as shown in Fig. 4.34(b). In Fig. 4.34, a negative drop occurs on correlation $C_{\tau_{12}}$ in the buffer layer, and $C_{\tau_{11}}$ and $C_{\tau_{33}}$ are negative in the near wall region in Fig. 4.34(b). This indicates that the correlation between τ_{12} and $\overline{S}_{12}$, τ_{11} and $\overline{S}_{11}$ as well as τ_{33} and $\overline{S}_{33}$ becomes worse in the inner region of a plane channel flow compared to previous research on homogeneous turbulence for which Pope 2000 [116] and Meneveau and Katz 2000 [93] reported that the correlation between τ_{ij} and the strain rate tensor $\overline{S}_{ij}$ is not as good as expected for the Smagorinsky model.

Furthermore, $C_{\tau_{11}}$, $C_{\tau_{22}}$ and $C_{\tau_{33}}$ in Fig. 4.34(a) are higher than the results of Carper and Porté-Agel 2008 [25], who obtained correlations less than 0.3. This difference is attributed to the fact that all components $i = j$ of the exact and modeled SGS stress tensor are mesured here. On the other hand, Carper and Porté-Agel 2008 [25] measure correlations between only a few components of the two stress tensors and the statistical data set in our case is substantially larger than theirs.

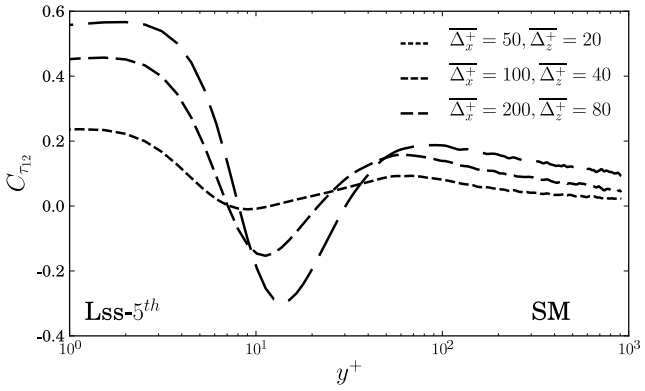

Figure 4.35: Influence of filter width on correlations $C_{\tau_{12}}$ using Lss-5^{th} filter.

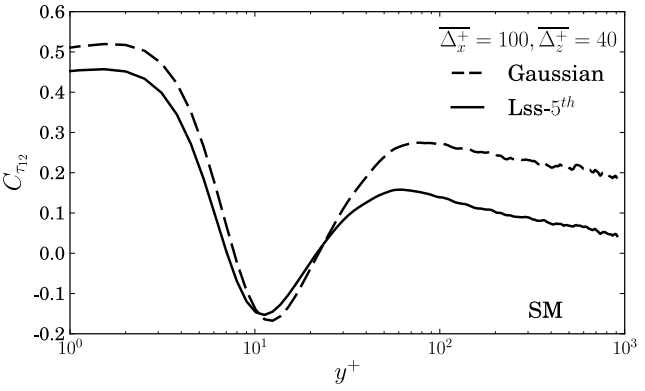

Figure 4.36: Influence of filter type on correlations $C_{\tau_{12}}$ using Lss-5^{th} filter.

The performance of Smagorinsky model in plane channel flow also depends on the choice of the filter width and type as shown in Fig 4.35 and 4.36, confirming the previous conclusions for Smagorinsky model in homogeneous turbulence (Pope 2000 [116]; Abbà 2003 [1]). The correlation $C_{\tau_{12}}$ increases in general for the larger filter width as given in Fig. 4.35, in agreement with observations of Borue and Orszag 1998 [14] in the inertial range of a high Reynolds number flow using classical filters, and Liu *et al.* 1994 [80] in a turbulent jet. The larger correlations with Gaussian filter are due to the overlapping between resolved and unresolved scales with this filter. Thus the modeled quantities with Gaussian filter are much more correlated to the exact ones than when a sharp Lss-5^{th}

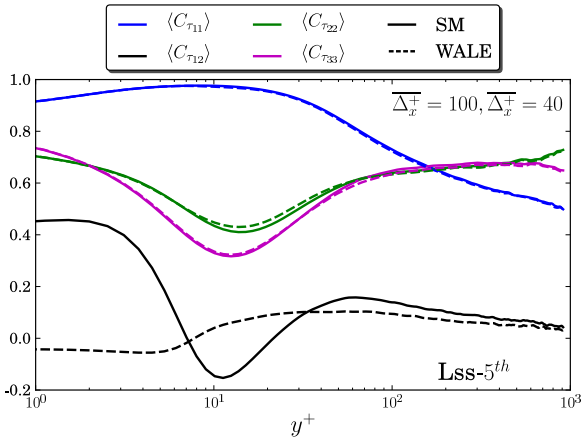

Figure 4.37: Comparison of correlations $C_{\tau_{ij}}$ between Smagorinsky and WALE models using Lss-5^{th} filter.

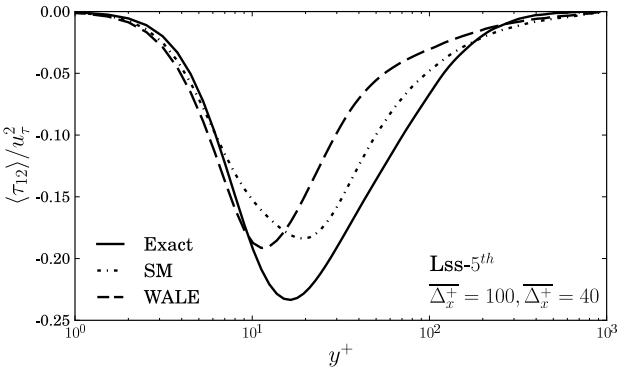

Figure 4.38: Exact $\langle \tau_{12}\rangle$ and its modeled counterparts by Smagorinsky and WALE models using Lss-5^{th} filter.

filter is employed (Abbà 2003 [1]; Park *et al.* 2005 [107]). However, low correlations of subgrid scale models in a priori tests do not indicate a failure of such models but the fundamental limitation of a priori test itself (Park 2005 [107]). However, the betrayal for the monotone increasing on larger filter width for correlation $C_{\tau_{12}}$ occurs in the buffer layer, this is also observed with Gaussian filter. Therefore, correlations between exact and modeled quantities of present plane channel flow exhibit more complex features depending on filter width and type, as well as the distance from the wall.

Comparison of correlations $C_{\tau_{ij}}$ between the Smagorinsky and WALE models with filter width $\overline{\Delta_x^+} = 100$, $\overline{\Delta_z^+} = 40$ is shown in Fig. 4.37. The WALE model has a lower correlation $C_{\tau_{12}}$ than the Smagorinsky model except in the buffer layer where no drop of correlation is observed. No significant difference occurs at the three high correlations $C_{\tau_{11}}$, $C_{\tau_{22}}$ and $C_{\tau_{33}}$ between the two models.

For the present plane channel flow, the spatial and temporal averaging of $\overline{S}_{11}$, $\overline{S}_{22}$ and $\overline{S}_{33}$ are zero due to streamwise and spanwise homogeneity. So the predicting capabilities of the subgrid scale models for the average SGS tensor components $\langle \tau_{11}\rangle$, $\langle \tau_{22}\rangle$ and $\langle \tau_{33}\rangle$ can not be evaluated. The exact $\langle \tau_{12}\rangle$ and its predicted counterpart by the Smagorinsky and WALE models are given in Fig. 4.38 and 4.39. Two filter sets $\overline{\Delta_x^+} = 50$, $\overline{\Delta_z^+} = 20$ and $\overline{\Delta_x^+} = 100$, $\overline{\Delta_z^+} = 40$ are analyzed. The predicting capabilities of both the Smagorinsky and WALE models are quite comparable in the range $y^+ < 10$. However, while $\langle \tau_{12}\rangle$ is better predicted by the WALE than by the Smagorinsky model in the buffer layer and the outer region with the Lss-5^{th} filter width $\overline{\Delta_x^+} = 50$, $\overline{\Delta_z^+} = 20$. $\langle \tau_{12}\rangle$ is underestimated by the two models for the larger Lss-5^{th} filter width $\overline{\Delta_x^+} = 100$, $\overline{\Delta_z^+} = 40$ and for the smaller Gaussian filter ($\overline{\Delta_x^+} = 50$, $\overline{\Delta_z^+} = 20$), while the Smagorinsky model performs better at predicting $\langle \tau_{12}\rangle$ at the same time. Therefore, the a priori predicting capacity of subgrid models for SGS stress tensor can not be evaluated independently of the filter width and filter type. However, it's important to denote that, the better predicting capability of both Smagorinsky and WALE models in the viscous layer than in outer region correspond to a lower correlation $C_{\tau_{12}}$ for the WALE model (see Fig. 4.37).

The standard deviation σ_{12} of the exact and modeled SGS stress tensor component $\langle \tau_{ij}\rangle$ is shown in Fig. 4.40. In the range $y^+ > 20$, the WALE model always has a better

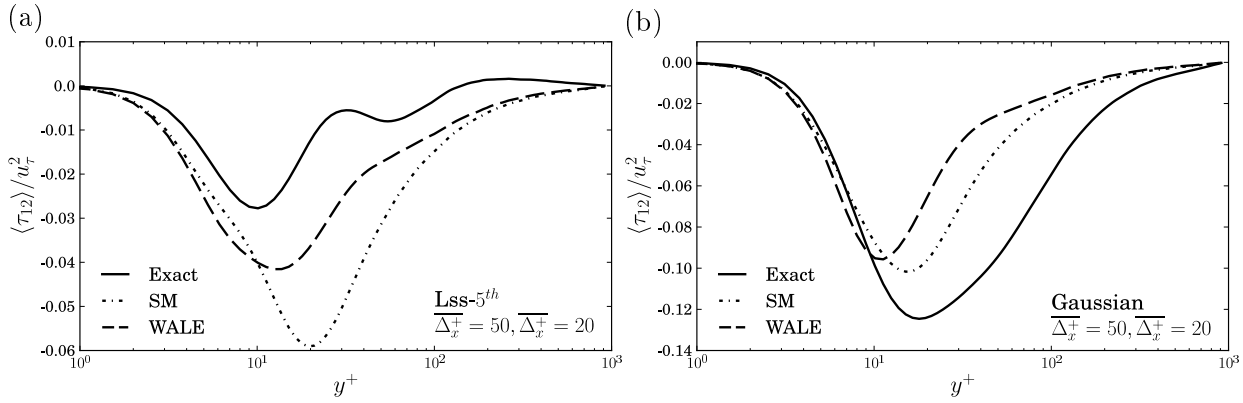

Figure 4.39: Exact $\langle \tau_{12} \rangle$ and its modeled counterparts by Smagorinsky model and the WALE model with filter width $\overline{\Delta_x^+} = 50$, $\overline{\Delta_z^+} = 20$ using Lss-5^{th} filter (a) and Gaussian filter (b).

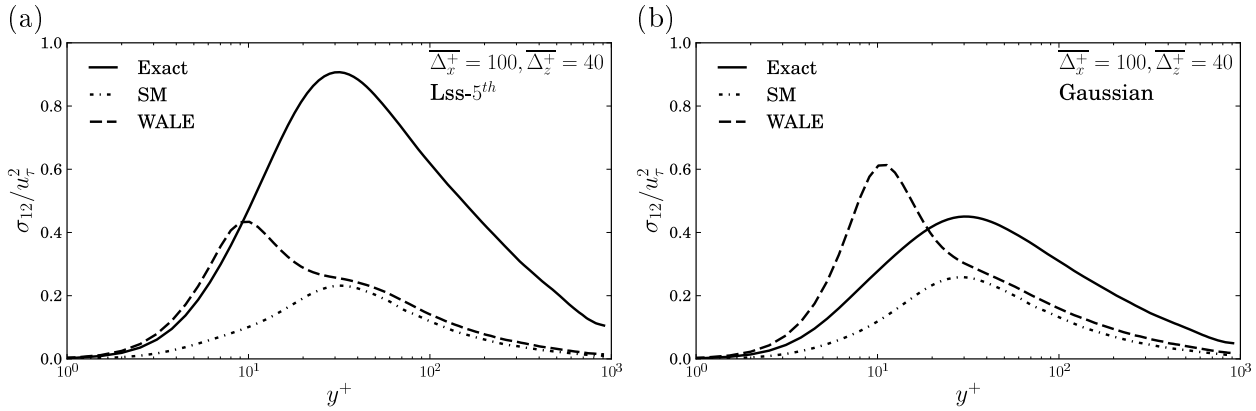

Figure 4.40: Standard deviation of the exact and modeled $\langle \tau_{12} \rangle$ with filter width $\overline{\Delta_x^+} = 100$, $\overline{\Delta_z^+} = 40$ using Lss-5^{th} filter (a) and Gaussian filter (b).

prediction for the standard deviations of τ_{12} with both filters. The standard deviation of τ_{12} is well predicted in range $y^+ < 10$ by the WALE model using a Lss-5^{th} filter. It is important to note, however, that while the WALE model has been shown to have a poor correlation with the SGS stress tensor τ_{12} in Fig. 4.37, the standard deviations predicted in the outer region are better than with the Smagorinsky model.

4.5.2. Correlation of SGS force

A good prediction of subgrid scale models for the SGS force (defined in Table 3.1 of Chapter 3) contained in the filtered Navier-Stokes equations is important to guaranntee the accuracy of LES. The normalized SGS force $\langle f_i \rangle$ with filter width $\overline{\Delta_x^+} = 100$, $\overline{\Delta_z^+} = 40$ are given in Fig. 4.41. Components $\langle f_1 \rangle$ and $\langle f_2 \rangle$ are looked at in the following analysis, since f_3 is zero due to homogeneity in spanwise direction. The two components are slightly larger with Gaussian filter than with Lss-5^{th} filter.

Correlations C_{f_1} and C_{f_2} using Lss-5^{th} filter are displayed in Fig. 4.42. The negative drop of C_{f_2} in the buffer layer and the negative correlation C_{f_1} toward the channel center in Fig. 4.42(a) are alleviated when term $1/3\tau_{kk}\delta_{ij}$ is not considered in Fig. 4.42(b). Similar

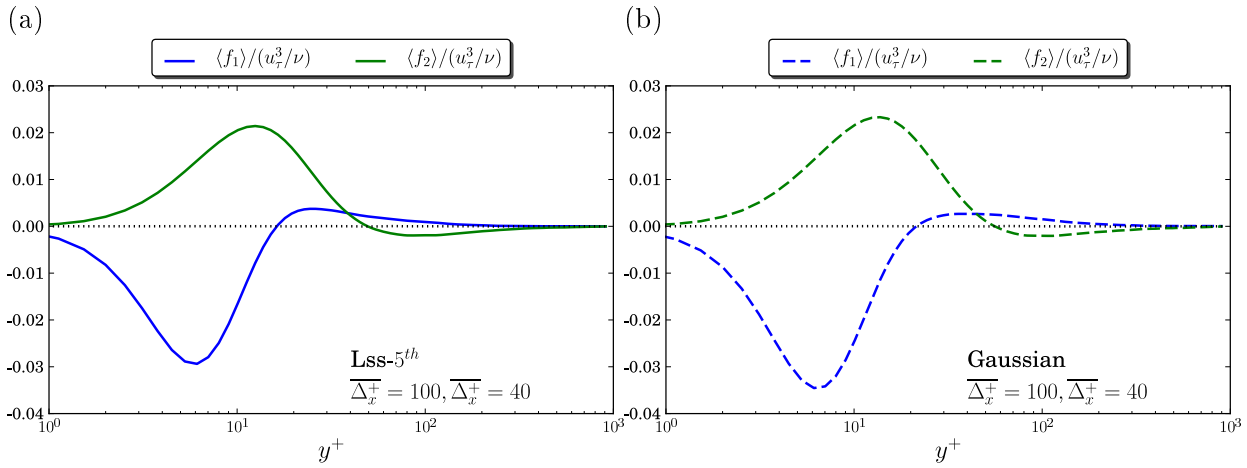

Figure 4.41: Distributions of normalized average SGS force $\langle f_i \rangle$ using Lss-5^{th} (a) and Gaussian filter (b) along wall normal position.

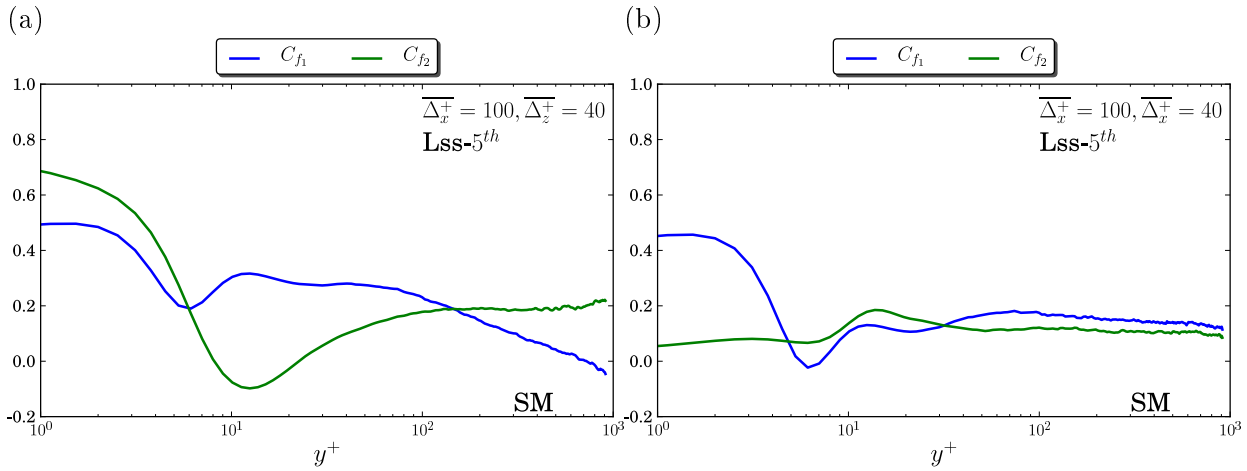

Figure 4.42: Correlations C_{f_1} and C_{f_2} between $\partial\tau_{ij}/\partial x_j$ and $\partial(\tau_{ij}^{SM} + 1/3\tau_{kk}\delta_{ij})/\partial x_j$ (a) or between $\partial\tau_{ij}/\partial x_j$ and $\partial\tau_{ij}^{SM}/\partial x_j$ (b) for Smagorinsky model, using Lss-5^{th} filter.

behavior is observed with Gaussian filter (see Fig. A.2 in Appendix A). The influence of filter width and filter type on correlations C_{f_1} and C_{f_2} is plotted in Fig 4.43 and 4.44. The results further show that the increment of each correlation also depends on the specific correlation component, beside the filter width and filter type. The monotone increase of correlations for larger filter width is inverse for C_{f_1} in the buffer layer. Moreover, for the large filter width $\overline{\Delta_x^+} = 200$, $\overline{\Delta_z^+} = 80$ in Fig. 4.44, there is no apparent growth of correlations, especially C_{f_1} in the near wall region with a Gaussian filter compared to Lss-5^{th} filter. Thus the dependence to the filter type is not universal for the correlation of SGS force in the present plane channel flow.

Comparisons between the WALE model and the Smagorinsky model are given in Fig. 4.45 and 4.46 for a small filter width. Both correlation and the average of the modeled SGS force have the same behavior as for larger filter width. No significant difference occurs on correlation C_{f_i} between the Smagorinsky model and the WALE model as shown in Fig. 4.45. Generally, both models perform better for predicting the SGS forces in the outer region than in the near wall region. Mason and Thomson 1992 [90] observed that the mean

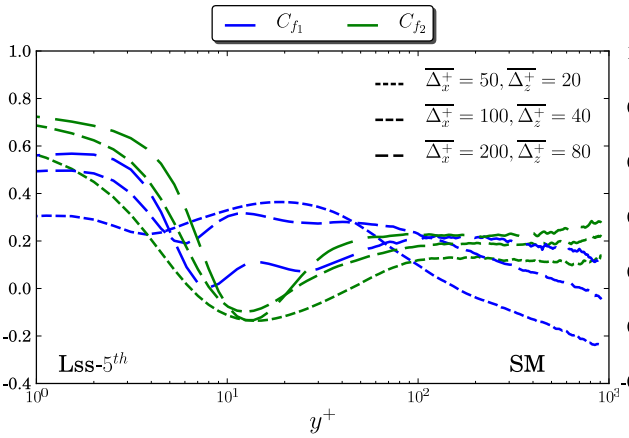

Figure 4.43: Influence of filter width on correlations C_{f_i} using Lss-5^{th} filter.

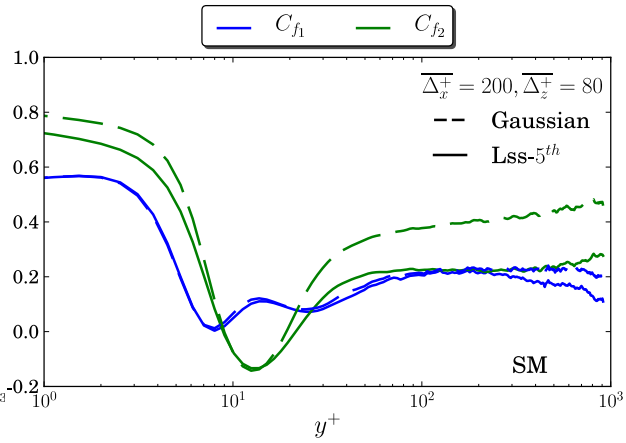

Figure 4.44: Influence of filter type on correlations C_{f_i}.

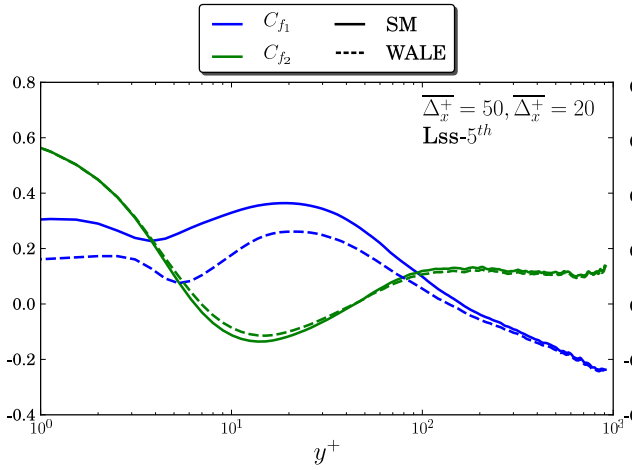

Figure 4.45: Comparison of correlations C_{f_i} between Smagorinsky model and WALE model using Lss-5^{th} filter.

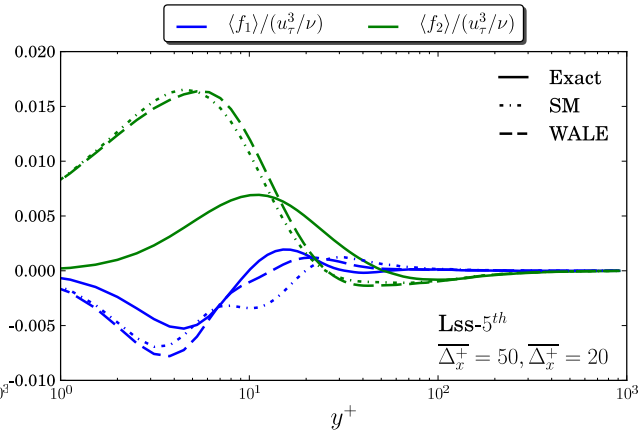

Figure 4.46: Exact f_i and its modeled counterparts by Smagorinsky model and WALE model using Lss-5^{th} filter.

velocity profile in the matching region has not had a logarithmic form and it is impossible to eliminate the error by adjustments of the subgrid lengthscale. They thought that an obvious defect of the Smagorinsky model is its failure to represent stochastic subgrid stress variations and showed that inclusion of these variations leads to a marked improvement in the near-wall flow simulation. Nevertheless, the SGS force predicting capabilities of the models are not consistent with their correlations which are higher in near wall region compared to the outer region. This discrepancy between correlation values and predicting capacities of the two models is independent of the filter width and type. These results reveal that strong correlations sometimes do not imply high predicting abilities of eddy-viscosity models, and vice versa. This is in good agreement with the results of Carper and Porté-Agel 2008 [25] who found that the eddy-viscosity model produces low correlation with the mesured SGS stress as well as unrealistically low fluctuation levels, while the differences in probability density functions (PDFs) of the exact τ_{12} and the modeled τ_{12}^{ev} by eddy-viscosity models are nearly indistinguishable.

4.5.3. Correlation of SGS energy dissipation

Although the coefficients of subgrid scale models discussed in Section 4.4 are computed a priori by matching the measured and modeled subgrid scale dissipation, this does not imply a good local correlation between the two terms along wall normal position. The exact quantity $\langle \tau_{ij}\overline{S}_{ij} \rangle$ has been given in Fig. 4.13. Correlation $C_{\epsilon_{sgs}}$ between $\tau_{ij}\overline{S}_{ij}$ and $\tau_{ij}^{mod}\overline{S}_{ij}$ using the small Lss-5^{th} filter along wall normal position is shown in Fig. 4.47. In

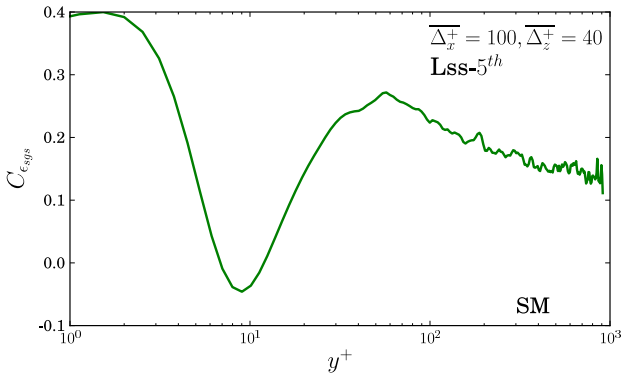

Figure 4.47: Correlation $C_{\epsilon_{sgs}}$ between exact SGS energy dissipation and the modeled one by Smagorinsky model using Lss-5^{th} filter.

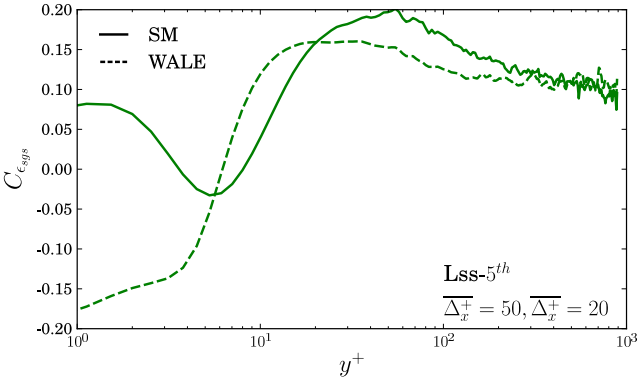

Figure 4.48: Comparison of correlations $C_{\epsilon_{sgs}}$ between Smagorinsky model and WALE model using Lss-5^{th} filter set $\overline{\Delta_x^+} = 50$, $\overline{\Delta_z^+} = 20$.

the outer region, the correlation $C_{\epsilon_{sgs}}$ gradually decreases when moving toward the channel center. Many studies showed that correlations of the three criteria considered here are generally ordered as $C_{\tau_{ij}} < C_{f_i} < C_{\epsilon_{sgs}}$ for homogeneous turbulence (Meneveau and Katz 2000 [93]). However, our a priori analysis on all the dominant correlations precisely reveals that the above order is not universal for each correlation component of each condition in a plane channel flow, even in the outer region. For example, in this outer region, $C_{\epsilon_{sgs}}$ is smaller than C_{f_2} in Fig. 4.42 or than $C_{\tau_{11}}$, $C_{\tau_{22}}$, $C_{\tau_{33}}$ in Fig. 4.34. Correlation $C_{\epsilon_{sgs}}$ has similar filter width and filter type dependent behavior with correlations $C_{\tau_{12}}$ and C_{f_1}, C_{f_2}, depending on distance from the wall. Slightly higher correlation $C_{\epsilon_{sgs}}$ is obtained with the Gaussian filter (see Fig. A.3 in Appendix A).

Comparison of correlations $C_{\epsilon_{sgs}}$ between Smagorinsky model and WALE model is given in Fig. 4.48. Both models correlate poorly along wall normal position, even though the averaged SGS energy dissipation is exactly modeled due to the definition of the model coefficients (equation 3.18 and 3.19 of Chapter 3). This confirms that even though the eddy viscosity models show very low correlations in a priori test, they work adequately in actual simulations (Park 2005 [107]). This explains why eddy-viscosity models always prevail despite their deficiency of correlation, such as their bad predicting capacities for subgrid stress tensor τ_{ij} and SGS force f_i in the near wall region of a plane channel flow. In fact, subgrid scale models are mainly designed to drain total energy from resolved scales in large eddy simulations.

4.6. Conclusion

In this chapter, a priori analysis of SGS energy transfer and SGS energy dissipation have been investigated in plane channel flow at high Reynolds number ($Re_\tau = 950$). A strong inhomogeneity of subgrid scale kinetic energy is observed along wall normal position. An anisotropy of subgrid scale kinetic energy between streamwise and spanwise direction occurs in the near wall region. Consequently, two contrary net SGS energy transfer directions are differentiated by a frontier lying in the buffer layer. The back scatter energy cascade of the net SGS energy transfer occurs in the viscous and buffer layers. This behavior has not been reported in previous research, but it is endorsed by different filter width using both the two dimensional Lss-5^{th} and Gaussian filters. This back scatter is stronger in magnitude than the forward scatter which begins in the buffer layer until the channel center, as it's powered by approximately up to 85% of grid points experiencing back scatter in near wall region, whereas slightly more than 50% of grid points experience forward scatter in the outer region. Meanwhile, the net SGS energy dissipation exhibits a single direction of energy cascade from large to small scales at all wall normal position. The fraction of points experiencing back scatter of net SGS energy dissipation is less than 40%. The turbulent kinetic energy concentrated in small spanwise turbulent scale is not significantly reflected by the SGS energy dissipation. Analysis of turbulence coherent structures associated with interscale energy exchange in near wall region are expected to provide more information for a deeper analysis of plane channel flows at a comparable Reynolds number.

The coefficients of the classical Smagorinsky model, the Dynamic Smagorinsky model, the WALE model as well as the recent σ model are estimated a priori subsequently. In the outer region, the coefficients $\langle C_s \rangle$ and $\langle C_d \rangle$ are close to a constant, while the near wall behavior of $\langle C_s \rangle / \langle C_{so} \rangle$ is sensitive to the ratio of the filter width in streanwise and spanwise directions. The underestimation of $\langle C_d \rangle$ is dependent on the filter width and filter type. This underestimation can be remedied by a small test filter width in condition of using a Gaussian filter, but not a Lss-5^{th} filter. The coefficients $\langle C_w \rangle$ and $\langle C_\sigma \rangle$ are found to have quite similar behavior for a priori analysis of present channel flow. They are greatly dependent on the spanwise filter width $\overline{\Delta_z^+}$ along wall normal position, and are especially sensitive to large $\overline{\Delta_z^+}$ in near wall region due to both the SGS dissipation and the differential operator $\langle S_{ij}^d S_{ij}^d \rangle$ of the WALE model as well as the differential operator $\langle D_\sigma \rangle$ for the σ model. The present analysis indicates that a small spanwise filter width $\overline{\Delta_z^+} < 40$ is recommended in the near wall region for the WALE model and σ model for present flow.

Correlations between exact SGS tensor τ_{ij}, the SGS force f_i, the SGS energy dissipation ϵ_{sgs} and their counterparts modeled by the Smagorinsky model and the WALE model are assessed. There is no great difference globally between the predictive capabilities of subgrid scale models tested here for correctly predict the SGS tensor τ_{12} and its standard deviation along wall normal position. The WALE model has a better prediction than Smagorinsky model for both the mean and the standard deviations of τ_{12}, but only for the Lss-5^{th} filter. The eddy viscosity models can correctly dissipate the total energy from resolved scales despite its deficiencies observed in the present analysis. The results confirm some well established conclusions, such as the larger correlations with Gaussian filter compared to the sharp Lss-5^{th} filter or for larger filter width compared to smaller

filter width (Pope 2000 [116]). But, based on the three examined criteria, contradictions with the existing conclusions occur in the buffer layer. Therefore, more studies are needed to investigate this behavior in the near wall region of plane channel flow.

Chapter 5

Results for APG channel flow

5.1. Introduction

Recently, turbulent flows with an adverse pressure gradient as a challenge for large eddy simulation have drawn a lot of attention. Several LES have been conducted on such turbulence with different configurations (Elsner *et al.* 2009 [46]; Kuban *et al.* 2010 [69]; Kuban *et al.* 2012 [70]). This chapter is based on the examination of the statistics in the near-wall region of channel flow with a curved wall documented in Marquillie *et al.* 2011 [87] and Laval *et al.* 2012 [73]. Description of the database is presented in Section 3.5.2 of Chapter 3. At Reynolds number $Re_\tau = 617$, the flow slightly separates at the lower curved wall and is at the onset of separation at the upper wall. Therefore, two different configurations of pressure gradient as well as the effect of wall curvature can be investigated and compared.

The energy transfer mechanisms are first analyzed in converging-diverging region. A priori evaluations of model coefficients ($\langle C_s \rangle$ of the Smagorinsky model, $\langle C_d \rangle$ of Dynamic Smagorinsky model, $\langle C_w \rangle$ of the WALE model and $\langle C_\sigma \rangle$ of σ model) are subsequently performed. Important information of correlations between exact quantities and their counterparts modeled by the subgrid scale models, as well as their predictive capacities as eddy viscosity models are provided finally.

In practical implementation, the filtering and spacial derivation are two important procedures, which could influence the accuracy of results. Jordan 1999 [67] investigated the order that whether one should filter the full resolution equations before or after the coordinate transformation. Two procedures were considered for obtaining a LES curvilinear coordinate form. The first procedure filters the Cartesian coordinate system prior to its transformation. The order of operations respectively appears as:

NS (Cartesian) $\Rightarrow$ Filter $\Rightarrow$ LES (Cartesian) $\Rightarrow$ Transform $\Rightarrow$ LES (curvilinear)

An alternative progression to this path involves reversing the order of operations. This second derivation proceeds as:

NS (Cartesian) $\Rightarrow$ Transform $\Rightarrow$ NS (curvilinear) $\Rightarrow$ Filter $\Rightarrow$ LES (curvilinear)

such that the filter operation is now sensibly directed along the grid lines. To justify this latter choice, satisfaction of the commutative property is required between the filtering and the transformed form of the differentiation. No discernible differences were detected in the spectral energies of the turbulent fluctuations by filtering in either the physical

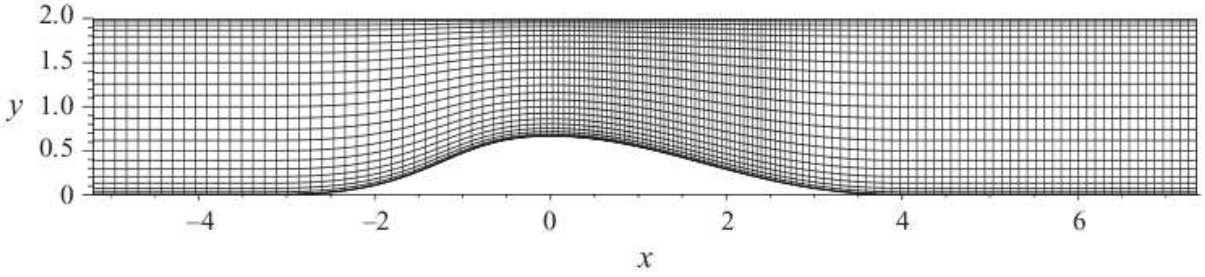

Figure 5.1: Computing grid in the (x, y) plane (every 16 meshes are plotted in each direction). The flow is coming from the left.

domain or the transformed space (Jordan 1999 [67]). As a preparatory a-priori analysis and in order to simplify the research, we adopt the first procedure which is a useful LES methodology for complex domains, without considering the variant of the subgrid stress tensor. The 2D filtering operation of both Lss-5^{th} and Gaussian filters are applied in Cartesian coordinate (x, z). Then, in order to take into account the complex geometry of the physical domain, the partial differential operators are transformed using the mapping that has the property of following a profile at the lower wall with a flat surface at the upper wall.

Wall units based on the friction velocity at summit of the bump $u_\tau^s = 0.0695$ are denoted with the superscript $+$, the reference wall units based on $u_\tau^o = 0.0494$ at the inlet have the superscript $\star$.

5.2. Choice of filter width

In order to analyze the effects of the filter width and filter type in the following a priori tests, the statistics are performed on three filter sets ($\overline{\Delta_x^+} = 50$, $\overline{\Delta_z^+} = 20$), ($\overline{\Delta_x^+} = 100$, $\overline{\Delta_z^+} = 40$) and ($\overline{\Delta_x^+} = 200$, $\overline{\Delta_z^+} = 80$) using both Lss-$5^{th}$ and Gaussian filters. The percentage of the averaged subgrid scale kinetic energy $\langle q_{sgs}^2 \rangle$ to the averaged turbulent kinetic energy $\langle q^2 \rangle$ are shown in Fig. 5.2. The 2D statistics of the latter is given in Fig. 3.14 of Chapter 3. Only few results with Gaussian filter are presented due to very similar behavior between both filter types.

The fraction of subgrid scale kinetic energy increases rapidly when increasing the filter width in the whole channel region, while $\langle q_{sgs}^2 \rangle / \langle q^2 \rangle$ is larger with Gaussian filter compared to Lss-5^{th} filter for the same filter width. This is in agreement with their behavior in plane channel flow (Fig. 4.2).

It should be noted that, in the diverging near wall regions, high fractions of SGS kinetic energy occur near the walls, at the same position as the two regions of strong turbulent kinetic energy (see Fig. 3.14). These fractions are stronger at the lower wall than at the upper wall, saliently for the larger filter width. For example, for the larger filter ($\overline{\Delta_x^+} = 200$, $\overline{\Delta_x^+} = 80$), the fraction $\langle q_{sgs}^2 \rangle / \langle q^2 \rangle$ reaches $80\% - 90\%$ near the lower wall. This region corresponds also to a high concentration of small scale vortices observed by Laval *et al.* 2012 [71], meaning that the large number of intense small vortices contain most of the subgrid turbulent kinetic energy in this region. Therefore, in order to resolve the energy-containing scales at best by large eddy simulation, the largest filter set ($\overline{\Delta_x^+} = 200$,

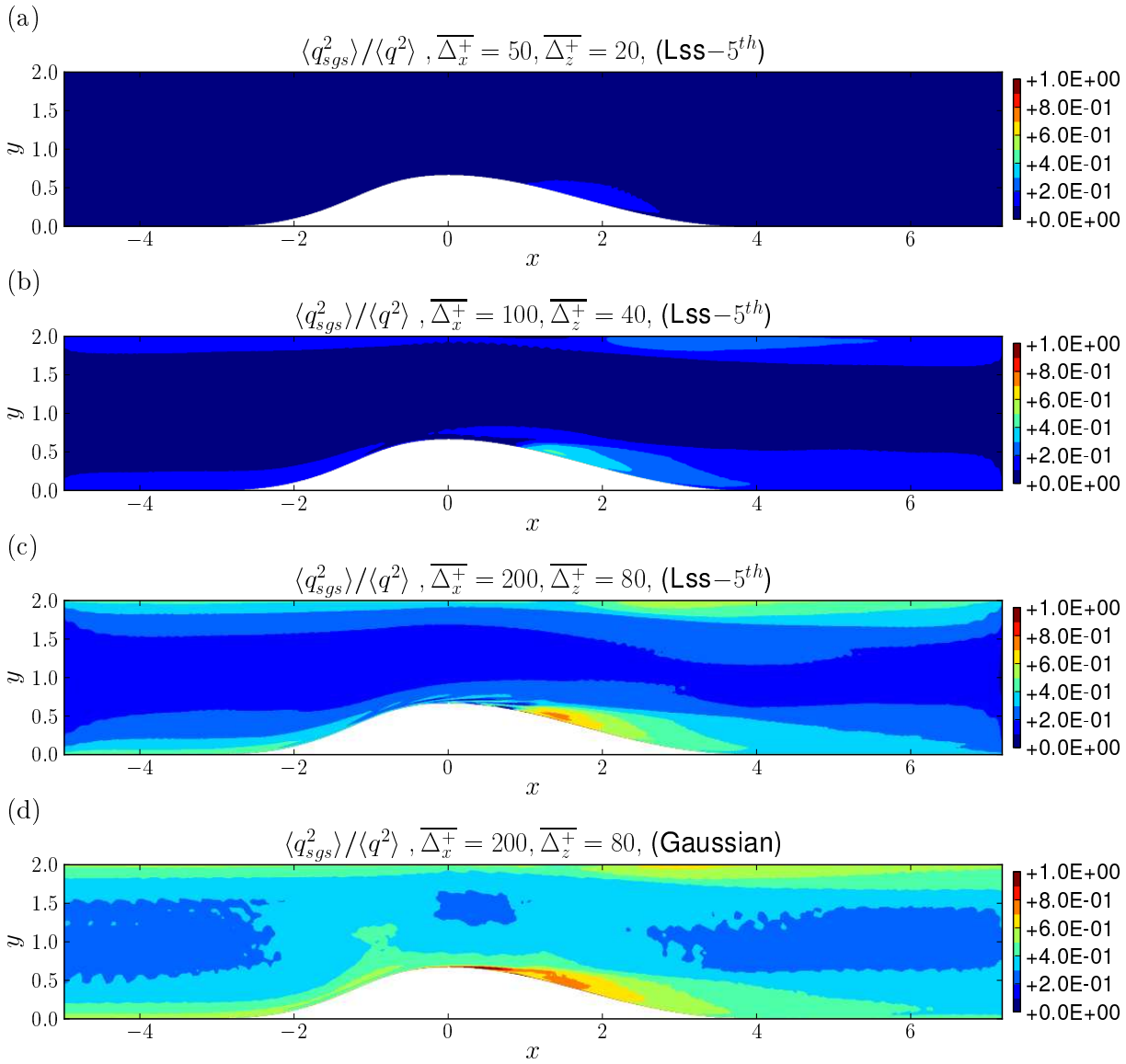

Figure 5.2: Fraction of subgrid scale kinetic energy $\langle q_{sgs}^2\rangle$ to the total turbulent kinetic energy $\langle q^2\rangle$ in x-y plane using the Lss-5^{th} and Gaussian filters.

$\overline{\Delta_z^+} = 80$) is probably too large to be recommended in diverging APG near wall region. However, the results with this large filter width are presented in order to show the trend of statistics, such as energy transfer with respect to filter width.

A more detailed analysis is given by 1D profiles of the fraction of subgrid scale kinetic energy along the two walls in the diverging region as shown in Fig. 5.3. Quite similar behavior at two walls are observed with Gaussian filter. At the lower wall, the fraction of $\langle q_{sgs}^2\rangle/\langle q^2\rangle$ is maximum at $x \simeq 1.3$, $20 < y^\star < 30$, whatever the filter width and filter type. This occurs roughly at the same streamwise and wall normal positions as the peak of turbulent kinetic energy (see Fig. 3.15(a)). Besides, the peak of $\langle q_{sgs}^2\rangle/\langle q^2\rangle$ at the upper wall occurs at $x \simeq 2.8$, $20 < y^\star < 40$, more downstream than the peak of turbulent kinetic energy (see Fig. 3.15(b)). Furthermore, the curves shape of $\langle q_{sgs}^2\rangle/\langle q^2\rangle$ in the near wall region of the upper wall (which corresponds to a weaker adverse pressure gradient) evolve similarly to that of the plane channel flow toward the wall (see Fig. 4.2).

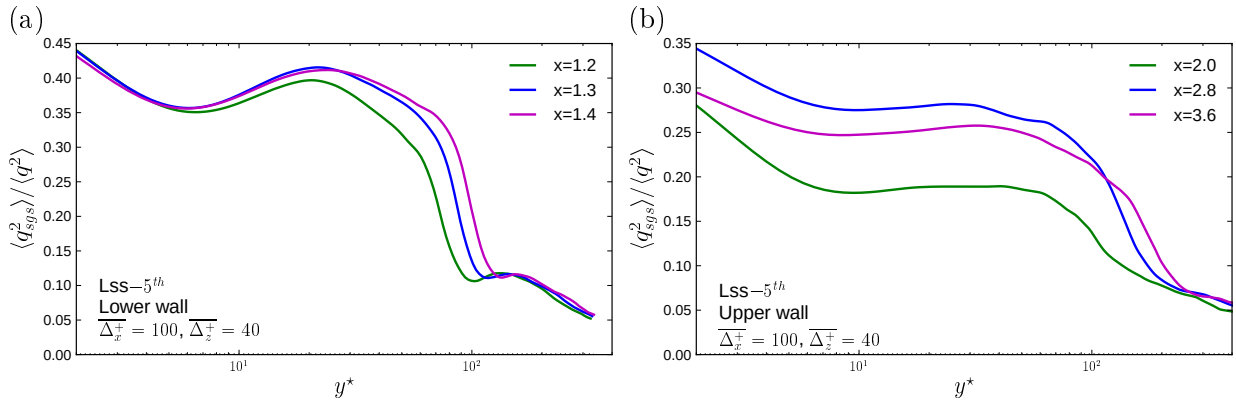

Figure 5.3: One-dimensional fraction of subgrid scale kinetic energy to the total turbulent kinetic energy at diverging lower wall (a) and flat upper wall (b) regions using Lss-5^{th} filter set ($\overline{\Delta_x^+} = 100$, $\overline{\Delta_z^+} = 40$).

5.3. Energy transfer mechanism

The stability analysis of the same flow has been investigated by Marquillie *et al.* 2011 [87] who found that the instability onset of low-speed streaks coincide with the strong production peaks of turbulent kinetic energy near the maximum of pressure gradient on both the curved and the flat walls. Laval *et al.* 2012 [73] reported that this adverse-pressure gradient turbulent flow is characterized by strong peaks of turbulent kinetic energy at both walls, as a consequence of the breakdown of more organized flow structures. However, the SGS energy transfer mechanism in APG turbulent boundary layer has found less attention. Here, we aim at assessing SGS energy transfer and SGS energy dissipation with different filter width using both Lss-5^{th} and Gaussian filters, to make progress in understanding the physics of such flows in order to improve statistical models for such turbulence.

5.3.1. SGS energy transfer

The SGS energy transfer in the x-y plane with three filter sets using Lss-5^{th} filter and Gaussian filter are given in Fig. 5.4. The energy transfer direction is defined the same way as in Section 4.3 of Chapter 4. The longitudinal oscillations appearing as bands through the channel center are due to the fact that the flow structures are strongly correlated in space and time. A good convergence of statistics would require more non-correlated fields which are not affordable for such DNS at large Reynolds number. The narrow white strips with Lss-5^{th} filter or the small white dots with Gaussian filter through the channel center are due to the statistics which are not perfectly converged, but they do not affect the analysis of the results. The statistics are more converged with Gaussian filter than Lss-5^{th} filter which shows more oscillations in physical space due to its strong sharpness (see Fig. 3.6).

On average, the turbulent energy is transfered from large to small scales ($\langle T_{sgs} \rangle > 0$) for most regions and this transfer is gradually reducing in magnitude toward the channel center. This behavior is obtained because the positive contribution $\langle T_{sgs}^+ \rangle$ is larger in magnitude than the negative one $\langle T_{sgs}^- \rangle$ through the whole region as shown in Fig. 5.5.

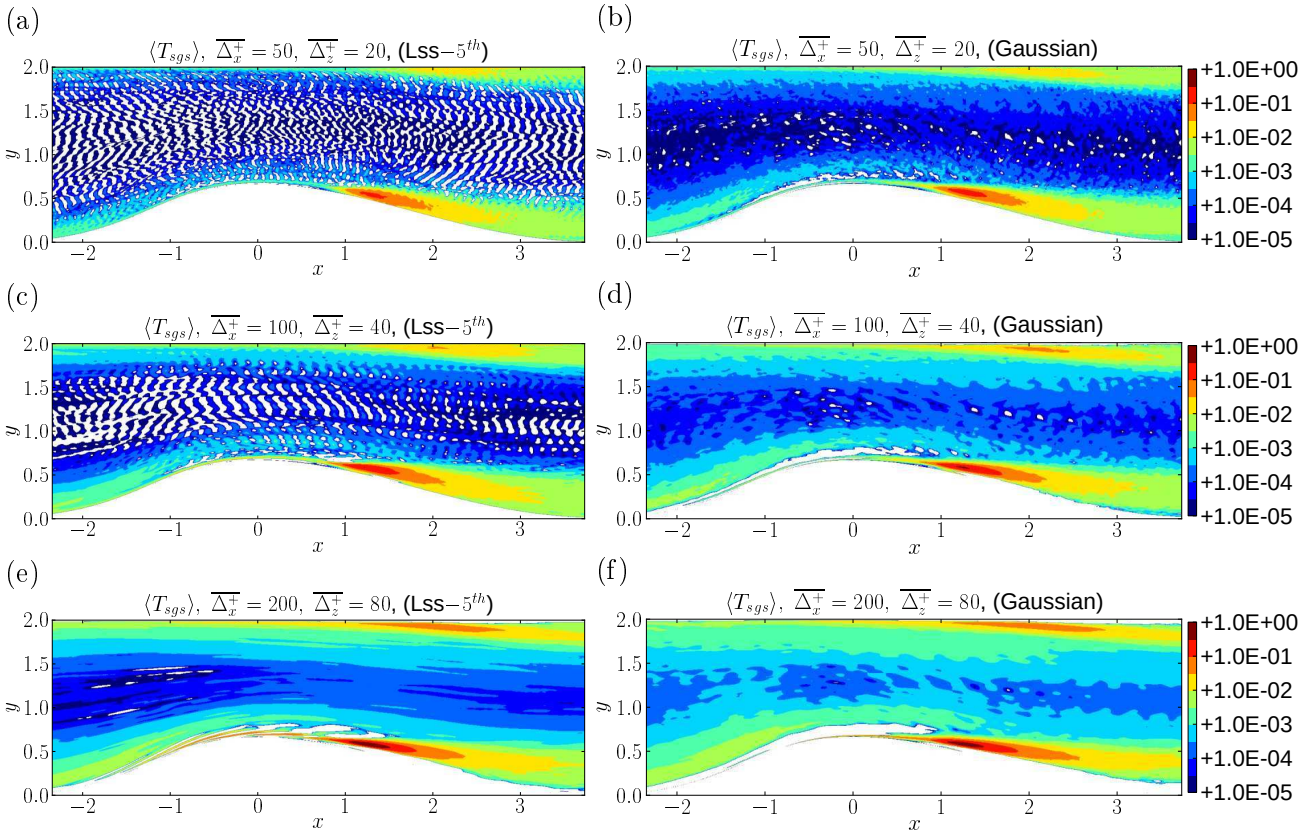

Figure 5.4: SGS energy transfer $\langle T_{sgs}\rangle$ with three filter widths in converging-diverging channel regions using Lss-5^{th} (a, c, e) and Gaussian (b, d, f) filters.

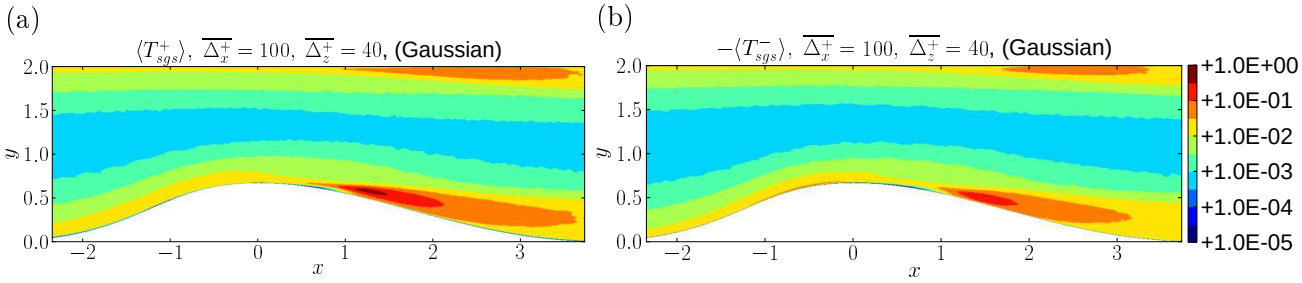

Figure 5.5: Positive (a) and negative (b) contributions of SGS energy transfer with the Gaussian filter set at $\overline{\Delta_x^+}=100$, $\overline{\Delta_z^+}=40$.

This is the same for all filter widths using both Lss-5^{th} and Gaussian filters. The number of points experiencing back scatter in most region is in general less than 50% (see Fig. 5.6), especially with the Gaussian filter. The enlarged views of $\langle T_{sgs}\rangle$, $\langle T^+_{sgs}\rangle$ and $\langle T^-_{sgs}\rangle$, as well as $P(T_{sgs}<0)$ near the two walls mostly in the diverging APG region are given in Fig. B.2-B.5 in Appendix B.

Two strong forward scatter regions appear in the APG region beginning at $x\simeq 0.8$ at the lower wall, and slightly more downstream at the upper wall (Fig. 5.4) and they are more intense for larger filter width. Two intense regions also occur at both the positive contribution $\langle T^+_{sgs}\rangle$, and the negative one $\langle T^-_{sgs}\rangle$ (see Fig. 5.5). $\langle T^+_{sgs}\rangle$ is more stronger than $\langle T^-_{sgs}\rangle$ in diverging APG near wall regions They are powered by two strong

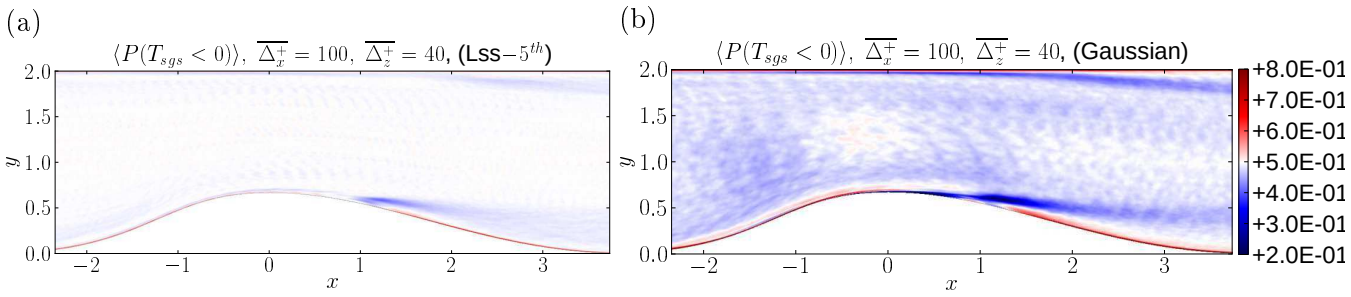

Figure 5.6: Fraction of points experiencing back scatter of SGS energy transfer using the Lss-5^{th} (a) and Gaussian (b) filter set at $\overline{\Delta_x^+}=100$, $\overline{\Delta_z^+}=40$.

elongated regions of the fraction of points experincing forward scatter ($> 50\%$) of SGS energy transfer (dark blue regions) near the two walls as illustrated in Fig. 5.6. Near the lower wall, Marquillie *et al.* 2011 [87] observed that, the turbulent streaks break down at $x = 0.78$ where a hairpin-type streamwise vortex emerge. Thus, the strong forward scatter of net SGS energy transfer is caused by the intense production of vortices.

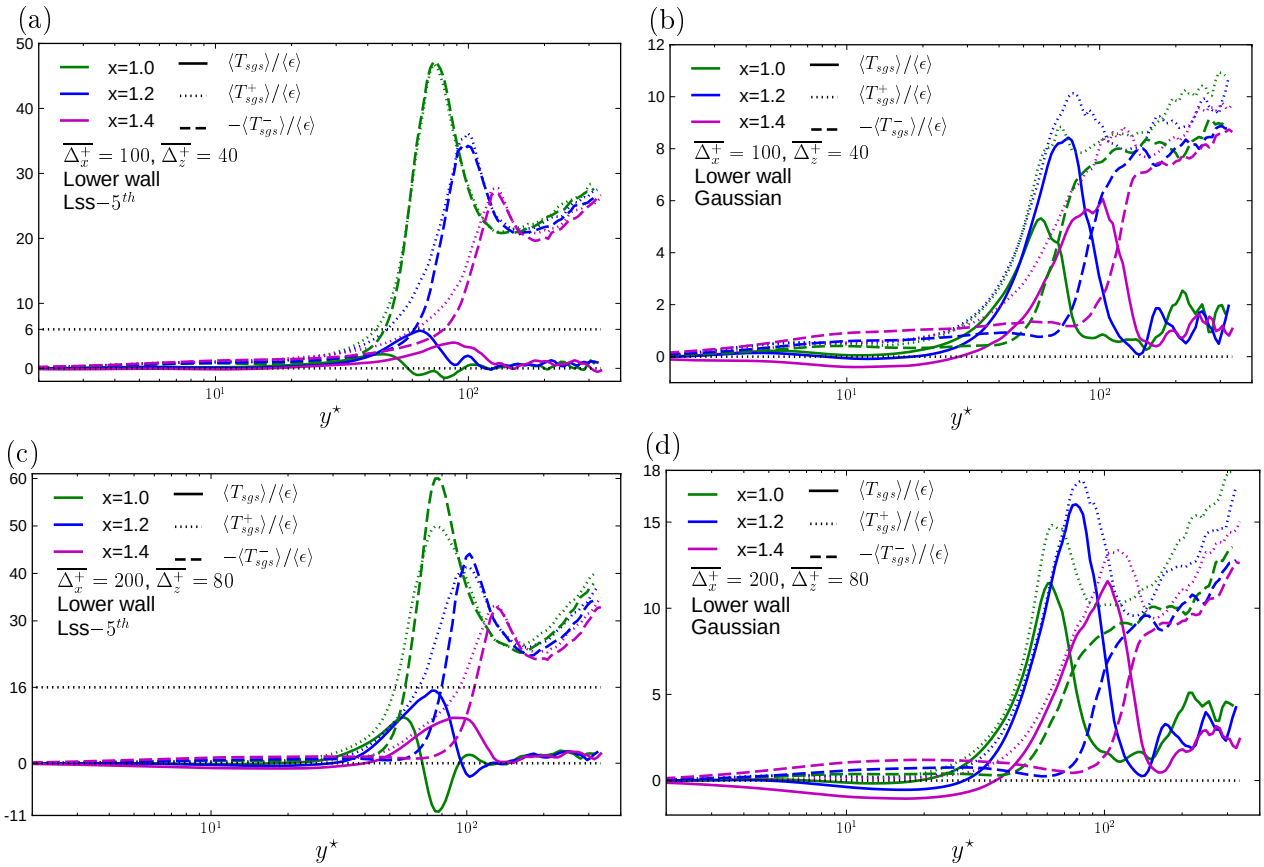

Figure 5.7: One-dimensional profiles of forward scatter of net SGS energy transfer in the diverging APG region at the lower wall, including the average of its positive and negative contributions, using Lss-5^{th} (a, c) and Gaussian filter (b, d). Statistics are normalized by the rate of kinetic energy dissipation.

The thin white band close to the wall of the bump in the converging region or along the two wall edges in APG diverging region for large filter width (Fig. 5.4(d), 5.4(e) ,

5.4(f)) is slightly negative, indicating a weak backscatter, due to a significantly negative contribution $\langle T_{sgs}^{-} \rangle$ in the same region (see Fig. 5.5(b)). Accordingly, a thin layer with high fraction of points ($> 50\%$, red region) experiencing back scatter of SGS energy transfer is visible along the edge of the bump and edges of the two walls in APG diverging region as shown in Fig. 5.6. For the same filter width, the fraction of back scatter (red region in Fig. 5.5) is more intense with Gaussian filter than Lss-5^{th} filter, corresponding to the larger region of backscatter with the Gaussian filter (see Fig. 5.4).

In order to investigate in detail the regions of large net SGS energy transfer, one-dimensional analysis at the lower wall are displayed in Fig. 5.7. Although the region of forward scatter becomes larger as increasing the filter width, the maximum of forward scatter always appears near $x = 1.2$, and $60 < y^{\star} < 70$, independently of the filter width and type. This corresponds to the same streamwise position of turbulent kinetic energy peak (see Fig. 3.15(a) of Chapter 3) and the peak of fraction of subgrid scale kinetic energy (see Fig. 5.3(a)), but more distant from the wall than the other two peaks.

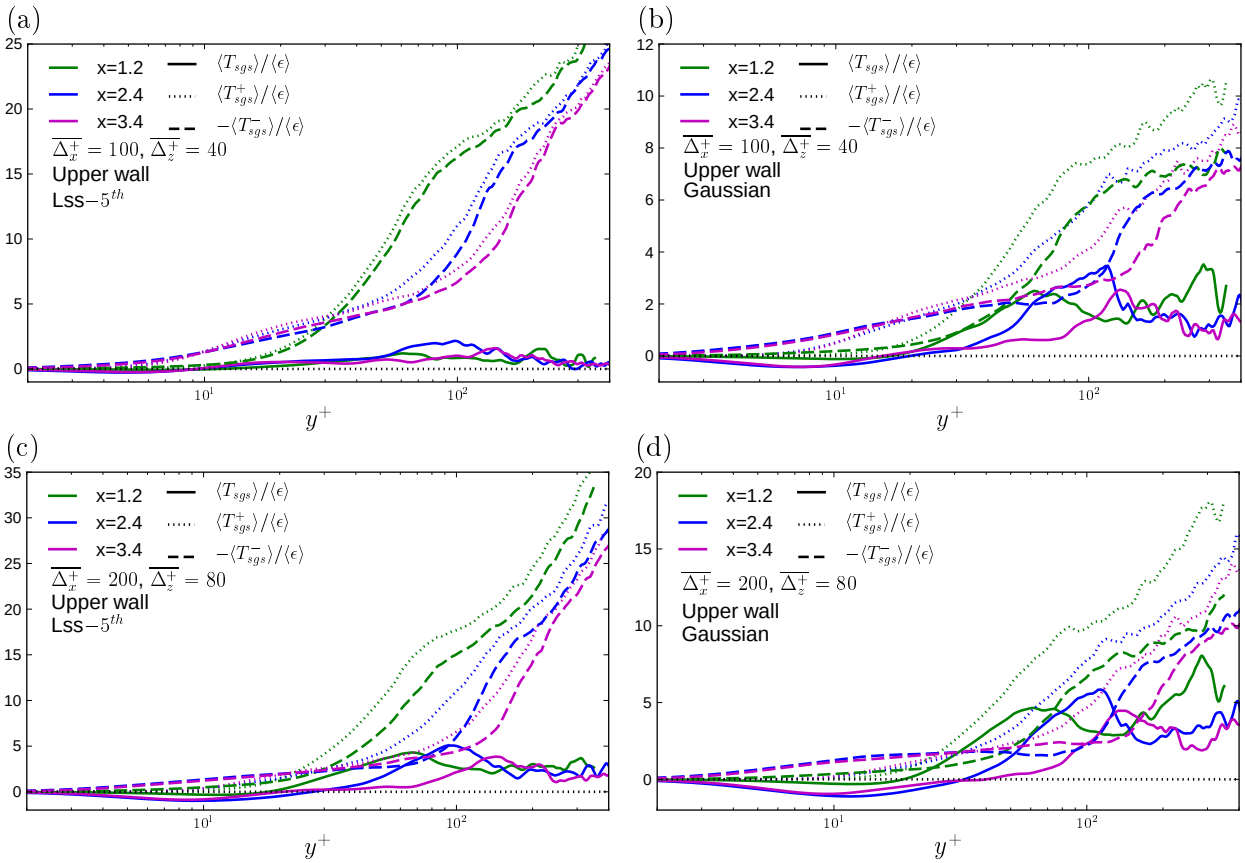

Figure 5.8: One-dimensional profiles of forward scatter of net SGS energy transfer in the diverging APG region at the upper wall, including the average of its positive and negative contributions using Lss-5^{th} (a, c) and Gaussian filter (b, d). Statistics are normalized by the rate of kinetic energy dissipation.

Furthermore, in Fig 5.7, both contributions $\langle T_{sgs}^{+} \rangle$ and $\langle T_{sgs}^{-} \rangle$ are significantly larger than the net SGS energy transfer $\langle T_{sgs} \rangle$ with Lss-5^{th} filter, while $\langle T_{sgs} \rangle$ is comparable to its two contributions with the Gaussian filter. This corresponds to a lower number of points experiencing back scatter than with Lss-5^{th} filter (see Fig. 5.6). A similar behavior

between filter type also occurs in the plane channel flow (see Fig. 4.3(a), and Fig. A.1 in Appendix A). The large magnitudes of both positive and negative contributions with Lss-5^{th} filter decrease continuously as moving downstream. This is due to the fact that the Lss-5^{th} filter is sharper than the Gaussian filter and introduces more oscillations. These oscillations become more significant when derivative operation is performed on the filtered quantities for the SGS energy transfer contributions and these are more salient than in plane channel flow (see Fig. 4.5(b)), because most vortices are much smaller than the filter width in diverging APG near wall regions. Furthermore, it should be noted that, contrary to their behavior in plane channel flow, the intense positive and negative contributions with Lss-5^{th} filter occur in a limited range $40 < y^\star < 200$. However, the large values of the averaged negative contribution with Gaussian filter are shifted toward larger $y^\star$ with respect to the positive one. Therefore, the peak position of both positive and negative contributions are largely dependent on the filter type.

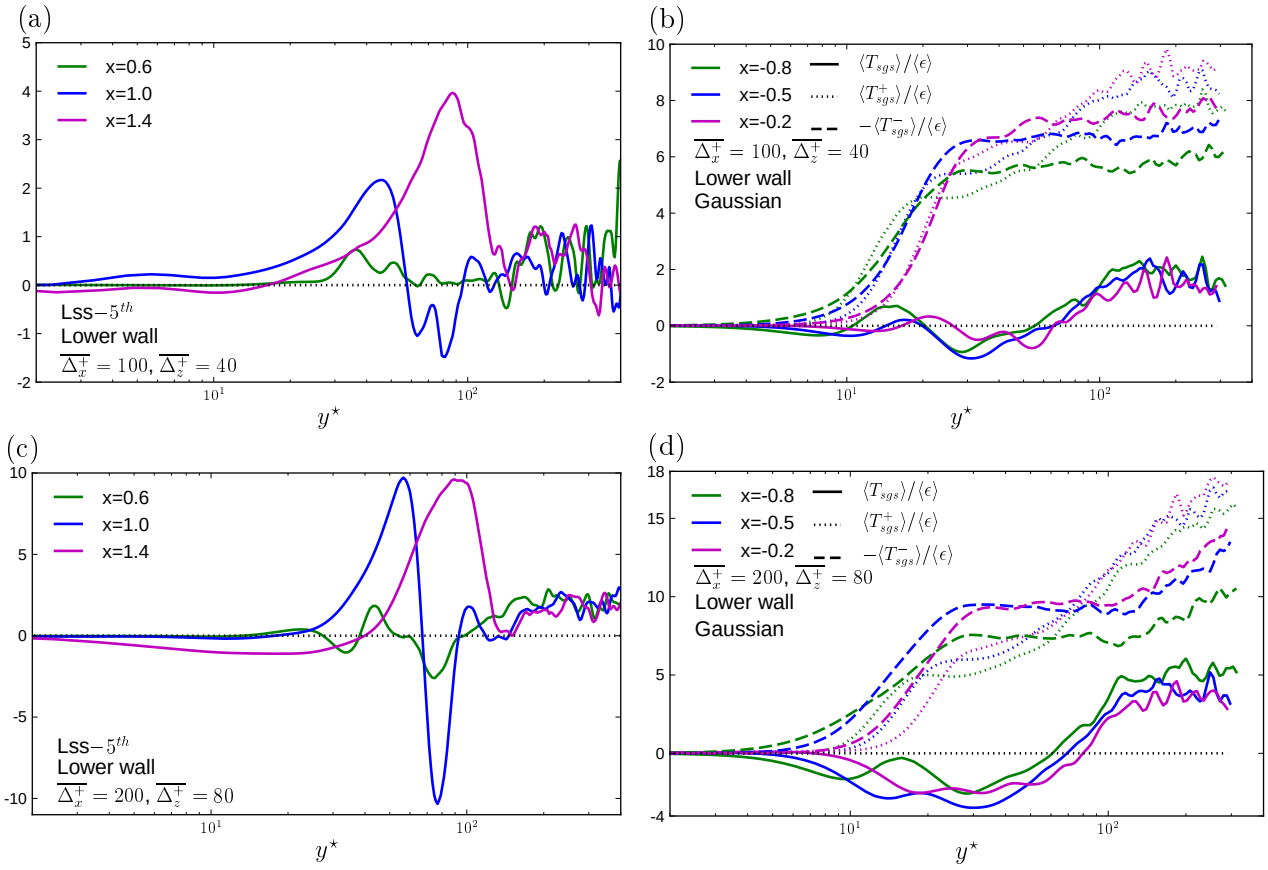

Figure 5.9: One-dimensional profiles of back scatter of net SGS energy transfer in the converging and diverging regions using Lss-5^{th} (a, c) and Gaussian (b, d) filters. Statistics are normalized by the rate of kinetic energy dissipation.

Fig. 5.7 also show that, weak back scatter with Gaussian filter occurs in the range $y^\star < 30$, but it is not discernable with Lss-5^{th} filter in the same range. However, significant back scatter appear for large filter width with Lss-5^{th} filter (see Fig. 5.7(c)), in the range $70 < y^\star < 80$. It is stronger than in plane channel flow for the same filter set (see Fig. 4.5(a)). These are consistent with net SGS energy transfer (see Fig. 5.4) and the fraction of points experiencing back scatter of $\langle T_{sgs}\rangle$ (see Fig. 5.6). A detail analysis of

back scatter regions is given later.

One-dimensional profile of forward scatter of net SGS energy transfer in the APG upper wall region is shown in Fig. 5.8. In this region, one can observe that, the larger the filter width, the larger the magnitude of net $\langle T_{sgs} \rangle$. The peak of forward scatter of net SGS energy transfer occurs at $x \simeq 2.4$, independently of the filter width and filter type. This is more downstream than the peak of turbulent kinetic energy (see Fig. 3.15(b)), but more upstream than the peak of fraction of subgrid scale kinetic energy (see Fig. 5.3(b)). Thus, at the diverging upper wall, the forward cascade is less correlated to the turbulent kinetic energy (see Fig. 3.15(b)) or the fraction of subgrid scale kinetic energy. Contrary to what was observed at lower wall, the influence of Lss-5^{th} filter on the magnitude of $\langle T^+_{sgs} \rangle$ and $\langle T^-_{sgs} \rangle$ is weaker at the upper wall. Furthermore, similarly to the plane channel flow (Fig. 4.3(a)), both $\langle T^+_{sgs} \rangle$ and $\langle T^-_{sgs} \rangle$ monotonically increase toward the channel center at the upper wall (which is experiencing a weaker adverse pressure gradient and no curvature compared to the lower wall). Nevertheless, back scatter is also observed for $y^\star < 30$ with large filter width (see Fig. 5.8(b)-5.8(d)), but more downstream than for the lower wall.

Finally, one-dimensional analysis of back scatter of net SGS energy transfer is given in Fig. 5.9. Both the streamwise and normal positions of back scatter peak is greatly dependent on the filter type, but independent on the filter width, despite the larger magnitude of back scatter cascade for the larger filter width. With Gaussian filter, the maximum of the back scatter of $\langle T_{sgs} \rangle$ occurs in the converging favorable pressure gradient region at $x = -0.5$, $y^\star \sim 30$. This is roughly the same streamwise position as the maximum skin friction (see Fig. 3.13 of Chapter 3). However, with Lss-5^{th} filter, the peak of back scatter is largely downstream to the diverging APG region at $x \simeq 1.0$, $70 < y^\star < 90$, near to the streamwise position of the peak of turbulent kinetic energy and peak of fraction of subgrid scale kinetic energy. Furthermore, in the near wall region, statistics with Gaussian filter evolves similarly to what has been observed for the plane channel flow as moving away from the wall (see Fig. 4.3(a)). However, the back scatter cascade is stronger and the frontier seperating the forward and backward scatter of $\langle T_{sgs} \rangle$ is further from the wall ($60 < y^\star < 80$), compared to the plane channel flow. Similarly to the forward scatter cascade of $\langle T_{sgs} \rangle$ in the diverging APG upper wall region, the magnitude of back scatter cascade of net SGS energy transfer is comparable for both filter types.

5.3.2. SGS energy dissipation

In this Section, the a priori analysis of net SGS energy dissipation and its positive and negative contributions are performed on the same filter set as in the above analysis of SGS energy transfer. The definitions of SGS energy dissipation and its positive and negative contributions are given in Section 4.3.2 of Chapter 4.

SGS energy dissipation $\langle \epsilon_{sgs} \rangle$ with three filter widths using both Lss-5^{th} and Gaussian filters are given in Fig. 5.10. As the SGS energy dissipation requires no derivative of filtered quantities, the results with both filter types are smoother than for $\langle T_{sgs} \rangle$. In most region, the net SGS energy dissipation is negative on average (meaning that the kinetic energy is extracted from large scales), since the negative contribution $\langle \epsilon^-_{sgs} \rangle$ is larger in magnitude than the positive one $\langle \epsilon^+_{sgs} \rangle$ independently of filter width and filter type as shown in Fig. 5.11. Accordingly, the fraction of points experiencing back scatter is in

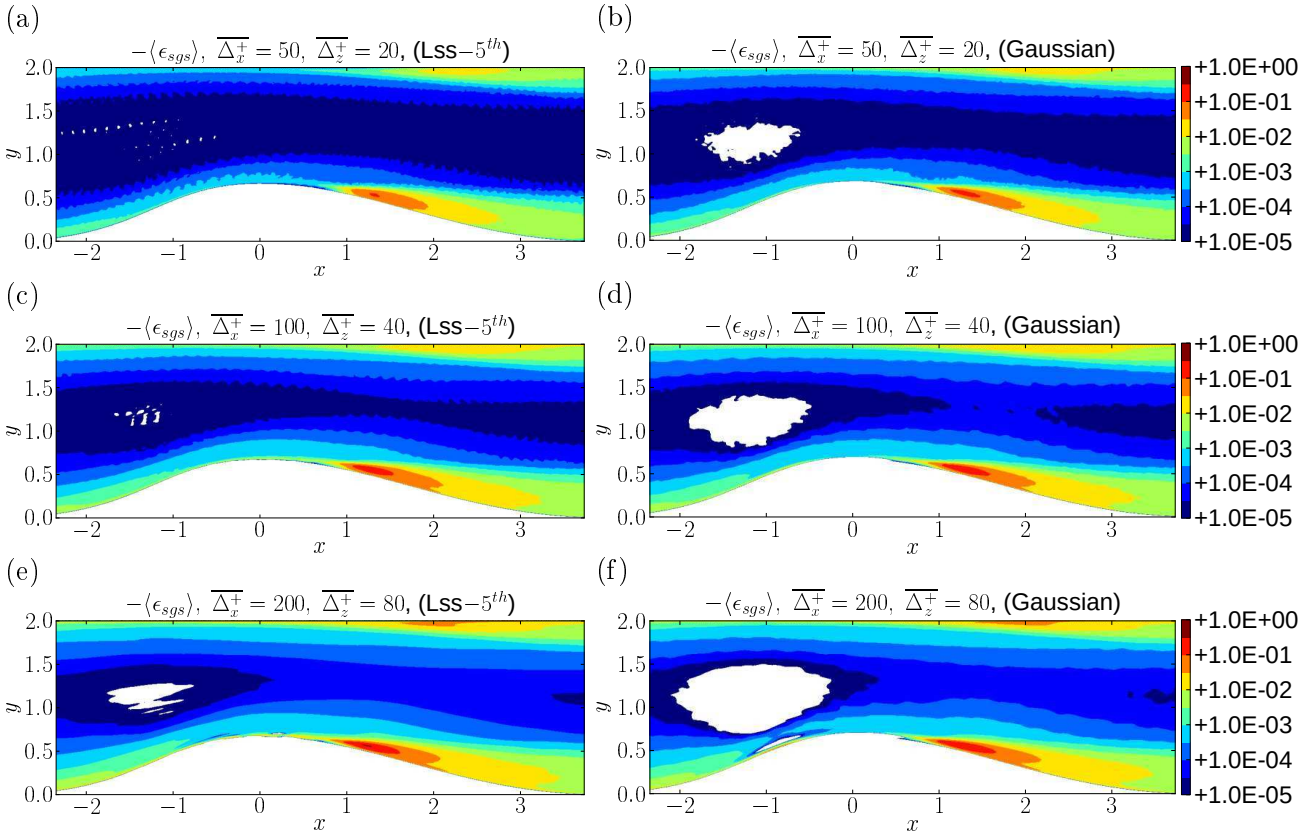

Figure 5.10: SGS energy dissipation $\langle\epsilon_{sgs}\rangle$ with three filter widths in converging-diverging channel regions using Lss-5^{th} (a, c, e) and Gaussian (b, d, f) filters.

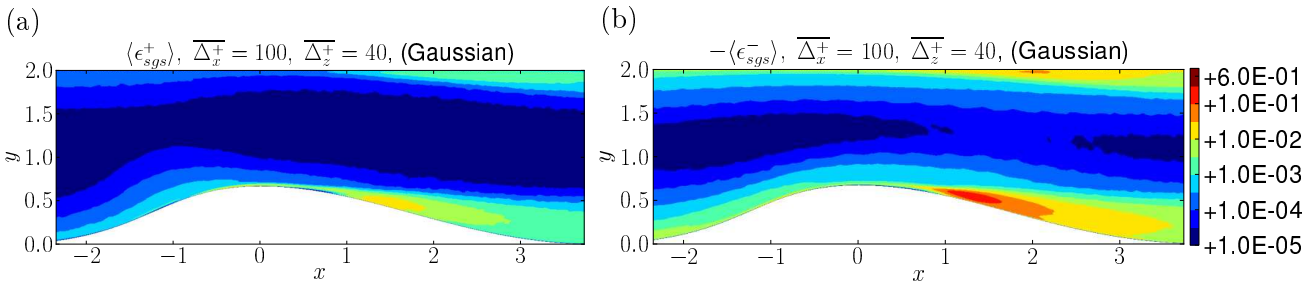

Figure 5.11: Positive (a) and negative (b) contributions of SGS energy dissipation with the Gaussian filter set at $\overline{\Delta_x^+}=100$, $\overline{\Delta_z^+}=40$.

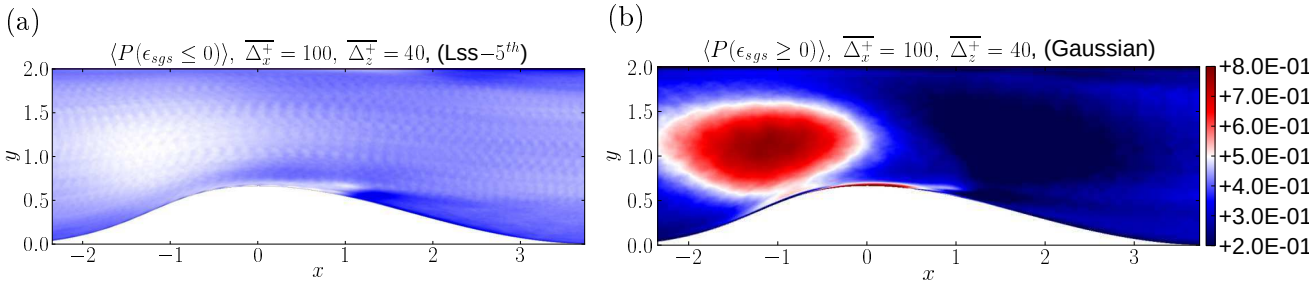

Figure 5.12: Fraction of points experiencing back scatter of SGS energy dissipation with the Lss-5^{th} (a) and Gaussian (b) filter set at $\overline{\Delta_x^+}=100$, $\overline{\Delta_z^+}=40$.

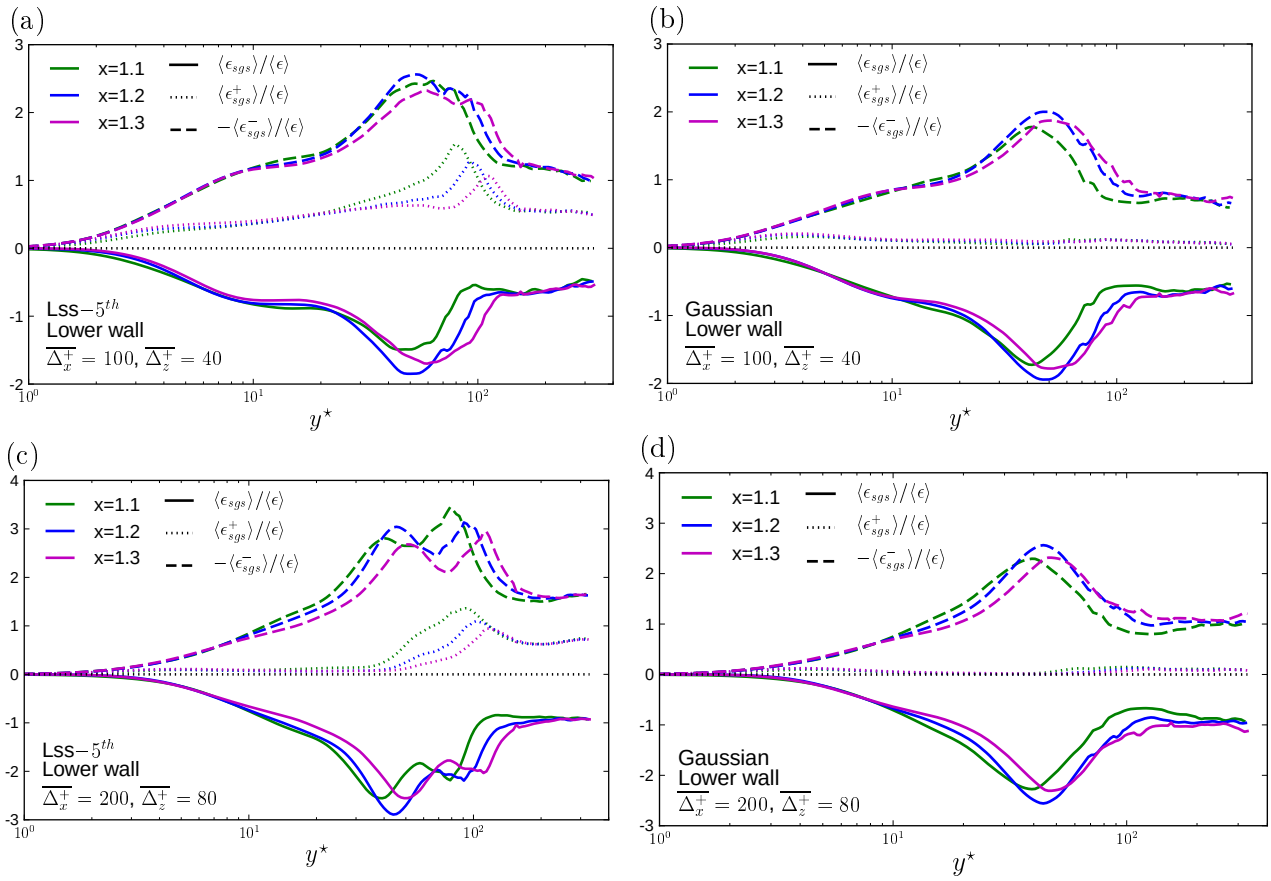

Figure 5.13: One-dimensional profiles of intensive forward scatter of net SGS energy dissipation in the diverging APG region at the lower wall, including the average of its positive and negative contributions using Lss-5^{th} (a, c) and Gaussian filter (b, d). Statistics are normalized by the rate of kinetic energy dissipation.

most regions less than 50%, especially with Gaussian filter as given in Fig. 5.12.

Moreover, two regions of strong negative SGS energy dissipation occur close to the two walls in the diverging APG region. These regions become stronger when increasing the filter width due to the larger fraction of subgrid scale kinetic energy for larger filter width in the same region (see Fig. 5.2). Accordingly, two stronger regions occur on the negative contribution $\langle\epsilon^-_{sgs}\rangle$ compared to the positive contribution $\langle\epsilon^+_{sgs}\rangle$ in the near wall regions of the diverging part as illustrated in Fig. 5.11. These correspond to two dark blue regions with $P(\epsilon_{sgs} \leq 0) < 0.5$ in Fig. 5.12, which are more pronounced for Lss-5^{th} filter. Furthermore, these forward cascade regions becomes more intense for larger filter width at the two walls for both filter types.

Large regions of back scatter occur in the center of the converging favorable pressure gradient region and also slightly above the edge of the bump just before the summit, more salient with the Gaussian filter. This back scatter of net $\langle\epsilon_{sgs}\rangle$ is not observed in plane channel flow (see Fig. 4.8(a)). Its occurence is owing to the negative contribution $\langle\epsilon^-_{sgs}\rangle$ is lower than the positive one $\langle\epsilon^+_{sgs}\rangle$ in the center of the converging region (see Fig. 5.11). It is important to note that, as shown in Fig. 5.12, the high fraction of points experiencing back scatter of dissipation with Gaussian filter (red-white region, up to 80%) does not imply a more intensive back scatter magnitude than Lss-5^{th} filter which corresponds to

a white region (slightly more than 50%) in the center of converging favorable pressure gradient region and along the edge of the bump. Moreover, these back scatter become stronger when increasing the filter width, but still weaker than most of forward scatter of net $\langle \epsilon_{sgs} \rangle$ for both Lss-5^{th} and Gaussian filters (see Fig. B.1 of Appendix B).

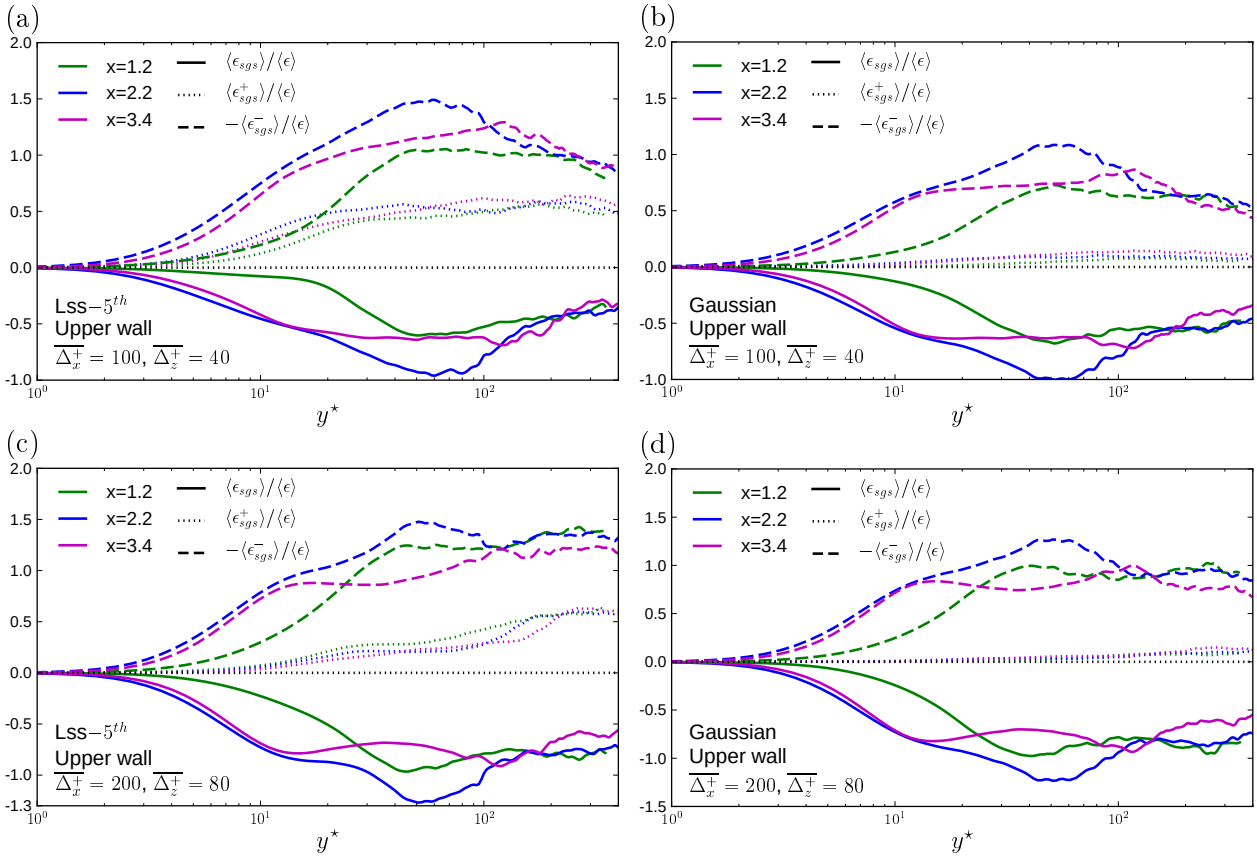

Figure 5.14: One-dimensional profiles of forward scatter of net SGS energy dissipation in the diverging APG upper wall region, including the positive and negative contributions using Lss-5^{th} (a, c) and Gaussian filter (b, d). Statistics are normalized by the rate of kinetic energy dissipation.

So as to inspect these intensive regions of both forward and back ward scatters, one-dimensional analysis of net SGS energy dissipation and its positive and negative contributions at the lower wall in the diverging APG region are given in Fig. 5.13. The maximum of net SGS energy dissipation occur at $x = 1.2$, $40 < y^\star < 60$, no matter what the filter width and filter type are. This is the same streamwise position as the peaks of turbulent kinetic energy (see Fig. 3.15(a) of Chapter 3) and the fraction of subgrid scale kinetic energy (see Fig. 5.3), but slightly further from the wall than the peak of turbulent kinetic energy. It also corresponds to the streamwise position of the peak of net SGS energy transfer in diverging APG lower wall region (see Fig. 5.7), but closer to the wall.

However, as moving away from the wall, evolutions of $\langle \epsilon^+_{sgs} \rangle$ and $\langle \epsilon^-_{sgs} \rangle$, as well as the net $\langle \epsilon_{sgs} \rangle$ are quite different from those of the plane channel flow (see Fig. 4.8(a)), as the shapes of these curves are very sensitive to the filter type. It should be noted that, a weak peak of the positive contribution $\langle \epsilon^+_{sgs} \rangle$ appears near $y^\star \simeq 4$ for all filter sets examined here, with marginal influence on the net SGS energy dissipation. Then, as moving away from the wall, a second peak of $\langle \epsilon^+_{sgs} \rangle$ occurs near $70 < y^\star < 100$, more pronounced than the

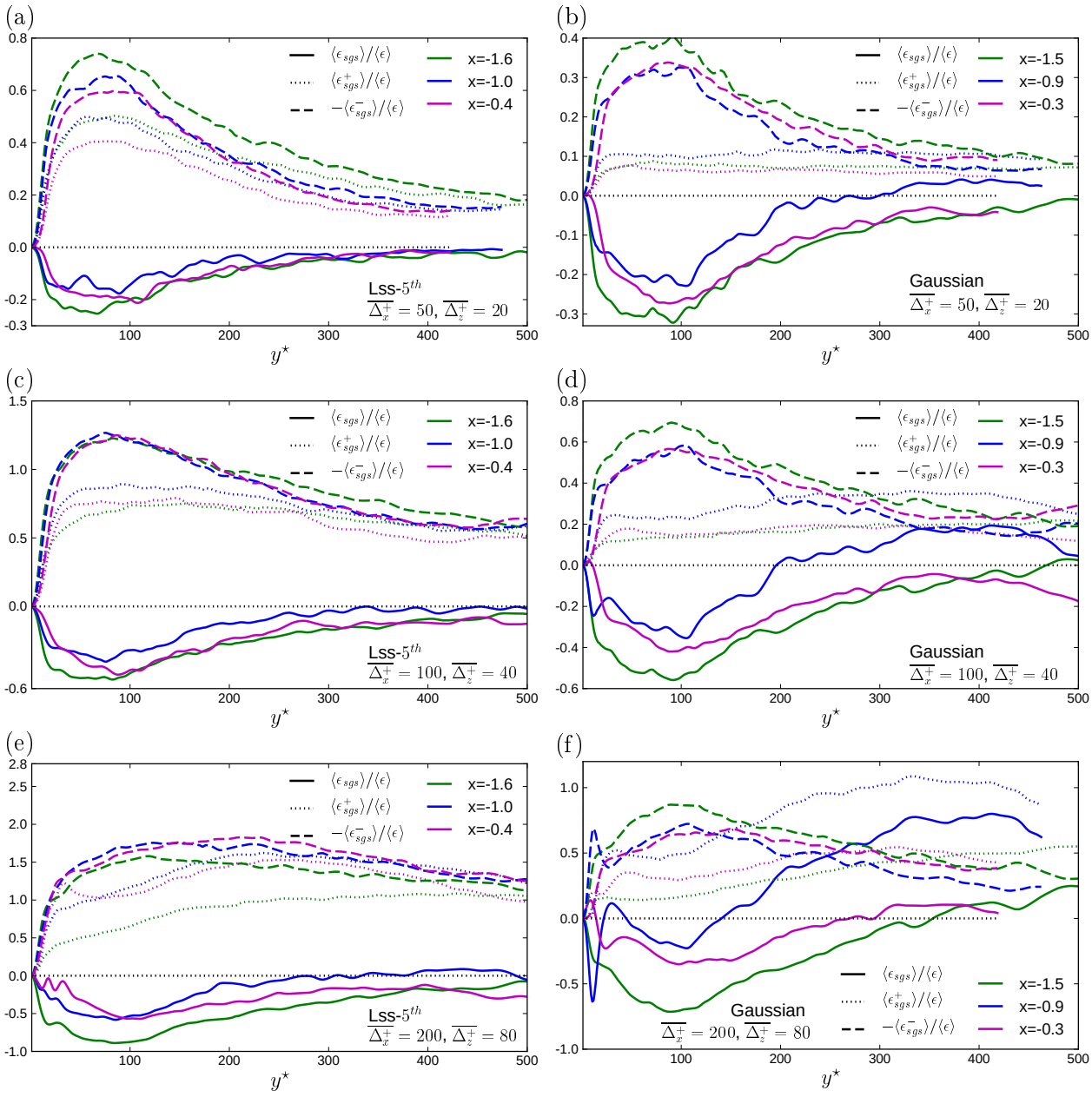

Figure 5.15: One-dimensional profiles of back scatter of net SGS energy dissipation in the converging-diverging channel region with respect to the lower wall, including the average of its positive and negative contributions using Lss-5th (a, c, e) and Gaussian filter (b, d, f). Statistics are normalized by the rate of kinetic energy dissipation.

first peak, and more salient with Lss-5th filter compared to Gaussian filter. Furthermore, the onset of sharp increase of $\langle\epsilon^+_{sgs}\rangle$ near its second peak contributes to the peak of net $\langle\epsilon^+_{sgs}\rangle$ in the range $40 < y^\star < 60$. Contrary to the significantly high magnitude of SGS energy transfer contributions $\langle T^+_{sgs}\rangle$ and $\langle T^-_{sgs}\rangle$, the positive and negative contributions of SGS energy dissipation are comparable for both filter types. Moreover, contrary to the other intense forward and backward cascade of SGS energy transfer (see Fig. 5.7, 5.8 and 5.9), the magnitude of forward scatter of net $\langle\epsilon_{sgs}\rangle$ is also slightly dependent on the filter width.

One-dimensional analysis of forward scatter of net SGS energy dissipation in the diverging APG upper wall region is shown in Fig. 5.14. In comparision to the lower wall region, the evolutions of all contributions are more similar to the statistics in plane channel flow (see Fig. 4.8(a)) toward the channel center. The magnitude of the net $\langle \epsilon_{sgs} \rangle$ is also slightly dependent on the filter width as in the diverging lower wall region. However, the peak of net SGS energy dissipation always occurs at $x \simeq 2.2$, $40 < y^\star < 70$. This is roughly the same streamwise position as the peak of turbulent kinetic energy in the diverging upper wall region (see Fig. 3.15(b)), while it is more upstream than the streamwise position of the peak of subgrid scale kinetic energy at the upper wall (see Fig. 5.3(b)). But this peak is further from the wall than the peaks of turbulent kinetic energy and fraction of subgrid scale kinetic energy. Therefore, at the upper wall, the forward cascade of net SGS energy dissipation is strongly correlated to the turbulent kinetic energy, but not related to the fraction of subgrid scale kinetic energy.

One-dimensional analysis of back scatter of net SGS energy dissipation and its positive and negative contributions in the converging favorable pressure gradient region are shown in Fig. 5.15. The magnitude of back scatter is largely dependent of the filter width and filter type. This back scatter appears in the channel center only for the large Lss-5^{th} filter width ($\overline{\Delta_x^+} = 200$, $\overline{\Delta_z^+} = 80$), while it is obvious for all the three Gaussian filter sets, and larger in magnitude for larger filter widths. The peak of back scatter with Gaussian filter happens distinctly at $x \simeq -0.9$, $y^\star > 400$, slightly more upstream than the streamwise position of the maximum of skin friction (see Fig. 3.13 of Chapter 3).

5.3.3. Conclusion

The results of the a priori analysis in a converging-diverging channel regions show that, the forward scatter of SGS energy transfer and SGS energy dissipation are closely correlated to the turbulent kinetic energy in the diverging APG region due to the strong adverse pressure gradient and the presence of curvature. The fraction of subgrid scale kinetic energy, the net SGS energy transfer and net SGS energy dissipation reach their maxima exactly at the same streamwise position as the peak of turbulent kinetic energy at the lower wall, independently of the filter width and filter type. It's interesting that, intense back scatter of SGS energy dissipation occurs in the converging channel center, which is absent in plane channel flow. The peak of this back scatter is slightly more upstream than the peak of skin friction, and its magnitude is greatly dependent on the filter width and filter type. However, the streamwise position of the peak of SGS energy back scatter is greatly dependent on the filter type, located near the maximum of skin friction with the Gaussian filter. Finally, it should be noted that, the influence of the sharpness of the Lss-5^{th} filter is larger for the positive and negative SGS energy transfer than for the contributions of the SGS energy dissipation, for the present channel flow with a curved wall compared to the plane channel flow.

5.4. A priori evaluation of model coefficients

The assessments of the role of the model coefficients has been investigated by Kuban *et al.* 2012 [70] on the same geometry as in the present study at two Reynolds numbers $Re_\tau = 395$ and $Re_\tau = 617$. It was shown that, in addition to the influence of numerical procedure, the mesh size is significantly important for a good quality of the LES solution. They also reported that, in some cases, the effect of the choice of subgrid scale model is larger than the effect of the mesh. However, to the best of our knowledge, no a priori tests of subgrid scale models have been performed on wall turbulence with adverse pressure gradient.

In the present a priori analysis, coefficients of the Smagorinsky model, dynamic Smagorinsky model, WALE model and σ model are evaluated on a channel flow with adverse pressure gradient at $Re_\tau = 617$. The definitions of the terms investigated in the a priori analysis are given in Section 4.4 of Chapter 4.

5.4.1. Smagorinsky model and Dynamic Smagorinsky model

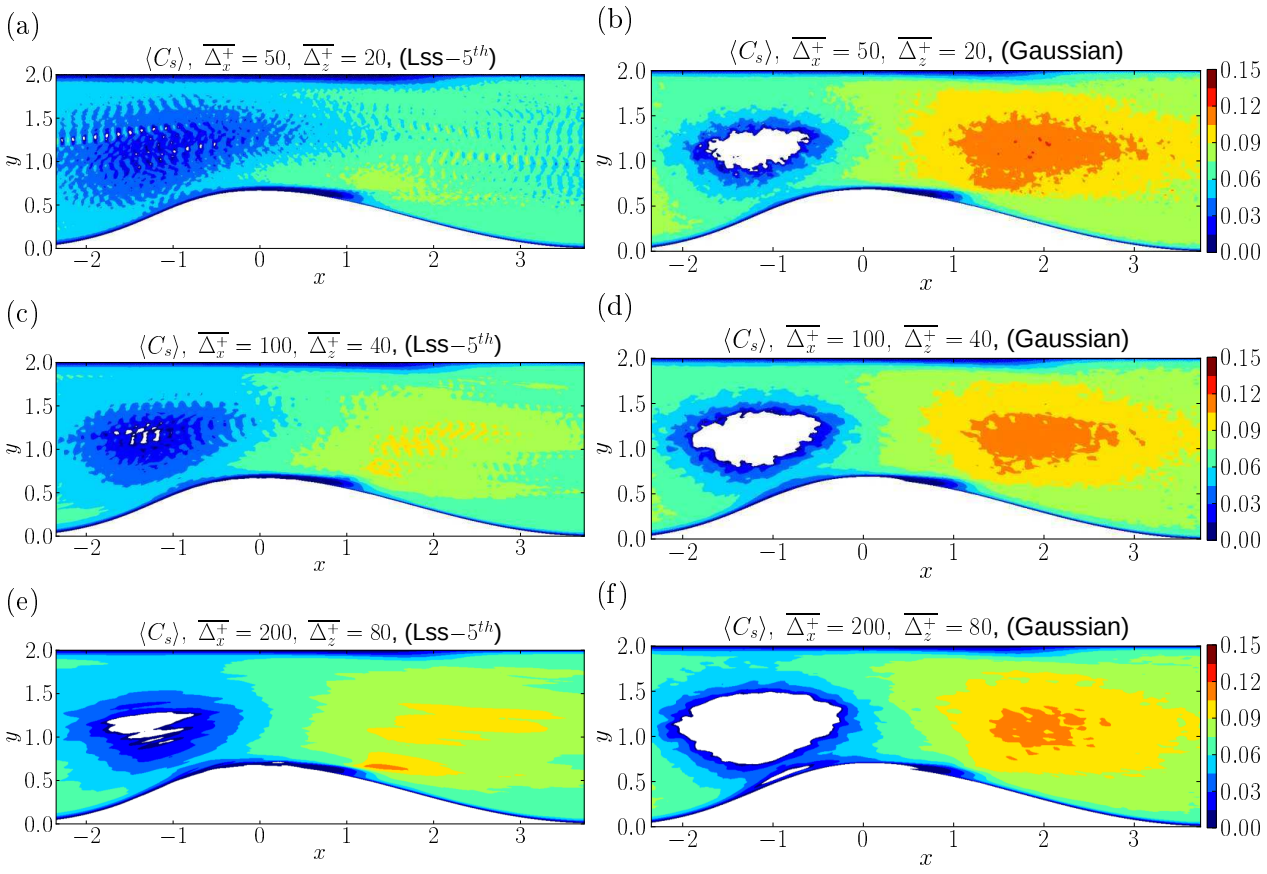

Figure 5.16: A priori estimate of the averaged Smagorinsky model coefficient $\langle C_s \rangle$ in converging-diverging region with three filter widths using Lss-5^{th} (a, c, e) and Gaussian (b, d, f) filters.

The a priori estimate of the average coefficient $\langle C_s \rangle$ of the Smagorinsky model is first analyzed in the converging-diverging channel region using both Lss-5^{th} and Gaussian

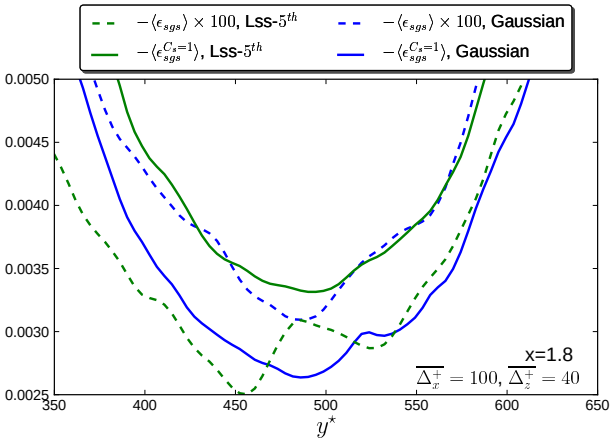

Figure 5.17: SGS energy dissipation $-\langle\epsilon_{sgs}\rangle$ and its modeled counterpart $-\langle\epsilon_{sgs}^{C_s=1}\rangle$ by the Smagorinsky model using $C_s = 1.0$ at $x = 1.8$, for the filter width $\overline{\Delta_x^+} = 100$, $\overline{\Delta_z^+} = 40$ using Lss-5^{th} and Gaussian filters.

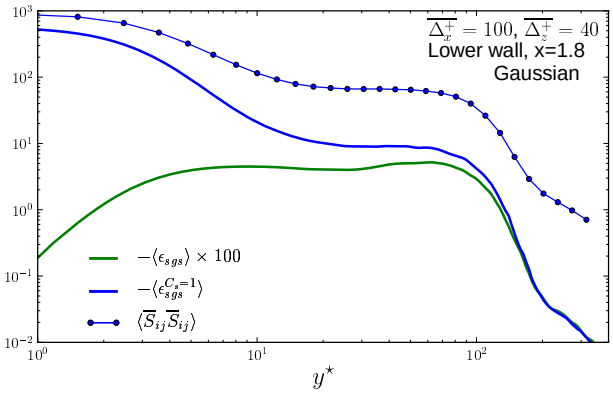

Figure 5.18: SGS energy dissipation $-\langle\epsilon_{sgs}\rangle$ and its modeled counterpart $-\langle\epsilon_{sgs}^{C_s=1}\rangle$ by the Smagorinsky model using $C_s = 1.0$ and the square of the norm of subgrid stress tensor at $x = 1.8$, using the Gaussian filter width $\overline{\Delta_x^+} = 100$, $\overline{\Delta_z^+} = 40$.

filters. The 2D distributions are given in Fig. 5.16. Only the positive values are displayed as, in a LES context, the negative values lead to numerical instabilities and are usually clipped to zero. As a clear difference with plane channel flow, negative values of $\langle C_s\rangle$ (white region) appear in the channel center of the converging (favorable pressure gradient) region and along the edges of the bump. The extent of the negative regions is larger with the Gaussian filter than with the Lss-5^{th} filter. This corresponds exactly to the back scatter regions of net SGS energy dissipation (see Fig. 5.10). A detailed analysis of the negative regions is given in Fig. B.6 in Appendix B. For each filter set, however, due to the influence of the pressure gradient, $\langle C_s\rangle$ extends over a larger range than in plane channel flow (see Fig. 4.14, and 4.16).

It should be noted that high positive values of $\langle C_s\rangle$ are observed in the channel center of the diverging APG region. They are more pronounced with the Gaussian filter. This is due to the fact that, in the diverging channel center, the absolute value of SGS energy dissipation $\langle\epsilon_{sgs}\rangle$ is slightly larger with Gaussian than with Lss-5^{th} filter, while the absolute value of SGS energy dissipation modeled by the Smagorinsky model ($\langle\epsilon_{sgs}^{C_s=1}\rangle = -2.0\langle(\nu_{sgs}/C_s^2)\overline{S}_{ij}^2\rangle$) using $C_s = 1$ is larger with Lss-5^{th} than with Gaussian

filter (see Fig. 5.17) in the same region. As a ratio between $\langle \epsilon_{sgs} \rangle$ and $\langle \epsilon_{sgs}^{C_s=1} \rangle$, a larger $\langle C_s \rangle$ is obtained using the Gaussian filter in the diverging channel center. A similar behavior is observed with other filter width.

Although the SGS energy dissipation is significantly larger in the near wall region than in the channel center of the diverging APG part (see Fig. 5.10), $\langle C_s \rangle$ is lower near the wall than in the channel center in the same region for each filter set. This is due to the fact that the SGS energy dissipation modeled by the Smagorinsky model $-\langle \epsilon_{sgs}^{C_s=1} \rangle$ is significantly larger than the real SGS energy dissipation $-\langle \epsilon_{sgs} \rangle$ in the near wall region $y^\star < 100$ compared to the channel center as shown in Fig. 5.18. The real and modeled SGS energy dissipation is analyzed at $x = 1.2$, which is the streamwise position of the peak of the $\langle \epsilon_{sgs} \rangle$. It is important to point out that, in the near wall region, the large $-\langle \epsilon_{sgs}^{C_s=1} \rangle$ is caused by the norm of the strain rate tensor $\langle \overline{S}_{ij} \rangle$, which is noticeably larger in near wall region than in the channel center at the same streamwise position as shown in Fig. 5.18. All of these observations are independent of the filter type and filter width.

The results of Fig. 5.16 also show that, the highest value of $\langle C_s \rangle$ is close to the standard value of $\langle C_s \rangle \simeq 0.16$ for isotropic turbulence (Lilly 1967 [77]; Meneveau 1997 [94]), but significantly higher than our results of plane channel flow (see Fig. 4.16). Meanwhile, as increasing the filter width, the peak positive values of $\langle C_s \rangle$ increase for Lss-5^{th} filter, but decrease for Gaussian filter. This agrees well with their behavior in the outer region of plane channel flow (see Fig. 4.16). Moreover, small positive $\langle C_s \rangle$ (less than 0.06) appear in the converging favorable pressure gradient channel center, corresponding to a weaker forward cascade of net SGS energy dissipation compared to the diverging region.

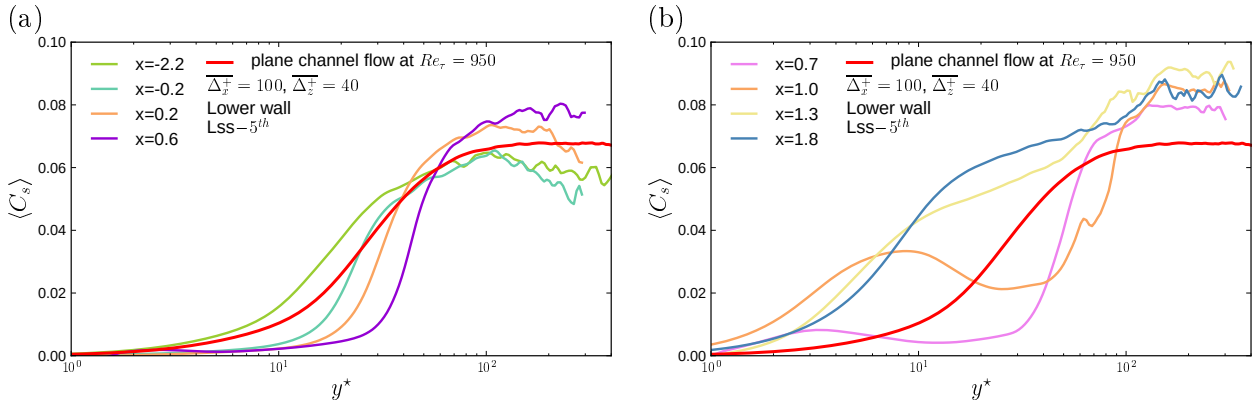

Figure 5.19: One-dimensional profiles of the averaged $\langle C_s \rangle$ of Smagorinsky model roughly before (a) and after (b) the onset of the recirculation region at the lower wall using Lss-5^{th} filter set $\overline{\Delta_x^+} = 100$, $\overline{\Delta_z^+} = 40$.

In order to examine the averaged $\langle C_s \rangle$ along the edge of the bump, one-dimensional analysis at the lower wall are given in Fig. 5.19. In the favorable pressure gradient region, the near wall behavior of $\langle C_s \rangle$ in the present research do not show significant difference with that in plane channel flow (see Fig. 5.19(a)). However, from at $x = -0.2$ (the position where the sign of the pressure gradient changes to positive, see Fig. 3.12), the position where $\langle C_s \rangle$ increases sharply moves away from the wall when moving downstream until the onset of the flow detachment at $x = 0.6$. Then, from $x = 0.7$ (see Fig. 5.19(b), a new peak of $\langle C_s \rangle$ appears in the near wall region ($10 < y^+ < 20$). This peak firstly becomes larger and moves away from the wall rapidly and then decreases gradually as

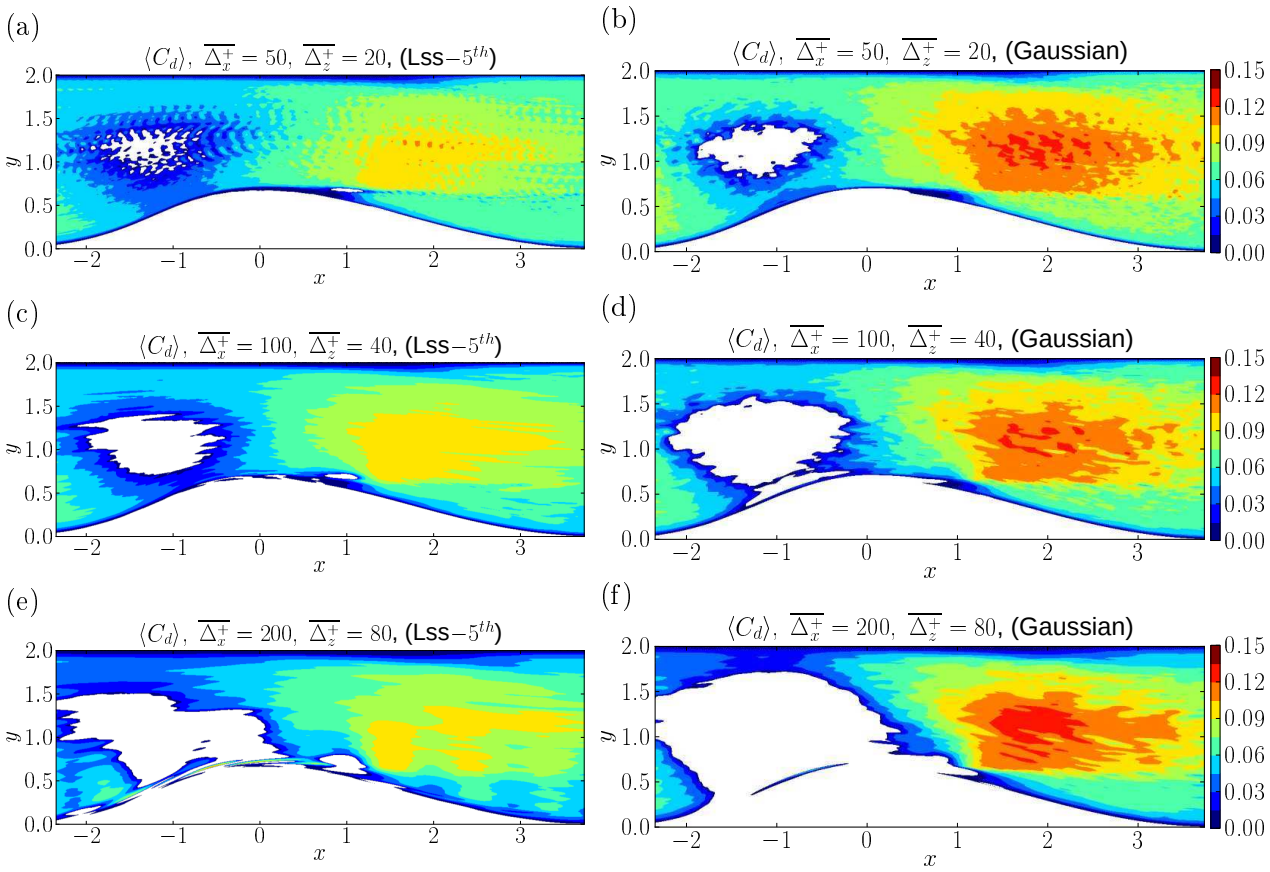

Figure 5.20: A priori estimate of coefficient $\langle C_d \rangle$ of Dynamic Smagorinsky model in converging-diverging regions with three filter widths ($\widehat{\Delta} = 2.0\overline{\Delta}$) using Lss-$5^{th}$ (left) and Gaussian (right) filters.

moving downstream. It is hardly discernible at $x = 1.8$ (roughly the streamwise position of the recirculation region). Similar behavior of $\langle C_s \rangle$ are observed at the lower wall with Gaussian filter and for small filter width ($\overline{\Delta_x^+} = 50$, $\overline{\Delta_z^+} = 20$). For $\langle C_s \rangle$ with the largest filter width ($\overline{\Delta_x^+} = 200$, $\overline{\Delta_z^+} = 80$), no sensitivity to dC_p/ds is observed. Therefore, in near wall regions of the lower wall, $\langle C_s \rangle$ with small and moderate filter widths using both Lss-5^{th} and Gaussian filters have significantly different behavior as varying the pressure gradient dC_p/ds. However, $\langle C_s \rangle$ is much less sensitive to the variations of dC_p/ds at the upper wall.

Similarly to what was done in plane channel flow, the averaged coefficient $\langle C_d \rangle$ of the dynamic Smagorinsky model estimated only by the resolved scales are investigated. Three filter widths using both filter types and with test filter width $\widehat{\Delta} = 2.0\overline{\Delta}$ are given in Fig. 5.20. For each filter set, the negative regions of $\langle C_d \rangle$ (in white) extend wider than the negative regions of $\langle C_s \rangle$ (see Fig. 5.16) or than the region of back scatter of net SGS energy dissipation (see Fig. 5.10). An examination of negative $\langle C_d \rangle$ in detail shows that they have similar behavior as negative $\langle C_s \rangle$ (see Fig. B.6 in Appendix B). In the center of the diverging channel part, however, the positive values of $\langle C_d \rangle$ are larger than the corresponding values of $\langle C_s \rangle$. Thus, $\langle C_d \rangle$ is more scattered than $\langle C_s \rangle$ in the whole channel region, especially for the large filter width ($\overline{\Delta_x^+} = 200$, $\overline{\Delta_z^+} = 80$) of both filter types. This is in agreement with the behavior in plane channel flow (see Fig. 4.17), and

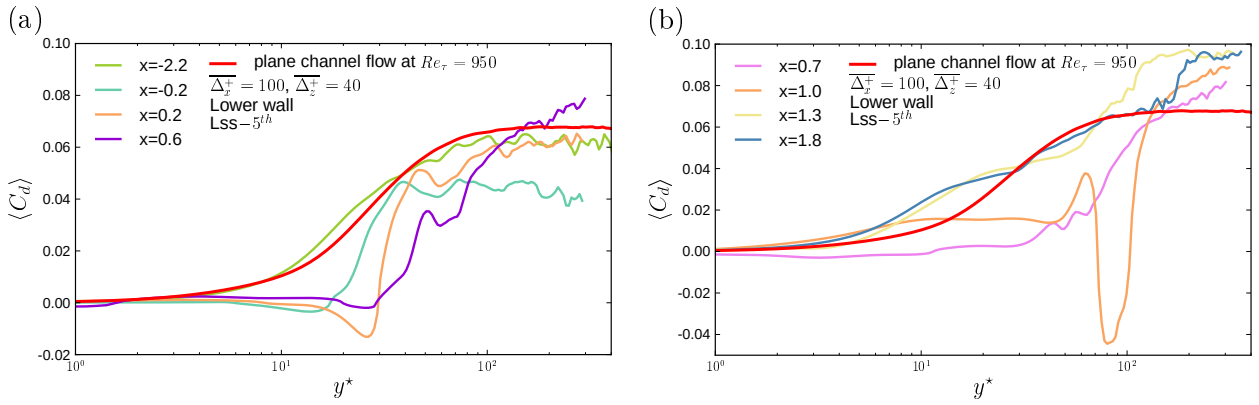

Figure 5.21: One-dimensional profiles of the averaged $\langle C_d \rangle$ of the Dynamic Smagorinsky model at the lower wall using Lss-5^{th} filter set $\overline{\Delta_x^+} = 100$, $\overline{\Delta_z^+} = 40$.

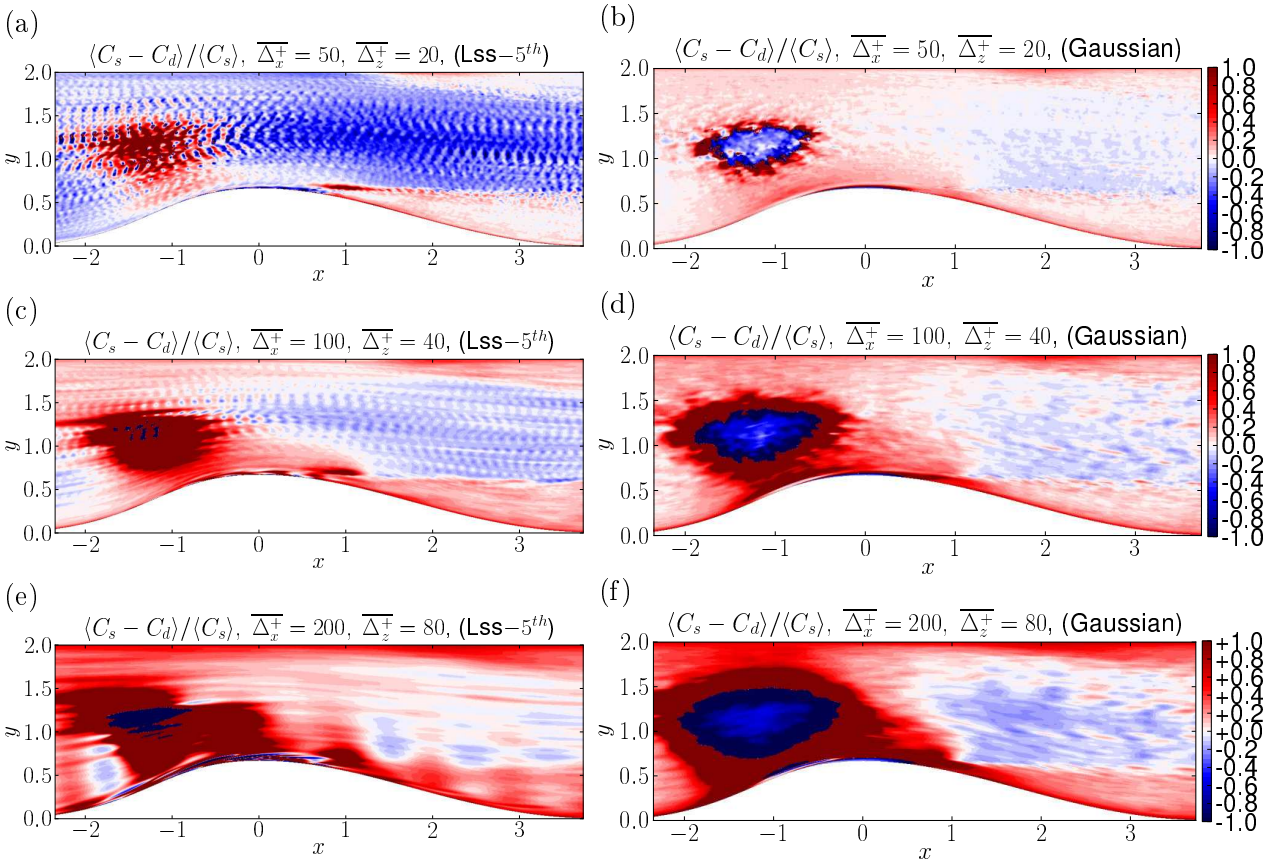

Figure 5.22: Relative errors between the a priori estimate of the averaged coefficient $\langle C_s \rangle$ of the Smagorinsky model and the averaged $\langle C_d \rangle$ of the Dynamic Smagorinsky model in converging-diverging regions using Lss-5^{th} (a, c, e) and Gaussian (b, d, f) filters.

may be due to a too large test filter width as reported by Carper and Porté-Agel 2008 [24].

A closer look at one-dimensional analysis of the averaged $\langle C_d \rangle$ at the lower wall is given in Fig. 5.21. The behavior of $\langle C_d \rangle$ at the lower wall is similar to that of $\langle C_s \rangle$ (see Fig. 5.19). A near wall peak of $\langle C_d \rangle$ appears in the range $0.7 \leq x \leq 1.8$, roughly corresponding to the recirculation region of the flow. However, negative $\langle C_d \rangle$ is observed at $x = 1.0$. Therefore, $\langle C_d \rangle$ is more scattered than $\langle C_s \rangle$ for the same filter set, due to the

influence of test filter of the Dynamic Smagorinsky model. At the upper wall, however, $\langle C_d \rangle$ has a similar behavior to that in plane channel flow.

A more detailed comparison based on the relative errors between $\langle C_s \rangle$ and $\langle C_d \rangle$ is given in Fig. 5.22. The figure depicts that both underestimation and overestimation of $\langle C_d \rangle$ compared to $\langle C_s \rangle$ occur at all filter sets examined here. In the converging channel center, $\langle C_d \rangle$ is mainly overestimated (about 0-60%, in blue region). The overestimation is weakened for the larger filter width of Lss-5^{th} filter, but strengthened as increasing the Gaussian filter width. Meanwhile, the underestimation (about 40-80%) of $\langle C_d \rangle$ occurs mostly in the near wall regions of the diverging part. This is comparable with our results in near wall regions of plane channel flow (see Fig. 4.18 and 4.19). However, the underestimation of $\langle C_d \rangle$ become stronger for larger filter width of both Lss-5^{th} and Gaussian filters. They even go up to 100% in the range $0.0 < x < 2.0$ for the largest filter width ($\overline{\Delta_x^+} = 200$, $\overline{\Delta_z^+} = 80$). This is in contradiction to the only occurrence of underestimation of $\langle C_d \rangle$ in plane channel flow (see Fig. 4.18 and 4.19). Both significant underestimation (up to 100%) and overestimation (down to -100%) of $\langle C_d \rangle$ occur in the converging channel center. Thus, the deviation of $\langle C_d \rangle$ from $\langle C_s \rangle$ in converging channel center is much larger than in plane channel flow.

Meanwhile, two additional test filter widths ($\widehat{\Delta} = 1.5\overline{\Delta}$ and $\widehat{\Delta} = 3.0\overline{\Delta}$) are also investigated for the estimation of the Dynamic Smagorinsky model coefficient. The results are given in Figs. B.7-B.10 in Appendix B. Contrary to the high sensitivity of $\langle C_d \rangle$ to the test filter width $\widehat{\Delta}$ in plane channel flow (see Fig. 4.20), the best comparison between $\langle C_d \rangle$ and $\langle C_s \rangle$ are obtained with a test filter width $\widehat{\Delta} = 2.0\overline{\Delta}$, in agreement with the previous results of plane channel flow at $Re_\tau = 640$ conducted by Tsubokura 2006 [139] .

5.4.2. Wall-Adapting Local Eddy-Viscosity model

As an interesting alternative to the Smagorinsky model, the WALE model coefficient is also estimated a priori using the same database of converging-diverging channel flow. The results are given in Fig. 5.23. Similarly to the observations for $\langle C_s \rangle$, the negative $\langle C_w \rangle$ mainly appear in the center of the converging favorable pressure gradient region and along the lower wall of the converging part for the largest filter width ($\overline{\Delta_x^+} = 200$, $\overline{\Delta_z^+} = 80$). An inspection of negative $\langle C_w \rangle$ shows that it behaves the same way as negative $\langle C_s \rangle$ and $\langle C_d \rangle$.

Similarly to what was observed for $\langle C_s \rangle$, $\langle C_w \rangle$ is larger with Gaussian than with Lss-5^{th} filter in the diverging channel center. This is due to the contribution of both the SGS energy dissipation $\langle \epsilon_{sgs} \rangle$ and its counterpart ($\langle \epsilon_{sgs}^{C_w=1} \rangle = -2.0 \langle (\nu_{sgs}/C_w^2) \overline{S}_{ij}^2 \rangle$) modeled by the WALE model using $C_w = 1.0$ as shown in Fig. 5.24. One can observe that, with the Gaussian filter, $-\langle \epsilon_{sgs} \rangle$ is larger than with the Lss-5^{th} filter, while a smaller $-\langle \epsilon_{sgs}^{C_w=1} \rangle$ is obtained with the Gaussian filter at the same position $x = 1.8$. Thus, a larger $\langle C_w \rangle$ can be obtained by the ratio between $\langle \epsilon_{sgs} \rangle$ and $\langle \epsilon_{sgs}^{C_w=1} \rangle$ in the diverging channel center. This behavior is independent of the filter width for both filter types.

Furthermore, the positive $\langle C_w \rangle$ becomes larger as increasing the filter width both in the diverging channel center and along the two walls. The strongly positive values of $\langle C_w \rangle$ in the diverging APG near wall regions largely exceed the standard value $\langle C_w \rangle \simeq 0.5$ for isotropic turbulence. This is more pronounced for the larger filter width. In order to explain the strong $\langle C_w \rangle$ for the filter width ($\overline{\Delta_x^+} = 200$, $\overline{\Delta_z^+} = 80$) in the diverging APG

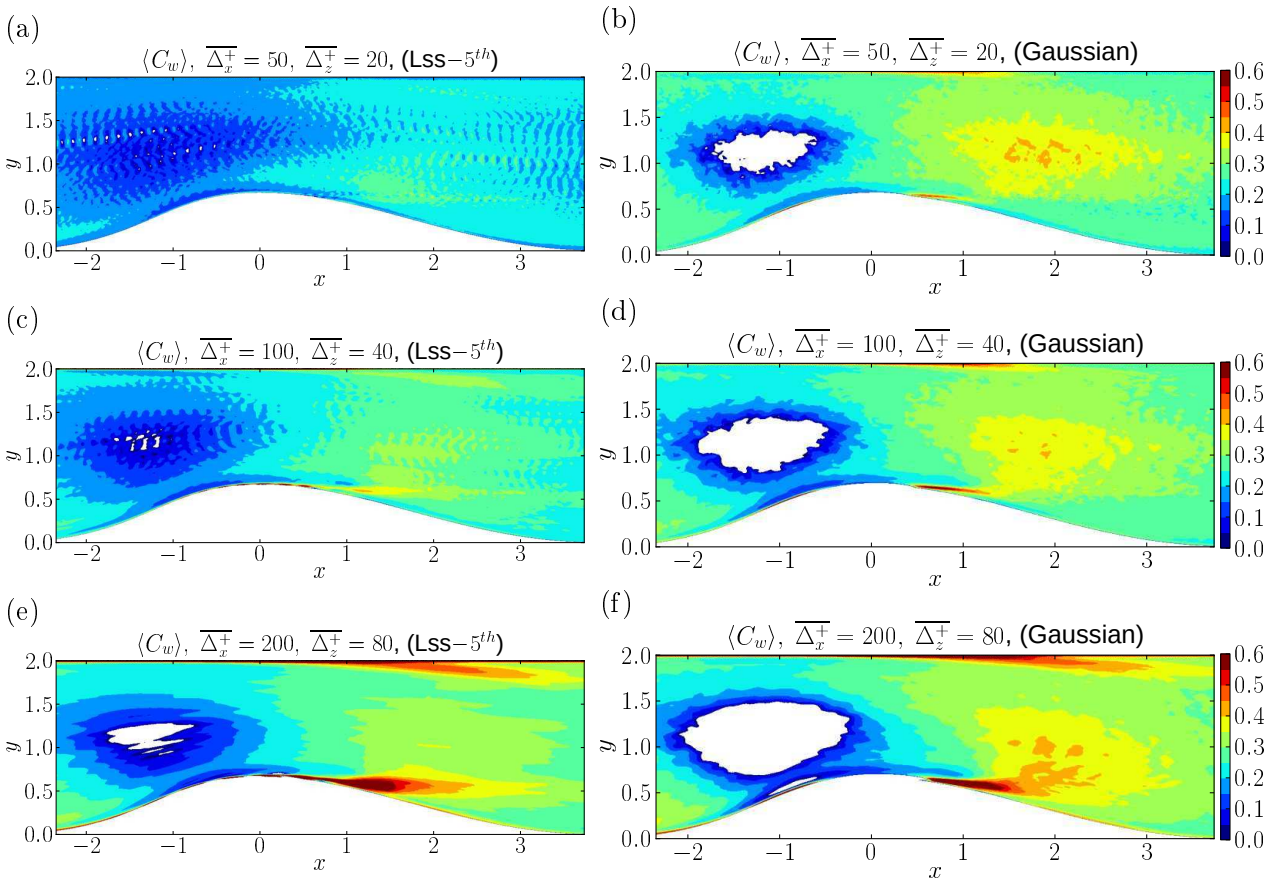

Figure 5.23: A priori estimate of the averaged coefficient $\langle C_w \rangle$ of the WALE model in the converging-diverging region with three filter widths using Lss-5^{th} (a, c, e) and Gaussian (b, d, f) filters. The maximum of $\langle C_w \rangle$ reaches up to 2.3 with Lss-5^{th} filter in the near wall region.

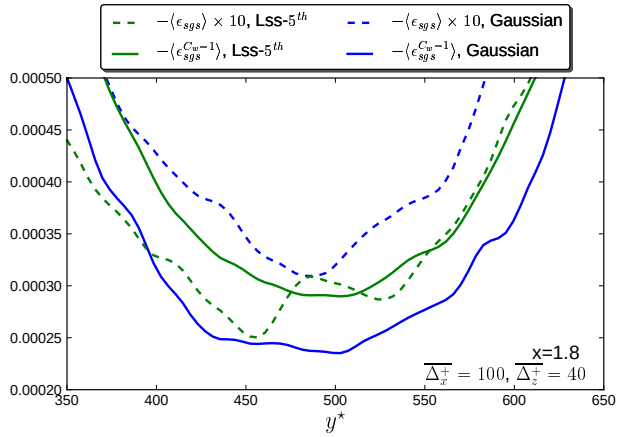

Figure 5.24: SGS energy dissipation $-\langle \epsilon_{sgs} \rangle$ and its modeled counterpart $-\langle \epsilon_{sgs}^{C_w=1} \rangle$ by the WALE model using $C_w = 1.0$ at $x = 1.8$ for the filter width $\overline{\Delta_x^+} = 100$, $\overline{\Delta_z^+} = 40$ using Lss-5^{th} and Gaussian filters.

near wall regions, one-dimensional profiles of the exact SGS energy dissipation $\langle \epsilon_{sgs} \rangle$ and its counterpart modeled by the WALE model $\langle \epsilon_{sgs}^{C_w=1} \rangle$ using $C_w = 1$ are given in Fig. 5.25. Statistics are analyzed with two Lss-5^{th} filter widths at $x = 1.8$. The exact SGS energy

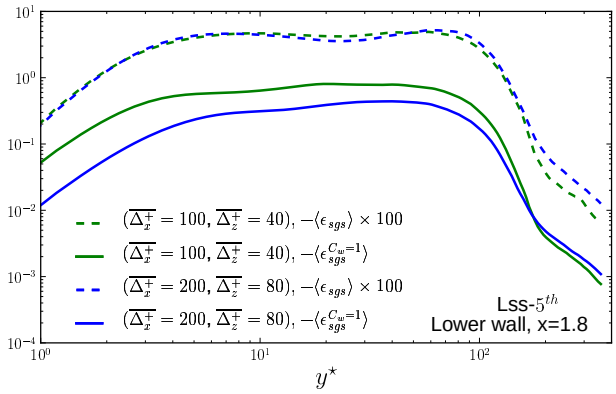

Figure 5.25: SGS energy dissipation $-\langle\epsilon_{sgs}\rangle$ and its modeled counterpart $-\langle\epsilon_{sgs}^{C_w=1}\rangle$ by the WALE model using $C_w = 1.0$ at $x = 1.8$ for the Lss-5^{th} filter width $\overline{\Delta_x^+} = 100$, $\overline{\Delta_z^+} = 40$ and $\overline{\Delta_x^+} = 200$, $\overline{\Delta_z^+} = 80$.

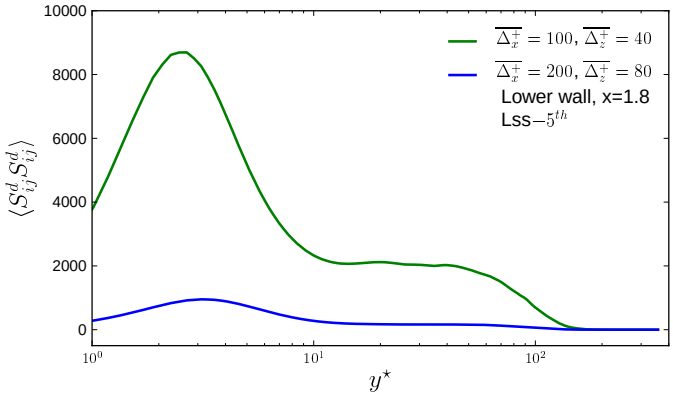

Figure 5.26: One-dimensional profiles of WALE model operator $\langle S_{ij}^d S_{ij}^d \rangle$ at the lower wall using Lss-5^{th} filter width $\overline{\Delta_x^+} = 100$, $\overline{\Delta_z^+} = 40$ and $\overline{\Delta_x^+} = 200$, $\overline{\Delta_z^+} = 80$.

dissipation $-\langle\epsilon_{sgs}\rangle$ is almost the same for the Lss-5^{th} filter width ($\overline{\Delta_x^+} = 100$, $\overline{\Delta_z^+} = 40$) and ($\overline{\Delta_x^+} = 200$, $\overline{\Delta_z^+} = 80$) in the near wall range $y^\star < 100$ at the lower wall. Meanwhile, $-\langle\epsilon_{sgs}^{C_w=1}\rangle$ is smaller with ($\overline{\Delta_x^+} = 200$, $\overline{\Delta_z^+} = 80$) than with ($\overline{\Delta_x^+} = 100$, $\overline{\Delta_z^+} = 40$) in the same region. Similar behavior of $-\langle\epsilon_{sgs}\rangle$ and $-\langle\epsilon_{sgs}^{C_w=1}\rangle$ are observed at the upper wall. Therefore, a larger $\langle C_w\rangle$ is obtained from the ratio between the SGS energy dissipation $\langle\epsilon_{sgs}\rangle$ and its counterpart $\langle\epsilon_{sgs}^{C_w=1}\rangle$ modeled by the WALE model with the larger filter width ($\overline{\Delta_x^+} = 200$, $\overline{\Delta_z^+} = 80$) than the smaller one ($\overline{\Delta_x^+} = 100$, $\overline{\Delta_z^+} = 40$).

It is important to note that, the larger values of $-\langle\epsilon_{sgs}^{C_w=1}\rangle$ for the smaller filter width in the near wall region are caused by the operator $\langle S_{ij}^d S_{ij}^d\rangle$ of the WALE model as shown in Fig. 5.26. Statistics are analyzed at the same position $x = 1.8$. One can observe that, in the near wall range $y^\star < 100$, $\langle S_{ij}^d S_{ij}^d\rangle$ is significantly amplified for the smaller filter width ($\overline{\Delta_x^+} = 100$, $\overline{\Delta_z^+} = 40$). This explains the larger $-\langle\epsilon_{sgs}^{C_w=1}\rangle$ for the filter width ($\overline{\Delta_x^+} = 100$, $\overline{\Delta_z^+} = 40$) compared to ($\overline{\Delta_x^+} = 200$, $\overline{\Delta_z^+} = 80$) in the near wall regions (see Fig. 5.25). The behavior of all statistics associated with the high values of $\langle C_w\rangle$ near both the curved and flat walls are the same for the Gaussian filter. Therefore, in the near wall region, the high values of $\langle C_w\rangle$ with a large filter width are greatly due to the sensitivity of the WALE operator $\langle S_{ij}^d S_{ij}^d\rangle$ which is significantly smaller for the larger filter width.

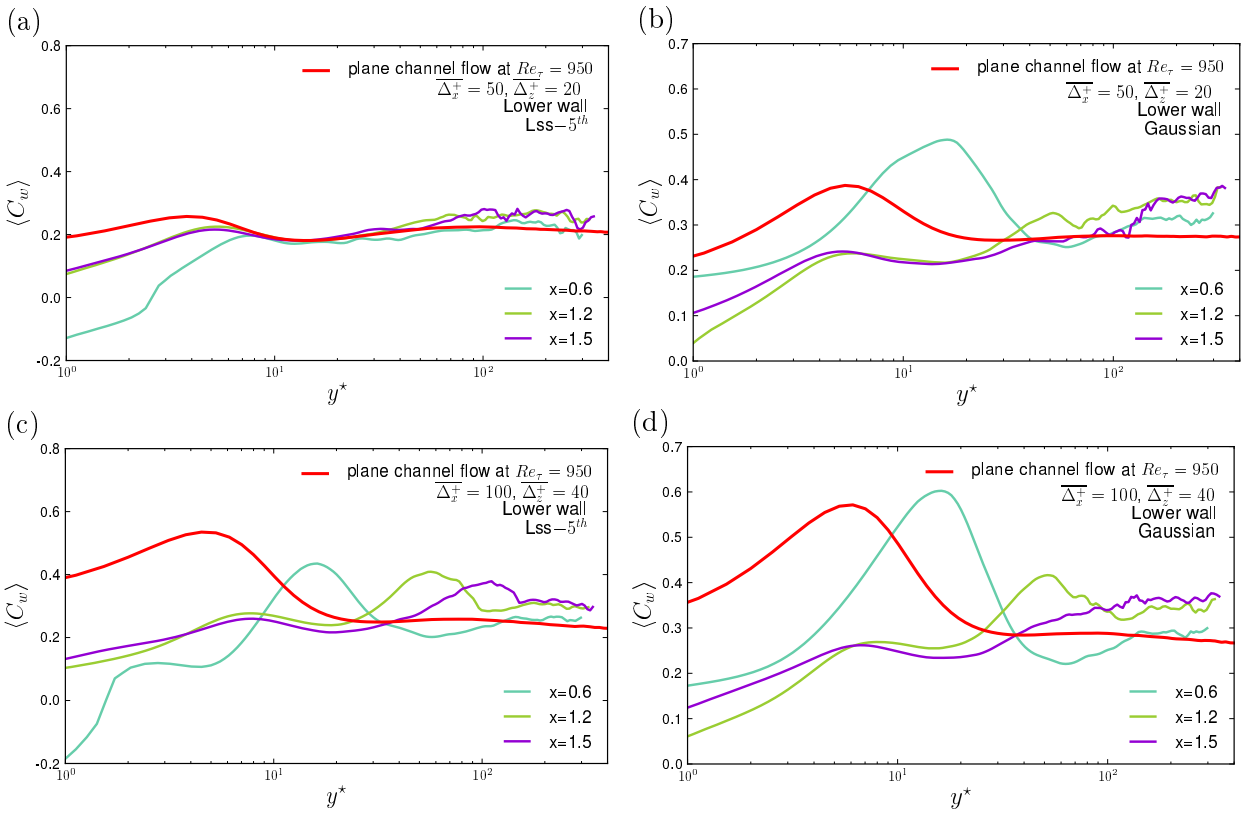

Figure 5.27: One-dimensional profiles of the averaged $\langle C_w \rangle$ of WALE model at the lower wall for the filter width $\overline{\Delta_x^+} = 100$, $\overline{\Delta_z^+} = 40$ using both Lss-5^{th} (a, c) and Gaussian (b, d) filters.

One-dimensional analysis of $\langle C_w \rangle$ along the edge of the curved wall are given in Fig. 5.27. Statistics are mainly analyzed in the recirculation region. Contrary to significantly high values in the near wall region of plane channel flow, $\langle C_w \rangle$ is considerably lower here in the range $y^\star < 6$ than in the region far from the wall. This low values of $\langle C_w \rangle$ increases from $x = 0.6$ as moving downstream. For the smaller Lss-5^{th} filter ($\overline{\Delta_x^+} = 50$, $\overline{\Delta_z^+} = 20$), very similar behavior of $\langle C_w \rangle$ to the plane channel flow is observed in the range $y^\star > 10$ in the recirculation region. For the larger Lss-5^{th} filter ($\overline{\Delta_x^+} = 100$, $\overline{\Delta_z^+} = 40$) and all the Gaussian filter widths, however, a peak of $\langle C_w \rangle$ occurs from the onset of the recirculation region $x = 0.6$, in the range $y^\star > 10$. This peak becomes smaller and moves away from the wall as moving downstream. A relatively flatter $\langle C_w \rangle$ than in plane channel flow is obtained at the end of the recirculation region ($x = 1.5$) for the larger filter width ($\overline{\Delta_x^+} = 100$, $\overline{\Delta_z^+} = 40$) for both filter types. This behavior of $\langle C_w \rangle$ in the recirculation region is also observed for the largest filter width ($\overline{\Delta_x^+} = 200$, $\overline{\Delta_z^+} = 80$). A similar behavior of $\langle C_w \rangle$ is observed at the upper wall.

5.4.3. σ Model

The a priori evaluation of the averaged coefficient $\langle C_\sigma \rangle$ of the σ model with three filter widths using both Lss-5^{th} and Gaussian filters are depicted in Fig. 5.28. $\langle C_\sigma \rangle$ has a similar behavior to $\langle C_w \rangle$ in the whole converging-diverging channel region. $\langle C_\sigma \rangle$ is larger with Gaussian filter than with Lss-5^{th} filter for each filter width. This is owing to the effects

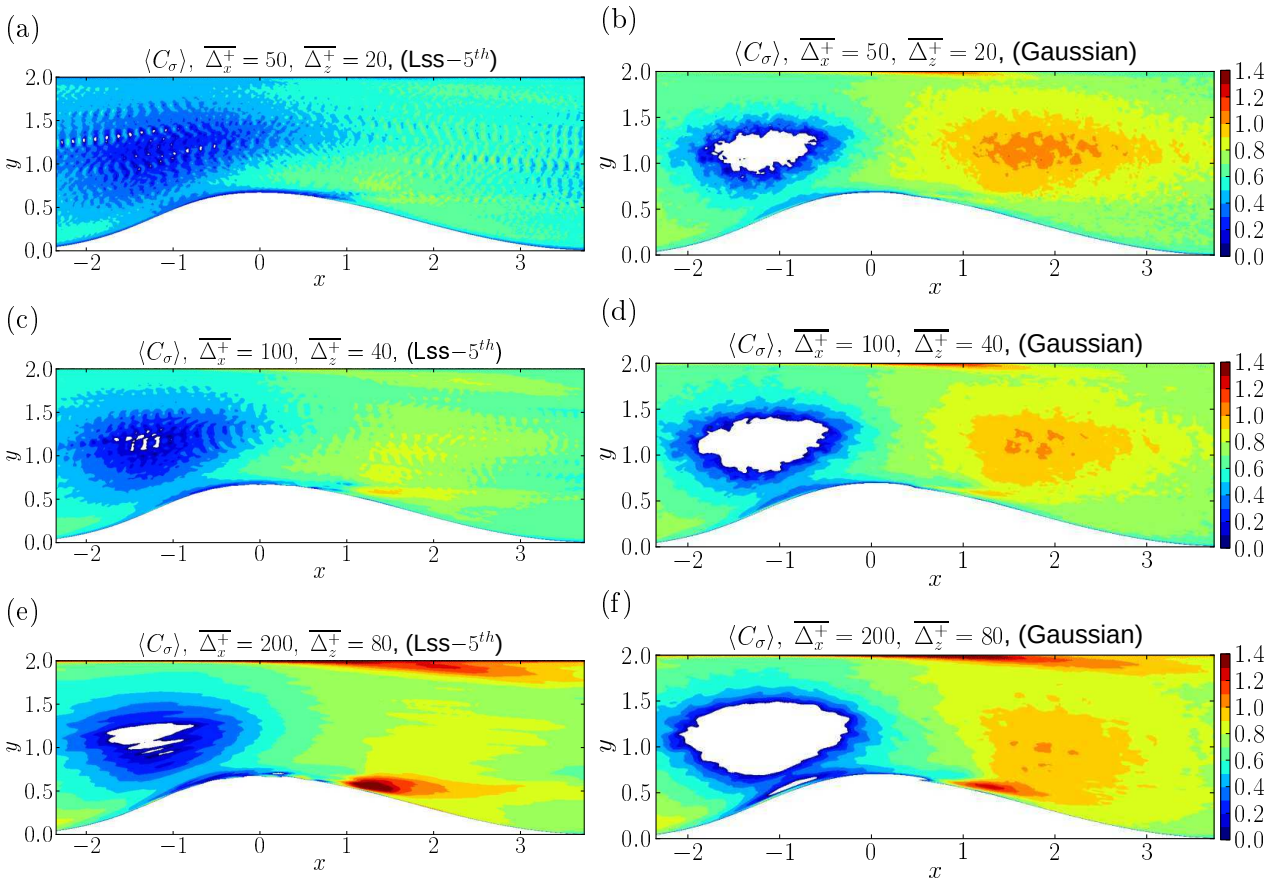

Figure 5.28: A priori estimate of coefficient $\langle C_\sigma \rangle$ of σ model in converging-diverging regions with three filter widths using Lss-5^{th} (a, c, e) and Gaussian (b, d, f) filters. The maximum of $\langle C_\sigma \rangle$ is 1.65 for both filter types.

of both the SGS energy dissipation $\langle \epsilon_{sgs} \rangle$ and its counterpart modeled by the σ model $\langle \epsilon_{sgs}^{C_\sigma=1} \rangle = -2.0 \langle (\nu_{sgs}/C_\sigma^2) \overline{S}_{ij}^2 \rangle$ using $C_\sigma = 1$. Detailed statistics are given in Fig. 5.29. At $x = 2.0$, larger absolute values of $\langle \epsilon_{sgs} \rangle$ and $\langle \epsilon_{sgs}^{C_\sigma=1} \rangle$ are obtained respectively with the Gaussian and Lss-5^{th} filters. Therefore, a larger $\langle C_\sigma \rangle$ is obtained in the channel center, by the ratio of $\langle \epsilon_{sgs} \rangle$ and $\langle \epsilon_{sgs}^{C_\sigma=1} \rangle$ using the Gaussian filter. This is independent of the filter width of both filter types.

In Fig. 5.28, large values of $\langle C_\sigma \rangle$ appear in the diverging APG near wall regions, more pronounced for the largest filter width ($\overline{\Delta_x^+} = 200$, $\overline{\Delta_z^+} = 80$). The maximum $\langle C_\sigma \rangle \simeq 1.65$ is even larger than the standard value $\langle C_\sigma \rangle \simeq 1.5$ for isotropic turbulence. The large values of $\langle C_\sigma \rangle$ for the larger filter width ($\overline{\Delta_x^+} = 200$, $\overline{\Delta_z^+} = 80$) in the near wall region is due to the contributions of both the SGS energy dissipation $\langle \epsilon_{sgs} \rangle$ and the modeled SGS energy dissipation $\langle \epsilon_{sgs}^{C_\sigma=1} \rangle$ by the σ model as shown in Fig. 5.30. The SGS energy dissipation $-\langle \epsilon_{sgs} \rangle$ is almost overlapped in the range $y^\star < 100$ for the two Lss-5^{th} filter width ($\overline{\Delta_x^+} = 100$, $\overline{\Delta_z^+} = 40$) and ($\overline{\Delta_x^+} = 200$, $\overline{\Delta_z^+} = 80$). Since $-\langle \epsilon_{sgs}^{C_\sigma=1} \rangle$ is smaller for the larger filter width ($\overline{\Delta_x^+} = 200$, $\overline{\Delta_z^+} = 80$) than for the smaller one ($\overline{\Delta_x^+} = 100$, $\overline{\Delta_z^+} = 40$) in the same range, so a larger $\langle C_\sigma \rangle$ is obtained by the ratio between $\langle \epsilon_{sgs} \rangle$ and $\langle \epsilon_{sgs}^{C_\sigma=1} \rangle$ with the larger filter width ($\overline{\Delta_x^+} = 200$, $\overline{\Delta_z^+} = 80$) in the near wall region of the diverging APG part.

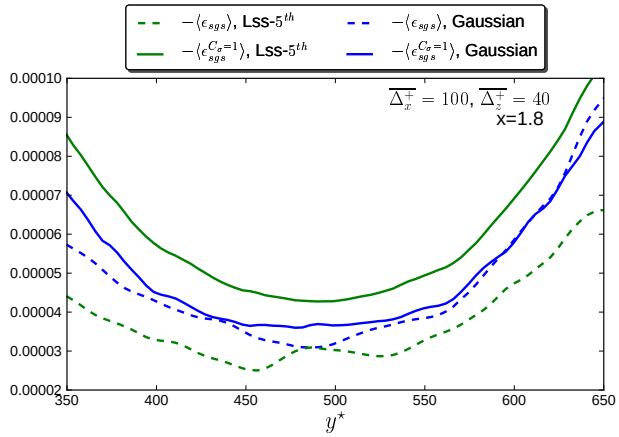

Figure 5.29: SGS energy dissipation $-\langle\epsilon_{sgs}\rangle$ and its modeled counterpart $-\langle\epsilon_{sgs}^{C_\sigma=1}\rangle$ by the σ model using $C_\sigma = 1.0$ at $x = 1.8$ for the filter width $\overline{\Delta_x^+} = 100$, $\overline{\Delta_z^+} = 40$ using Lss-5^{th} and Gaussian filters.

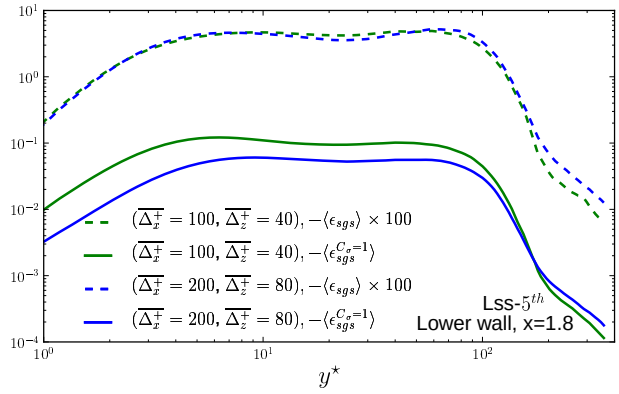

Figure 5.30: SGS energy dissipation $-\langle\epsilon_{sgs}\rangle$ and its modeled counterpart $-\langle\epsilon_{sgs}^{C_\sigma=1}\rangle$ by the σ model using $C_\sigma = 1.0$ at $x = 1.8$ for the Lss-5^{th} filter width $\overline{\Delta_x^+} = 100$, $\overline{\Delta_z^+} = 40$ and $\overline{\Delta_x^+} = 200$, $\overline{\Delta_z^+} = 80$.

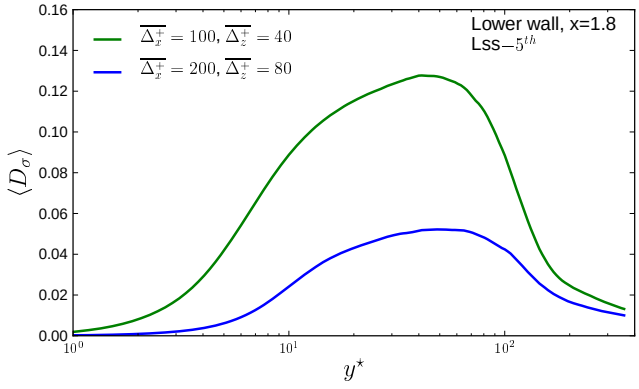

Figure 5.31: One-dimensional profiles of σ model operator $\langle D_\sigma\rangle$ at the lower (a) and upper (b) walls using Lss-5^{th} filter width $\overline{\Delta_x^+} = 100$, $\overline{\Delta_z^+} = 40$ and $\overline{\Delta_x^+} = 200$, $\overline{\Delta_z^+} = 80$.

The sensitivity of $\langle\epsilon_{sgs}^{C_\sigma=1}\rangle$ to the filter width is dependent of the σ model operator $\langle D_\sigma\rangle$ in the near wall region. One-dimensional profiles of $\langle D_\sigma\rangle$ at the same position $x = 1.5$ is given in Fig. 5.31. At the lower wall, the magnitude of $\langle D_\sigma\rangle$ with the smaller filter

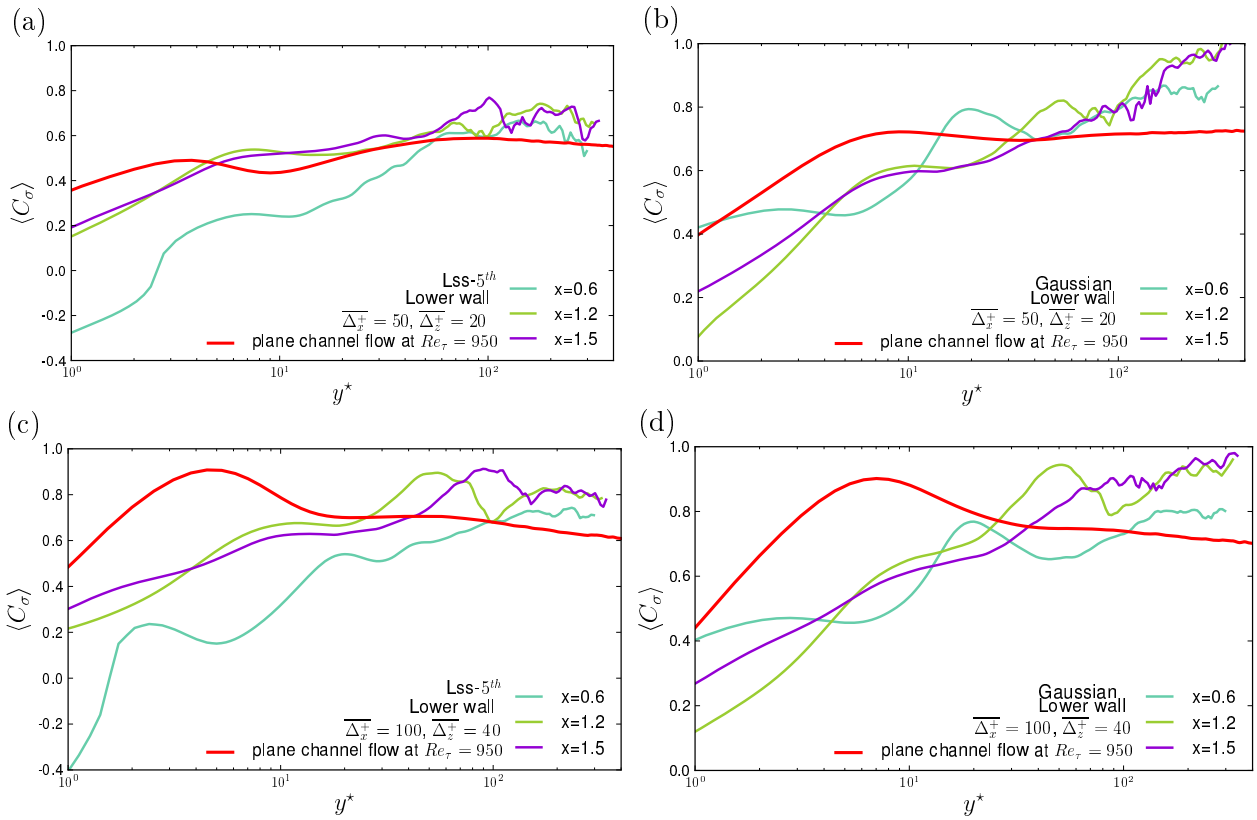

Figure 5.32: One-dimensional profiles of the averaged $\langle C_\sigma \rangle$ of σ model at the lower wall using Lss-5^{th} (a, c) and Gaussian (b, d) filters.

width ($\overline{\Delta_x^+} = 100$, $\overline{\Delta_z^+} = 40$) is almost 4 times that with the larger one. This causes a larger SGS energy dissipation $-\langle \epsilon_{sgs}^{C_\sigma=1} \rangle$ modeled by the σ model for the smaller filter width ($\overline{\Delta_x^+} = 100$, $\overline{\Delta_z^+} = 40$) in the near wall region (see Fig. 5.30). Similar behavior of $\langle D_\sigma \rangle$ and $\langle \epsilon_{sgs}^{C_\sigma=1} \rangle$ are observed with the Gaussian filter. Therefore, the large sensitivity of the σ model operator $\langle D_\sigma \rangle$ to the filter width contributes significantly to generate the large values of $\langle C_\sigma \rangle$ in the near wall region of the diverging APG part.

A deeper examination of $\langle C_\sigma \rangle$ in the recirculation region of the lower wall is given in Fig. 5.32. Contrary to the high values in plane channel flow, very low values of $\langle C_\sigma \rangle$ are observed in the near wall region. Beginning at the onset of recirculation region, the low values of $\langle C_\sigma \rangle$ gradually increase as moving downstream, but keep lower than in the near wall region of plane channel flow. Similarly to $\langle C_w \rangle$ (but less pronounced), a peak of $\langle C_\sigma \rangle$ is also observed in the range $y^\star > 10$ in the recirculation region. At each position, $\langle C_\sigma \rangle$ increases faster than $\langle C_w \rangle$ as moving away from the wall. The values obtained are higher than in plane channel flow in the logarithmic and outer region. Globally, in the recirculation region, $\langle C_\sigma \rangle$ is steeper than in plane channel flow. A similar but slightly less steeper behavior of $\langle C_\sigma \rangle$ is observed at the upper wall.

5.4.4. Conclusion

In the present analysis, the coefficients of four subgrid scale models are evaluated a priori with different filter widths using both Lss-5^{th} and Gaussian filters. The results are

compared with the plane channel flow. Due to the pressure gradient and curvature at the lower wall, the model coefficients show much more scatter than in plane channel flow as analyzed in Section 4.4 of Chapter 4. Significant negative coefficients of subgrid scale models corresponding to the back ward of SGS energy dissipation occur in the converging channel center. These negative coefficients are not observed in our results of plane channel flow, as no back scatter is present in the SGS energy dissipation.

Due to the influence of the adverse pressure gradient, high values of the coefficients, which are even larger than their standard values for isotropic turbulence, occur in the diverging channel region. Both the SGS energy dissipation and its counterpart modeled by the subgrid scale models are very sensitive to the filter type. This leads to larger coefficients of the four subgrid models with Gaussian than with Lss-5^{th} filter in the diverging channel center. $\langle C_s \rangle$ and $\langle C_d \rangle$ are smaller in the near wall region than in the channel center. This is due to a significantly larger value of the norm of the strain rate tensor $\langle \overline{S}_{ij} \rangle$ near the wall, independently of the filter type and filter width. However, $\langle C_d \rangle$ is found to be more scattered and further from $\langle C_s \rangle$ than in plane channel flow. The filter width dependent behavior of the operator $\langle S_{ij}^d S_{ij}^d \rangle$ of the WALE model and the operator $\langle D_\sigma \rangle$ of the σ model give rise to stronger values of $\langle C_w \rangle$ and $\langle C_\sigma \rangle$ near both the lower and upper walls in the diverging APG region, especially for the larger filter width ($\overline{\Delta_x^+} = 200$, $\overline{\Delta_z^+} = 80$) with both filter types. The coefficients $\langle C_w \rangle$ and $\langle C_\sigma \rangle$ are found to have quite similar behavior in the present a priori analysis.

The one-dimensional analysis shows that, all the model coefficients at both walls have different behavior to the plane channel flow. At the lower wall, $\langle C_s \rangle$ and $\langle C_d \rangle$ are quite sensitive to the variation of the pressure gradient. A new peak of each model coefficient is observed in the recirculation region. Near the end of the recirculation region, $\langle C_w \rangle$ is flatter than in plane channel flow. However, in all recirculation region, $\langle C_\sigma \rangle$ is steeper than in plane channel flow.

5.5. Tests of models behavior

In this section, the correlations of the SGS stress tensor, the SGS force, the SGS energy dissipation and their counterparts modeled by the Smagorinsky and WALE models are investigated in detail. The predictive capabilities of different models are also investigated. The a priori analysis are performed using the average model coefficients calculated in Section 5.4. This means that the averaged SGS dissipation is modeled exactly. Statistics in the diverging APG part will be analyzed in more detail, as the large eddy simulation usually fails to predict correctly the flow in this region.

5.5.1. Correlation of SGS tensor

The exact SGS stresses $\langle\tau_{ij}\rangle$ normalized by the square of the friction velocity $(u_\tau^o)^2$ at the inlet are given in Fig. 5.33 for a filter width $\overline{\Delta_x^+} = 100$, $\overline{\Delta_z^+} = 40$. The evaluation of model performances is conducted on the components $\langle\tau_{11}\rangle$, $\langle\tau_{12}\rangle$, $\langle\tau_{22}\rangle$ and $\langle\tau_{33}\rangle$, as $\langle\tau_{13}\rangle$ and $\langle\tau_{23}\rangle$ are zero due to the spanwise homogeneity. Fig. 5.33 shows that the magnitude of the different components of $\langle\tau_{ij}\rangle$ is larger than in plane channel flow. Two peaks of positive $\langle\tau_{11}\rangle$, $\langle\tau_{22}\rangle$ and $\langle\tau_{33}\rangle$, as well as both positive and negative $\langle\tau_{12}\rangle$ occur near the wall in the diverging channel region, due to the strong occurrence of small scale vortices as shown in Fig. 3.17. One-dimensional analysis shows that the peak of SGS stress tensor occurs at the same streamwise position as the peak of the turbulent kinetic energy at the lower wall, but not at the upper wall (see Fig. B.11 in Appendix B). The Gaussian filter gives larger peaks with stronger intensity compared to the Lss-5^{th} for all components of $\langle\tau_{ij}\rangle$.

Correlations $C_{\tau_{ij}}$ between the exact SGS stress tensor and its counterpart modeled by Smagorinsky model with a filter width $\overline{\Delta_x^+} = 100$, $\overline{\Delta_z^+} = 40$ using both Lss-5^{th} and Gaussian filters are given in Fig. 5.34. In accordance with plane channel flow, all correlations are in general higher with Gaussian than with Lss-5^{th} filter. The worse correlations $C_{\tau_{12}}$ occur in the converging channel center, in addition to the very near wall regions as observed in plane channel flow (see Fig. 4.34). The higher correlations $C_{\tau_{11}}$, $C_{\tau_{22}}$ and $C_{\tau_{33}}$ compared to $C_{\tau_{12}}$ are due to $1/3\tau_{kk}$ which is added to the modeled subgrid scale tensor as already observed in plane channel flow. However, a peak of $C_{\tau_{11}}$ (up to 1.0) appears at both walls from the throat until $x \simeq 2.0$, while the low values of $C_{\tau_{12}}$, $C_{\tau_{22}}$ and $C_{\tau_{33}}$ occur near the wall. Moreover, it is important to note that, the regions of SGS stress tensor intensive in Fig. 5.33 do not correspond to the highest correlation regions in Fig. 5.34.

In order to investigate the correlation $C_{\tau_{12}}$ in detail, one-dimensional profiles with both Lss-5^{th} and Gaussian filter width ($\overline{\Delta_x^+} = 100$, $\overline{\Delta_z^+} = 40$) and ($\overline{\Delta_x^+} = 50$, $\overline{\Delta_z^+} = 20$) at the lower wall are given in Fig. 5.35. In the viscous layer, for each filter set, $C_{\tau_{12}}$ is lower than in plane channel flow for each filter set. It is closed to a constant, which is comparable to the plane channel flow, for the smaller Lss-5^{th} filter width ($\overline{\Delta_x^+} = 50$, $\overline{\Delta_z^+} = 20$) in the whole channel region. However, $C_{\tau_{12}}$ is not well converged with the smaller Gaussian filter width ($\overline{\Delta_x^+} = 50$, $\overline{\Delta_z^+} = 20$) as moving away from the wall in the recirculation region. For the larger filter width ($\overline{\Delta_x^+} = 100$, $\overline{\Delta_z^+} = 40$) with both filter types, a peak of $C_{\tau_{12}}$ appears from the onset of recirculation region at $x = 0.5$. This peak firstly increases and then decreases as moving downstream, finally, with the Gaussian filter, $C_{\tau_{12}}$ is slightly larger than in the outer region of plane channel flow. A similar behavior is observed for

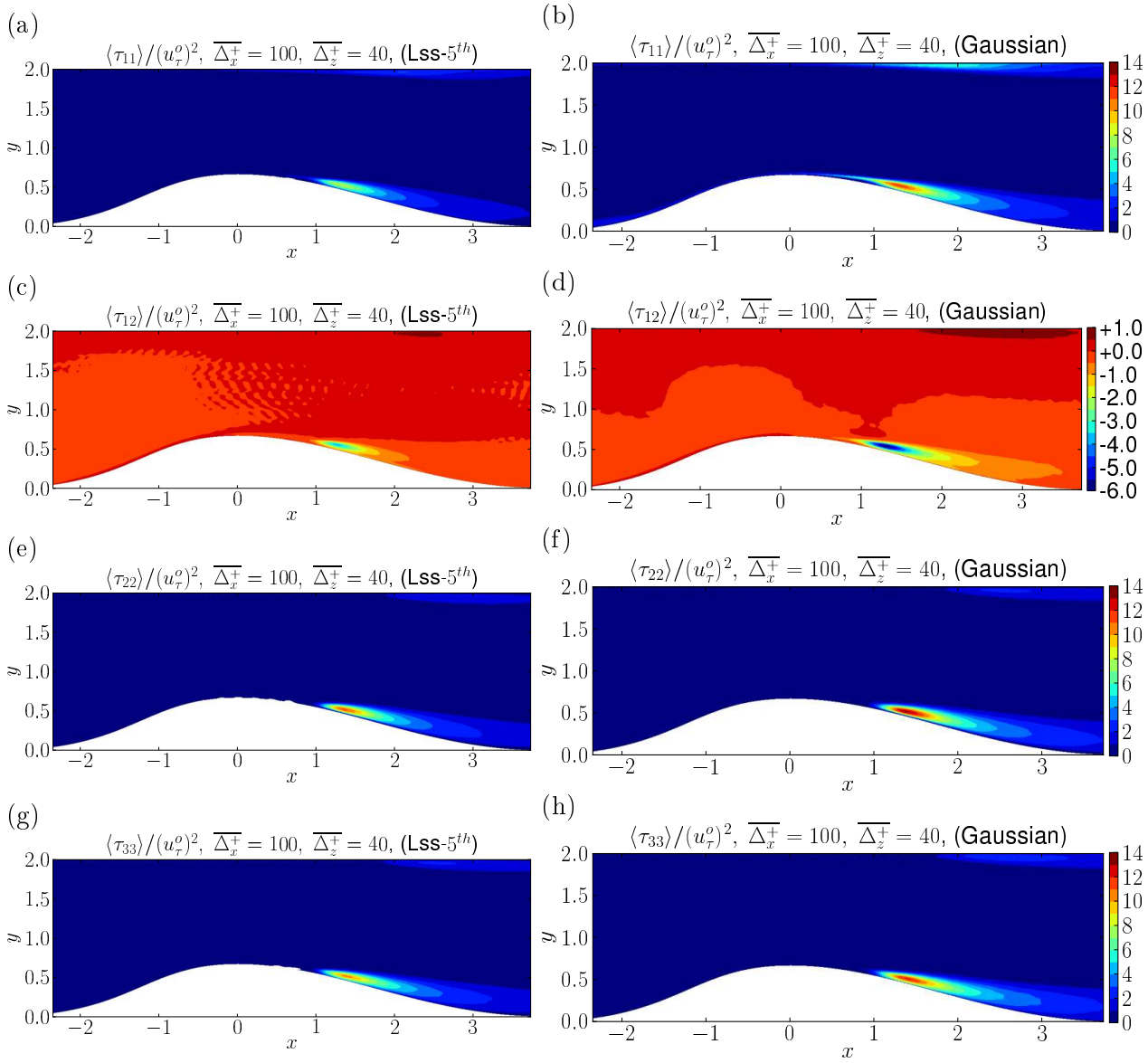

Figure 5.33: Distributions of normalized SGS tensor $\langle\tau_{11}\rangle/(u_\tau^o)^2$, $\langle\tau_{12}\rangle/(u_\tau^o)^2$, $\langle\tau_{22}\rangle/(u_\tau^o)^2$ and $\langle\tau_{33}\rangle/(u_\tau^o)^2$ (u_τ^o being the friction velocity) using Lss-5^{th} (a, c, e, g) and Gaussian (b, d, f, h) filters.

the largest filter width ($\overline{\Delta_x^+}=200$, $\overline{\Delta_z^+}=80$) of both filter types. Therefore, in the recirculation region, with small filter width, $C_{\tau_{12}}$ is more influenced by the filter type, than with large filter width. Similar one-dimensional analysis for the other correlations $C_{\tau_{11}}$, $C_{\tau_{22}}$ and $C_{\tau_{33}}$ are given in Appendix B (see Fig. B.12).

Further comparisons of correlations $C_{\tau_{12}}$ between the Smagorinsky and WALE models using both Lss-5^{th} and Gaussian filter width ($\overline{\Delta_x^+}=50$, $\overline{\Delta_z^+}=20$) and ($\overline{\Delta_x^+}=200$, $\overline{\Delta_z^+}=80$) at $x=1.3$ the lower wall (the peak position of τ_{12} along the lower wall) are given in Fig. 5.36. A peak of $C_{\tau_{12}}$ occurs at this station, in the range $y^\star\simeq 100$. It is more pronounced for the larger filter width ($\overline{\Delta_x^+}=200, \overline{\Delta_z^+}=80$). This is not observed in the plane channel flow for both models (see Fig. 4.37), and may be due to the strong turbulence developed above the separated region. For the larger Lss-5^{th} filter width

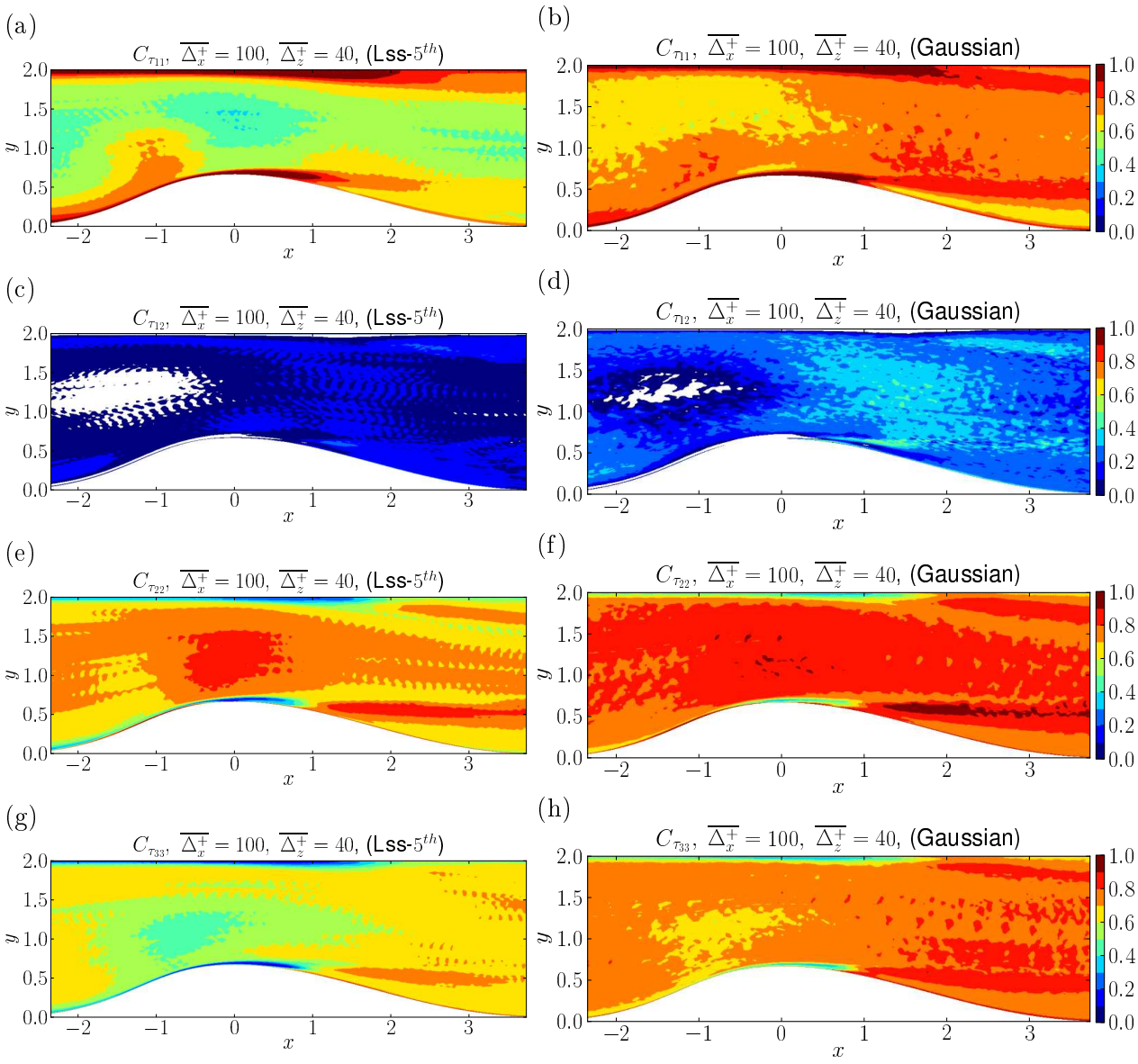

Figure 5.34: Correlations $C_{\tau_{ij}}$ between exact SGS stress tensor and the counterparts modeled by Smagorinsky model using Lss-5^{th} (a, c, e, g) and Gaussian (b, d, f, h) filters.

($\overline{\Delta_x^+} = 200$, $\overline{\Delta_z^+} = 80$) and both Gaussian filters, the Smagorinsky model has a higher $C_{\tau_{12}}$ than the WALE model in the outer region. This is the same for the small filter width ($\overline{\Delta_x^+} = 50$, $\overline{\Delta_z^+} = 20$), where a low value of $C_{\tau_{12}}$ (in the range $[0, 0.2]$) is obtained by both models. In the near wall region, except for the small Gaussian filter width ($\overline{\Delta_x^+} = 50$, $\overline{\Delta_z^+} = 20$), $C_{\tau_{12}}$ for both models, shows a similar behavior along $y^\star$ to the plane channel flow. In the near wall region, $C_{\tau_{12}}$ is significantly lower than in plane channel flow (see Fig. 4.37).

A more detailed analysis is provided by looking at the statistics along wall normal direction of the exact SGS tensor τ_{12} and its predicted counterpart by the Smagorinsky and WALE models at $x = 1.3$ as given in Fig. 5.37. As τ_{12} does not contain the $1/3\tau_{kk}$ term, it can provide an accurate comparison between the real and modeled quantities. Two filter sets ($\overline{\Delta_x^+} = 50$, $\overline{\Delta_z^+} = 20$) and ($\overline{\Delta_x^+} = 200$, $\overline{\Delta_z^+} = 80$) using both Lss-$5^{th}$

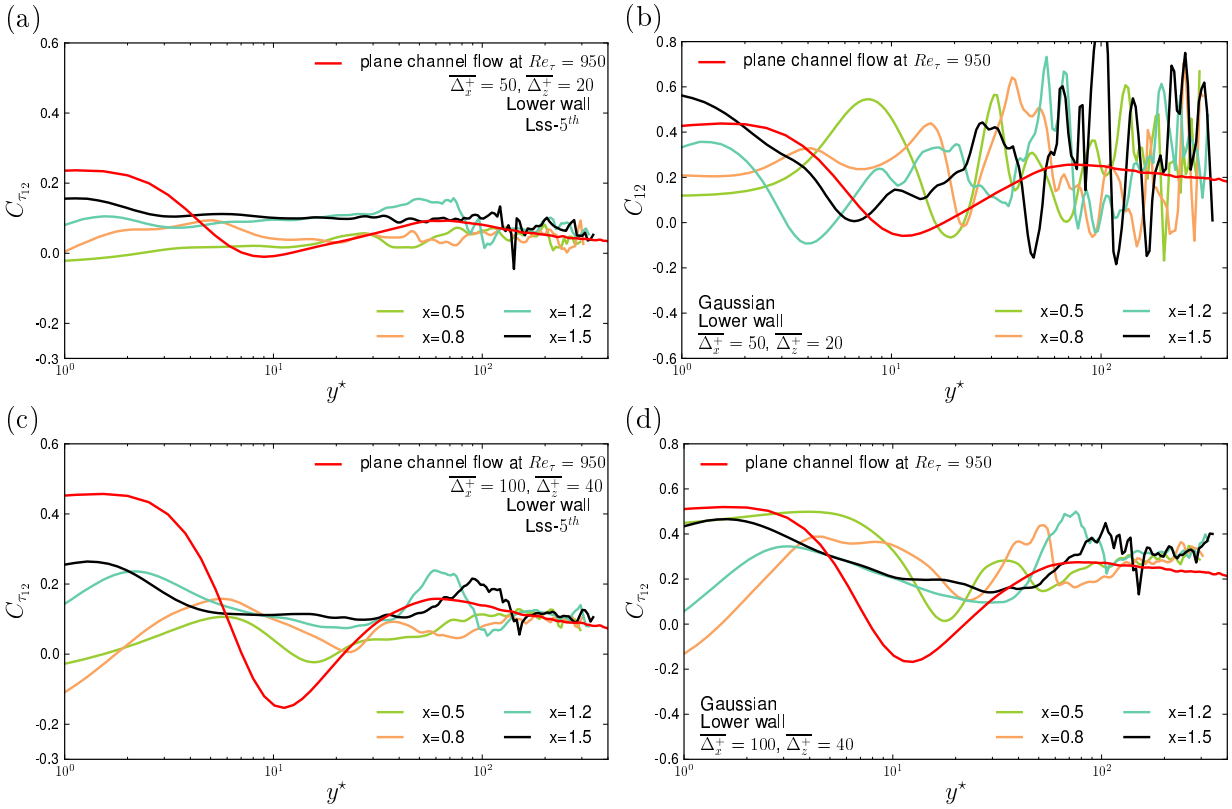

Figure 5.35: One-dimensional profiles of correlation $C_{\tau_{12}}$ at the lower wall using Lss-5^{th} (a, c) and Gaussian (b, d) filters.

and Gaussian filters are analyzed. Contrary to their behavior in plane channel flow (see Fig. 4.38), both the exact τ_{12} and its counterparts predicted by both models collapse to zero in the range $y^\star > 100$. In the near wall range $5 < y^\star < 80$, for the small Lss-5^{th} filter width ($\overline{\Delta_x^+} = 50$, $\overline{\Delta_z^+} = 20$), a slightly higher $C_{\tau_{12}}$ is obtained with the WALE model than the Smagorinsky model, while τ_{12} is better predicted by the Smagorinsky model for the filter set ($\overline{\Delta_x^+} = 50$, $\overline{\Delta_z^+} = 20$) with Gaussian filter in the same range. The difference between the exact τ_{12} and its counterparts becomes larger as increasing the filter width in the near wall region. For the largest filter width ($\overline{\Delta_x^+} = 200$, $\overline{\Delta_z^+} = 80$) with Lss-$5^{th}$, the worst prediction is obtained by the WALE model in range $40 < y^\star < 50$, where a deep drop of $\langle \tau_{12} \rangle$ occurs in the same range as the peak of turbulent kinetic energy (see Fig. 3.15(a)). It also corresponds to a low correlation $C_{\tau_{12}}$ obtained by both models in the same range (see Fig. 5.36). A similar behavior is observed at the upper wall (see Fig. B.13 in Appendix B).

A closer look at the standard deviation σ_{12} of the exact and modeled SGS stress tensor τ_{12} at the lower wall is shown in Fig. 5.38. Both models underpredict the fluctuations of τ_{12}, while the WALE model performs slightly better than the Smagorinsky model in the range $y^\star < 100$. With both filter types, large differences between the exact σ_{12} and its counterparts modeled by the Smagorinsky and WALE models are observed, with a peak in the range $30 < y^\star < 50$. This corresponds to a low correlation $C_{\tau_{12}}$ and a bad prediction for τ_{12} by both models in the same region. Thus, both the Smagorinsky and WALE models perform poorly in predicting the mean and fluctuation of SGS stress tensor τ_{12} in the recirculation region at the lower wall.

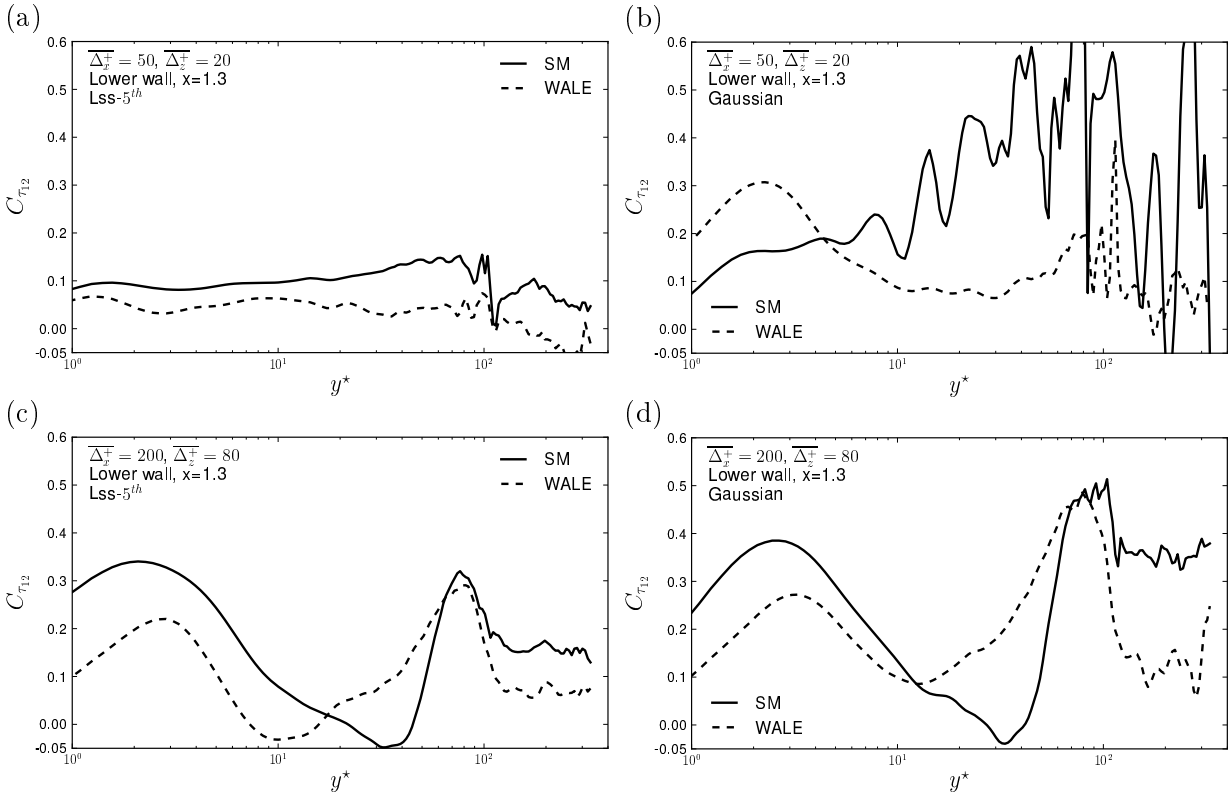

Figure 5.36: Comparison of correlation $C_{\tau_{12}}$ between Smagorinsky and WALE models using Lss-5^{th} filter (a, c) and Gaussian filter (b, d) at the lower wall.

5.5.2. Correlation of SGS force

Correlation of the SGS force f_i defined by equation (3.24) in Chapter 3 is an interesting alternative to evaluate the a priori performances of subgrid scale models, as it corresponds to the exact term involved in the Navier-Stokes equations. In our case, $\langle f_3 \rangle$ is zero due to the homogeneity in spanwise direction. Therefore, only components f_1 and f_2 are analyzed in the following. The wall normal distribution of SGS force at several streamwise locations is given in Fig. B.15 in Appendix B.

Correlations C_{f_1} and C_{f_2} between the two components of exact SGS force and their modeled counterparts by Smagorinsky model using both Lss-5^{th} and Gaussian filter width $\overline{\Delta_x^+} = 100$, $\overline{\Delta_z^+} = 40$ are given in Fig. 5.39. One can observe that, C_{f_1} and C_{f_2} with Lss-5^{th} filter and C_{f_1} with Gaussian filter is lower than 0.4 both in the converging and the diverging regions. In most regions of the channel, however, larger C_{f_2} (in the range $[0.4, 0.6]$) is obtained with the Gaussian filter. This result is in agreement with plane channel flow (see Fig. 4.42(a) and Fig. A.2). This large correlation may be due to the influence of $1/3\tau_{kk}$ which is added to the modeled SGS stress tensor. However, significantly higher correlation regions of C_{f_1} and C_{f_2} are observable above the two walls in the diverging APG part. In most regions, C_{f_1} and C_{f_2} are generally larger than in plane channel flow (see Fig. 4.43).

Comparison of correlations C_{f_1} and C_{f_2} between Smagorinsky and WALE models using both Lss-5^{th} and Gaussian filters at the lower wall are given in Fig. 5.40 at $x = 1.3$. As a difference with the plane channel flow, a peak of C_{f_1} and C_{f_2} occurs around $y^\star \simeq 100$ for

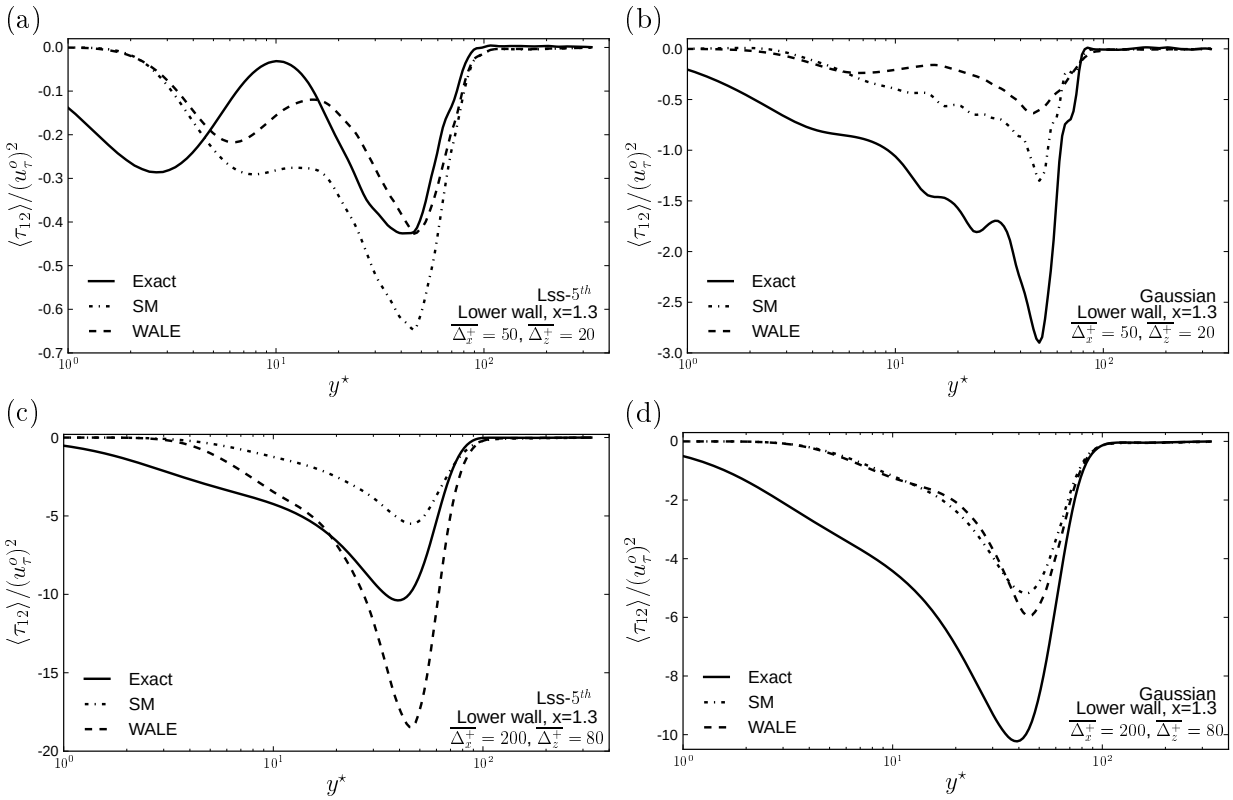

Figure 5.37: One-dimensional profiles of the exact τ_{12} and its modeled counterparts by the Smagorinsky and WALE models using the Lss-5^{th} (a, c) and Gaussian (b, d) filters at the lower wall.

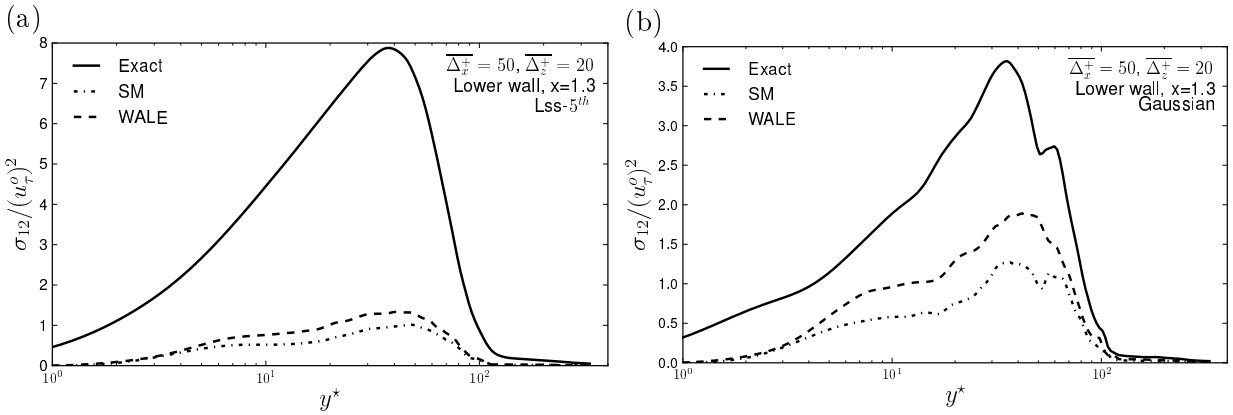

Figure 5.38: Standard deviation of the exact and modeled τ_{12} with filter width $\overline{\Delta_x^+} = 50$, $\overline{\Delta_z^+} = 20$ using Lss-5^{th} (a) and Gaussian (b) filters at the lower wall.

both models. These are roughly the same positions as the peak of $C_{\tau_{12}}$ both in streamwise and wall normal positions as shown in Fig. 5.36. When moving downstream, both C_{f_1} and C_{f_2} tend to become equivalent to the correlations in the outer region of plane channel flow (see Fig. 4.45). Along all normal positions, C_{f_1} and C_{f_2} are comparable or larger with the Smagorinsky than with the WALE model, except that larger C_{f_1} and C_{f_2} are obtained with the WALE model respectively in the range $y^\star > 100$ and $y^\star < 10$ using the largest Lss-5^{th} filter width ($\overline{\Delta_x^+} = 200$, $\overline{\Delta_z^+} = 80$). The main conclusion is that, the

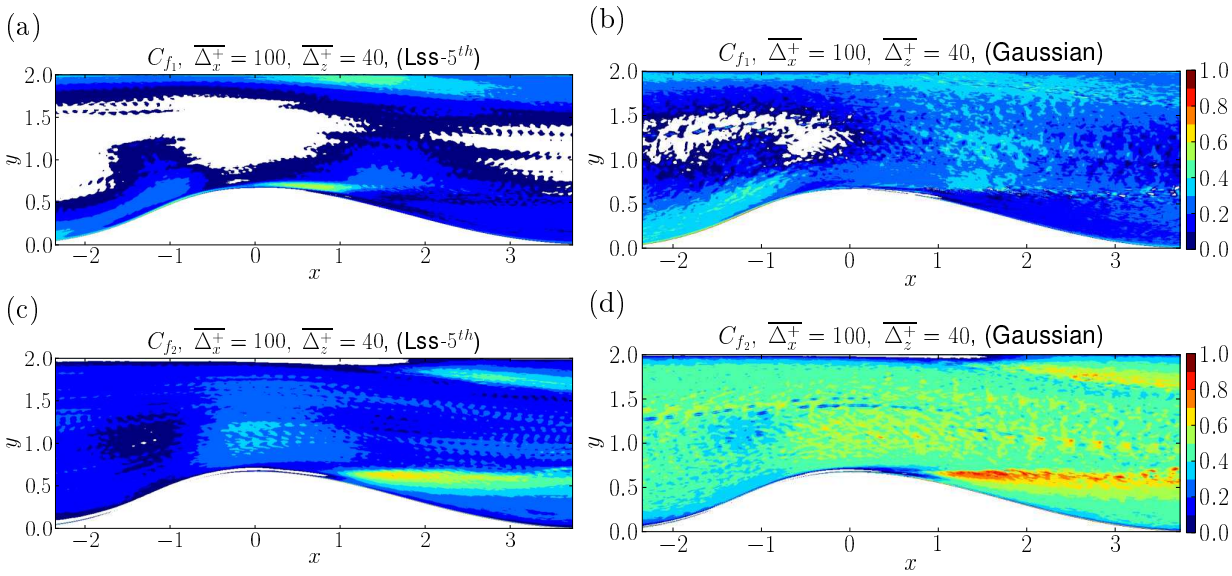

Figure 5.39: Correlations C_{f_1} and C_{f_2} between the exact SGS force and its counterpart modeled by the Smagorinsky model using Lss-5^{th} (a, c) and Gaussian (b, d) filters.

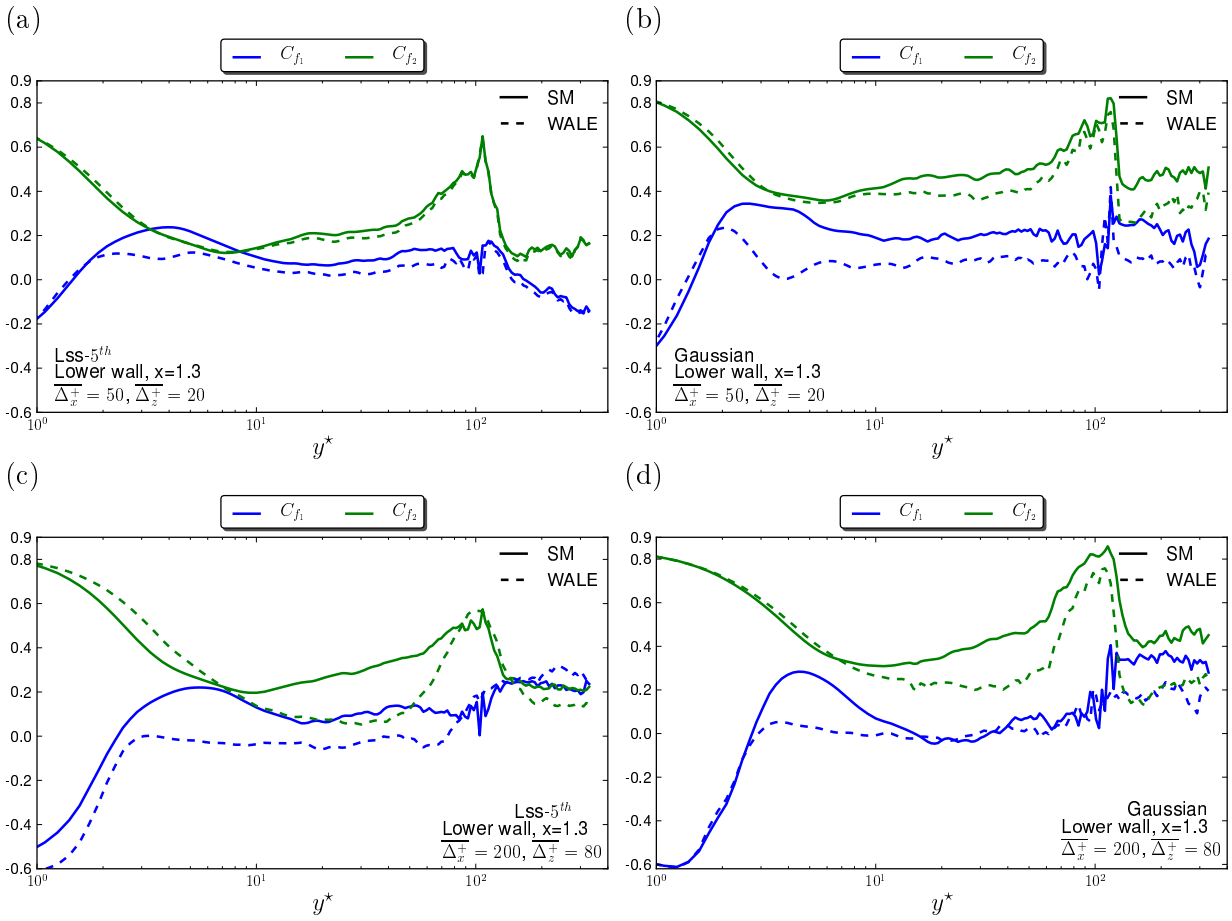

Figure 5.40: Comparison of correlations C_{f_1} and C_{f_2} obtained by the Smagorinsky and WALE models using Lss-5^{th} (a, c) and Gaussian (b, d) filters at the lower wall.

correlations C_{f_1} and C_{f_2} are larger with the Smagorinsky model than the WALE model in the outer region, while they are more dependent of the filter type and filter width in the near wall region.

5.5.3. Correlation of SGS energy dissipation

This section investigates the correlation between the SGS energy dissipation and its counterparts modeled by the subgrid scale models. The statistics of exact $\langle \epsilon_{sgs} \rangle$ are presented in Fig. 5.10 in Section 5.3. Correlation $C_{\epsilon_{sgs}}$ between ϵ_{sgs} and its modeled counterparts by Smagorinsky model using Lss-5^{th} and Gaussian filters is given in Fig. 5.41. In most region, poor correlation (in the range $[0.0, 0.4]$) is observed with the Lss-5^{th} filter, while higher correlation (in the range $[0.4, 0.6]$) is obtained with the Gaussian filter. This is in agreement with the influence of the filter type in plane channel flow (see Fig. 4.47 and A.3). However, with the Gaussian filter, significantly high correlation $C_{\epsilon_{sgs}}$ (up to 0.8) appear in the diverging channel center and in the turbulent layer above the lower wall. This value is higher than the correlation in plane channel flow and may be due to the influence of adverse pressure gradient.

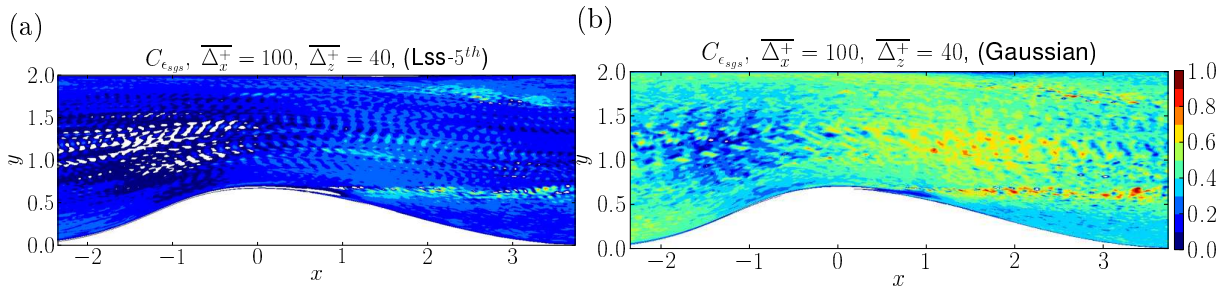

Figure 5.41: Correlations $C_{\epsilon_{sgs}}$ between exact SGS energy dissipation and its modeled counterparts by Smagorinsky model using Lss-5^{th} (a) and Gaussian (b) filters.

Comparison of $C_{\epsilon_{sgs}}$ obtained by the Smagorinsky and WALE models at the lower wall and at $x = 1.3$ is shown in Fig. 5.42. Similarly to $C_{\tau_{12}}$ and C_{f_1}, C_{f_2}, a peak of $C_{\epsilon_{sgs}}$ appears close to $y^\star \simeq 100$ for both models, independently of the filter type and filter width. With the larger filter width ($\overline{\Delta_x^+} = 200$, $\overline{\Delta_z^+} = 80$) for both filter types, higher correlation is obtained with the Smagorinsky than with the WALE model in the whole channel region. However, for the small Gaussian filter width ($\overline{\Delta_x^+} = 50$, $\overline{\Delta_z^+} = 20$), the behavior of $C_{\epsilon_{sgs}}$ is close to the plane channel flow. For the small Lss-5^{th} filter width ($\overline{\Delta_x^+} = 50$, $\overline{\Delta_z^+} = 20$), no significant difference between models occurs in the range $y^\star > 20$, while a worse correlation $C_{\epsilon_{sgs}}$ occurs close to the wall with the WALE model. Therefore, although the coefficients of subgrid scale models are calculated by matching the real and the modeled SGS energy dissipation, the correlation between them, which is dependent of the filter type and filter width, is not high at the lower wall, and it depends on the filter type and filter width. A similar behavior is observed at the upper wall (see Fig. B.18 in Appendix B).

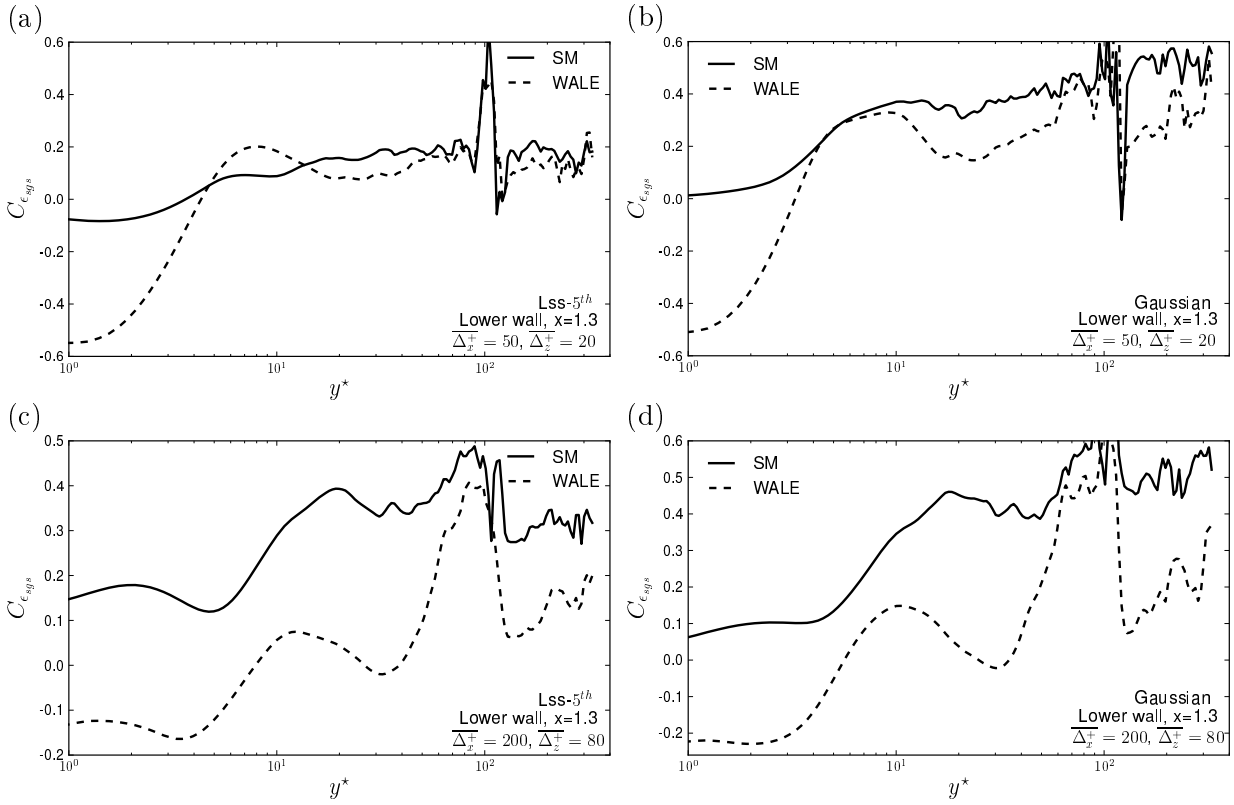

Figure 5.42: Comparison of correlation $C_{\epsilon_{sgs}}$ obtained by the Smagorinsky and WALE models at the lower wall using Lss-5^{th} (a, c) and Gaussian (b, d) filters.

5.5.4. Conclusion

This section has investigated the correlations and the predictive capabilities of subgrid scale models based on three criteria. The SGS tensor is found to be more correlated with the turbulent kinetic energy at the lower wall than at the upper wall. This agrees well with the behavior of SGS energy dissipation. But the large values of the SGS stress tensor do not correspond to regions of high correlation. In the recirculation region, low $C_{\tau_{12}}$ is observed, and the influence of the filter type on $C_{\tau_{12}}$ is larger for the small than for large filter width. A peak of $C_{\tau_{12}}$ appears for the large filter width. Due to the influence of $1/3\tau_{kk}$, C_{f_2} is significantly larger with Gaussian than with Lss-5^{th} filter. Higher correlation of ϵ_{sgs} is also observed with Gaussian than with Lss-5^{th} filter. In the diverging APG region, the maximum of ϵ_{sgs} is even larger than in plane channel flow.

The difference between model performances are also analyzed. In most outer regions at the lower wall, the Smagorinsky model has higher correlations $C_{\tau_{12}}$, C_{f_1}, C_{f_2}, as well as $C_{\epsilon_{sgs}}$ than the WALE model. It is important to note that, the mean and the fluctuation of SGS stress tensor τ_{12} is badly predicted by the Smagorinsky and WALE models in the near wall region, corresponding to a low correlation $C_{\tau_{12}}$ in the same range. However, although the coefficients of subgrid scale models are calculated by matching the real and modeled SGS energy dissipation, the correlation between them is low.

5.6. Conclusion

This Chapter firstly investigated the energy transfer mechanisms in converging-diverging channel flow, with special attention on the APG region. Two regions of both strong SGS energy transfer and strong SGS energy dissipation are observed in the diverging APG near wall regions, with a higher intensity at the lower wall than at the upper wall. These regions correspond to an intense production of vortices, observed by Laval *et al.* 2012 [73] for the same flow. The one-dimensional analysis of the energy transfer mechanisms reveal that, both $\langle T_{sgs} \rangle$ and $\langle \epsilon_{sgs} \rangle$ are more correlated with the turbulent kinetic energy and the fraction of subgrid scale kinetic energy at the lower wall than at the upper wall, independently of the filter width and type. The influence of the sharpness of the Lss-5^{th} filter is larger for the positive and negative SGS energy transfer than for the contributions of the SGS energy dissipation, for the present converging-diverging channel flow compared to the plane channel.

Secondly, the coefficients of four subgrid scale models are evaluated. Contrary to the plane channel flow, significant negative coefficients of subgrid scale models, corresponding to backward SGS energy dissipation, occur in the converging channel center. Due to the filter type dependent behavior of the SGS energy dissipation and its counterparts modeled by the subgrid scale models, the coefficients of the four subgrid models are larger with Gaussian than with Lss-5^{th} filter in the diverging channel center. Owing to a larger norm of the strain rate tensor $\langle \overline{S}_{ij} \rangle$ in the near wall region than in the channel center, small $\langle C_s \rangle$ and $\langle C_d \rangle$ are obtained near the wall, independently of the filter type and filter width. The coefficients $\langle C_w \rangle$ and $\langle C_\sigma \rangle$ are found to have quite similar behavior in the present a priori analysis. The filter width dependent behavior of the operator $\langle S^d_{ij} S^d_{ij} \rangle$ of the WALE model and the operator $\langle D_\sigma \rangle$ of the σ models leads to higher $\langle C_w \rangle$ and $\langle C_\sigma \rangle$ near both the lower and upper walls in the diverging APG region, especially for the larger filter width with both filter types. The one-dimensional analysis show that, a new peak of each model coefficient is observed in the recirculation region.

Finally, the model performances based on three criteria are analyzed. The Smagorinsky model has higher correlations $C_{\tau_{12}}$, C_{f_1}, C_{f_2}, and $C_{\epsilon_{sgs}}$ than the WALE model in most regions of the lower wall. In the near wall region, the mean and the fluctuation of SGS stress tensor τ_{12} is badly predicted by the Smagorinsky and WALE models, corresponding to a low correlation $C_{\tau_{12}}$ in the same range. A similar but less pronounced behavior compared to the circulation region is observed at the upper wall. However, the low correlation based on the SGS energy dissipation is slightly higher than in plane channel flow.

Chapter 6

Conclusions and Perspectives

6.1. Conclusions

In order to investigate the behavior of subgrid scale models under the effect of different pressure gradients, an a priori analysis is first conducted in a plane channel flow at fairly high Reynolds number to provide a reference for the a priori analysis of a flow with a more complex geometry. Compared to the previous research of plane channel flow at low or moderate Reynolds number (Piomelli *et al.* 1991 [112]; Horiuti 1997 [65]), a significant peak of the SGS energy dissipation is observed near the peak of turbulent kinetic energy at $y^\star = 10$. In addition to the SGS energy dissipation traditionally analyzed at low Reynolds number, the full terms of SGS energy transfer are investigated. A net back-scatter of SGS energy transfer is observed in the viscous layer. But the averaged positive and negative contributions of local SGS energy transfer are significantly larger than the net SGS energy transfer, especially with the sharp Lss-5^{th} filter. So, only considering the net term may be misleading, as it does not reveal the full energy transfer mechanisms of turbulence.

Then the coefficients of four eddy-viscosity models are evaluated a priori in the plane channel flow. In the outer region, lower values of the Smagorinsky model coefficient are obtained as compared to previous a priori estimates for plane channel flow (Liu *et al.* 1999 [78]). One part of the explanation may be due to the 2D filtering or the sensitivity of the model coefficients to the mesh size. However, this a priori estimate is rather independent of the filter type and only slightly function of the filter width in the range investigated. The averaged Smagorinsky coefficient computed from large scales using the dynamic procedure is on average underpredicted compared to the standard Smagorinsky coefficient. However, a good agreement between the two coefficients is obtained with small filter width, when the ratio between the streamwise and spanwise filter widths is small. The a priori analysis reveals a strong sensitivity of the averaged coefficients of both the WALE and σ models in the viscous and the beginning of the buffer layer regions. Therefore, the uniformity of both the WALE and the σ model coefficients breaks down when approaching the wall. In the outer region, the averaged coefficient of the WALE model in the range $(0.2, 0.35)$ and the averaged coefficient of the σ model in the range $(0.5, 0.85)$ are significantly smaller than their recommended values for homogeneous isotropic turbulence (0.5 for the WALE model, according to Nicoud and Ducros 1999 [102]) or plane channel flow (1.5 for the σ model, according to Nicoud *et al.* 2011 [103]). The

ratio between the WALE model coefficient and the Smagorinsky model coefficient is higher than the ratio estimated by Nicoud and Ducros 1999 [102] for homogeneous isotropic turbulence.

Subsequently, a closer look at how well the subgrid scale models reproduce the statistics of subgrid scale quantities is investigated by comparing the statistics and the correlation of the exact and modeled quantities based on the SGS stress tensor. The correlations of the normal components of the SGS stress tensor τ_{ii} are higher than the results of Carper and Porté-Agel 2008 [25]. However, it is shown that the correlations of these components are largely dependent of the way of considering or non-considering the trace of the SGS stress tensor which is not modeled. The statistics of τ_{12} is investigated in more detail and it is found that the correlation between its exact and modeled counterpart is lower than the correlation obtained by Carper and Porté-Agel 2008 [25] in a wind tunnel with a low Reynolds number. Higher correlations are obtained with the smoother Gaussian filter. This is known as a consequence of the overlapping between resolved and unresolved scales. Although the coefficients of subgrid scale models are computed by matching the measured and modeled subgrid scale dissipation, the correlation of the SGS energy dissipation is low both in the near wall and outer regions. The present a priori analysis of correlations and models performances indicates that, the local characteristics of the subgrid scale quantities including the SGS energy dissipation are poorly modeled. The role of eddy viscosity models is only to reproduce the averaged dissipative effect of turbulence. However, low correlations do not indicate a failure of such models but a fundamental limitation of a priori test itself (Park 2005 [107]).

To the best of our knowledge, the present work is the first attempt to perform an a priori analysis of subgrid scale models in wall turbulence with pressure gradient and wall curvature. Contrary to what has been observed in plane channel flow, weak back scatter of SGS energy transfer and SGS energy dissipation are observed in the converging channel center and above the edge of the bump before the summit, under the effect of favorable pressure gradient. However, the present a priori analysis is mainly focused on the diverging APG region, with special attention to the recirculation region at the lower wall, as it is the most difficult region of the flow to be modeled. Due to the intense production of turbulent kinetic energy, two strong forward scatter regions of SGS energy transfer and SGS energy dissipation occur in the diverging APG regions. This forward scatter is more intense along the lower wall. Above the recirculation region, the forward scatter begins further from the wall, compared to plane channel flow. In the diverging APG near wall regions, the averaged SGS energy transfer in the diverging APG near wall regions reveal that, the kinetic energy of strong vortices generated by the streaks instability upstream of the separation point is not transfered to the large resolved scales when moving downstream, as the net averaged energy flux is going from the large resolved to small unresolved scales in this region. This is corroborated by a higher probability of points experiencing forward scatter.

The a priori evaluation of the subgrid scale model coefficients reveals strong non-uniformity within the whole simulated region. This is due to the different behavior of both the exact SGS energy dissipation and its modeled counterpart, which are sensitive to the filter type and filter width. Low values of coefficients of the standard Smagorinsky model and Dynamic Smagorinsky model occur in the diverging APG near wall regions with both filter types, while high values with Gaussian filter are observed in the diverging

channel center. Meanwhile, higher values of coefficients of the WALE and σ models are observed in the diverging channel center with Gaussian filter. However, both filter type lead to high coefficients of the WALE and σ models in the region of strong energy production, near the two walls, especially for large filter width. Therefore, when a constant appropriate to the core flow is adopted in a LES, statistics in the diverging APG near wall regions may be incorrectly predicted, especially with a coarse mesh or a large explicit or smooth filter. This confirms the results of Kuban *et al.* 2012 [70] in LES of the same flow configuration but with different simulating parameters (different mesh grid, different filter) as compared to the present analysis. They adopted a constant coefficient of the WALE model and obtain results which are not very accurate in the diverging near wall regions. The coefficient of the σ model is also variable in a quite similar way as the coefficient of the WALE model in the whole channel region.

The correlations of the SGS stress tensor, the SGS force and the SGS energy dissipation are also investigated in this database of channel flow with a curved wall. Low $C_{\tau_{12}}$ correlation is obtained independently of the filter type and filter width. But slightly higher $C_{\tau_{12}}$ is observed with the Gaussian filter in the recirculation region somewhat above the lower wall, indicating a slightly better correlation between the SGS stress tensor τ_{12} and its counterpart modeled by the Smagorinsky model. However, both the Smagorinsky and WALE models perform poorly in predicting the mean and fluctuation of SGS stress component τ_{12} in the recirculation region. Similarly to what has been observed in plane channel flow, the correlation of the SGS energy dissipation is low. Higher correlation of the SGS energy dissipation is observed with the Gaussian filter compared to the plane channel flow, in the diverging channel center and even near the lower wall in the diverging APG region.

6.2. Perspectives

For the plane channel flow, additional a priori analysis with various Reynolds number and with the same filter sets as in present analysis would be useful to address the effect of the Reynolds number. As the peaks of coefficients of the WALE and σ models with the large spanwise filter width are observed in the near wall region, both models with coefficients obtained by a priori estimate with small spanwise filter width could be tested in a posteriori analysis of the same configuration and with equivalent explicit filters.

For the converging-diverging channel flow, the size and shape of vortices associated with the streaks instability as well as the statistics of the resulting vortices were investigated by Laval *el al.* 2012 [71] [73]. The present a priori analysis shows that, both the forward and backward contributions are more significant than the net SGS energy transfer term. Therefore, a more detailed analysis of the turbulence structures is expected to provide information on the full energy transfer mechanisms. As significant back scatter of both SGS energy transfer and SGS energy dissipation is observed, other non-eddy viscosity models which can reflect the back scatter energy cascade of turbulence, like the Scale Similarity Model, or other models with high correlations or good predictive capabilities of statistics could be tested both a priori and a posteriori.

Using the same flow configuration, Kuban *et al.* 2012 [70] showed that, using a single filter in the wall normal direction and different subgrid scale models, they could not

get a good near wall agreement with DNS in the diverging APG region. Therefore, a posteriori analysis with a comparable explicit filtering both in the streamwise and spanwise directions as our a priori analysis could be tested. The explicit filtering allows the filter size to be chosen independently of the mesh spacing, which can alleviate the sensitivity of the results to the mesh and minimizes the effects of numerical error in practical simulations.

According to Kuban *et al.* 2012 [70], the near wall results obtained with a constant WALE model coefficient are close to the results obtained using the Dynamic Smagorinsky model. Thus, it is interesting to conduct a priori analysis for the WALE and σ models with a dynamic procedure for a deep comparison with their standard formulations, in order to investigate the local behavior of these model coefficients.

Unfortunately, due to the limitation of computational resources, a limited number of filter width have been tested in the present study. Since the coefficients of the WALE and σ models are found to be sensitive to the spanwise filter width in the plane channel flow, a more complete analysis could be useful to evaluate their specific sensitivity to the filter width in different direction and in different regions of the converging-diverging channel.

In our study, performances of four eddy viscosity models have been investigated in the converging-diverging channel flow with a curved wall. As in the present configurations, the pressure gradient strongly evolves in space, the physics of the flow is far from equilibrium. The results of our a priori analysis are difficult to generalize to other APG flows. Unfortunately, a priori research of subgrid scale models at such kind flow is scarce, as full 3D databases of flows with complex geometry at a high Reynolds number is not easy to be acquired. However, more a priori and a posteriori tests of these models are required to be conducted in other databases of turbulent flow with various pressure gradients at a large enough Reynolds number, in order to improve our knowledge on the effect of pressure gradient or curvature on the subgrid scale models behavior.

Bibliography

[1] A. Abbà, C. Cercignani, and L. Valdettaro. Analysis of subgrid scale models. *Computers and Mathmatics with Application*, 46:521–535, 2003.

[2] E.T.M. Andrés and E.J. Kenneth. A dynamic smagorinsky model with dynamic determination of the filter width ratio. In *This material is based upon work supported by the National Science Foundation under Grant No. 9985340. b Present address: Center for Coastal Physical Oceanography,Old Dominion University, Norfolk, VA 23529*, 2004.

[3] C. D. Aubertine. *Reynolds number effects on an adverse pressure gradient turbulent boundary layer*. PhD thesis, The Department of Mechanical Engineering of Stanford University, 2005.

[4] C. D. Aubertine and J. K. Eaton. Turbulence development in a non-equilibrium turbulent boundary layer with mild adverse pressure gradient. *J. Fluid. Mech.*, 532:345–364, 2005.

[5] E. Balaras, C. Benocci, and U. Piomelli. Two-layer approximate boundary conditions for large eddy simulation. *AIAA Jornal*, 34:1111, 1996.

[6] J. Bardina, J. H. Ferziger, and W. C. Reynolds. Improved subgrid models for large eddy simulation. *AIAA paper*, 80:1357, 1980.

[7] J. Bardina, J. H. Ferziger, and W. C. Reynolds. Improved turbulence models based on large eddy simulation of homogeneous, incompressible, turbulent flows. Technical report, Technical Report TF-19, Thermal sciences div., Dept. of Mech. Engg., Stanford, 1983.

[8] G. I. Barenblatt, A. J. Chorin, and V. M. Prostokishin. A model of a turbulent boundary layer with a nonzero pressure gradient. *PNAS*, 99(9):5772–5776, 2002.

[9] H. Baya Toda, O. Cabrit, G. Balarac, S. Bose, J. Lee, Choi H., and F. Nicoud. A subgrid-scale model based on singular values for les in complex geometries. In *Center for Turbulence Research, Proceedings of the Summer Program.*, 2010.

[10] K. H. Bech, D. S. Henningson, and R. A. W. M. Henkes. Linear and nonlinear development of localized disturbances in zero and adverse pressure gradient boundary-layers. *Phys. Fluids*, 10(6):1405–1418, 1998.

[11] A. Bernard, J. M. Foucaut, P. Dupont, and M. Stanislas. Decelerating boundary layer : a new scaling and mixing length model. *AIAA Journal*, 41(2):248–255, 2003.

[12] L.C. Berselli and T. Iliescu. A higher-order subfilter-scale model for large eddy simulation. *Journal of computaional and applied mathenatics*, (159):411–430, 2003.

[13] L.C. Berselli, T. Iliescu, and W.J. Layton. Mathematics of large eddy simulation of turbulent flow. *Phys. Fluids*, 1991.

[14] V. Borue and S. A. Orszag. Local energy flux and subgrid-scale statistics in three-dimensional turbulence. *J. Fluid Mech.*, 366:1–31, 1998.

[15] F.V.D. Bos and B.J. Geurts. Commutator errors in the filtering approach to large-eddy simulation. *Phys. Fluids*, 17, 2005.

[16] S. T. Bose, P. Moin, and D. You. Grid-independent large-eddy simulation using explicit filtering. *Phys. Fluids*, 22(105103):1–11, 2010.

[17] E. Bou-Zeid, M. B. Vercauteren, N.and Parlange, and C. Meneveau. Breaking of standing waves through two-dimensional instabilities. *Phys. Fluids*, 20, 2008.

[18] E. Bou-Zeid, N. Vercauteren, M. B. Parlange, and C. Meneveau. Scale dependence of subgrid-scale model coefficients: An a priori study. *Phys. Fluids*, 20, 2008.

[19] T Brandt. A priori tests on numerical errors in large eddy simulation using finite differences and explicit filtering. *International Journal for Numerical Methods in Fluids, Int. J. Numer. Meth. Fluids*, 51:635–657, 2006.

[20] T Brandt. Use of explicit filtering, second-order scheme and sgs models in les of turbulent channel flow. In *European Conference on Computational Fluid Dynamics*, TU Delft, The Netherlands, 2006.

[21] W. Cabot and P. Moin. Approximate wall boundary conditions in the large-eddy simulation of high reynolds number flow. *Flow, Turbul. Combust.*, 63, 2000.

[22] V. M. Canuto and Y. Cheng. Determination of the Smagorinsky-Lilly constant cs. *Phys. Fluids*, 9, 1997.

[23] D. Carati, G. S. Winckelmans, and H. Jeanmart. On the modelling of the subgrid-scale and filtered-scales stress tensors in large eddy simulation. *J. Fluid. Mech.*, pages 119–138, 2001.

[24] M. A. Carper and F. Porté-Agel. Subfilter-scale fluxes over a surface roughness transition. part i: Measured fluxes and energy transfer rates. *Boundary-Layer Meteorol*, 126:157–179, 2008.

[25] M. A. Carper and F. Porté-Agel. Subfilter-scale fluxes over a surface roughness transition. part ii: A priori study of large-eddy simulation models. *Boundary-Layer Meteorol*, 127:73–95, 2008.

[26] D.R. Chapman. Computational aerodynamic development and outlook. *AIAA Journal*, 17:1293, 1979.

[27] J.-P. Chollet and M. Lesieur. Parametrization of small scales of three-dimensional isotropic turbulence utilizing spectral closure. *J. Atmos. Sci.*, 38:2747–2757, 1981.

[28] F. K. Chow and P. Moin. A further study of numerical errors in large eddy simulations. *Journal of Computational Physics*, 184:366–380, 2003.

[29] D. Chung and D. I.. Pullin. Large-eddy simulation and wall modelling of turbulent channel flow. *J. Fluid Mech.*, 631:281–309, 2009.

[30] A. Cimarelli and E. De Angelis. Anisotropic dynamics and sub-grid energy transfer in wall-turbulence. *Phys. Fluids*, 24(015102):1–18, 2012.

[31] R. Clark, J. Ferziger, and W. Reynolds. Evaluation of subgrid-scale models using an accurately simulated turbulent flow. *J. Fluid Mech.*, 91:1–16, 1979.

[32] F. H. Clauser. Turbulent boundary layers in adverse pressure gradients. *J. Aero. Sci.*, 21(2):91–108, 1954.

[33] C. B. Da Silva. The behavior of subgrid-scale models near the turbulent/nonturbulent interface in jets. *Phys. Fluids*, 21:081702, 2009.

[34] C. B. Da Silva and J. C. F. Pereira. The effect of subgrid-scale models on the vortices computed from large-eddy simulations. *Phys. Fluids*, 16(12), 2004.

[35] C. De Stefano, O. V. Vasilyev, and D. E. Goldstein. A-priori dynamic test for deterministic/stochastic modeling in large-eddy simulation of turbulent flow. *Computer Physics Communications*, pages 210–213, 2005.

[36] J. Deardorff. A numerical study of three-dimensional turbulent channel flow at large Reynolds numbers. *J. Fluid Mech.*, 41:453–480, 1970.

[37] J. C. del Alamo and J. Jiménez. Direct numerical simulation of the very large anasotropic scales in a turbulent channel. *Center for Turbulence Research, Annual Research Brief*, pages 329–341, 2001.

[38] J.C. del Álamo. *The largest scales in turbulent channel flow.* PhD thesis, Ph. D. Thesis Universidad Politécnica de Madrid, 2003.

[39] P. Diercks. An algorithm for smoothing, differenciation and integration of experimental data using spline functions. *J. Comp. Appl. Math.*, 1(3):165–184, 1975.

[40] J. A. Domaradzki, W. Liu, C. Härtel, and L. Kleiser. Energy transfer in numerically simulated wall-bounded turbulent flows. *Phys. Fluids*, 6:1583–1599, 1994.

[41] S. Drobniak, W. Elsner, A. Drozdz, and M. Materny. Experimental analysis of turbulent boundary layer with adverse pressure gradient corresponding to turbomachinery conditions. In M. Stanislas, J. Jimenez, and I. Marusic, editors, *Progress in wall turbulence : understanding and modelling*, ERCOFTAC Series, Villeneuve d'Ascq, France, April 21-23, 2009. Springer.

[42] F. Ducros, F. Nicoud, and T. Poinsot. Wall-adapting local eddy-viscosity models for simulation in complex geometies. In *Nmerical Methods for Fluid Dynamics VI*, pages 293–299, 1998.

[43] C. Duprat, G. Balarac, O. M´ etais, P. M. Congedo, and O. Brugiére. A wall-layer model for large-eddy simulations of turbulent flows with/out pressure gradient. *Phys. Fluids*, 23(015101):1–12, 2011.

[44] V. Efros. Large eddy simulation of channel flow using wall functions. Master's thesis, Department of Applied Mechanics, Chalmers University of Technology, 2006.

[45] W. Elsner, L. Kuban, and A. Tyliszczak. LES of turbulent channel flow with pressure gradient corresponding to turbomachinery condition. In M. Stanislas, J. Jimenez, and I. Marusic, editors, *Progress in wall turbulence : understanding and modelling*, ERCOFTAC Series, Villeneuve d'Ascq, France, April 21-23, 2009. Springer.

[46] W. Elsner, L. Kuban, and A. Tyliszczak. Subgrid scale modeling of turbulent channel flow with adverse pressure gradient. *PAMM, Proc. Appl. Math. Mech. (to be publish)*, 2009.

[47] J. H. Ferziger. Direct and large eddy simulation of turbulence. Technical report, Department of Mechanical Engineering, Stanford University, Stanford, CA, 1995.

[48] J. Fröhlich, C. P. Mennen, W. Rodi, L. Temmerman, and A. Leschziner. Highly resolved large-eddy simulation of separated flow in a channel with streamwise periodic constrictions. *J. Fluid. Mech.*, 526:19–66, 2005.

[49] J. Fröhlich and D. von Terzi. Hybrid LES/RANS methods for the simulation of turbulent flows. *Progress in Aerospace Sciences*, 44(5):349–377, 2008.

[50] W. K. George, M. Stanislas, and J.-P. Laval. New insights into adverse pressure gradient boundary layers,. In *Bulletin of the American Physical Society, 63th Annual Meeting of the APS Division of Fluid Dynamics, Long Beach, California APS Bull, USA*, volume 55 (16), 2010.

[51] W.K. George. Recent advancements toward the understanding of turbulent boundary layers. *AIAA Journal*, 44(11):2435–2449, 2006.

[52] M. Germano. Turbulence: the filtering approach. *J. Fluid Mech.*, 238:325, 1992.

[53] M. Germano, U. Piomelli, P. Moin, and W. H. Cabot. A dynamical subgrid-scale eddy viscosity model. *Phys. Fluids A*, 3:1760–1765, 1991.

[54] B.J. Geurts. *Elements of direct and large-eddy simulation*. Edwards, Philadelphia, 2004.

[55] B.J. Geurts and D.D. Holm. Commutator errors in large-eddy simulation. *J. Phys. A: Math. Gen.*, 39, 2006.

[56] S. Ghosal. An analysis of numerical errors in large-eddy simulations of turbulence. *J. Comp. Phys.*, 125:187, 1996.

[57] S. Ghosal, T. S. Lund, P. Moin, and K. Akselvoll. A dynamical localization model for large-eddy simulation of turbulent flows. *J. Fluid Mech.*, 286:229–255, 1995.

[58] S. Ghosal and P. Moin. The basic equations for the large eddy simulation of turbulent flows in complex geometry. *Journal of computational physics*, 118:24–37, 1995.

[59] G. Grötzbach. Direct numerical and large eddy simulation of turbulent channel flows. *Encyclopedia of Fluid Mechanics*, 6:1337–1391, 1987.

[60] J. Gullbrand. Explicit filtering and subgrid-scale models in turbulent channel flow. *Center for Turbulence Research*, Annual Research Briefs 2001:31–42, 2001.

[61] C. Hartel and L. Kleiser. Analysis and modelling of subgrid-scalemotions in near-wall turbulence. *J. Fluid Mech.*, 356:327–352, 1998.

[62] C. Hartel, L. Kleiser, F. Unger, and R. Friedrich. Subgrid-scale energy transfer in the near wall region of turbulent flows. *Phys. Fluids*, 6(9):3130–3143, 1994.

[63] Z. Harun, V. Kulandaivelu, B. Nugroho, M. Khashhchi, J. P. Monty, and I. Maruzic. Large-scale structures in an adverse pressure gradient turbulent boundary layer. In *8^{th} International Symposium on Engineering Turbulence Modelling and Measurements - ETMM8*, pages 183–188, Marseille, France, 9-11 June, 2010.

[64] G. Hauët, C. B. da Silva, and J. C. Pereira. The effect of subgrid-scale models on the near wall vortices: A priori tests. *Phys. Fluids*, 19, 2007.

[65] K. Horiuti. Backward scatter of subgrid-scale energy in wall-bounded and free shear turbulence. *Journal of the Physical Society of Japan*, 66(1):91–107, 1997.

[66] N. Hutchins and I. Marusic. Large scale influences in near wall turbulence. *Philosophycal transactions of the royal society A*, 365:647–664, 2007.

[67] S. A. Jordan. A large-eddy simulation methodology in generalized curvilinear coordinates. *Journal of Computational Physics*, 148:322–340, 1999.

[68] C. A. Kennedy and M. H. Carpenter. Several new numerical methods for compressible shear-layer simulations. *Applied Numerical Mathematics*, 14:397–433, 1994.

[69] L. Kuban, W. Elsner, and A. Tyliszczak. Les of converging-diverging channel flow with seperation. *Task Quarterly*, 14(3):283–295, 2010.

[70] L. Kuban, J.-P. Laval, and W. Elsner. Les modeling of converging diverging turbulent channel flow. *Journal of Turbulence*, 13(11):1–19, 2012.

[71] J-P. Laval. *Analyse et modélisation des interactions de la turbulence à petites échelles*. HDR thesis, University of Lille 1, 2012.

[72] J.-P. Laval, M. Marquillie, and U. Ehrenstein. Stability analysis of turbulent boundary layer flows with adverse pressure gradient. In *The 11th Experimental Chaos and Complexity Conference*, Lille, France, 1-4 June, 2010.

[73] J.-P. Laval, M. Marquillie, and U. Ehrenstein. On the relation between kinetic energy production in adverse-pressure gradient wall turbulence and streak instability. *Journal of Turbulence*, 13(21):1–19, 2012.

[74] M. Lesieur and O. Métais. New trends in large-eddy simulations of turbulence. *Ann. Rev. Fluid Mech.*, 28:45–82, 1996.

[75] D. Leslie and G. Quarini. The application of turbulence theory to the formulation of subgrid modeling procedure. *J. Fluid Mech.*, 91:65–91, 1979.

[76] D. K. Lilly. A proposed modification of the Germano subgrid-scale closure method. *Phys. Fluids A*, 4:633–635, 1992.

[77] D.K. Lilly. The representation of small-scale turbulence in numerical simulation experiments. *Proceedings of the IBM Scientific Computing Symposium on Environmental Sciences*, 1967.

[78] C. H. Liu and J. D. Doorly. Evolution and modelling of subgrid scales during rapid straining of turbulence. *J. Fluid Mech.*, 387:281–320, 1999.

[79] M. Liu, X-P. Chen, and N. P. Kannan. Comparative study of the large eddy simulations with the lattice boltzmann method using the wall-adapting local eddy-viscosity and vreman subgrid scale models. *CHIN. PHYS. LETT.*, 29(10), 2012.

[80] S. Liu, C. Meneveau, and J. Katz. On the properties of similarity subgrid-scale models as deduced from measurments in a turbulent jet. *J. Fluid Mech.*, 275:83–119, 1994.

[81] G. Lodato, L. Vervisch, and P. Domingo. A compressible wall-adapting similarity mixed model for large-eddy simulation of the impinging round jet. *Phys. Fluids*, 21, 2009.

[82] H. Lu and F. Porté-Agel. A modulated gradient model for large-eddy simulation: Application to a neutral atmospheric boundary layer. *Phy. of Fluids*, 22, 2010.

[83] D. Lucor, J. Meyers, and P. Sagaut. Sensitivity analysis of LES to subgrid-scale-model parametric uncertainty using polynomial chaos. *J. Fluid Mech.*, 585:255–279, 2007.

[84] T. S. Lund. On the use of discrete filters for large eddy simulation. *Center for Turbulence Research, Annual Research Briefs*, pages 83–95, 1997.

[85] T. S. Lund and H. J. Kaltenbach. Experiments with explicit filtering for les using a finite-difference method. *Center for Turbulence Research, Annual Research Briefs*, 1995.

[86] T.S. Lund. The use of explicit filters in large eddy simulation. *Computers and Mathematics with Applications*, 46:608–618, 2003.

[87] M. Marquillie, U. Ehrenstein, and J.-P. Laval. Instability of streaks in wall turbulence with adverse pressure gradient. *J. Fluid Mech.*, 681:205–240, 2011.

[88] M. Marquillie, J.-P. Laval, and R. Dolganov. Direct numerical simulation of separated channel flows with a smooth profile. *J. Turbulence*, 9(1):1–23, 2008.

[89] M.P. Martín, U. Piomelli, and G.V. Candler. Subgrid-scale models for compressible large-eddy simulations. *Theoret. Comput. Fluid Dynamics*, 13:361–376, 2000.

[90] P. J. Mason and D. J. Thomson. Stochastic backscatter in large-eddy simulations of boundary layers. *J. Fluid Mech.*, 242:51–78, 1992.

[91] O. J. McMillan and J. H. Ferziger. Direct testing of subgrid-scale models. *AIAA J.*, 17:1340–1346, 1979.

[92] C. Meneveau. Statistics of turbulence subgrid scale stresses: necessary conditions and experimental tests. *Phys. Fluids*, 6:815–833, 1994.

[93] C. Meneveau and J. Katz. Scale-invariance and turbulence models for large eddy simulation. *Annu. Rev. Fluid Mech.*, 32:1–32, 2000.

[94] C. Meneveau and T. S. Lund. The dynamic smagorinsky model and scale-dependent coefficients in the viscous range of turbulence. *Phys. Fluids*, 9(12):3932–3934, 1997.

[95] O. Métais, P. Bartello, E. Garnier, J. J. Riley, and M. Lesieur. Inverse cascade in stably stratified rotating turbulence. *Dynamics of Atmospheres and Oceans*, 23:193–203, 1996.

[96] O. Métais and M. Lesieur. Spectral large-eddy simulation of isotropic and staby stratified turbulence. *J. Fluid Mech.*, 239:157–194, 1992.

[97] J. Meyers and P. Sagaut. On the model coefficients for the standard and the variational multi-scale smagorinsky model. *J. Fluid Mech.*, 569:287–319, 2006.

[98] J. Meyers and P. Sagaut. Is plane channel flow a friendly test-case for the testing of LES subgrid scale models ? *Phys. Fluids*, 19:048105, 2007.

[99] P. Moin and J. Kim. Numerical investigation of turbulent channel flow. *J. Fluid. Mech.*, 118:341–377, 1982.

[100] F. M. Najjar and D. K. Tafti. Study of discrete test filters and finite difference approximations for the dynamic subgrid scale stress model. *Phys. Fluids*, 8, 1996.

[101] V. K. Natrajan and K. T. Christensen. The role of coherent structures in subgrid-scale energy transfer within the log layer of wall turbulence. *Phys. Fluids*, 18(065104):1–14, 2006.

[102] F. Nicoud and F. Ducros. Subgrid-scale stress modelling based on the square of the velocity gradient tensor. *Flow, Turbulence and Combustion*, 62:183–200, 1999.

[103] F. Nicoud, H. B. Toda, O. Cabrit, S. Bose, and J. Lee. Using singular values to build a subgrid-scale model for large eddy simulations. *Phys. Fluids*, 23, 2011.

[104] J. O'Neil and C. Meneveau. Subgrid-scale stresses and their modelling in a turbulent plane wake. *J. Fluid Mech.*, 349:253–293, 1997.

[105] P. O. O'Sullivan, S. Biringen, and A. Huser. A priori evaluation of dynamic subgrid models of turbulence in square duct flow. *Journal of Engineering Mathematics*, 40:91–108, 2001.

[106] N. Park, S. Lee, J. Lee, and H. Choi. A dynamic subgrid-scale eddy viscosity model with a global model coefficient. *Phys. Fluids.*, 18(125109), 2006.

[107] N. Park, J. Y. Yoo, and H. Choi. Toward improved consistency of a priori tests with a posteriori tests in large eddy simulation. *Phys. Fluids.*, 17(015103):1–20, 2005.

[108] A. E. Perry, S. Henbest, and M. S. Chong. A theoritical and experimental study of wall turbulence. *J. Fluid Mech.*, 165:163–199, 1986.

[109] U. Piomelli. Large-eddy simulation of turbulence flows. Department of Mechanical and Materials Engineering, Queen's University, Kingston (Ontario) Canada, February.

[110] U. Piomelli. Wall-layer models for large-eddy simulations. *Progress in Aerospace Sciences*, 44:437–446, 2008.

[111] U. Piomelli and E. Balaras. Wall-layer models for large-eddy simulations. *Annu. Rev. Fluid Mech.*, 34:349–374, 2002.

[112] U. Piomelli, W. H. Cabot, P. Moin, and S. Lee. Subgrid-scale backscatter in turbulent and transitionnal flows. *Phys. Fluids A*, 3(7):1766–1771, 1991.

[113] U. Piomelli, P. Moin, and J. H. Ferziger. Model consistency in large eddy simulation of turbulence channel flows. *Phys. Fluids*, 31:1884–1891, 1988.

[114] U. Piomelli, Y. Yu, and R. J. Adrian. Subgridscale energy transfer and nearwall turbulence structure. *Phys. Fluids*, 8, 1996.

[115] U. Piomelli and T. A. Zang. Large-eddy simulation of transitional channel flow. In *Computer Physics Communications*, pages 224–230, 1991.

[116] S. B. Pope. *Turbulent Flows*. Cambridge Univ. Press, Cambridge, UK, 2000.

[117] H.S. Pordal. Practicing the science of computational fluid dynamics. *Continuing Education for Engineers*, 2006.

[118] F. Porté-Aget, M. B. Parlange, C. Meneveau, and W. E. Eichinger. A priori field study of the subgrid-scale heat fluxes and dissipation in the atmospheric surface layer. *Journal of the atmospheric sciences*, 58, 2001.

[119] Proceedings of the Second AFOSR International Conference on DNS/LES, New Brunswick, NJ/USA 1999. *On the use of LES with a dynamic subgrid-scale model for optimal control of wall bounded turbulence*, 1999.

[120] Adams N. A. Pruett C. D. A priori analyses of three subgrid-scale models for one-parameter families of filters. *Phys. Fluids*, 12:1133–1142, 2000.

[121] S.K. Robinson. Coherent motions in the turbulent boundary layer. *Annu. Rev. Fluid Mech.*, 23:601–639, 1991.

[122] R. S. Rogallo and P. Moin. Numerical simulation of turbulent flows. *Annu. Rev. Fluid Mech.*, 16:99–137, 1984.

[123] P. Sagaut. *Large Eddy Simulation for Incompressible Flows.* Springer-Verlag Berlin Heidelberg, 1998.

[124] F. Sarghini, U. Piomelli, and E. Balaras. Scale-similar models for large-eddy simulations. *Phys. Fluids*, 11:1596–1607, 1999.

[125] U. Schumann. Subgrid scale model for finite difference simulations of turbulent flows in plane channels and annuli. *Journal of computational physics*, 18:376–404, 1975.

[126] A Scotti, C. Meneveau, and D. K. Lilly. Generalized smagorinsky model for anisotropic grids. *Phys. Fluids*, 5:2306, 1993.

[127] S. I. Shah, M. Stanislas, and J.-P. Laval. A specific behavior of adverse pressure gradient near wall flows. In M. Stanislas, J. Jimenez, and I. Marusic, editors, *Progress in wall turbulence : understanding and modelling*, ERCOFTAC Series vol 14, pages 257–265, Villeneuve d'Ascq, France, April 21-23, 2010. Springer.

[128] L. Shao, S. Sarkar, and C. Pantano. On the relationship between the mean flow and subgrid stresses in large eddy simulation of turbulent shear flows. *Phys. Fluids*, 11:1229–1248, 1999.

[129] P. E. Skåre and P.-Å Krogstad. A turbulent boundary layer near separation. *J. Fluid Mech.*, 272:319–348, 1994.

[130] M. Skote, J. H. Haritonidis, and D. S. Henningson. Varicose instabilities in turbulent boundary layers. *Phys. Fluids*, 14(7):2309–2323, 2002.

[131] P. Spalart. Detached-eddy simulation. *Annu. Rev. Fluid Mech.*, 41:181–202, 2009.

[132] P. R. Spalart and G. N. Coleman. Numerical study of a separation bubble with heat transfer. *Europ. J. Mech. B*, 16:169–189, 1997.

[133] D.B. Spalding. A single formula for the law of the wall. *Trans. ASME, J. Appl. Mech.*, 28, 1961.

[134] M. Stanislas, J. Jimenez, and I. Marusic. *Progress in wall turbulence : understanding and modelling.* Springer, 2009.

[135] S. Stolz, P. Schlatter, and L. Kleiser. High-pass filtered eddy-viscosity models for large-eddy simulations of transitional and turbulent flows. *Phys. Fluids*, 17:065103, 2005.

[136] P. P. Sullivan, J. C. McWilliams, and C. H. Moeng. A subgrid-scale model for large-eddy simulation of planetary boundary-layer flows. *Boundary-Layer Meteorology*, 71:247–276, 1994.

[137] M. Taeibi-Rahni, M. Ramezanizadeh, A. Darvan, D. D. Ganji, S. Soleimani, E. Ghasemi, and H. Bararnia. Large-eddy simulations of three dimensional turbulent jet in a cross flow using a dynamic subgrid-scale eddy viscosity model with a global model coefficient. *World Applied Sciences Journal*, 9:1191–1200, 2010.

[138] A. A. Townsend. *The structure of turbulent shear flow (second edition)*. Cambridge university press, Cambridge, 1976.

[139] M. Tsubokura. Subgrid scale modeling of turbulence for the dynamic procedure using finite difference method and its assessment on the thermally stratified turbulent channel flow. *Transactions of the ASME*, 73, 2006.

[140] B.J.H. van Stratum. *A Priori Study of Sub-grid Models in Large-Eddy Simulation using Direct Numerical Simulation of a Turbulent Channel Flow*. PhD thesis, Minor MSc-Thesis Meteorology and Air Quality Section, Wageningen University, 2012.

[141] O. V. Vasiliev, T. S. Lund, and P. Moin. A general class of commutative filters for LES in complex geometries. *J. Comp. Phys.*, 146(CP986060):82–104, 1998.

[142] D. Vergano. Turbulence theory gets a bit choppy, 2006.

[143] A. Vorobev and O. Zikanov. Smagorinsky constant in les modeling of anisotropic mhd turbulence. *Theor. Comput. Fluid Dyn.*, 22:317–325, 2007.

[144] A. W. Vreman. An eddy-viscosity subgrid-scale model for turbulent hear flow: Algebraic theory and applications. *Phys. Fluids*, 16(10):3670–3681, 2004.

[145] A.W. Vreman and B.J. Geurts. A new treatment of commutation-errors in large-eddy simulation. *Turbulence IX*, pages 199–202, 2002.

[146] B Vreman, B Geurts, and H Kuerten. On the formulation of the dynamic mixed subgrid-scale model. *Phys. Fluid*, 6, 1994.

[147] G. S. Winckelmans, A. A. Wray, and O. V. Vasilyev. Testing of a new mixed model for les: the leonard model supplemented by a dynamic smagorinsky term. *Astronomy & Astrophysics*, 414(3):807–824, 1998.

[148] C. Wollblad and L. Davidson. Pod based reconstruction of subgrid stresses for wall bounded flows using neural networks. *Flow Turbulence Combust*, 81:77–96, 2008.

[149] T. A. Zang. Numerical simulation of the dynamics of turbulent boundary layers: Perspectives of a transition simulator. *Phil. Trans. R. Soc. Lond*, A 336:95–102, 1991.

[150] Y. Zang, R. Street, and R. Koseff. A dynamical mixed subgrig-scale model and its application to turbulent recirculating flows. *Phys. Fluids A*, 5:3186–3196, 1993.

Appendices

Appendix A

A priori results for plane channel flow

A.1. SGS energy transfer

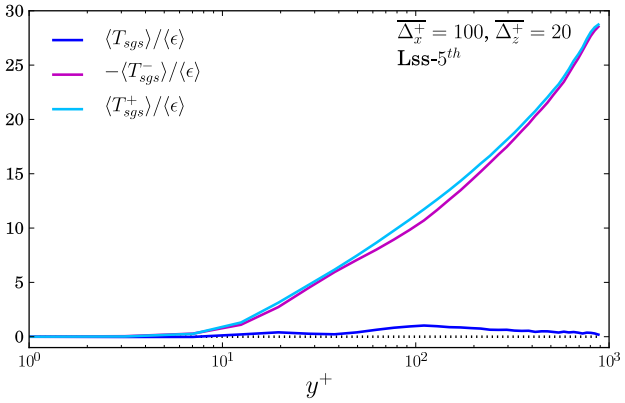

Figure A.1: Net SGS energy transfer including the average of its positive and negative contributions using the Lss-5^{th} filter set $\overline{\Delta_x^+} = 100$ and $\overline{\Delta_z^+} = 20$. Statistics are normalized by the rate of kinetic energy dissipation.

A.2. Correlations of SGS force f_1 and f_2 using Gaussian filter

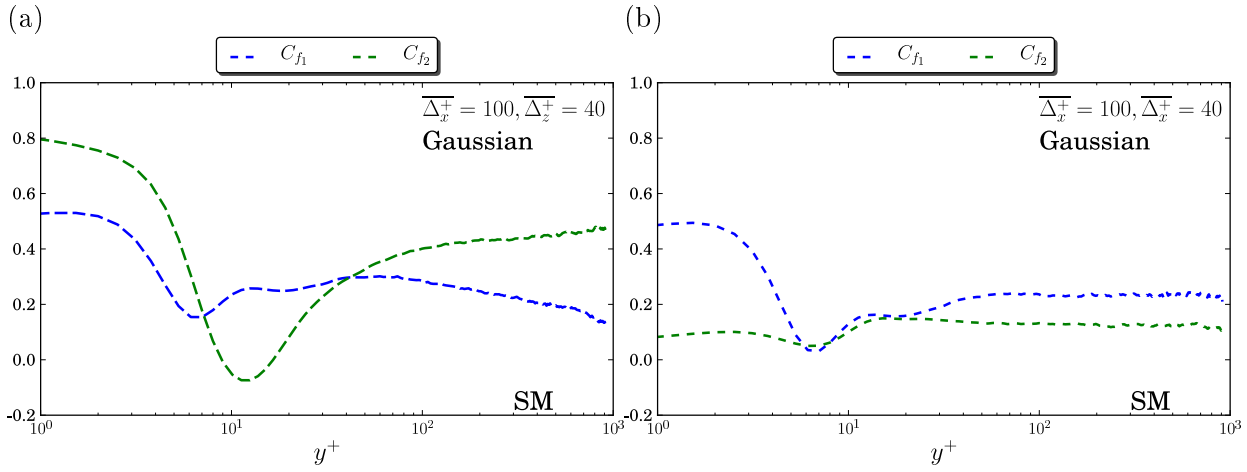

Figure A.2: Correlations C_{f_1} and C_{f_2} between $\langle \partial \tau_{ij}/\partial x_j \rangle$ and $\langle \partial(\tau_{ij}^{SM} + 1/3\tau_{kk})/\partial x_j \rangle$ (a) or between $\langle \partial \tau_{ij}/\partial x_j \rangle$ and $\langle \partial \tau_{ij}^{SM}/\partial x_j \rangle$ (b) for Smagorinsky model, using Gaussian filter.

Fig. A.2 shows that, in the outer region, C_{f_1} is larger without than with item $1/3\tau_{kk}$, while a larger C_{f_2} is obtained by considering $1/3\tau_{kk}$. It should be noted, however, that by considering $1/3\tau_{kk}$, C_{f_2} is significantly larger with Gaussian than with Lss-5^{th} filter (see Fig. 4.42(a)) in the outer region, while C_{f_2} is almost the same using both Lss-5^{th} and Gaussian filters when $1/3\tau_{kk}$ is not considered.

A.3. Correlations of SGS energy dissipation using Gaussian filter

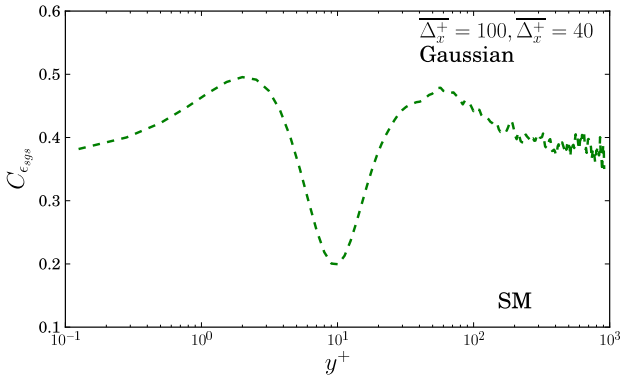

Figure A.3: Correlation $C_{\epsilon_{sgs}}$ between exact SGS energy dissipation and the modeled one by Smagorinsky model using Gaussian filter.

Appendix B

A priori results for APG channel flow

B.1. Energy transfer mechanism

B.1.1. Back scatter of net SGS energy dissipation

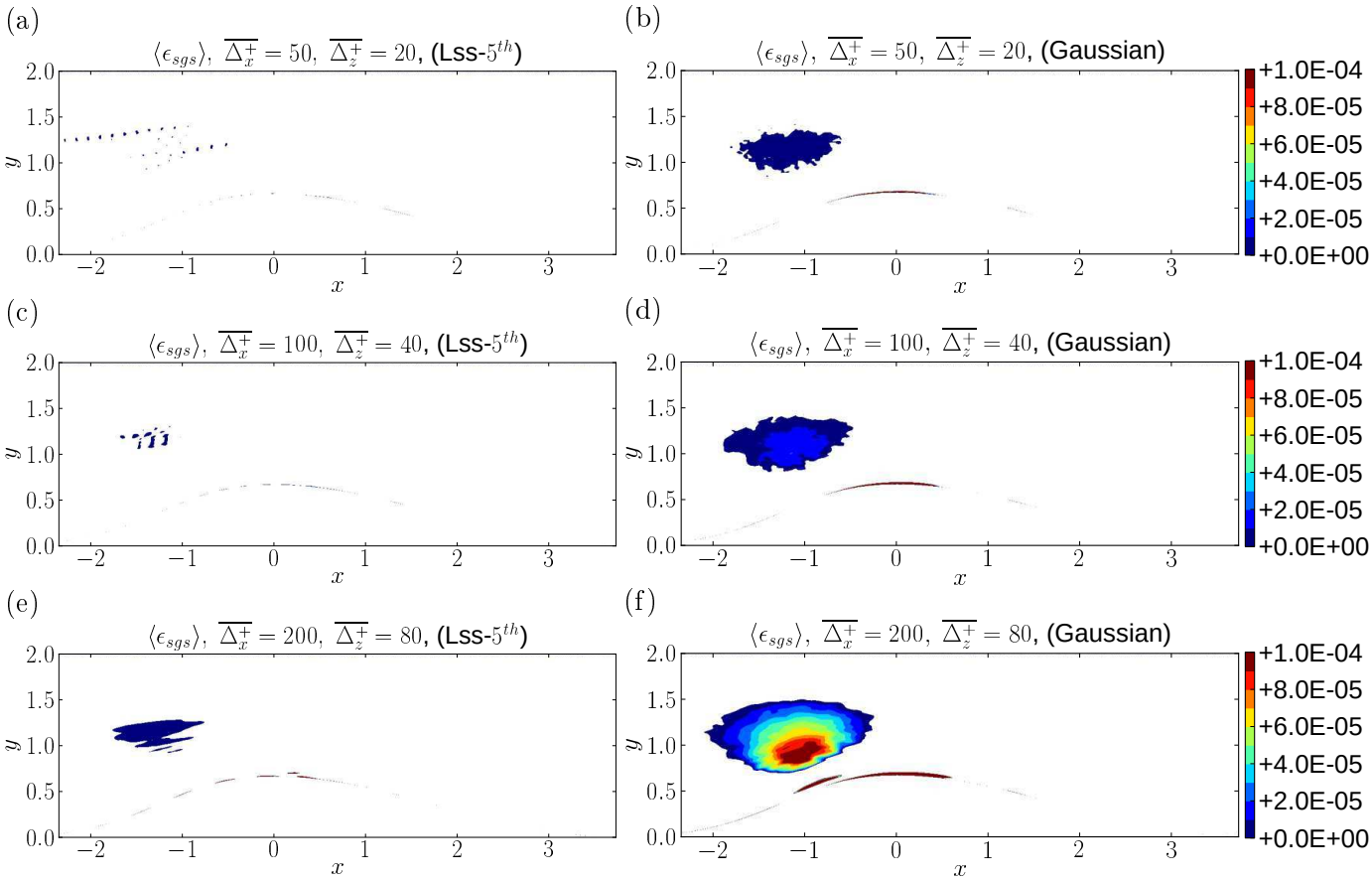

Figure B.1: Back scatter of net SGS energy dissipation $\langle\epsilon_{sgs}\rangle$ in converging favorable pressure gradient region using Lss-5^{th} (a, c, e) and Gaussian (b, d, f) filters.

B.1.2. SGS energy transfer in APG regions

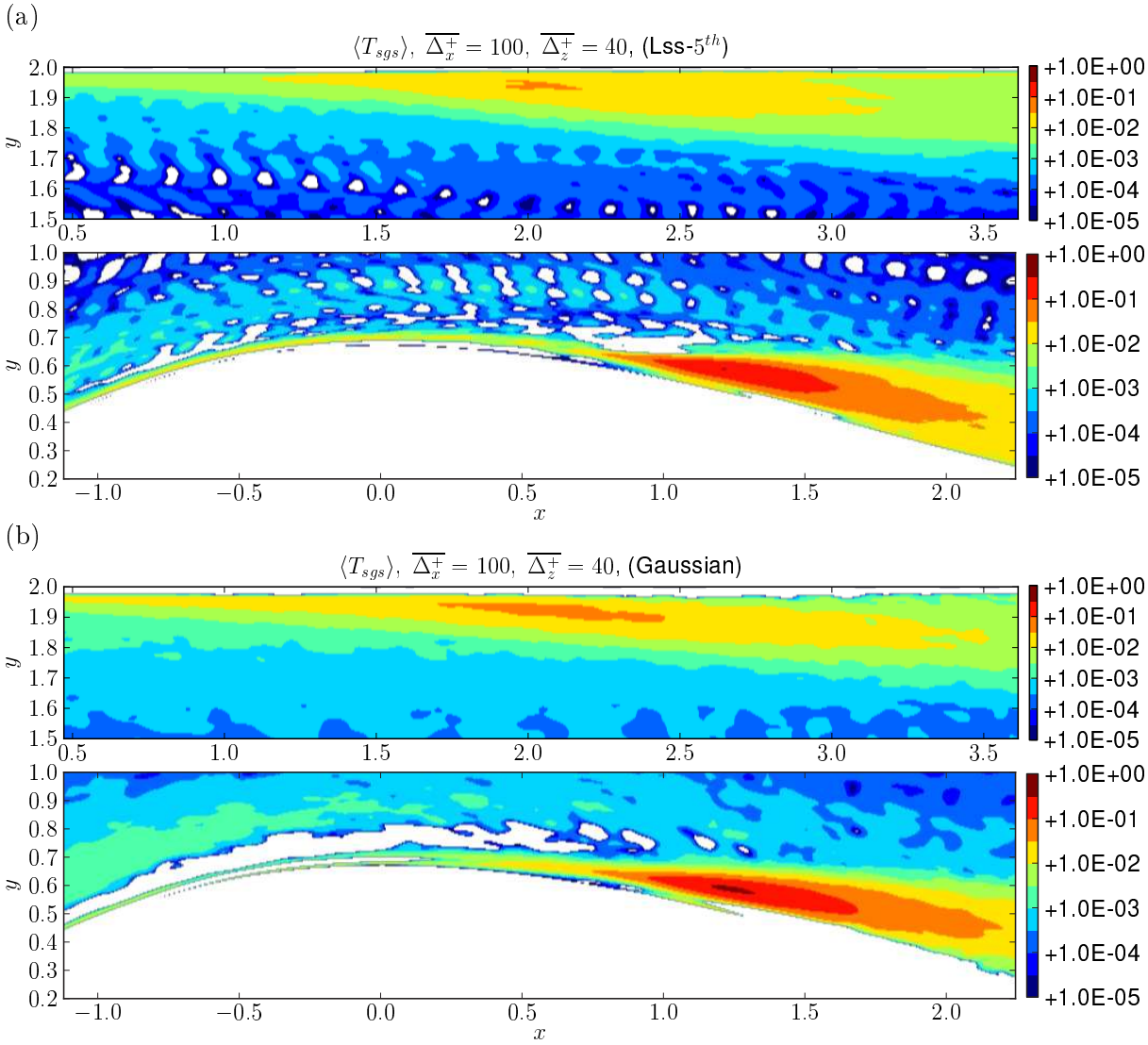

Figure B.2: SGS energy transfer for filter width $\overline{\Delta_x^+} = 100$, $\overline{\Delta_z^+} = 40$ using Lss-5^{th} (a) and Gaussian (b) filters.

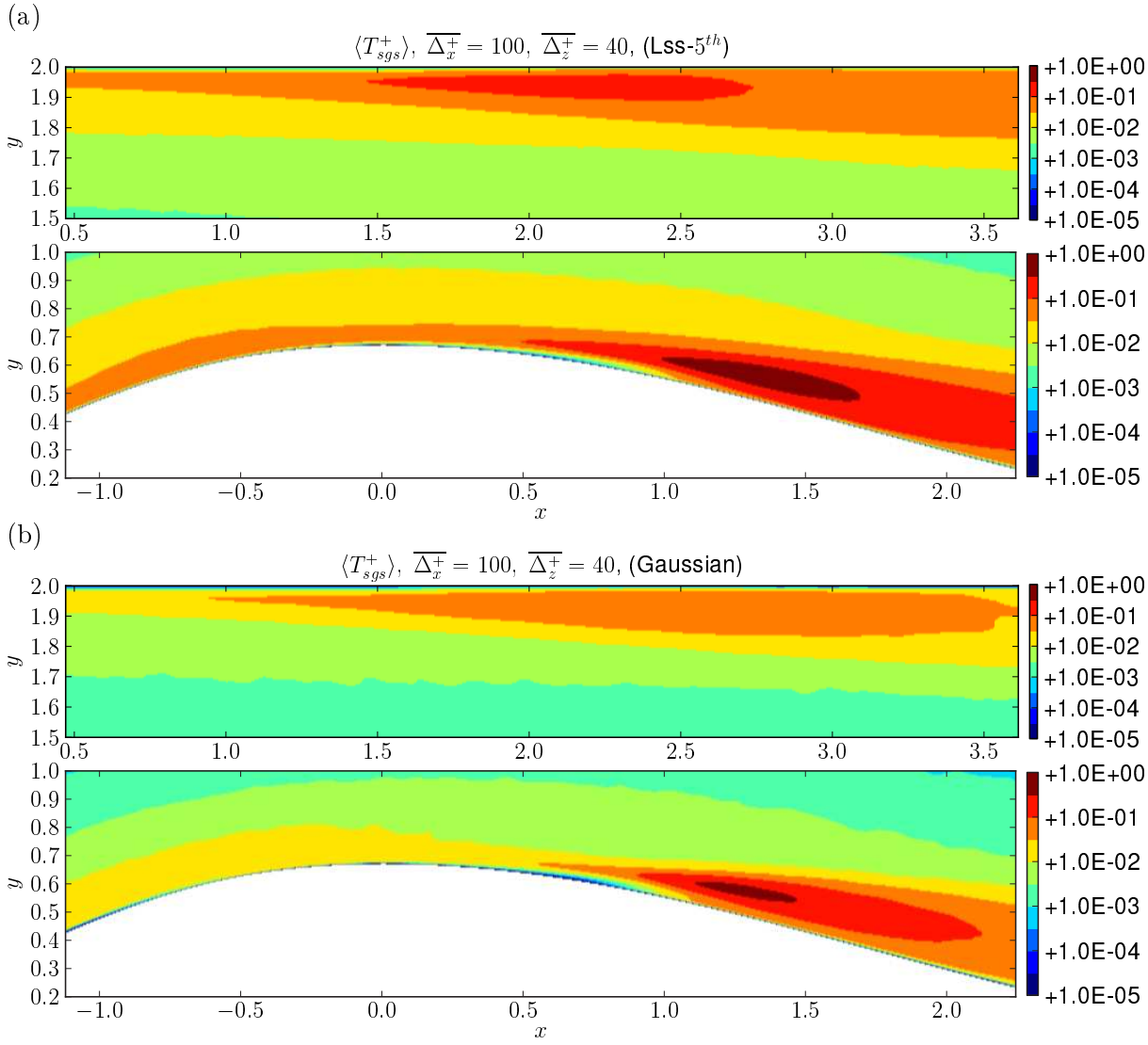

Figure B.3: Positive contribution of SGS energy transfer for filter set $\overline{\Delta^+_x} = 100$, $\overline{\Delta^+_z} = 40$ using Lss-5^{th} (a) and Gaussian (b) filters.

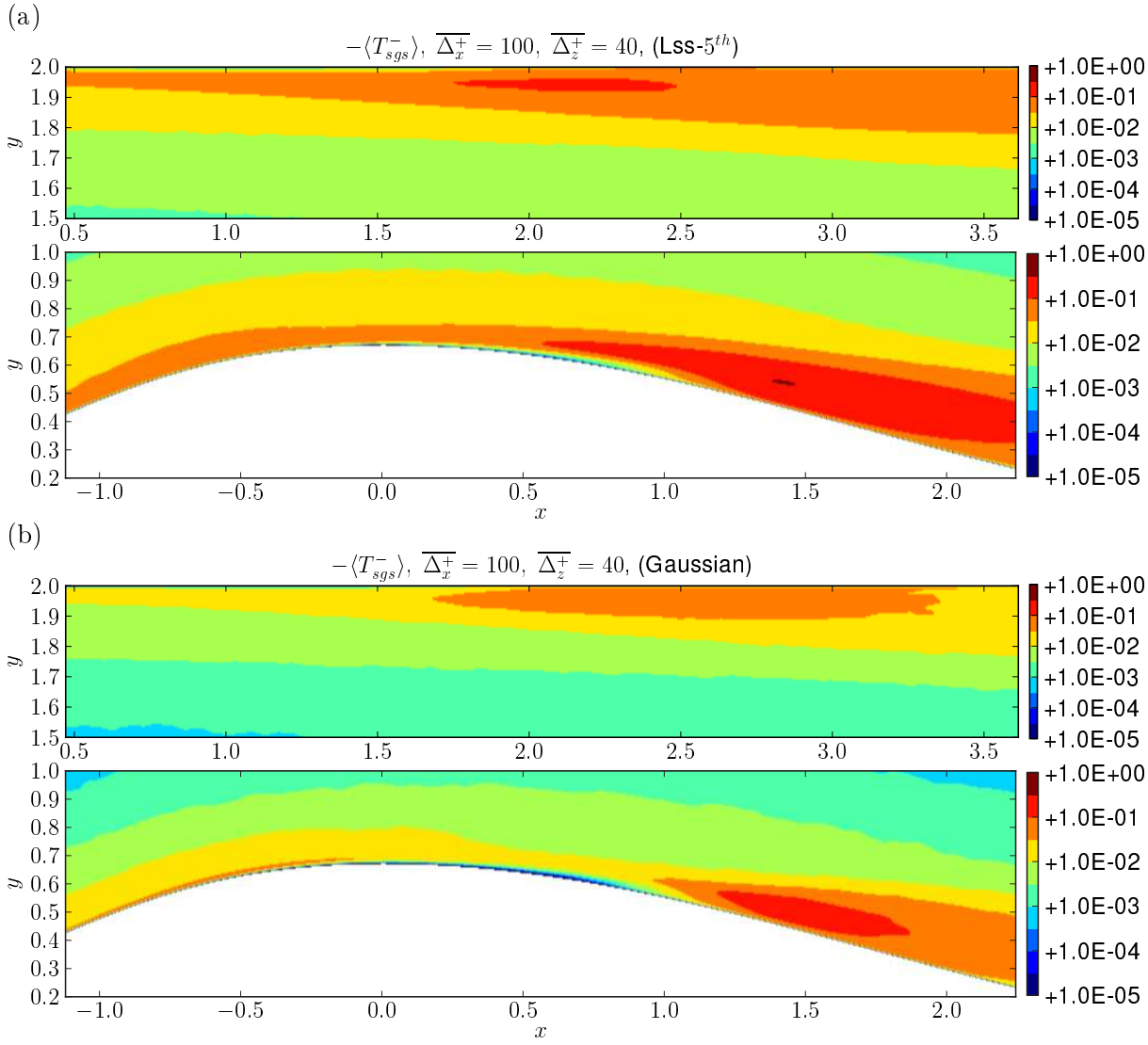

Figure B.4: Negative contribution of SGS energy transfer for filter set $\overline{\Delta^+_x} = 100$, $\overline{\Delta^+_z} = 40$ using Lss-5^{th} (a) and Gaussian (b) filters.

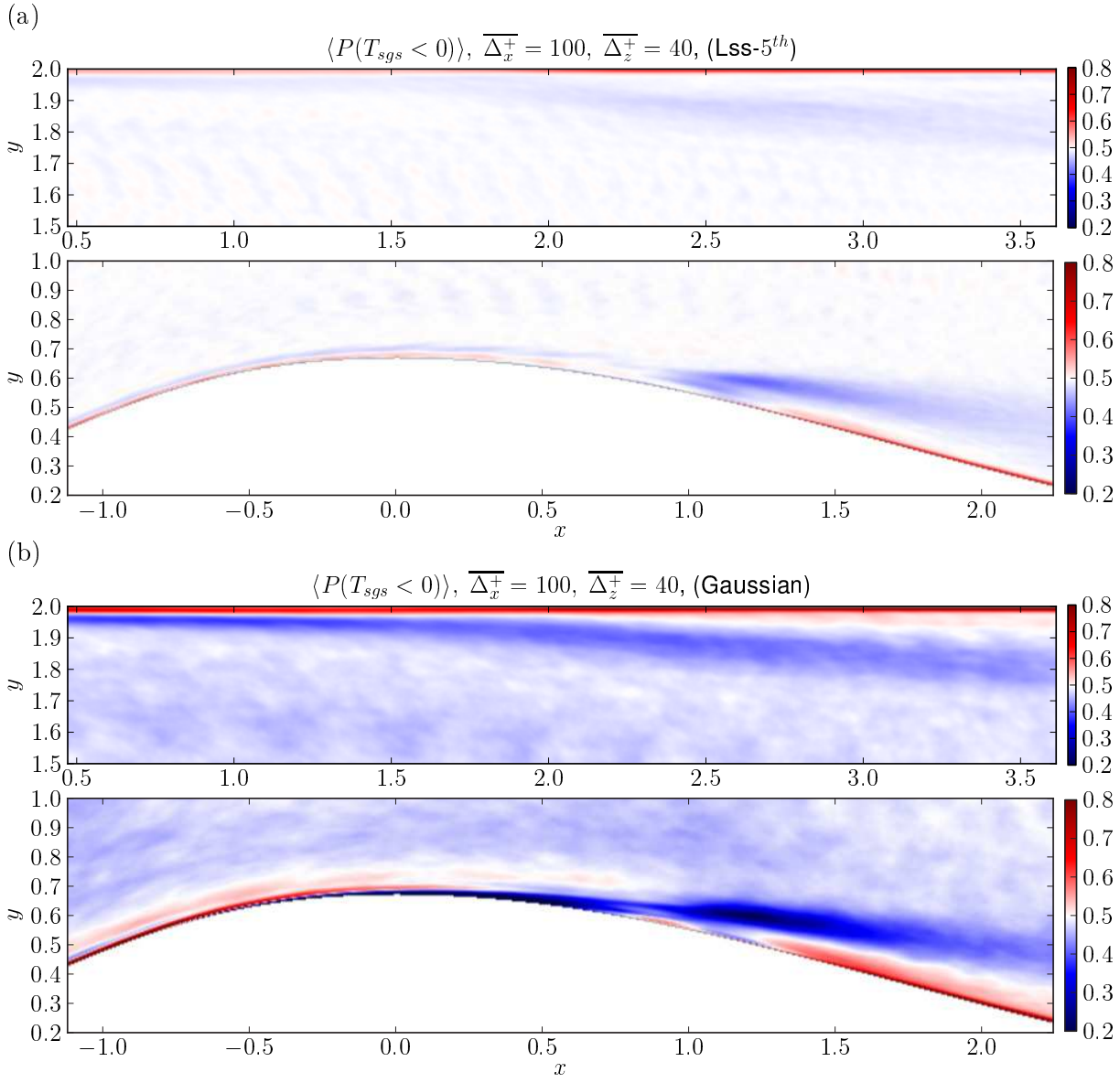

Figure B.5: Fraction of points experincing back scatter of SGS energy transfer for filter set $\overline{\Delta_x^+} = 100$, $\overline{\Delta_z^+} = 40$ using Lss-5^{th} (a) and Gaussian (b) filters.

B.2. A priori evaluation of model coefficients

B.2.1. A priori estimate of negative $\langle C_s \rangle$ with Gaussian filter

A detail concentration of negative $\langle C_s \rangle$ with Gaussian filter is given in Fig. B.6. One can observe that, the smallest values of $\langle C_s \rangle$ (approximately -0.08) appear in the center of converging channel region. This corresponds roughly to the maximum of back scatter of net $\langle \epsilon_{sgs} \rangle$ (see Fig. B.1 of Appendix). Furthermore, the absolute value of negative $\langle C_s \rangle$ become larger as increasing the filter width, in agreement with the increasing trend of back scatter of net SGS energy dissipation.

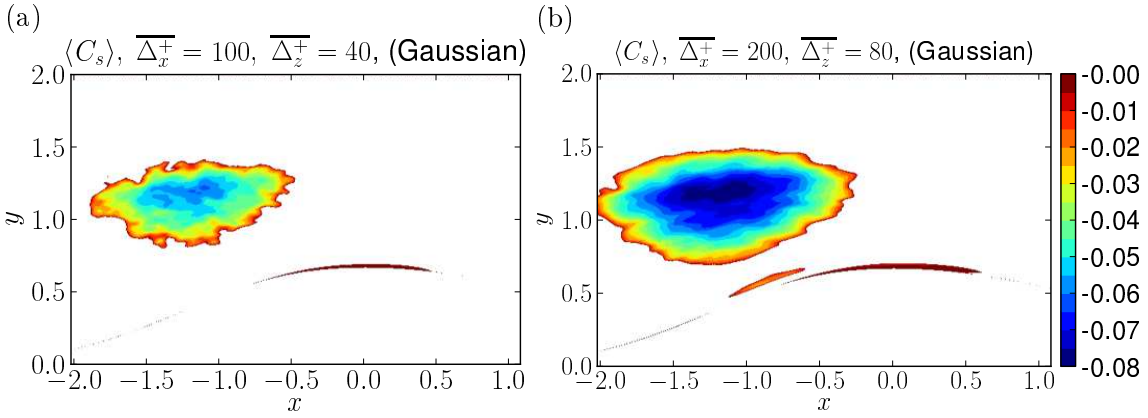

Figure B.6: A priori estimate of negative regions of $\langle C_s \rangle$ (Smagorinsky model) in the converging channel region using the Gaussian filter set ($\overline{\Delta_x^+} = 100$, $\overline{\Delta_z^+} = 40$) (a) and ($\overline{\Delta_x^+} = 200$, $\overline{\Delta_z^+} = 80$) (b).

B.2.2. A priori estimate of the DSM coefficient $\langle C_d \rangle$ using different test filters

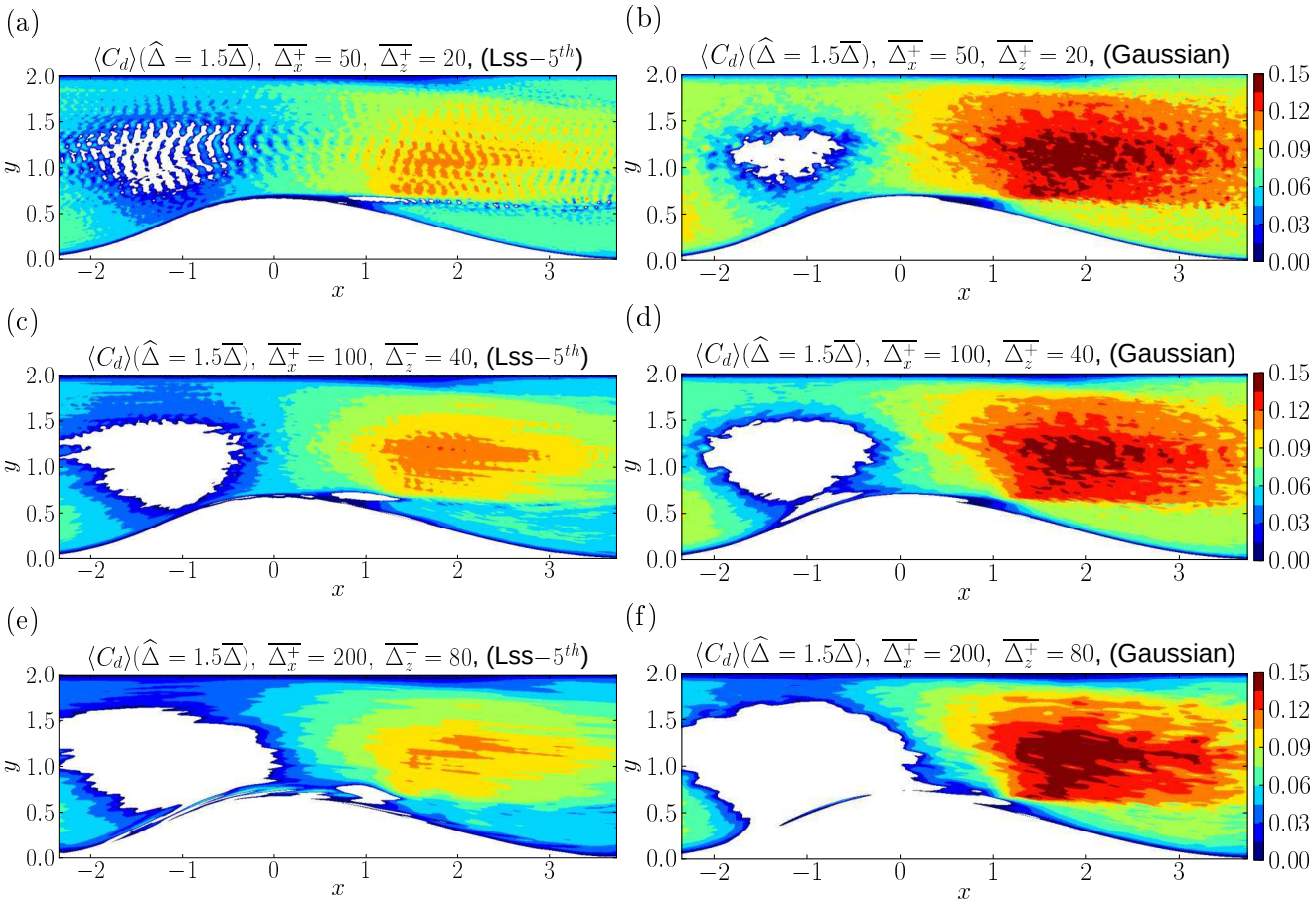

Figure B.7: A priori estimate of coefficient $\langle C_d \rangle$ of Dynamic Smagorinsky model in the converging-diverging channel regions with three filter sets ($\widehat{\Delta} = 1.5\overline{\Delta}$) using Lss-$5^{th}$ (a, c, e) and Gaussian (b, d, f) filters.

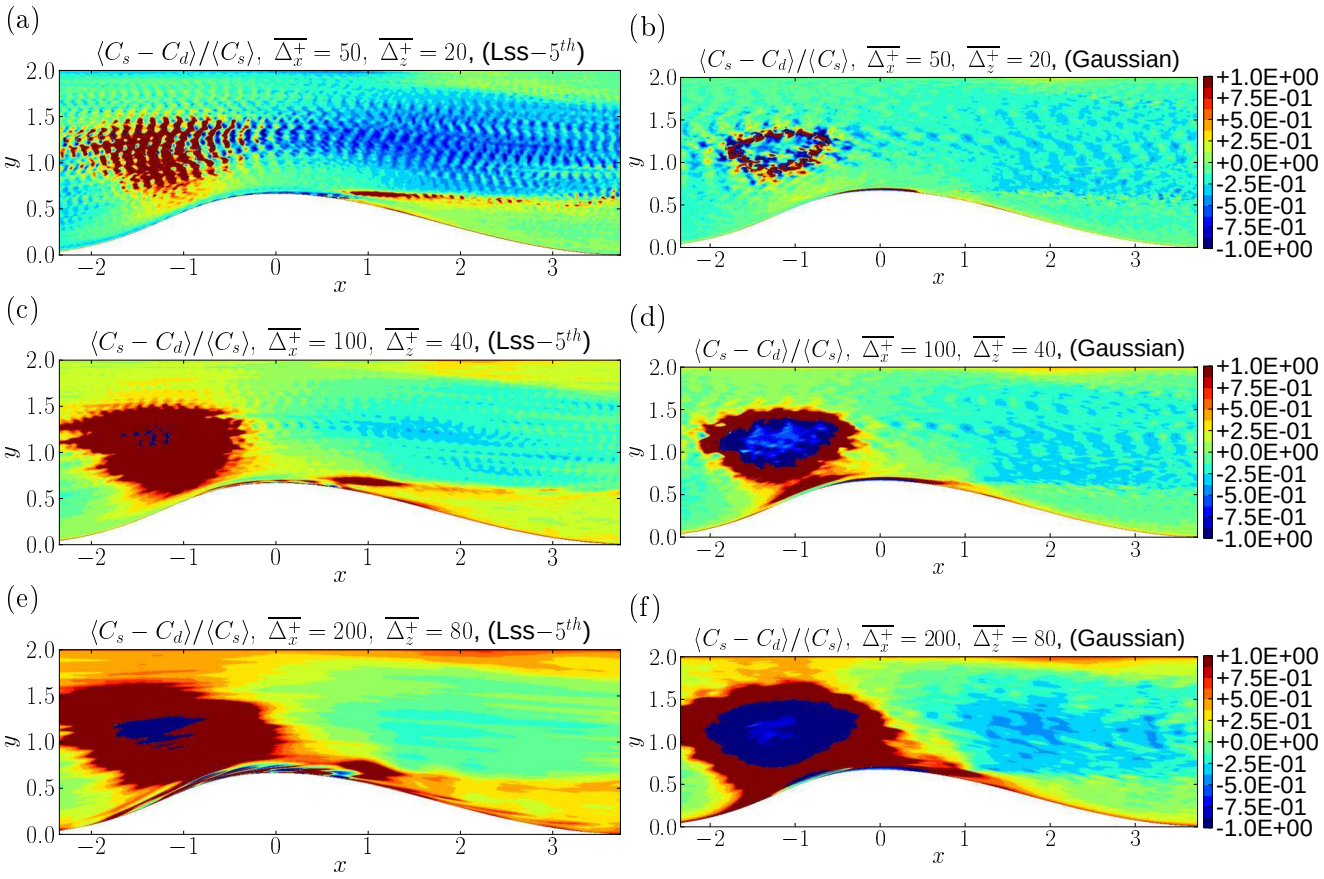

Figure B.8: Relative error between coefficient $\langle C_s \rangle$ and $\langle C_d \rangle$ in the converging-diverging channel regions using Lss-5^{th} (a, c, e) and Gaussian (b, d, f) filters ($\widehat{\Delta} = 1.5\overline{\Delta}$).

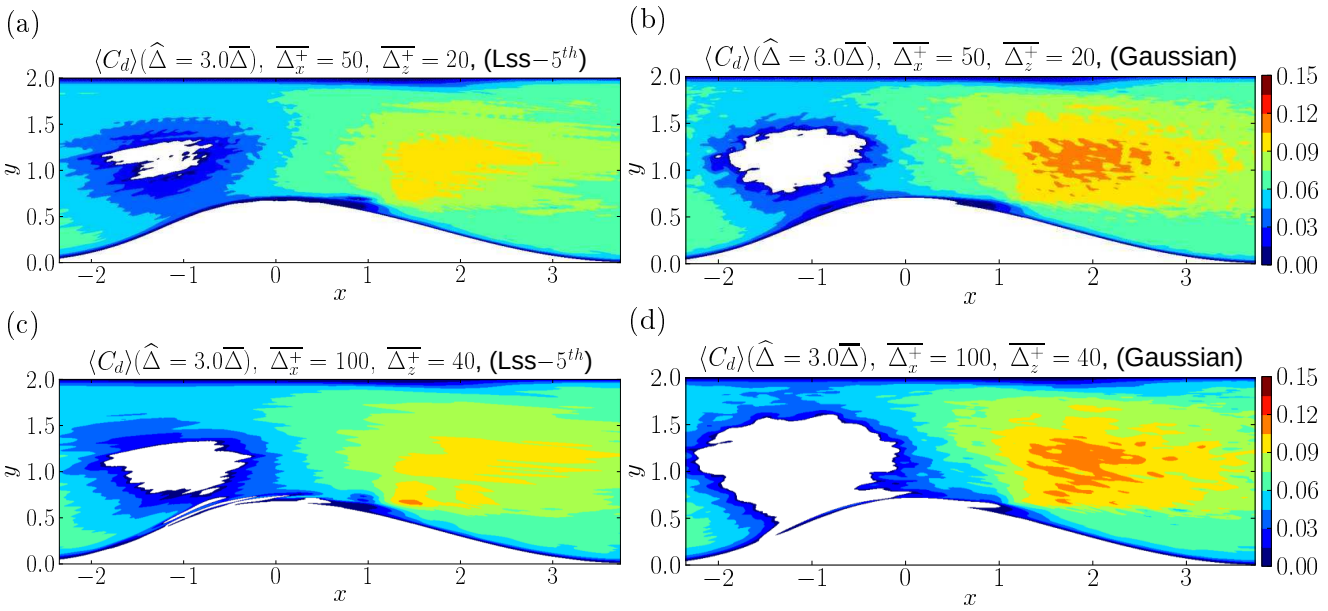

Figure B.9: A priori estimate of coefficient $\langle C_d \rangle$ of Dynamic Smagorinsky model in the converging-diverging channel regions with three filter sets ($\widehat{\Delta} = 3.0\overline{\Delta}$) using Lss-$5^{th}$ (a, c) and Gaussian (b, d) filters.

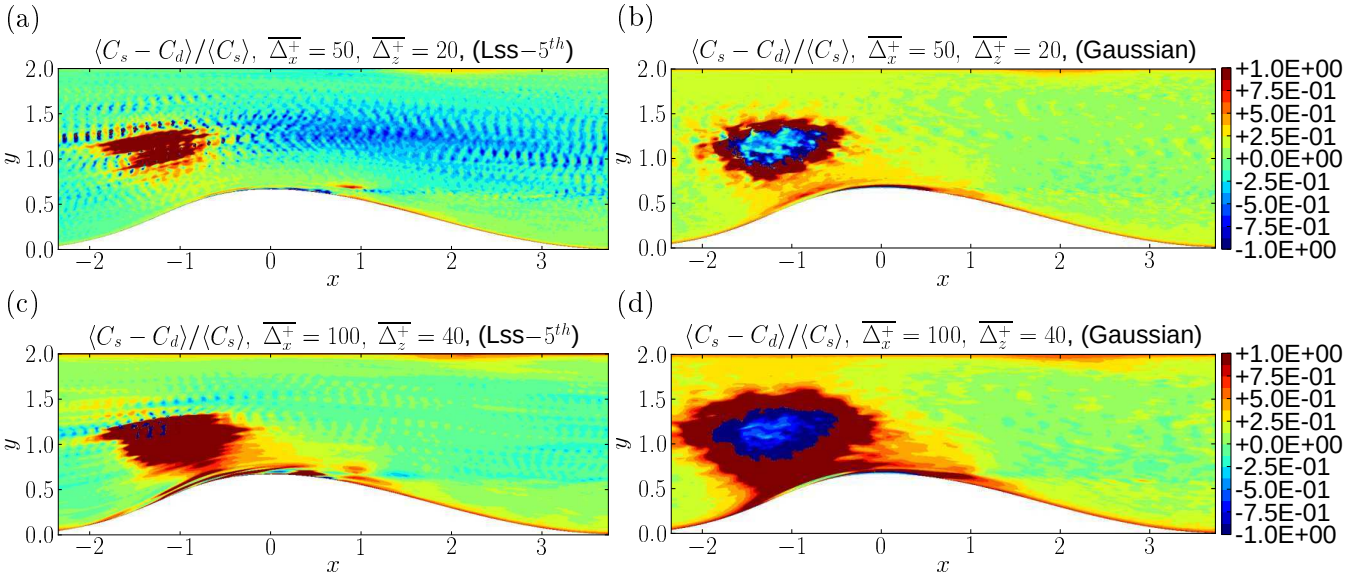

Figure B.10: Relative error between coefficient $\langle C_s \rangle$ and $\langle C_d \rangle$ in the converging-diverging channel regions using Lss-5^{th} (a, c) and Gaussian (b, d) filters ($\widehat{\Delta} = 3.0\overline{\Delta}$).

B.3. Tests of models behavior

B.3.1. SGS stress tensor

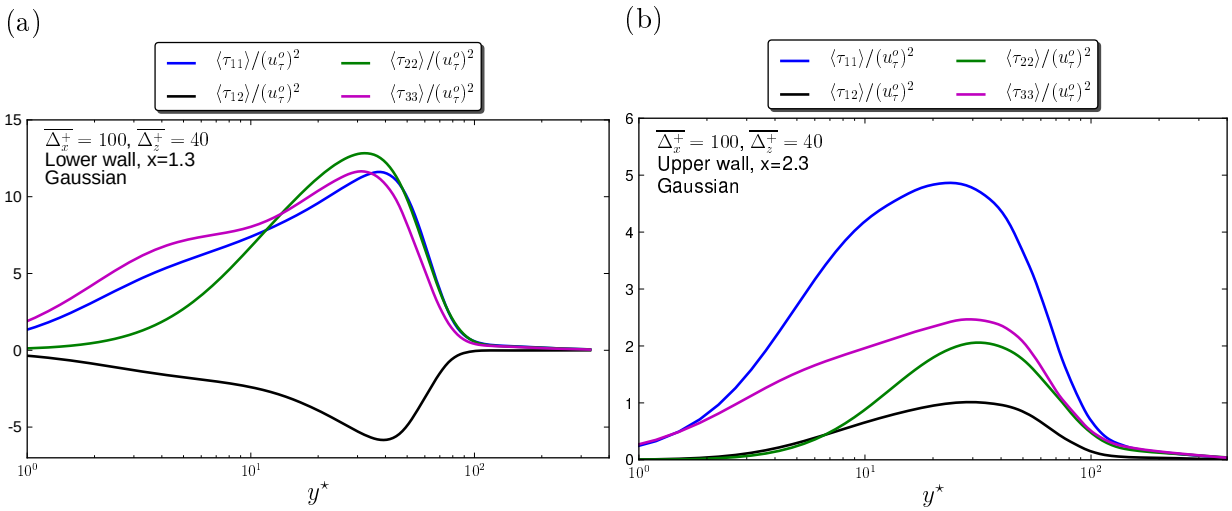

Figure B.11: One-dimensional profiles of the normalized SGS stress tensor at the lower (a) and upper (b) walls using the Gaussian filter width $\overline{\Delta_x^+} = 100$, $\overline{\Delta_z^+} = 40$.

One-dimensional analysis of SGS stress tensor with Gausian filter width $\overline{\Delta_x^+} = 100$, $\overline{\Delta_z^+} = 40$ are given in Fig. B.11. At the lower wall, the peaks of components $\langle\tau_{11}\rangle$, $\langle\tau_{12}\rangle$, $\langle\tau_{22}\rangle$ and $\langle\tau_{33}\rangle$ occur at the same position $x = 1.3$ in the range $30 < y^\star < 50$, collapsing to the streamwise and normal positions of the peak of turbulent kinetic energy (see Fig. 3.15(a)) and the streamwise position of the peak of fraction of subgrid scale kinetic energy (see Fig. 5.3(a)). However, the peaks of SGS stress tensor are different dependently of different component at the upper wall. Only the peak of $\langle\tau_{11}\rangle$ occurs at $x = 2.0$, $20 < y^\star < 30$, as the same position of the peak of turbulent kinetic energy (see Fig. 3.15(b)) at the upper wall. A similar one-dimensional behavior of all these components are observed with Lss-5^{th} filter and with other filter width. Therefore, the SGS stress tensor is more correlated with the turbulent kinetic energy at the lower wall than at the upper wall where the effect of subgrid scale kinetic energy becomes larger.

B.3.2. Wall normal profiles of correlations $C_{\tau_{11}}$, $C_{\tau_{22}}$ and $C_{\tau_{33}}$

In order to investigate these correlations in detail, one-dimensional analysis near both the flat and curved walls are given in Fig. B.12. $C_{\tau_{11}}$ keeps high (near to 1.0) along the lower wall from the diverging part. A pits begins to appear at $x = 0.7$ with Lss-5^{th} and at $x = 0.6$ with Gaussian filter in range $y^\star < 10$, roughly collapsing to the onset of the flow detachment. This pits reaches minimum at $x = 1.9$ with Lss-5^{th} and at $x = 1.6$ with Gaussian filter, almost the end of the flow detachment. Besides, the peak of $C_{\tau_{11}}$ gradually decreases and moves away from the wall, in the range $0.7 < x < 1.9$, $y^\star > 30$ with Lss-5^{th}, $0.6 < x < 1.6$, $y^\star > 30$ with Gaussian filter, as moving downstream along streamwise positions. Near the end of the diverging channel, $C_{\tau_{11}}$ is smaller than in near wall region of plane channel flow. A new peak of $C_{\tau_{22}}$ begins to appear at $x = 0.2$ with Lss-5^{th} and $x = 0.6$ with Gaussian filter. It moves away from the wall and disappears at the end of the channel $x = 7.0$ when moving downstream. The minimum of $C_{\tau_{33}}$ occurs at $x = 0.3$ with Lss-5^{th} and $x = 0.5$ with Gaussian filter. A peak of $C_{\tau_{33}}$ is observed from the onset of circulation region $x = 0.3$, $y^\star < 10$ with Gaussian filter, while a similar peak only appears from $x = 0.9$, $y^\star < 10$ with Lss-5^{th}. This peak moves away from the wall and gradually disappears as moving downstream. Thus, in circulation regions, a new peak is observed respectively on $C_{\tau_{11}}$, $C_{\tau_{22}}$ and $C_{\tau_{33}}$ very near to the wall, while it begins at a position which is more downstream with Gaussian compared to with Lss-5^{th} filter. Besides, slightly larger correlations ($C_{\tau_{11}}$, $C_{\tau_{22}}$ and $C_{\tau_{33}}$) are observed using Gaussian than Lss-5^{th} filter in accordance with the observations in plane channel flow (see Fig. 4.36). This is the same for the other filter width with both filter types. Quite similar behavior to the plane channel flow are observed at the upper wall, independently of the filter type and filter width.

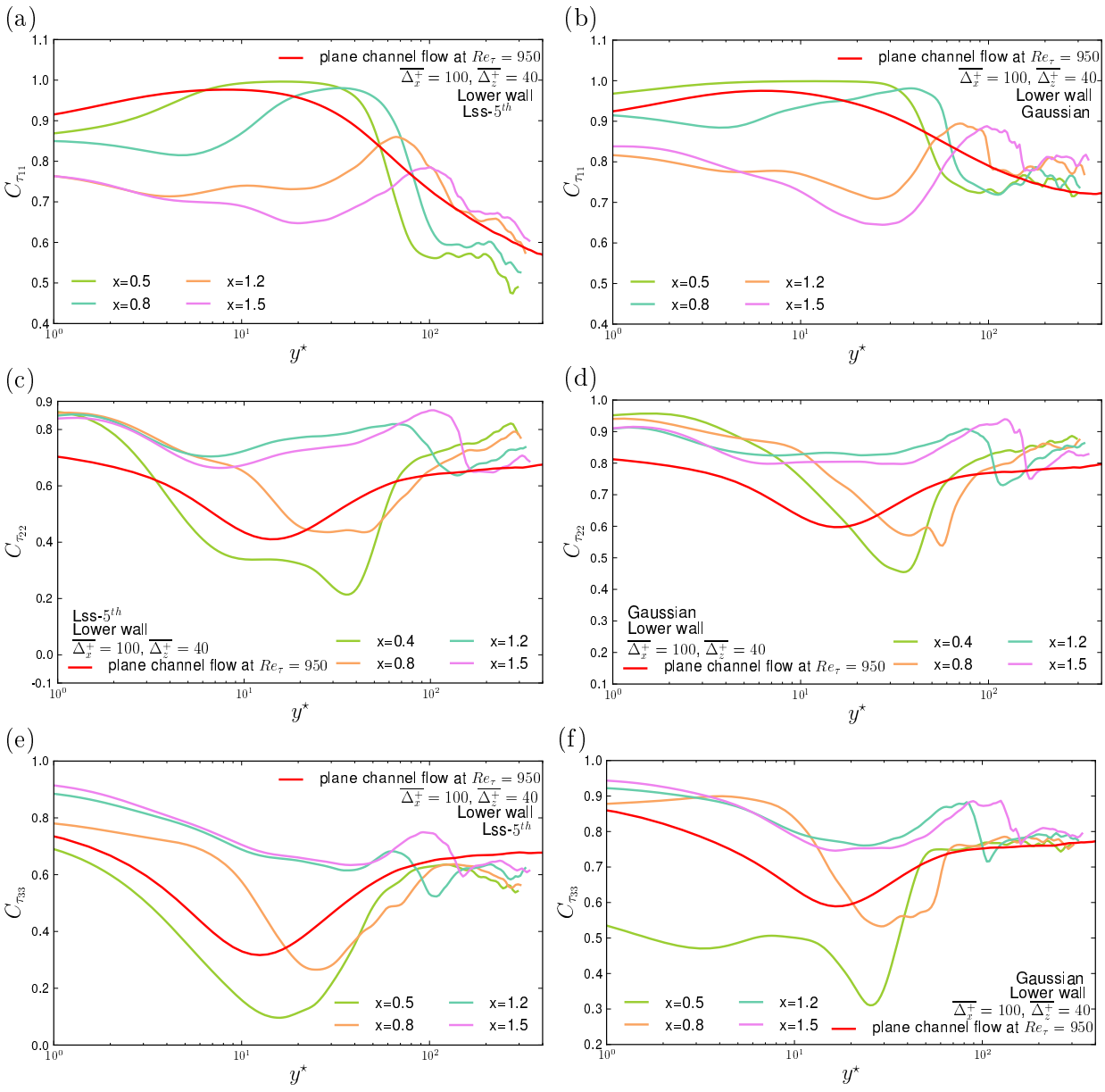

Figure B.12: Wall normal profiles of correlations $C_{\tau_{11}}$, $C_{\tau_{22}}$ and $C_{\tau_{33}}$ at the lower wall using Lss-5^{th} (a, c, e) and Gaussian (b, d, f) filter width $\overline{\Delta_x^+} = 100$, $\overline{\Delta_z^+} = 40$.

B.3.3. Statistics of $\langle \tau_{12} \rangle$ at the upper wall

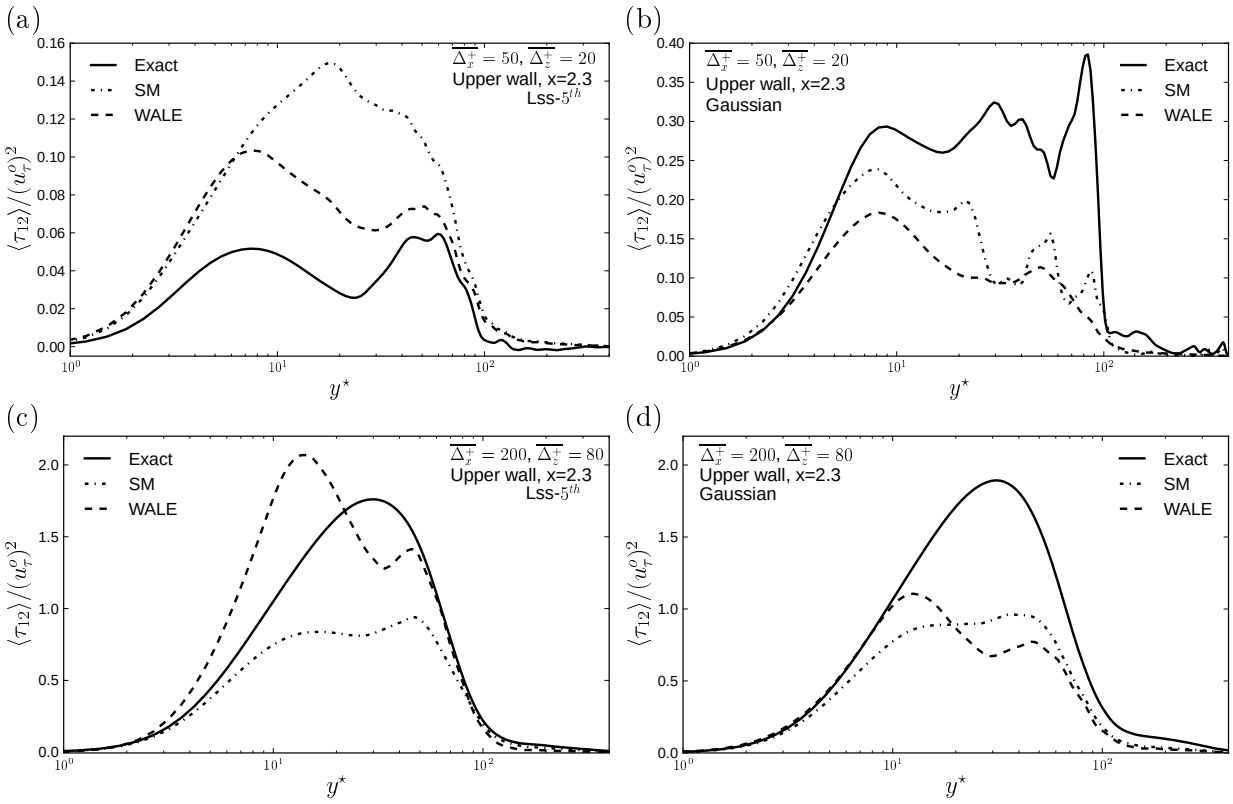

Figure B.13: Wall normal profiles of exact $\langle \tau_{12} \rangle$ and its modeled counterparts by the Smagorinsky and WALE models using the Lss-5^{th} (a, c) and Gaussian (b, d) filters at the upper wall.

B.3.4. Standard deviation at the upper wall

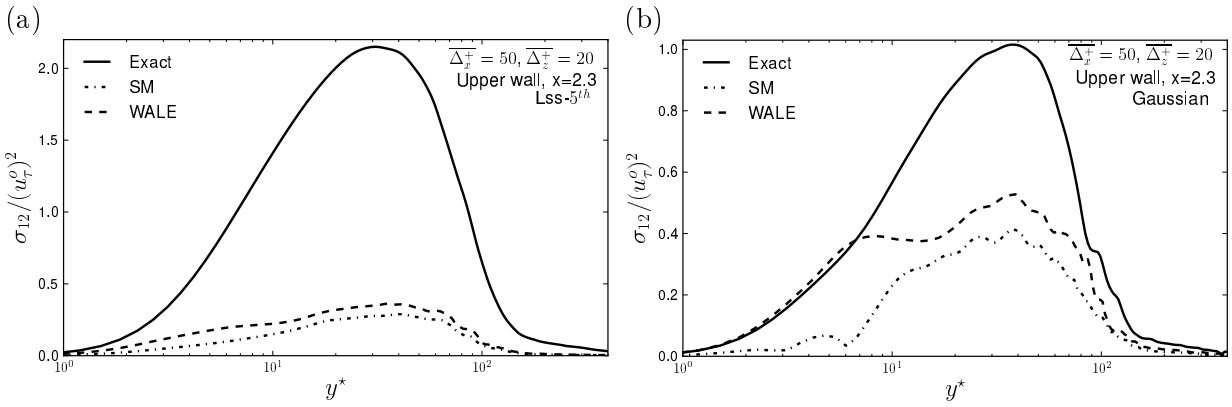

Figure B.14: Standard deviation of the exact and modeled $\langle \tau_{12} \rangle$ with filter width $\overline{\Delta_x^+} = 50$, $\overline{\Delta_z^+} = 20$ using Lss-5^{th} (a) and Gaussian (b) filters at the upper wall.

B.3.5. Behavior of the exact SGS force

One-dimensional analysis of the normalized $\langle f_1 \rangle$, $\langle f_2 \rangle$ using the Gaussian filter at both lower and upper walls are given in Fig. B.15. At the lower wall, the positive maxima of $\langle f_1 \rangle$ and $\langle f_2 \rangle$ occur at the same streamwise position $x = 1.3$, respectively in the range $40 < y^\star < 70$ and $y^\star < 10$. It corresponds to the same streamwise position of the peaks of both turbulent kinetic energy (see Fig. 3.15(a)) and the fraction of subgrid scale kinetic energy (see Fig. 5.3(a)). At the upper wall, the positions of these peaks occur at $x = 2.3$, $50 < y^\star < 80$. This is slightly more downstream than the peak of turbulence kinetic energy (see Fig. 3.15(b)), but more upstream than the peak of fraction of subgrid scale kinetic energy (see Fig. 5.3(b)). The peaks of $\langle f_1 \rangle$ and $\langle f_2 \rangle$ occur at the same positions for other filter type and filter width at both walls. Therefore, $\langle f_1 \rangle$ and $\langle f_2 \rangle$ are more correlated with the turbulent kinetic energy or the fraction of subgrid scale kinetic energy at the lower wall than at the upper wall.

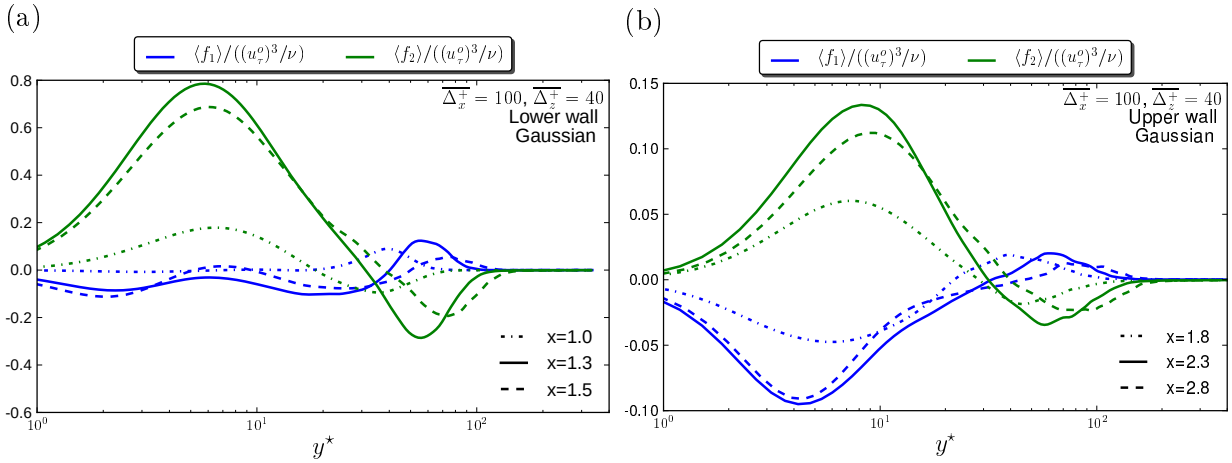

Figure B.15: One-dimensional profiles of the normalized SGS force $\langle f_1 \rangle$, $\langle f_2 \rangle$ at the lower (a) and upper (b) walls using Gaussian filter width $\overline{\Delta_x^+} = 100$, $\overline{\Delta_z^+} = 40$.

B.3.6. Comparison of the exact SGS force $\langle f_1 \rangle$ and $\langle f_2 \rangle$ and their modeled counterparts

A closer look at the models predictive capabilities at streamwise positions $x = 1.3$ corresponding to the peaks of SGS forces at the lower wall are given in Fig. B.16. One-dimensional profiles of exact $\langle f_1 \rangle$, $\langle f_2 \rangle$ and their modeled counterparts by the Smagorinsky and WALE models are analyzed using the Lss-5^{th} and Gaussian filters. A peak of $\langle f_1 \rangle$ and $\langle f_2 \rangle$ (with negative sign) occur at $x = 1.3$, in the range $40 < y^\star < 70$. This is caused by the peak of turbulent kinetic energy roughly in the same range. In the range $y^\star > 100$, both the exact SGS force and the modeled counterparts collapse to zero, corresponding to a poor correlations C_{f_1} and C_{f_2} in the same region (see Fig. 5.40).

In the near wall range $y^\star < 100$, both $\langle f_1 \rangle$ and $\langle f_2 \rangle$ are badly predicted by the two models, especially at $y^\star = 1$. In the range $10 < y^\star < 100$, for the small filter width ($\overline{\Delta_x^+} = 50$, $\overline{\Delta_z^+} = 20$), $\langle f_1 \rangle$ is better predicted with Lss-5^{th} than with the Gaussian filter. However, a better prediction for $\langle f_1 \rangle$ with a large filter width ($\overline{\Delta_x^+} = 200$, $\overline{\Delta_z^+} = 80$) is obtained using the Gaussian filter in the near wall range $4 < y^\star < 100$, while $\langle f_1 \rangle$ is better predicted by the Smagorinsky model for the larger Lss-5^{th} filter width ($\overline{\Delta_x^+} = 200$, $\overline{\Delta_z^+} = 80$). It should be noted that, an identical prediction for $\langle f_2 \rangle$ is obtained by both models with all the Gaussian filter widths and the small Lss-5^{th} filter width ($\overline{\Delta_x^+} = 50$, $\overline{\Delta_z^+} = 20$), through the whole channel. For the large Lss-5^{th} filter width ($\overline{\Delta_x^+} = 200$, $\overline{\Delta_z^+} = 80$), the Smagorinsky model predicts $\langle f_2 \rangle$ better than the WALE model. Therefore, the difference between models for predicting $\langle f_1 \rangle$ and $\langle f_2 \rangle$ is not striking when the Gaussian filter or small Lss-5^{th} filter width is adopted, while the Smgorinsky model performs better than the WALE model for a large Lss-5^{th} filter width ($\overline{\Delta_x^+} = 200$, $\overline{\Delta_z^+} = 80$). A similar behavior is observed at the upper wall.

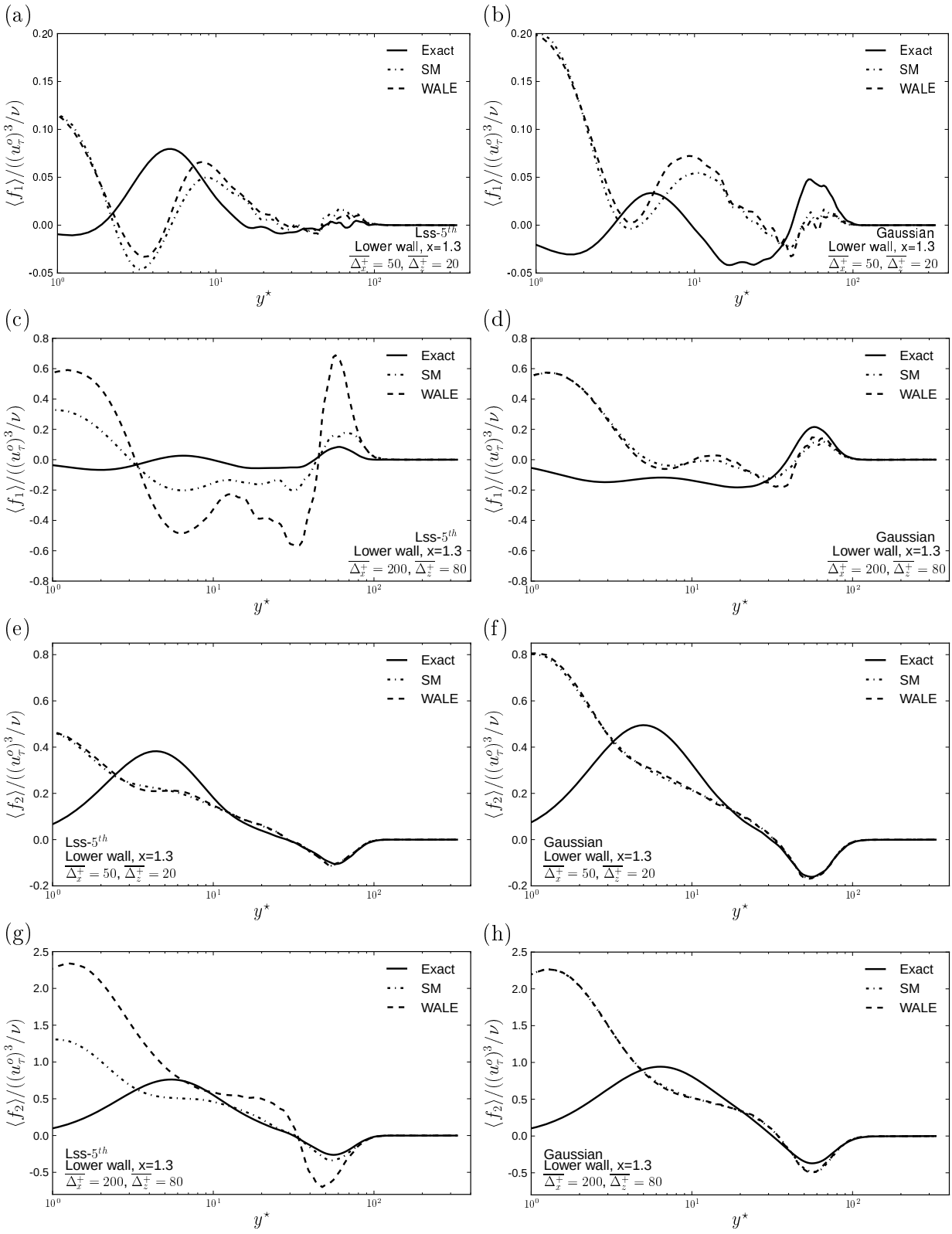

Figure B.16: Comparison of one-dimensional profiles of exact $\langle f_1 \rangle$, $\langle f_2 \rangle$ and their counterparts modeled by the Smagorinsky and WALE models using Lss-5^{th} (a, c, e, g) and Gaussian (b, d, f, h) filters at the lower wall.

In order to complete the analysis of the mean quantities, the standard deviations between the exact and modeled SGS force with a small filter width ($\overline{\Delta_x^+} = 50$, $\overline{\Delta_z^+} = 20$) using both Lss-$5^{th}$ and Gaussian filters at the lower wall are shown in Fig. B.17. In the range $y^\star < 2$, the fluctuations of both $\langle f_1 \rangle$ and $\langle f_2 \rangle$ are badly predicted by the two models using both filter types, while no difference of the predictive capacities is observed between the Smagorinsky and WALE models in the same range. This corresponds to the bad predictions of $\langle f_1 \rangle$ and $\langle f_2 \rangle$ in Fig. B.16. In the range $3 < y^\star < 70$, the WALE model does slightly better than the Smagorinsky model for predicting the fluctuations of f_1 and f_2 with Lss-5^{th} filter. But no better prediction of f_1 is observed by the WALE model in the same range in Fig. B.16. Meanwhile, the level of f_2 fluctuation is better predicted by the WALE model in the range $3 < y^\star < 70$ using the large Gaussian filter width ($\overline{\Delta_x^+} = 200$, $\overline{\Delta_z^+} = 80$), while $\langle f_2 \rangle$ is not better predicted by the WALE model in Fig. B.16. Therefore, the models predictive capabilities for the fluctuations of f_1 and f_2 and for $\langle f_1 \rangle$ and $\langle f_2 \rangle$ are not consistent, and dependent on the filter type and filter width.

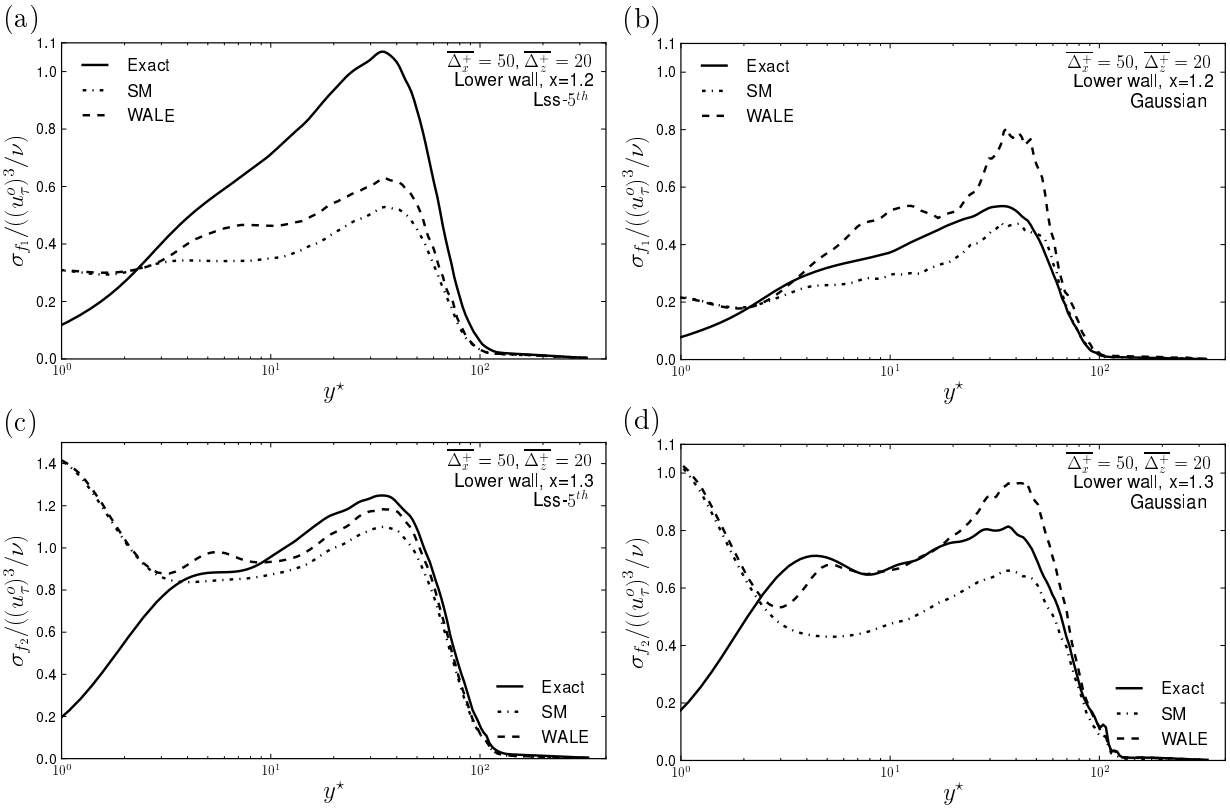

Figure B.17: Comparison of standard deviation of the exact f_1, f_2 and the modeled counterparts obtained by the Smagorinsky and WALE models with filter width $\overline{\Delta_x^+} = 50$, $\overline{\Delta_z^+} = 20$ using Lss-5^{th} (a, c) and Gaussian (b, d) filters at the lower wall.

B.3.7. Correlation of exact and modeled SGS dissipation at the upper wall

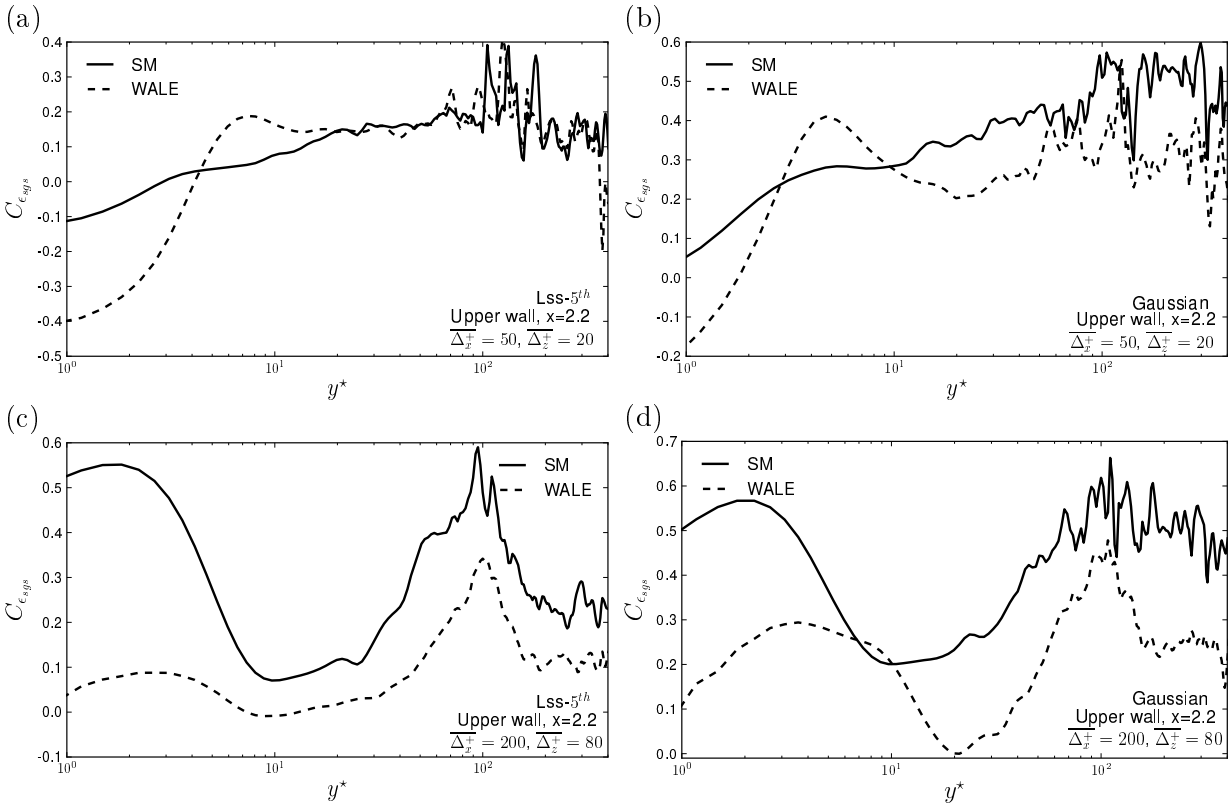

Figure B.18: Comparison of correlation $\langle C_{\epsilon_{sgs}} \rangle$ obtained by the Smagorinsky and WALE models at the upper wall using Lss-5^{th} (a, c) and Gaussian (b, d) filters.

Résumé étendu

Au cours de ces dernières années, la turbulence a beaucoup attiré l'attention de la communauté scientifique, en raison de sa complexité, de la difficulté à comprendre les mécanismes physiques et à les modéliser. Parmis les différents types de turbulence, la turbulence près d'une paroi est particulièrement complexe car les échelles sont d'autant plus petites que l'on se rapproche de la paroi. Les couches limites (régions affectés par la présence d'une paroi) peuvent être soit laminaires ou soit turbulentes en fonction de la valeur du nombre de Reynolds. Notre étude porte sur les couches limites turbulentes.

L'étude de la turbulence de paroi peut être réalisée sur plusieurs types de géométrie simple dont les écoulements de canal plan. La plupart des recherches numériques sur cette géométrie sont axées sur la turbulence à faible nombre de Reynolds (Piomelli *et al.* 1991 [112]; Härtel *et al.* 1994 [62]; Abbà *et al.* 2003 [1]; Cimarelli and De Angelis 2012 [30]). Notre étude a pour objectif de réaliser une analyse a priori des mécanismes de transfert d' énergie et une évaluation a priori des coefficients et des performances des modèle sous-mailles, sur un écoulement de canal plan et un écoulement de canal convergent-divergent à grand nombre de Reynolds. Les coefficients de plusieurs modèles de type "viscosité turbulente" sont étudiés en détail pour plusieurs types et tailles de filtres. Ensuite, les capacités prédictives des différents modèles sous-mailles sont également évaluées dans les deux configurations découlement.

Parmis les modèles sous-mailles pour la simulation des grandes échelles, il existe une famille de modèle de type “viscosité turbulente" basé sur l'hypothèse de Boussinesq. Plusieurs de ces modèles sont analysés dans notre étude. Parmi eux, le modèle de Smagorinsky est capable de prédire correctement la dissipation globale d'énergie cinétique, mais ne permet pas de prédire le bon comportement de la viscosité turbulente proche des parois. Afin de compenser ce défaut, une procédure dynamique a été proposée par Germano *et al.* (1991). Le coefficient du modèle Smagorinsky dynamique n'est alors plus constant mais évalué en fonction des échelles résolues. Le coefficient obtenue retrouve alors le bon comportement près d'une paroi de sorte qu'il est plus adapté pour la simulation des écoulements de paroi. Un autre altenative est le modèle “Wall Adapting Local Eddy viscosity" (WALE). En tenant compte de l'effet du taux de tension et de rotation, ce modèle est capable de reproduire la transition d'un écoulement laminaire à un écoulement turbulent. Le modèle génère une viscosité sous-maille qui possède un bon comportement à proximité d'une paroi et ceci avec une complexité moindre par rapport au modèle de Smagorinsky dynamique. Les mêmes auteurs ont développé récemment un nouveau modèle du même type. Le modèle σ a la propriété de s'annuler automatiquement dès que le champ résolu est bidimensionnel ou à deux composantes, y compris pour les cas de cisaillement pur et de rotation solides. Ce modèle a un faible coût de calcul, il est facile à mettre en œuvre et ne nécessite pas de direction homogène dans l'espace ou dans

le temps. C'est donc un modèle qui possède des qualités intéressantes pour la simulation de la turbulence de paroi.

L'influence du type de filtre et de la largeur de filtre sur l'évaluation a priori des modèles sous-mailles est examinée en détail, en utilisant à la fois un filtre Gaussian et le filtre 'least square spline' que l'on a développé et qui peut être utilisé pour filtrer un champ avec une grille homogène ou non-homogène. Le filtre 'least square spline' (LSS) est défini par des B-splines d'ordre n ajustés par moindre carrés pondérés. Ceci signifie que la somme $\sum_i W_i |f(x) - \overline{f}(x)|^2$ est minimisé (W_i est le coefficient de poids, $f(x)$ est le signal original et $\overline{f}(x)$ est le signal filtré). La relation entre le nombre d'onde de coupure k_c et la largeur du filtre $\overline{\Delta}$ peut être approchée par $k_c \approx L/(2\overline{\Delta})$, indépendamment de l'ordre des splines. La fonction de transfert $\widehat{G}(k\overline{\Delta})$ décroit comme $k^{-(n+1)}$. L'erreur de commutation du filtre LSS est fonction de l'ordre des splines utilisées ($Err(\overline{\Delta}) \approx \overline{\Delta}^n$). L'erreur de commutation avec $n = 5$ (Lss-5^{th}) est $Err(\overline{\Delta}) \approx \overline{\Delta}^5$, ce qui est inférieur à l' erreur de commutation des filtres classiques (souvent au deuxième ordre). Cependant, en raison du fait que la répartition des nœuds utilisée pour le calcul des B-splines est fixé, des fluctuations importantes apparaissent dans le calcul de certaines statistiques. Par conséquent une version améliorée du filtre Lss-5^{th} (filtrage d'un champ deux fois avec un déplacement des noeuds) est proposée et utilisée dans toute les analyses.

Après avoir défini les modèles et les filtres, nous procédons à une analyse a priori sur plusieurs configurations d'écoulement différents avec et sans gradient de pression. Même si les écoulements turbulents homogènes isotropes ne sont pas d'intérêt pratique, ils sont interessant pour une première calibration et validation des modèles sous-mailles. Dans notre étude, l'analyse a priori est d'abord validé sur la turbulence homogène et isotrope à $Re_\lambda = 144$ (où λ est l'échelle de Taylor). La résolution du maillage est 512^3 est la taille du domaine de simulation est $(2\pi \times 2\pi \times 2\pi)$. Les mêmes nombres d'onde de coupure du filtre k_c sont adoptées dans les trois directions et sont situé dans la zone inertielle. Les résultats montrent, en accord avec les recherches antérieures, que tous les coefficients des modèles sous-mailles sont sensibles à la largeur du filtre et au type de filtre. Cependant, les coefficients du modèle de Smagorinsky $\langle C_s \rangle$, du modèle de Smagorinsky Dynamique $\langle C_d \rangle$, du modèle WALE $\langle C_w \rangle$ ainsi que du modèle σ $\langle C_\sigma \rangle$ sont environ 30% plus petits que les valeurs standard préconisée pour ce type d'écoulement.

Afin d'étudier le mécanisme de transfert d'énergie et les performances des modèles sous-maille sur l'écoulement de canal plan à grand nombre de Reynolds la base de données de DNS à $Re_\tau = 950$ fourni par J. Jimenez *et al.* a été utilisée. La simulation DNS a été réalisée en utilisant des conditions limites périodiques dans le sens longitudinal (x) et transverse (z) alors qu'une condition de non-glissement est imposée sur les deux parois parallèles. La résolution de la grille est $N_x \times N_y \times N_z = 2048 \times 385 \times 1535$, dans un domaine de calcul de $8\pi \times 2 \times 3\pi$. Une discrétisation de Chebychev est utilisé dans le sens normal à la paroi (y). Le nombre de Reynolds de cette base de données est plus élevé que ceux utilisé pour les analyses a priori des recherches antérieures. Les opérations de filtrage 2D avec les filtres Lss-5^{th} et Gaussian sont effectuées dans les directions longitudinale et transverse. Aucun filtrage n'est effectué dans la direction normale à la paroi, puisque, dans cette direction, une résolution fine est nécessaire pour résoudre les gradients de l'écoulement moyen.

Dans notre analyse, la fraction de l'énergie cinétique sous-maille sur l'énergie cinétique turbulente est examinée. Une forte inhomogénéité est observée en fonction de la distance à

la paroi, en utilisant différentes tailles de filtres dans les directions longitudinale et transverse. Le transfert d'énergie et la dissipation sous-maille ainsi que leurs contributions positives et négatives respectives sont explorées dans l'espace physique avec différentes largeurs de filtre Lss-5^{th} et Gaussien. Le changement de signe du transfert d'énergie net se produit dans la zone tampon. Le transfert d'énergie inverse, c'est à dire de petites échelles vers les grandes échelles, est observé dans la couche visqueuse et au début de la couche tampon. Ce comportement n'a pas été rapporté dans les études antérieures, mais il est observé dans notre étude pour différentes largeurs du filtre bidimensionnel Lss-5^{th} et Gaussien. Le transfert d'énergie inverse est plus fort que le transfert d'énergie direct qui commence de la couche tampon jusqu'au centre du canal. Ce comportement est en accord avec les statistiques des pourcentages de points pour lesquels le transfert est inverse (jusqu'à 85% à proximité de la paroi pour un peu plus de 50% dans la zone extérieure). Lorsque l'on se rapproche du centre du canal, c'est une cascade directe d'énergie qui domine. Conformément a ce qui avait été montré dans les recherches précédentes à nombre de Reynolds faible ou modéré, nos résultats confirment tout d'abord un pic de dissipation d'énergie proche de paroi. Dans le même temps, les statistiques de dissipation d'énergie net en fonction de la distance à la paroi sont toujours de même signe, correspondant à une dissipation de l'énergie des échelles résolue. Etant donné que les deux contributions de transfert d'énergie sont significativement plus grandes que le transfert net d'énergie, l'analyse plus approfondie des structures cohérentes de la turbulence associés à l'échange d'énergie entre les échelles dans la région proche de paroi devraient fournir plus d'informations sur le mécanisme de transfert.

Dans un second temps, les coefficients du modèle Smagorinsky classique ($\langle C_s \rangle$), du modèle Smagorinsky dynamique ($\langle C_d \rangle$), du modèle WALE ($\langle C_w \rangle$) ainsi que modèle σ ($\langle C_\sigma \rangle$) sont estimés a priori dans la même configuration de canal plan. Dans la zone extérieure, les coefficients $\langle C_s \rangle$ et $\langle C_d \rangle$ sont proche d'une constante, tandis que le comportement du coefficient de Smagorinsky près de la paroi est sensible au rapport de la largeur de filtre dans les directions longitudinale et transverse. La sous-estimation du coefficient de Smagorinsky dynamique $\langle C_d \rangle$ est fonction de la largeur du filtre et du type de filtre. Cette sous-estimation est plus faible en utilisant une petite largeur de filtre test pour un filtre Gaussian, mais pas avec filtre Lss-5^{th}. Les coefficients $\langle C_w \rangle$ et $\langle C_\sigma \rangle$ ont un comportement assez similaire pour cette analyse a priori sur l'écoulement du canal plan. Ils dépendent largement de la largeur du filtre transverse $\overline{\Delta_z^+}$ et sont particulièrement sensibles aux grandes valeurs de celle-ci dans la région proche de paroi. Ceci est due au comportement à la fois de la dissipation sous-maille et de l'opérateur différentiel $\langle S_{ij}^d S_{ij}^d \rangle$ du modèle WALE ainsi que de l'opérateur différentiel $\langle D_\sigma \rangle$ pour le σ modèle. La présente analyse indique qu'une faible largeur du filtre transverse $\overline{\Delta_z^+} < 40$ est recommandée pour les simulations avec les modèles WALE et σ dans la région près de la paroi.

Les corrélations du tenseur sous-maille τ_{ij}, de la force sous-maille f_i, de la dissipation sous-maille ϵ_{sgs} et de leurs homologues modélisés par les modèle sous-maille Smagorinsky et WALE sont ensuite évalués et analysées. Les analyses ne permettent pas de mettre en évidence globalement de grande différence entre les capacités prédictives des modèles sous-maille testés, notamment pour la composante τ_{12}, tant sur la valeur moyenne que sur la déviation standard. Cette analyse permet de confirmer certaines conclusions déjà établies, telles qu'un niveau de corrélation plus grand avec le filtre Gaussien par rapport au filtre Lss-5^{th} ou pour les plus grandes largeurs de filtre (Pope 2000). Cependant, nos

conclusions basé sur les trois critères examinés ne sont pas toujours en accord avec les résultats précédent en particulier dans la couche tampon.

Une étude équivalente est ensuite menée sur une base de données de simulation numérique directe d'un écoulement de canal convergent-divergent documenté dans Marquillie *et al.* 2011 [87] et Laval *et al.* (2012) [73]. Le nombre de Reynolds basé sur la vitesse de frottement à l'entrée ($u_\tau^o = 0.0494$) et la moitié de la largeur du canal ($h = 1$) est $Re_\tau = 617$. Le domaine de simulation est de $4\pi \times 2 \times \pi$ avec une résolution spatiale de $2304 \times 385 \times 576$. Une discrétisation aux différence finis explicite du 4ème ordre est utilisée dans la direction longitudinale tandis que les deux autres directions sont traités par une méthode spectrale (collocation Chebyshev dans la direction normale et Fourier dans la direction transverse). La courbure de la paroi inférieure a été obtenu par un changement de variables pour les opérateurs de dérivées partielle du domaine physique vers un domaine cartésien. Les détails sur le changement de coordonnées sont disponibles dans Marquillie *et al.* 2008 [88]. Afin d'augmenter la convergence des statistiques, les résultats sont moyennés dans la direction transverse et dans le temps. Les unités de paroi basé sur la vitesse de frottement au sommet de la bosse ($u_\tau^s = 0.0695$) sont indiqués par l'exposant $+$, les unités paroi de référence basés sur $u_\tau^o = 0.0494$ à l'entrée du domaine de calcul ont l'exposant $\star$. Sur la paroi inférieure, le gradient de pression adimensionné dC_p/ds (où s est la direction tangente à la paroi) devient positif à $x = -0.2$ et augmente très fortement vers $x = 0.2$. Le gradient de pression à la paroi supérieure plane est, quant à lui, plus lisse et plus faible qu'à la paroi inférieure. Une région de recirculation très fine (visible sur le coefficient de frottement $C_f = \tau_w/(\frac{1}{2}\rho U_o^2)$ se produit dans l'intervalle de $0.5 < x < 1.5$ à la paroi inférieure.

Les résultats de l' analyse a priori dans la région divergente montrent que le transfert d'énergie direct et la dissipation d'énergie directe sont étroitement liés à l'énergie cinétique turbulente engendrée par le fort gradient de pression adverse dû à la courbure. La fraction de l'énergie cinétique sous-maille, les valeurs nettes du transfert et de la dissipation d'énergie atteignent leur maximum exactement à la même position que le pic d'énergie cinétique turbulente à la paroi inférieure, et ceci indépendament de la largeur et du type de filtre. Il est intéressant de noter la présence de dissipation d'énergie inverse net dans le centre du canal convergent alors qu'il n'y a pas de dissipation inverse dans le canal plan. Le pic de cette dissipation d'énergie inverse est un peu plus en amont que le pic de frottement à la paroi, et son intensité dépend fortement de la largeur et du type de filtre. Cependant, la position longitudinale du pic de transfer d'énergie inverse dépend beaucoup du type de filtre. Il est situé près du maximum de frottement à la paroi avec le filtre Gaussien. Enfin, il convient de noter que, pour cet écoulement de canal convergent divergent, l'influence de la raideur du filtre est plus importante pour les transferts d'énergie positive et négative que pour les contributions de la dissipation d'énergie. Ce phénomène est plus prononcé pour l'écoulement de canal convergent-divergent que pour l'écoulement de canal plan. Suite à l'analyse des transfert d'énergie dans la configuration de canal convergent-divergent, les coefficients de quatre modèles sous-maille sont évaluées a priori avec différentes largeurs de filtre Lss-5^{th} et Gaussien. Les résultats sont comparés avec les résultats du canal plan.

En raison du gradient de pression due à la courbure de la paroi inférieure, les coefficients des modèles sont beaucoup plus dispersés que pour le canal plan (voir la section 4.4 du Chapitre 4). Les coefficients négatifs des modèles sous-mailles (correspondant à

la dissipation d'énergie inverse) apparaissent dans le centre du canal convergent. Ces coefficients négatifs ne sont pas observés dans nos résultats de canal plan, car aucune dissipation inverse n'a été observée. Les valeurs des coefficients les plus grandes, supérieure aux valeurs standards pour la turbulence isotrope, se produisent dans la région de canal divergent. La dissipation d'énergie réelle ainsi que son homologue modélisé par des modèles sous-mailles étant très sensibles au type de filtre ceci conduit à de plus grandes valeurs des coefficients des quatre modèles sous-mailles avec le filtre Gaussien qu'avec le filtre Lss-5^{th} au centre du canal divergent. A l'inverse, les coefficients $\langle C_s \rangle$ et $\langle C_d \rangle$ sont plus petits dans la région proche de paroi que dans le centre du canal divergent. Cela est dû à une plus grande valeur de la norme du tenseur des taux de déformation $\langle \overline{S}_{ij} \rangle$ près de la paroi et ceci indépendamment du type de filtre et de la largeur du filtre. Le coefficient de Smagorinsky dynamique $\langle C_d \rangle$ s'étend sur une gamme plus large et est plus éloigné de l'estimation a-priori de $\langle C_s \rangle$ par rapport aux résultats du canal plan. Les comportements en fonction de la largeur du filtre de l'opérateur $\langle S^d_{ij} S^d_{ij} \rangle$ du modèle WALE et de l'opérateur $\langle D_\sigma \rangle$ du modèle σ donnent lieu à des valeurs fortes de $\langle C_w \rangle$ et $\langle C_\sigma \rangle$ près des parois inférieure et supérieure dans la région divergente, en particulier pour la plus grande largeur du filtre ($\overline{\Delta_x^+} = 200$, $\overline{\Delta_z^+} = 80$) et ceci pour les deux types de filtres. Les coefficients des modèles WALE et σ ont un comportement assez similaire dans notre analyse a priori. Une analyse plus détaillée dans la région de gradient de pression adverse montre que les coefficients des modèles ont des comportements différents près des deux parois par rapport aux résultats de canal plan. A la paroi inférieure, $\langle C_s \rangle$ et $\langle C_d \rangle$ sont très sensibles à la variation du gradient de pression. Un extremum du coefficient de modèle sous-maille est observé dans la zone de recirculation pour chacun des modèles. Près de la fin de la zone de recirculation, $\langle C_w \rangle$ est légèrement plus homogène que pour le canal plan. Cependant, dans toute la région de recirculation, $\langle C_\sigma \rangle$ change plus rapidement que les résultats du canal plan.

Les corrélations entre quantité sous-maille réelles et les mêmes quantités modélisées sont étudiés. Les grandes valeurs des composantes du tenseur sous-maille sont positionné aux même endroit que les grandes valeurs de l'énergie cinétique turbulente à la paroi inférieure alors quelles sont légèrement décalées à la paroi supérieure. Ceci est en accord avec le comportement de la dissipation d'énergie. Mais les grandes valeurs du tenseur ne correspondent pas aux fortes corrélations dans la région de recirculation. Dans la région de recirculation, une faible corrélation $C_{\tau_{12}}$ de la composante faible τ_{12} est observée. L'influence du type de filtre sur $C_{\tau_{12}}$ est plus grande pour les plus petites que pour les plus grandes largeurs du filtre. Une corrélation plus élevée de ϵ_{sgs} et de $f_2 = \partial \tau_{2j} / \partial x_j$ est également observée avec le filtre Gaussien comparé au filtre Lss-5^{th}. Dans la région du canal divergent, le maximum de ϵ_{sgs} est encore plus grand que pour le canal plan. La différence entre les performances des modèles sont également analysés. Dans la plupart des régions externes de la paroi inférieure, le modèle de Smagorinsky conduit à des corrélations de $C_{\tau_{12}}$, C_{f_1}, C_{f_2}, ainsi que $C_{\epsilon_{sgs}}$ plus grandes qu'avec le modèle WALE . Il est important de noter que la moyenne et la fluctuation du tenseur τ_{12} sont mal prédites par les modèles Smagorinsky et WALE dans la région proche de la paroi, ce qui est en accord avec la faible corrélation de $C_{\tau_{12}}$ observée dans le même intervalle. D'autre part, bien que les coefficients des modèles sous-mailles sont calculés en faisant correspondre la dissipation réelle à la dissipation modélisé, les corrélations entre les deux termes reste faible pour tous les modèles.

Dans la configuration d'écoulement analysée dans notre étude conduisant à des gradients de pressions différents sur les deux parois, le gradient de pression est fort et évolue rapidement dans l'espace. La physique de l'écoulement est donc loin de l'équilibre et les résultats de notre analyse a priori sont difficiles à généraliser à d'autres écoulements. Par conséquent, il serait intéressant de faire des analyses a priori et a posteriori pour d'autres configuration avec gradients de pression différents. Ceci permettrait d'améliorer nos connaissances sur le lien entre les mécanismes de transfert d'énergie et les performances des modèles sous-mailles dans des configurations d'écoulements plus variés et donc plus représentatives des problèmes réels.

Analyse a-priori de modèles LES sous-mailles appliqués à la turbulence de paroi avec gradients de pression

Après plus de 50 ans de recherche, l'intéret de la simulation des grandes échelles pour la simulation des écoulements instationnaire a été largement démontrée et cette méthode est aujourd'hui utilisée pour une grande variété d'applications industriels. Plusieurs classes de modèles sous-maille ont été proposées dont celle très connue des modèles de viscosité sous-maille souvent préférrées pour leur simplicité et leur robustesse. La formulation de ces modèles comporte un coefficient qui doit être ajusté ppour chaque type d'écoulement et qui a été analysé pour des géométries simples. L'objectif de ce travail est de réaliser des analyses a-priori de modèles sous-mailles dans un canal plan et un canal convergent-divergent à relativement grand nombre de Reynolds. Les influences du type de filter et de la largeur du filtre sont systématiquement abordées pour chacune des statistiques. Le transfert d'énergie sous-maille et la dissipation sous-maille sont tout d'abord étudiés. Ensuite, les coefficients des modèles Smagorinsky, Smgorinsky dynamique, WALE et du modèle Sigma nouvellement proposé sont estimés a-priori. Il est démontré que les coefficients des quatres modèles sont non-homogème dans le domaine de simulation est sont largement affectés par le gradient de pression adverse, principalement dans la zone de recirculation. enfin, les corrélations entre les quantités exactes et leur équivalents modélisés sont examinés. Les résultats montrent un faible niveau de prédiction des modèles sous-maille et une grande variabilité des quantités modélisées dans les regions de fort gradient de pression adverse. Ceci peut expliquer les difficultés pour obtenir de bons résultats LES dans une telle configuration.
Mots Clés : Simulation des grandes échelles, turbulence, filtrage, simulation numérique directe.

A-priori analysis of LES subgrid scale models applied to wall turbulence with pressure gradients

After more than 50 years of investigation, Large Eddy Simulation has demonstrated its benefit for unsteady flow simulation and is currently applied in a wide variety of engineering applications. Several classes of subgrid scale models were proposed, including the well known eddy viscosity models, usually preferred because of their simplicities and robustness. The formulation of these models includes a coefficient which needs to be analyzed for each flow configuration and which has been investigated in simple geometries. The aim of present work is to perform a-priori analysis of subgrid scale models in plane channel flow and in a converging-diverging channel flow at fairly large Reynolds number. The influences of the filter type and filter width are systematically addressed in analyses of all statistics. The SGS energy transfer and SGS energy dissipation are firstly analyzed. Then, the a priori estimate of the coefficients of subgrid scale models, including the standard Smagorinsky, Dynamic Smagorinsky, the WALE and the new updated σ models, are investigated in detail. It is shown that, the coefficients of the four models are non-homogeneous in the simulation domain and are largely affected by the adverse pressure gradient, especially in the recirculation region. Finally, the correlations between the exact quantities and their counterparts modeled by the subgrid scale models with respect to three criteria are explored. The results show a low predictability of subgrid scale models and a strong variability of the modeled quantities in the region of strong adverse pressure gradient. This may explain the difficulty to obtain accurate LES results in such flow configuration.
Keywords: Large Eddy Simulation, turbulence, filter, direct numerical simulation